

Synthesis and Characterization of Al6061/Al₂O₃ Metal Matrix Nanocomposites Fabricated by Stir-Casting

Doctoral Thesis

To be awarded the degree
Doctor of Engineering (Dr.-Ing)

Submitted by

Othman Ahmed Othman Mohamed

from Bani Souwaif, Egypt

approved by the
Faculty of Natural and Material Sciences,
Clausthal University of Technology

Date of oral examination

10.04.2019

Bibliografische Information der Deutschen Bibliothek

Die Deutsche Bibliothek verzeichnet diese Publikation in der Nationalbibliografie; detaillierte Bibliografische Daten sind im Internet über <http://dnb.ddb.de> abrufbar.

Bibliographic information published by the Deutsche Nationalbibliothek

The Deutsche Nationalbibliothek lists this publication in the Deutsche Nationalbibliografie; detailed bibliographic data are available by Internet at <http://dnb.dnb.de>.

Zugl.: Clausthal, Technische Uni., Diss., 2019

„Dissertation Technische Universität Clausthal“

Dekan:	Prof. Dr.-Ing. Karl-Heinz Spitzer
Vorsitzender der Promotionskommission:	Prof. Dr.-Ing. Albrecht Wolter
Hauptberichterstatter:	Prof. Dr.-Ing. habil. Lothar Wagner
Mitberichterstatter:	Prof. Dr.-Ing. Volker Wesling

D 104

© Oberharzer Druckerei, Fischer & Thielbar GmbH

Alte Fuhrherrenstraße 5. 38678 Clausthal-Zellerfeld. www.oberharzer-druckerei.de

Dieses Werk ist urheberrechtlich geschützt.

Alle Rechte, auch die der Übersetzung, des Nachdruckes und der Vervielfältigung des Buches, oder Teilen daraus, vorbehalten. Kein Teil des Werkes darf ohne schriftliche Genehmigung des Verlages in irgendeiner Form reproduziert oder unter Verwendung elektronischer Systeme verarbeitet, vervielfältigt oder verbreitet werden.

This document is protected by copyright law.

No part of this document may be reproduced in any form by any means without prior written authorization of the publisher.

1. Auflage 2019

Printed in Germany.

Bezugsadresse: Prof. Dr.-Ing. habil. Lothar Wagner
Institut für Werkstoffkunde und Werkstofftechnik (IWW)
Technische Universität Clausthal
Agricolastraße.6
D-38678 Clausthal-Zellerfeld

ISBN 978-3-948171-02-5

„Gedruckt mit Unterstützung des Deutschen Akademischen Austauschdienstes“

Acknowledgments

In the frame of the DAAD GERLS 2014 scholarship under supervision of Prof Lothar Wagner in the Institute of Materials Science and Engineering– Clausthal University of Technology, this doctoral work was carried out.

All praises to Allah the Almighty for giving me the blessing, chance, strength and endurance to complete this study.

My greatest and deepest gratitude is dedicated to my supervisor Prof. Lothar Wagner for accepting me in his research group and giving me the opportunity to pursue my Ph.D. degree at TU-Clausthal under his supervision, the continuous support of my Ph.D. study and research, his patience, motivation, enthusiasm, and immense knowledge. His guidance helped me in all the time of research and writing of this thesis. I could not have imagined having a better advisor and mentor for my Ph.D. study. Besides, I would like to direct my special thanks and appreciation to co-referent Prof. Volker Wesling for his consideration, valuable notes and time during reviewing my thesis.

For the financial support in the framework of the German Egyptian Research Long-term Scholarship program (GERLS) I would like to acknowledge the German Academic Exchange Service (DAAD) and the Egyptian Ministry of Higher Education (MoHE)

Special acknowledgement to Dr. rer. Nat. M. Wollmann and Dr.-Ing. M. Mhaede for their continuous support during this study, whose office doors were always open whenever I ran into a trouble spot or had a question about my research or writing. I would like to direct my gratitude to my best friend during the PhD time M. Sc. M. Basha for his considerable contributions and discussions throughout this work. Moreover, I would like to thank Dr.-Ing. M. Harhash for his valuable review and comments on this work.

Not to forget thanking all the members in our research group for their friendly and scientific assistance especially, M. Sc. S. Levin. Moreover, I would like to thank the technical staffs at IWW, especially Mr. J. Schumann, Mr. G. Neuse, Mr. P. König, Mr. T. Gerhardt and Mr. U. Körner for their technical support. Furthermore, I owe thanks to my students who supported me performing the experimental tasks.

Finally, I must express my very profound gratitude to my parents, my dear wife, and my children for providing me with unfailing support and continuous encouragement throughout my years of study and through the process of researching and writing this thesis. This accomplishment would not have been possible without them.

Thank you.

This page intentionally left blank

Abstract

Over the past decade, the metal matrix nanocomposites (MMNCs) have been used in many applications, owing to their competing properties such as high strength to weight ratio, high corrosion resistance, and fatigue strength. The reduction in vehicle weight or increasing the strength to weight ratio of the materials used, provides both fuel efficiency and reducing the CO₂ emissions. The fabricate of such composites should be carried out through fulfilling two main considerations; the constitutes (matrix and reinforcement nanoparticles) and the fabrication method. Aluminum alloys, as a matrix, possess remarkable properties of low density, good corrosion resistance, and low thermal expansion. Such characteristics make them attractive chose to perform as matrices in the world of MMNCs. The conventional aluminum alloys are usually used in automotive, aerospace industry, and structural materials owing to their higher performance either mechanically, or functionally. The aluminum features do not end at this point, but it is also characterized by excellent recyclability which makes aluminum a good environment friend by different means of reducing the energy consumption for their production, emissions accompanied with production, and the consumption of fresh raw materials. In this concern, Al6061 was utilized in this research as a matrix, due to its wide range of applications in automotive and ground transportation, thermal management, aerospace, industrial, recreational and infrastructure industries, as well as advanced military systems. Choosing the reinforcement nanoparticles too is subjected to many aspects of durability, cost considerations, ease of introducing into the matrix, and phase stability. With high strength elastic modulus, good wettability, and low thermal expansion coefficient, was Alumina (Al₂O₃) a promising candidate in the MMNCs synthesizing in this work. The reinforcing role of the nanoparticles raise from the fact of their small size which enables them to direct to the lattice defects like dislocations and reveal several strengthening mechanisms such as load bearing, Hall-Pitch, difference in elastic modulus and thermal expansion coefficient, and Orowan mechanisms. Consequently, the hybrid materials (Aluminum Matrix Nanocomposites (AMNCs)) attract attention to design lightweight materials with improved mechanical, metallurgical and physical properties.

Choosing a compatible manufacturing technique is of the same importance degree as choosing the matrix and the reinforcement nanoparticles. Proper method for nanoparticles addition should guarantee uniform, simplicity, and homogenous destruction of the reinforcements over the matrix and ability of use on large scale. Therefore, stir casting is considered is probably the simplest and most economical technique used to produce MMNCs by a liquid state route. However, the process is restricted by the high agglomeration rates resulted from the poor wettability of the nanoparticles and the air entrapment, which occurred during stirring with a tendency of the nanoparticles to sink or float due to the density difference between the matrix and particles.

The present study focuses on the fabrication and characterization of the AMNCs. The AMNCs synthesizing is carried out through stir casting using Al₂O₃ nanoparticles and Aluminum 6061 as a matrix. The proposed research provides robust empirical approaches to overcome the main restrictions of AMNCs fabrications such as poor wettability, agglomeration, porosity, inhomogeneous distribution, high production costs, and durability. The objective of this research is to investigate the process feasibility, the effective reinforcement weight fraction (over which the properties deteriorate), and the fabricated hybrid materials properties (at room and elevated temperature (300°C)) compared to the monolithic alloy.

Furthermore, the metallurgical/mechanical/and functional behavior of the produced materials were evaluated utilizing different mechanical tests (tensile, hardness, fatigue and creep tests) and microstructure investigation techniques (optical and scanning electron microscopy). For further enhancement of the fatigue and the functional behavior of the AMNCs, the mechanical surface treatments (MSTs), namely shot peening and roller burnishing, were conducted. The

impact of the shot peening and roller burnishing on the fatigue and the creep behavior was unveiled. The wear and corrosion behavior of the different composites were tested, as well. Furthermore, the weldability of the AMNCs was investigated using the rotary friction welding technique. The optimization of the welding parameters was carried out based on the design of experiment method using Minitab 17. Economically, the recyclability of the AMNCs was clarified by re-fabrication of the produced AMNCs through investigating the change of their behavior compared to unreinforced alloy.

The nanocomposites exhibited finer grain size with enhanced mechanical behavior. The yield strength and ultimate tensile strength are improved by 50% and 32% respectively compared to the unreinforced alloy. Moreover, the nanocomposites represented an enhancement in the fatigue life (Electropolished) about 26% and 64% in air and 3.5% NaCl electropolished condition with improved creep rate and corrosion resistance, with further improvement after conducting mechanical surface treatments such as shot peening and roller burnishing to reach 37% and 127% after conducting shot peening in air and 3.5% NaCl compared to the electropolished unreinforced alloy, while it reaches 48% and 154% after conducting roller burnishing. Besides, the AMNCs show higher creep life than the unreinforced alloy not only without further mechanical surface treatments, but also after conducting shot peening. The tribological properties and corrosion resistance of the AMNCs are also enhanced compared to the unreinforced matrix. The AMNCs proved good durability not only by the good weldability, but also by the competed properties obtained after recycling.

In conclusion, an analytic model is proposed to reach a simple equation which could describe and detect the expected behavior of the AMNCs based on the weight fraction and both matrix and reinforcements properties. The experimental results show good agreement and effectiveness of the model to predict the mechanical properties of the AMNCs.

Kurzfassung

In den letzten zehn Jahren wurden die Metall-Matrix-Nanocomposites (MMNCs) aufgrund ihrer konkurrenzfähigen Eigenschaften, wie zum Beispiel der hohen spezifischen Festigkeit, der sehr guten Korrosionsbeständigkeit und Dauerfestigkeit, in vielen Anwendungen eingesetzt. Die Reduzierung des Fahrzeuggewichts durch die Erhöhung der spezifischen Festigkeit dieser Composite sorgt sowohl für eine höhere Kraftstoffeffizienz als auch für eine Reduzierung der CO₂-Emissionen. Die Herstellung und Entwicklung solcher Verbundwerkstoffe sollte sich an den folgenden zwei Gesichtspunkten orientieren der Komponenten (Matrix- und Verstärkungsnanopartikel) und der Herstellungsmethode. Aluminiumlegierungen besitzen, als Matrix, bemerkenswerte Eigenschaften wie die gute Korrosionsbeständigkeit, die geringe Dichte und die geringe Wärmeausdehnung. Solche Eigenschaften machen sie attraktiv, wenn sie als Matrix in der Welt der MMNCs eingesetzt werden. Die konventionellen Aluminiumlegierungen werden aufgrund ihrer höheren mechanischen und funktionellen Leistungsfähigkeit in der Regel in der Automobil-, Luft- und Raumfahrtindustrie zur Herstellung von Strukturwerkstoffen eingesetzt. Weiterhin zeichnet sich Aluminium durch seine ausgezeichnete Recyclingfähigkeit aus, welche es zu einen umweltfreundlichen Werkstoff macht, da sich der Energieverbrauch bei der Herstellung, die mit der Produktion verbundenen Emissionen und der Verbrauch von frischen Rohstoffen reduziert. In diesem Zusammenhang wurde die Aluminiumlegierung Al6061 in dieser Forschungsarbeit als Matrix verwendet, da sie ein breites Anwendungsspektrum in den Bereichen Automobil, Wärmemanagement, Luft- und Raumfahrt, Industrie, Freizeit, Infrastruktur sowie fortschrittliche militärische Systeme bietet.

Die Wahl der Verstärkungs-Nanopartikel unterliegt vielen dabei Aspekten. Diese können sein: Haltbarkeit, Kostenbetrachtung, einfache Einführung in die Matrix und die Phasenstabilität. Mit hohem Elastizitätsmodul, guter Benetzbarkeit und niedrigem Wärmeausdehnungskoeffizienten stellt Aluminiumoxid (Al₂O₃) eine viel versprechende Option dar um MMNCs in dieser Forschungsarbeit künstlich zu erzeugen. Die verstärkende Wirkung der Nanopartikel ergibt sich aus ihrer geringen Größe, die es ihnen ermöglicht sich auf Gitterdefekte wie Versetzungen zu platzieren und dort verschiedene Verstärkungsmechanismen wie zum Beispiel Tragfähigkeit, Hall-Pitch, Differenz von Elastizitätsmodul und thermische Ausdehnungskoeffizient und Orowan-Mechanismen zu bewirken. Die Hybridmaterialien (Aluminum-Matrix-Nano-Composites (AMNCs)) erlangen deshalb zunehmend Bedeutung, wenn es um Leichtbauwerkstoffe mit verbesserten mechanischen, metallurgischen und physikalischen Eigenschaften geht.

Die Wahl eines kompatiblen Herstellungsverfahrens ist ebenso wichtig wie die Wahl der Matrix und der Verstärkungs-Nanopartikel. Die Methode für die Zugabe von Nanopartikeln muss eine gleichmäßige, einfache und homogene Verteilung der Verstärkungsnanopartikeln über die Matrix und die Fähigkeit zur Verwendung in großem Maßstab gewährleisten. Daher wird das Rührgießen als die wahrscheinlich einfachste und wirtschaftlichste Technik zur Herstellung von MMNCs betrachtet. Der Prozess wird jedoch durch die hohen Agglomerationsraten eingeschränkt, die aus der schlechten Benetzbarkeit der Nanopartikel und der Lufteinschlüsse resultieren. Aufgrund der Dichtedifferenz zwischen der Matrix und

den Partikeln kam es beim Rühren nur teilweise zum Schweben, teilweise aber auch zum Herabsinken der Nanopartikel.

Die vorliegende Studie konzentriert sich auf die Herstellung und Charakterisierung der AMNCs. Die Synthese der AMNCs erfolgt durch Rührgießen mit Al_2O_3 -Nanopartikeln und Aluminiumlegierung 6061 als Matrix. Die vorliegende Arbeit bietet empirische Ansätze zur Überwindung der Hauptrestriktionen der AMNC-Fertigung wie schlechte Benetzbarkeit, Agglomeration, Porosität, inhomogene Verteilung, hohe Produktionskosten und geringe Haltbarkeit. Ziel dieser Forschung ist es, die Machbarkeit des Verfahrens, den effektiven Gewichtsanteil der Verstärkung (über den sich die Eigenschaften verschlechtern) und die Eigenschaften der hergestellten Hybridmaterialien bei Raum- und erhöhter Temperatur (300°C) im Vergleich zur monolithischen Legierung zu untersuchen .

Darüber hinaus wurde das metallurgische, mechanische und funktionelle Verhalten der hergestellten Werkstoffe mittels verschiedener mechanischer Tests (Zug-, Härte-, Ermüdungs- und Kriechversuche) und Mikrostrukturuntersuchungen (Licht und Rasterelektronenmikroskopie) bewertet. Zur weiteren Verbesserung des Ermüdungs- und des Funktionsverhaltens der AMNCs wurden die mechanischen Oberflächenbehandlungen (MSTs) Kugelstrahlen und Festwalzen durchgeführt. Der Einfluss des Kugelstrahlens und des Festwalzens auf das Ermüdungs- und das Kriechverhalten wurde ermittelt. Auch das Verschleiß- und Korrosionsverhalten der verschiedenen Verbundwerkstoffe wurde getestet. Weiterhin wurde die Schweißbarkeit der AMNCs für das Rotations-Reibschweißverfahren untersucht. Die Optimierung der Schweißparameter erfolgte auf Basis der Versuchsplanung mit Minitab 17. Ökonomisch wurde die Recyclingfähigkeit der AMNCs durch ein erneutes Vergießen der produzierten AMNCs hinsichtlich Untersuchung der Veränderung ihres Verhaltens im Vergleich zu unverstärkten Legierungen untersucht.

Die Nanocomposites zeigten eine feinere Korngröße mit verbessertem mechanischem Verhalten als die unverstärkte Legierung. Die Streckgrenze und die Zugfestigkeit wurden gegenüber der unverstärkten Legierung um 50 % bzw. 32 % verbessert. Darüber hinaus erzielten die Nanocomposites eine Erhöhung der Ermüdungslebensdauer in Luft um 26 % (elektroliert) und um 64 % in 3,5 % NaCl (elektroliert) mit einer zusätzlich verbesserten Kriechrate und Korrosionsbeständigkeit. Nach der Durchführung der mechanischen Oberflächenbehandlungen wie Kugelstrahlen und Festwalzen konnte eine weitere Verbesserung auf 37 % in Luft und 127 % in 3,5% NaCl nach dem Kugelstrahlen und dem entsprechend 48 % und 154 % nach dem Festwalzen erreicht werden. Zudem weisen die AMNCs nicht nur ohne weitere mechanische Oberflächenbehandlung, sondern auch nach dem Kugelstrahlen eine höhere Kriechfestigkeit auf, als die unverstärkte Legierung. Auch die tribologischen Eigenschaften und die Korrosionsbeständigkeit der AMNCs werden gegenüber der unverstärkten Matrix verbessert. Die gute Einsatzbarkeit der AMNC resultiert nicht nur aus der guten Schweißbarkeit, sondern auch aus den interessanten Eigenschaften nach dem Recycling .

Abschließend wird ein analytisches Modell vorgeschlagen, um eine einfache Gleichung ableiten zu können, die das erwartete Verhalten der AMNCs auf der Grundlage des Gewichtsanteils und der Matrix- und Verstärkungseigenschaften beschreibt. Die experimentellen Ergebnisse zeigen eine gute Übereinstimmung und beweisen die Zuverlässigkeit des Modells zur Vorhersage der mechanischen Eigenschaften der AMNCs.

Table of Contents

Acknowledgments	III
Abstract	V
Kurzfassung	VII
Nomenclature	XI
1 Introduction	1
1.1 Motivation and objectives:	2
1.2 Thesis synopsis	5
2 Literature Review	7
2.1 Aluminum and Aluminum Alloys	7
2.1.1 Aluminum Production Overview	7
2.1.2 Aluminum 6061 alloy	8
2.2 Aluminum Matrix Nanocomposites (AMNCs)	10
2.2.1 Properties of the AMNCs	11
2.3 Synthesis of MMNCs	18
2.3.1 Liquid Processes	18
2.3.2 Solid Processes	20
2.3.3 Semi-solid-State Processes	21
2.4 Fabrication of the AMNCs by stir casting	22
2.5 Strengthening mechanisms in the AMNCs.....	25
2.6 Recycling of the MMNCs.....	28
3 Experimental Procedures	29
3.1 Materials	29
3.2 Fabrication	30
3.3 Microstructure evaluation	32
3.4 Mechanical characterization:	33
3.4.1 Tensile test and Hardness measurements:	33
3.4.2 Fatigue test	34
3.4.3 Creep-rupture test:	35
3.4.4 Wear resistance test:	36

3.5	Mechanical surface treatments.....	37
3.5.1	Shot peening.....	37
3.5.2	Roller Burnishing:.....	38
3.5.3	Optimization of the shot peening and roller burnishing parameters:	39
3.6	Surface roughness	42
3.7	Residual stresses measurements by Incremental Hole Drilling Method (IHD).....	43
3.8	Corrosion resistance:.....	44
3.9	Weldability of the AMNCs	45
4	Results and Discussion.....	47
4.1	Microstructure evaluation	47
4.1.1	Fundamental characterization of the Al6061 matrix.....	47
4.1.2	Characterization/Analysis of the Al6061/Al₂O₃ composites.....	50
4.1.3	Summary of the grain refinement, Porosity and agglomeration results.....	58
4.2	Mechanical characterization	62
4.2.1	Tensile properties and hardness	62
4.2.2	Fatigue behavior:	66
4.2.3	Creep behavior	86
4.3	Wear resistance	97
4.4	Corrosion behavior.....	99
4.5	Weldability of the 1wt.% Al ₂ O ₃ Aluminum Matrix Nanocomposites.....	101
4.6	Analytical model of the strength contributors in the AMNCs	113
5	Conclusions and prospective recommendations.....	119
5.1	Prospective recommendation	121
6	References	123

Nomenclature

Greek symbols

Symbol	Term	Unit
v_p	Volume fraction	[-]
σ	Strength	[MPa]
$\Delta\alpha$	Difference in the thermal expansion coefficients	[K ⁻¹]
ΔT	Temperature difference	[K]
γ	Gamma phase of aluminium/Surface tension	[-]
ϕ	Deformation degree	[-]
σ_a	Stress amplitude	[MPa]
\emptyset	Diameter	[mm]
σ	True stress	[MPa]
ρ	Density	[g/cm ³]
α	Alpha aluminum	[-]
β	Beta intermetallic	[-]
μ_G	Chemical potential of gas	[J/mol]
μ_L	Chemical potential of liquid	[J/mol]
η	Viscosity	[Pa.sec]
ϵ	strain	[-]
ϵ°	Strain rate	[sec ⁻¹]

Latin symbols

Symbol	Term	Unit
O	Annealing heat treatment of aluminum alloys	[-]
T4	Natural precipitation hardening heat treatment of aluminum alloys	[-]
T6	Artificial precipitation hardening heat treatment of aluminum alloys	[-]
Al ₂ O ₃	Aluminum oxide	[-]
SiC	Silicon carbide	[-]
AlN	Aluminum nitride	[-]
MgO	Magnesium oxide	[-]
B ₄ N	Boron nitride	[-]
TiC	Titanium carbide	[-]
TiO ₂	Titanium oxide	[-]

CO ₂	Carbon dioxide	[-]
NaCl	Sodium chloride	[-]
Al ₂ O ₃ .3H ₂ O	Gibbsite	[-]
Al ₂ O ₃ .H ₂ O	Boehmite	[-]
Na ₃ K(AlSiO ₄) ₄	Nepheline	[-]
KAl ₃ (SO ₄) ₂ (OH) ₆	Alunite	[-]
Mg ₂ Si	Magnesium silicate	[-]
ZrO ₂	Zirconia oxide	[-]
WC	Tungsten carbide	[-]
b	Burger's vector	[nm]
dp	Particle diameter	[nm]
G	Shear modulus	[GPa]
σ _m	Yield strength	[MPa]
l	Size of particulate parallel to the loading direction	[nm]
t	Size of the particulate perpendicular to the loading direction	[nm]
k _y	Strengthening coefficient	[MPa.nm ^{0.5}]
Vol.%	Volume fraction	[-]
Wt.%	Weight fraction	[-]
HF	Hydrofluoric acid	[-]
KMnO ₄	Potassium permanganate	[-]
NaOH	Sodium hydroxide	[-]
EDX	Energy Dispersive X-Ray Spectroscopy	[-]
HV	Hardness Vickers	[-]
R	Fatigue strength ratio	[-]
J _{crp}	Creep compliance	[MPa ⁻¹]
E _{rel}	Relaxation modulus	[MPa]
SCCW14	Spherically conditioned cut wire shots with diameter of 0.36 mm	[-]
Ra	Average roughness	[μm]
Rz	Ten-spot average roughness	[μm]
Rmax/Ry	Maximum roughness height	[μm]
I _{corr}	corrosion current density	[A/mm]
EW	Equivalent weight	[g/equivalent]

A	Area	[mm ²]
G	ASTM grain size number	[-]
k	Boltzmann's constant	[J/K]
E	Young's modulus	[GPa]

Abbreviations

Acronym	Term
MMNC	Metal Matrix Nanocomposites
AMNC	Aluminum Matrix Nanocomposites
MMC	Metal Matrix Micro-composites
MST	Mechanical Surface Treatment
DRA	Discontinuously Reinforced Aluminium
TIG	Tungsten Inert Gas
MIG	Metal Inert Gas
YS	Yield Strength
UTS	Ultimate Tensile Strength
HIP	Hot Isostatic Pressure
MWCNT	Multiwall Carbon Nanotubes
CNT	Carbon Nanotubes
DMD	Disintegrated Melt Deposition
PM	Powder Metallurgy
MA	Mechanical Alloying
HPDC	High Pressure Die Casting
GND	Geometrically Necessary Dislocations
CTE	Coefficient of Thermal Expansion
EM	Elastic Modulus
SP	Shot Peening
USP	Ultrasonic Shot Peening
LSP	Laser Shock Peening
RFW	Rotary Friction Welding
SPD	Sever Plastic Deformation
EP	Electropolishing
ATS	Applied Test Systems
RB	Roller Burnishing
IHD	Incremental Hole-Drilling Method

SCE	Saturated Calomel Electrode
Ps	Forging pressure
ts	Forging time
Pr	Friction pressure
tr	Friction time
rpm	Rotational speed
SEM	Scanning Electron Microscope
RT	Room temperature
Rec	Recycled 1wt.% Al ₂ O ₃ composites
SSCS	Saturation Curve Solver by Shock form Aeronautique Inc.
XRD	X-ray diffraction

1 Introduction

Aluminum and its alloys come in the third place among the commercially used engineering materials due to their wide range applications. The Al 6000 alloys have received a boost in their castings production in recent decades starting by strengthening through copper and chromium to control the recrystallization. Al 6061 (Aluminum-Silicon-Copper-Magnesium) is one of the most common 6000 series due to its desirable characteristics such as high strength to weight ratio, good workability, good toughness, good surface finish, desirable workability, excellent conductivity and corrosion resistance. The excellent corrosion resistance, even after welding, enabled it to be used in some railroad and marine applications [1]. In this work, a heat-treated aluminum Al 6061 is used with Silicon and magnesium as major alloying elements. The commonly available Al6061 commercial grades are pre-tempered and tempered grades 6061-O (annealed), 6061-T6 (solution heat treated and artificially aged), 6061-T651 (Solution heat treated, stress-relieved stretched and artificially aged) and 6061-T4(solution heat treated and naturally aged) [2].

High strength lightweight materials are the key feature in most of the modern design. Manufacturing materials with high stress to weight ratio to reduce the fuel consumption in the structural applications, particularly aerospace, and automotive industries was the researchers' concern in the past few years [3]. Considerable attention has been given to composite materials as the most appropriate candidates for fulfilling the requirements of high strength to weight ratio required by energy saving limitations. One of the composite materials categories is the metal matrix nanocomposite (MMNCs), which proved over its attractive combination of properties that they are the interesting suitable choice for this field of applications. Of the materials category MMNCs are the Aluminum matrix nanocomposites (AMNCs) providing unique properties set of high specific strength, stiffness, wear resistance, fatigue strength, corrosion resistance, thermal stability, and enhanced properties at elevated temperature [3]. The AMNCs could be produced using both cast and wrought aluminum alloys as a matrix with Al_2O_3 , SiC, AlN, MgO, B_4N , TiC, or TiO_2 as commonly used reinforcements.

There are different manufacturing techniques to produce the AMNCs such as liquid metal infiltration, spray decomposition, squeeze casting, compocasting, powder metallurgy and mechanical alloying [4]. Of these techniques, stir casting of MMNCs is an attractive processing method for these advanced materials since it is a low-cost with large production scale process, and offers a wide variety of materials and treatment condition options. The process involves melting of the matrix and introduces the nanoparticles to the melt during the melting process with the aid of mechanical stirring. Reinforcement of aluminum alloys with Al_2O_3 has been observed to enhance the ultimate tensile and the yield strengths of the metal. Furthermore, the fatigue and properties at elevated temperature have been improved [4-5].

Further enhancements in the fatigue and creep behavior can be achieved by mechanical surface treatments such as shot peening and roller burnishing. Mechanical surface treatments are attributed to induce cold working by local plastic yielding on the surface layers. The theory

beyond them is to localize pressure on a particular area exceeding its elastic limit, and after pressure removal, deposit the surface layers a part of deformation. The internal layers, which have not reached the elastic limit, tend to restore its position. Thus, compressive residual stresses arise between the inner layers and the plastically deformed outer layer resulting in restricting both crack initiation and propagation with a prolonged fatigue life [6-7].

1.1 Motivation and objectives:

The long-lasting challenge in the automotive and aerospace industry is to satisfy the equation of high performances with low fuel consumption. The reduction in vehicle weight or increasing the strength to weight ratio of the materials used, provides both fuel efficiency and reduces the CO₂ emissions. Such concept of choosing a lightweight material with improved mechanical and functional properties (strength, corrosion, and wear resistance) recommended aluminum to be an efficient steel-substitution. Furthermore, the aluminum recycling is tremendously less expensive than its production, which means with a fraction of the energy aluminum could be produced at the same quality without damaging its structure. Nevertheless, the conventional aluminum alloys are hard to meet the modern market demands of high dimensional stability, strength, and durability. Therefore, Al-based metal matrix nanocomposites are considered as exciting candidates owing the ability to design lightweight structures having balanced mechanical and metallurgical properties, as well as tribological characteristics improvement and enhanced high-temperature strength. The strength stability at high temperature is attributed to the thermodynamic stability of the reinforcement particles at the elevated temperatures. The MMNCs are suitable for high-performance applications in which the traditional cast alloys or precipitation strengthened material cannot be utilized because of their limited properties. Moreover, nanocomposite materials performances are far superior compared to micro-composites because of the small reinforcements size which enhances the interaction with the lattice defects such as dislocations and activates new strengthening mechanisms. However, these enhanced properties are accompanied with some fabrication hindering that have been detected in many production techniques. The conventional synthesizing methods could not overcome these fabrication restrictions such as agglomeration and porosity. Besides, the traditional production processes do not provide a homogeneous distribution of the nanoparticles at low-cost, and they are not applicable for the industrial scale leaving behind many challenges for the researchers [3-5].

The aim of this work consisted in the development of Al6061-nanocomposites with enhanced mechanical properties at room and high temperature (300°C) and good weldability. The proposed research provides robust empirical approaches to overcome the main restrictions of MMNCs fabrications such as poor wettability, agglomeration, porosity, inhomogeneous distribution, high production costs, and durability. In this concern, stir casting is considered as one important production method of the Al6061/Al₂O₃ composites due to its low-cost and durability. The optimum weight fraction of the alumina nanoparticles addition was determined. Besides, the metallurgical/mechanical/and functional behavior of the produced materials were evaluated utilizing different mechanical tests (tensile, hardness, fatigue and creep tests) and microstructure

investigation techniques (optical and scanning electron microscopy). For further enhancement of the fatigue and the functional behavior of the AMNCs, the mechanical surface treatments (MSTs), namely shot peening and roller burnishing, were conducted. The impact of the shot peening and roller burnishing on the fatigue and the creep behavior was unveiled. The wear and corrosion behavior of the different composites were tested, as well. Furthermore, the weldability of the AMNCs was investigated using the rotary friction welding technique. The optimization of the welding parameters was carried out based on the design of experiment method using Minitab 17. Economically, the recyclability of the AMNCs was clarified by re-fabrication of the produced AMNCs through investigating the change of their behavior compared to the as-cast state [3-5].

In a summary, the current thesis aims at:

- Carrying out the necessary literature review to determine the process parameters of the stir casting.
- Studying the feasibility of stir casting method as a production method of the AMNCs.
- Investigating the manufacturing problems (such as agglomeration, porosity and inhomogeneous dispersion of the nanoparticles) and defining the weight fraction of nano-phase at which such problems could be minimized.
- Characterizing the mechanical behavior of the AMNCs at room temperature and elevated one (300°C).
- Finding out the optimum parameters of conducting mechanical surface treatments (MSTs), shot peening and roller burnishing, on the AMNCs.
- Identifying the mechanical behavior of the AMNCs after applying the MSTs.
- Evaluating the fatigue life of the AMNCs in air and corrosive medium (3.5% NaCl) before and after conducting the MSTs.
- Revealing the creep properties of the AMNCs and the effect of the MSTs on the creep behavior.
- Investigating the corrosion and wear behavior of the AMNCs.
- Study the weldability of the AMNCs and optimize the welding parameters of the friction welding method.
- Proposing an analytical model describes the strengthening mechanism in the AMNCs.

Figures 1.1 and 1.2 summarize the study plan and the experimental approaches considered in this work.

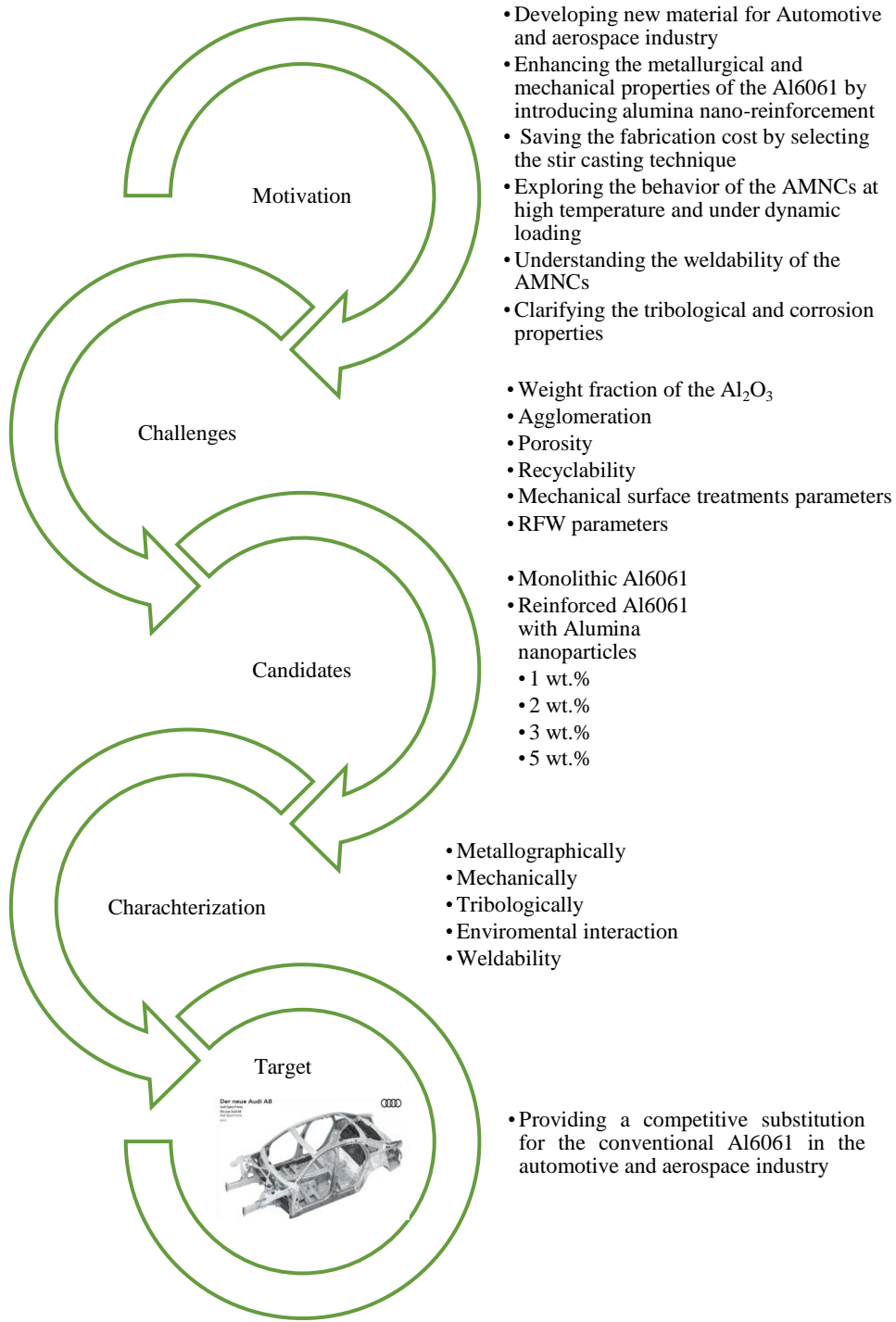


Figure 1-1: Research flow chart [8]

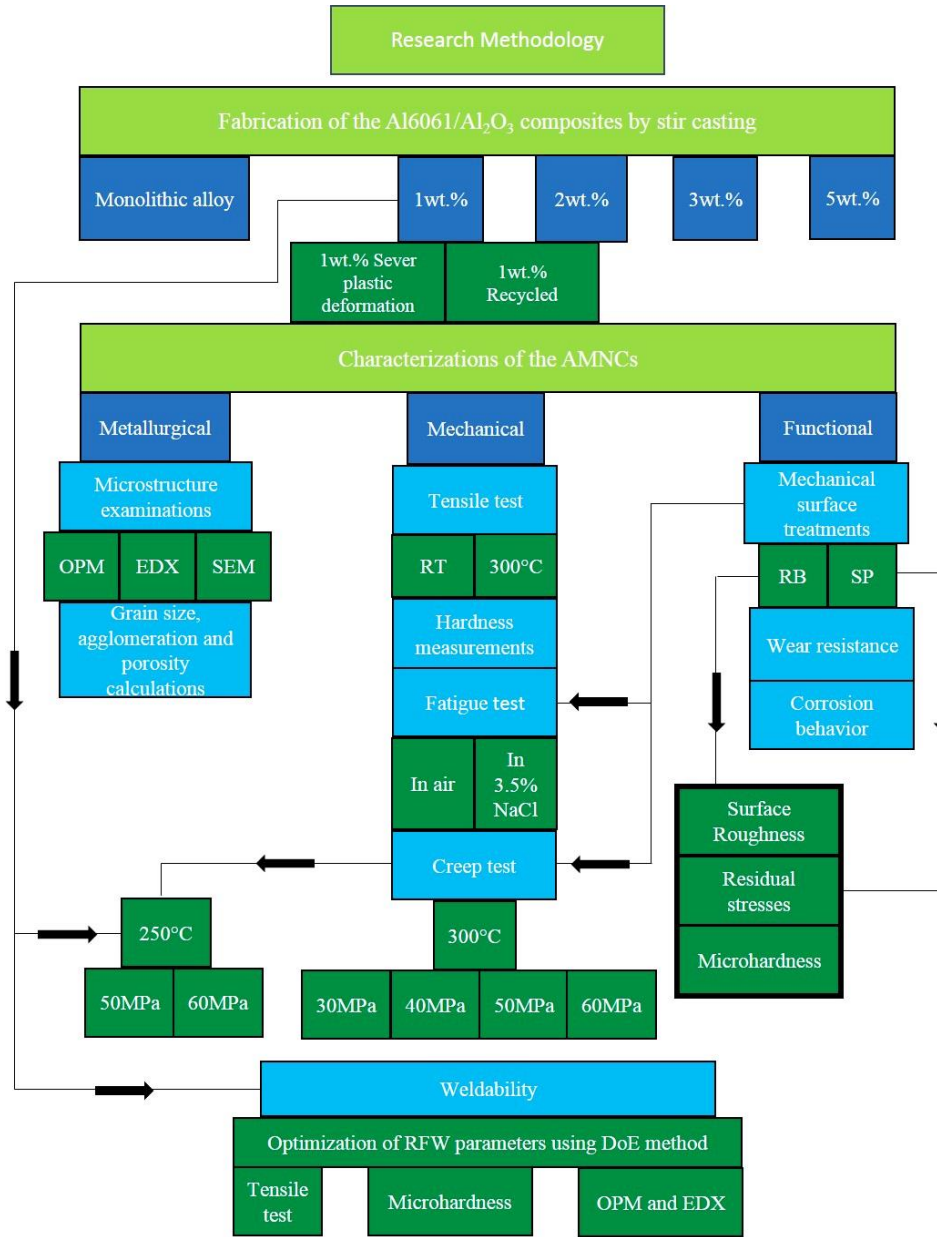


Figure 1-2: Research methodology

1.2 Thesis synopsis

This thesis consists mainly of four chapters. The thesis starts with this chapter in which a general view of the main motivation of the work, small introduction and the research objectives are covered. The state of the art is discussed extensively in Chapter 2 focusing on the subject-related theoretical background of the main characteristics and production considerations of the Al6061. As well as, the Metal Matrix Nanocomposites (MMNCs) properties, fabrication methods, strengthening mechanisms, and their recycling aspects. Chapter 3 is concerned with a detailed

description of the experimental procedures used in these investigations. Through different mechanical and metallurgical techniques, the behaviour of the MMNCs was characterized and the optimum nanoparticles weight fraction was determined to achieve the most enhanced properties with minimum agglomeration and porosity. The results and discussion are described deeply in Chapter 4 followed by the research conclusions and the future proposed work.

2 Literature Review

Aluminum and its alloys are traditionally known as light alloys, which are frequently used to reduce the weight of components and structural parts with a relative density of 2.7. In this chapter, the state of the art is discussed covering the main characteristics and production considerations of the Al6061. Then, the Metal Matrix Nanocomposites (MMNCs) were surveyed to comprise their properties, fabrication methods, strengthening mechanisms, and their recycling aspects.

2.1 Aluminum and Aluminum Alloys

Possessing the lightness property improves the use of aluminum alloys in many products where the high strength to weight ratio is required. This reason made aluminum and its alloys a basic part in many industries and applications such as transportation, aerospace and marine industry inducing the development of this category of alloy over the past 50 years. Low-density materials have a great importance in engineering design regarding other parameters such as stiffness and buckling resistance. Beside the fact of weight saving, aluminum alloys have other important properties of high corrosion resistance, good machinability, and high thermal conductivity. Aluminum possesses the third place with 8% by weight ratio in the crustal abundance. However, the extent to which aluminum will be used may depend on the costs of other materials like steel and polymers and the cost of electrical energy required for extraction [1,9].

2.1.1 Aluminum Production Overview

The annual aluminum production increased from 6000 tons to 1.5 million tons with about 250 times from 1900 to 1950, and after 25 years it increased eight times because of aluminum surpassed copper to be the second most used metal. Over this period, the annual inflation rate in aluminum production had an average of 9.2%. In 1970 the demand for basic materials had fluttered with a small overall annual production due to the emergence of Russia and China with greater attention to recycling. Between 1980 and 2000 the world production of primary aluminum increased with average 4% to reach 29.2 million tons in 2004 and the production of recycled aluminum boosted from 3.8 to 8.4 million tons in 2004. Aluminum is used in five core areas all over the world: construction and building, packing and containers, electrical conductors, transportation and machinery, and equipment. In 2002, the aluminum consumption by the major aluminum users China and the United States was in transportations 31.6% by the United States to 24% in China, wherein the packing field comes China with 5% compared to 21.1% in the United States. In building and construction consumed China 33% to 14.6% by the United States. The largest demand for raising the aluminum industry is the automotive industry. The increment in using aluminum in vehicles increased from 8kg per vehicle in 1971 to 90 kg in 1994 and 130kg in 2004 in the United States, where in Europe is about 200kg in 2015[1,9-11].

Unlike iron, aluminum combines strongly with oxygen and cannot be reduced by carbon, which makes it difficult to be extracted from ores. The name “aluminum” was first used in 1809 after Sir Humphry Davy produced it from alum (its bisulphate salt). Aluminum was first commercially prepared in France by H. Sainte-Claire Deville through reduction of aluminum chloride in 1855

with less than 95% pure, and it was higher in cost than gold. From 1855 to 1859 the price of aluminum decreased from \$US 500 to \$US 40. The discoveries of Hall in 1886 in the US and Héroult in France made a revolution in the economic method for extraction of high-purity aluminum electrochemically, which are the basis until today. It led to a price cut in 1888 to less than \$US 4 and in recent times from \$US 2 to \$US 1 per kg. Aluminum extraction depends on bauxite which was discovered by P. Berthier. Bauxite contains several forms of hydrated aluminum oxide e.g. gibbsite ($\text{Al}_2\text{O}_3 \cdot 3\text{H}_2\text{O}$) and boehmite ($\text{Al}_2\text{O}_3 \cdot \text{H}_2\text{O}$). According to statistics in 2004, Australia produces 38% (55.6 million tons) of the world supply, then comes Guyana with 10.6%, Jamaica 9.25%, Brazil 9% and China with 8.6%. The ore bodies contain typically 30-60% hydrated Al_2O_3 with some impurities of iron oxide, silica, and titania. Aluminum could also be found in clays, shales or other minerals and extracted by acid and alkaline processes. Aluminum could be acidically extracted and recovered from kaolinite which is found in clay. Besides, it may also be recovered from nepheline ($\text{Na}_3\text{K}(\text{AlSiO}_4)_4$) or alunite ($\text{KAl}_3(\text{SO}_4)_2(\text{OH})_6$) but with higher cost about 1.5 to 2.5 times more expensive than that produced by Bayer process [1,11].

2.1.2 Aluminum 6061 alloy

Al 6061 is an aluminum alloy containing magnesium and silicon as the main alloying elements, which makes it a heat treatable (precipitation hardening) alloy. The aluminum-magnesium-silicon system is illustrated in Figure 2.1.

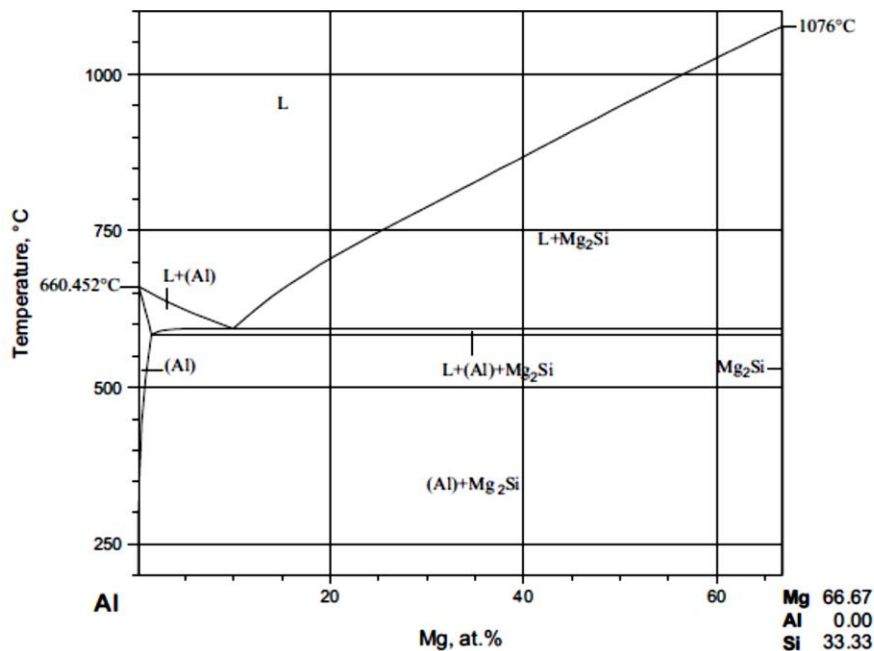


Figure 2-1: Al-Mg-Si section from Al to Mg₂Si [12]

Properties such as good weldability, corrosion resistance, and stress-corrosion cracking resistance made it widely used alloy as medium-strength structural and general-purpose alloys. The alloy is available in the forms of sheets, rods, tubes, or plates. The main alloying elements, magnesium and silicon, are mainly added to form Mg₂Si precipitates. Aluminum 6061 also may

contain other alloying elements to add some features and properties. Copper and zinc additions improve the strength of the alloy without significantly reducing its corrosion resistance. For grain size refining purpose, titanium may be added. Excess of Magnesium or Silicon could be used for better corrosion resistance with an adverse effect on strength and formability. However, using silicon can increase the strength without retarding the formability or weldability [13]. The typical chemical composition of Al6061 is represented in Table 2.1.

Table 2-1: Al6061 Chemical composition [9]

% Composition (by weight)	Element
95.8 -98.6 %	Al
0.80 -1.20 %	Mg
0.40 – 0.80 %	Si
0.15 – 0.40 %	Cu
0.040 -0.35 %	Cr
Max 0.7	Fe
Max 0.25	Zn
Max 0.15	Ti
Max 0.15	Mn

Al6061 is commercially available in pre-tempered grades such as 6061-0 (annealed), 6061-T4 (solution heat treated, quenched, and naturally aged) and 6061-T6 (solution heat treated, quenched, and artificially aged). The alloy is commonly used in aircraft and aerospace components, automotive parts, marine fittings, transport, bicycle frames, drive shafts, tanks, electrical fittings and connectors, brakes, coupling, and valves [9-13].

The properties of Al 6061 alloy vary with the magnitude of alloying elements and processing such as cold working, hot working, ageing, and annealing processes [2,12-13]. Table 2.2 illustrates a comparison between the different mechanical properties of the most commercial grades of Al6061 under annealed (O), T4, and T6 conditions.

Table 2-2: Mechanical properties of Al6061 at O, T4, and T6 temper conditions [14]

Alloy	6061 O	6061 T4	6061 T6
Hardness, Vickers	30	75	107
Yield strength(MPa)	55.2	145	276
Tensile strength(MPa)	124	241	310
Elongation%	25-30	22-25	12-17
Elastic modulus(GPa)	68.9	68.9	68.9
Fatigue strength(MPa)	62.1	96.5	96.5
Shear strength(MPa)	82.7	165	207
Shear modulus(GPa)	26	26	26

2.2 Aluminum Matrix Nanocomposites (AMNCs)

To obtain a high specific strength with high thermal stability at elevated temperature, the MMCs were developed by impeding hard reinforcement particles (usually ceramics) into a ductile metallic matrix. These hard particles introduction permits significantly the material performance improvement with increasing strength, stiffness, and wear resistance, even at high temperature [15]. Traditionally, carbides, nitrides, borates, or oxides are used to reinforce the Al-based composites by several fabrication methods either through powder metallurgy techniques or casting methods [15, 16-18]. In the 1980s and early 1990s, the development of MMC has been taken into consideration among all the main aluminum producers and using it in a wide spectrum of applications. The applications vary to cover automotive, electronic packaging, diesel engine pistons, brake rotors and drums, pick-up truck drive shafts, bicycle components, aeronautic engine fan, exit guide vanes, aircraft ventral fins and fuel access covers, and golf clubs [19]. In the automotive industry, a numerous attention has been paid to discontinuously reinforced aluminum composites (DRA) due to its attractive properties, as well as the weight saving that they have presented. Another factor that was considered by the manufacturer is the cost effectiveness of producing the DRA. It was remarked that the expense of the raw materials of the MMCs is higher than the replaced materials such as steels. But including the weight factor improves the cost comparison significantly to the MMCs [20]. Despite the premium properties offered by the Al-based metal matrix composites over the unreinforced alloys, they exhibit significant restrictions, such as low ductility and fracture toughness with poor machinability and weldability [15]. Moreover, some tribological problems were reported when the MMCs were used in engine design, especially in pistons, as they could induce relevant cylinder lines damage due to wear [15,21].

Furthermore, some microstructural defects (which lead to decrease their mechanical properties) were marked when the Al-based MMCs were welded by the conventional welding techniques (TIG, MIG, laser). The reason may be the presence of the ceramic reinforcement that causes particle segregation, undesired reactions between particulate matter and matrix, and evolution of the occluded gas [22-30].

These limitations outline the compelling need for an aluminum-based material possesses such outstanding properties and overcomes these restrictions of both monolithic aluminum alloys, and traditional MMCs reinforced with a relatively high-volume fraction of microparticles. Al-based nanocomposites have recently emerged as a candidate suitable for this need reinforced with ceramic nanoparticles such as SiC, Al₂O₃, AlN, or TiC with relatively low volume fractions (<5% wt.%) [15]. The homogenous dispersion of nano-sized particles within the aluminum matrix induces some relevant characteristics to the material. This group of aluminum alloys is characterized by superior specific stiffness and significant improvement in strength with enhanced ductility compared to the traditional MMCs [31-33]. As well as, properly wear resistance compared to both monolithic Al alloys and MMCs, remarkable improvement of creep resistance, and thermal stability than the conventional Al alloys [34-36].

Several studies have clearly reported the beneficial usage of nanoparticles instead of micro-sized particles. Sajjadi et al. [21] carried out a comparison between two A356 based composites

reinforced one with 20 μm and the other with 50 nm Al_2O_3 particles. The compression tests revealed that the alloy which was reinforced with nanoparticles demonstrated an improvement in strength having 610MPa with 3 wt.% of nano-alumina to 453 MPa for the alloy with 10 wt.% of micro-alumina, even with a smaller reinforcement content [15].

Ma et al. [38] found that the addition of 1 vol.% nano- Si_3N_4 to a certain aluminum alloy gave the similar ultimate tensile strength when the same alloy was reinforced with 15 vol.% micro-SiC (180 and 176 MPa respectively). The same concept was confirmed by Kang and Chan [23] when they compared nanocomposites with 1–7 vol.% of nano alumina, to a 10 vol.% micro-SiC reinforced composite. It was illustrated that both yield and ultimate tensile strength of the 1 vol.% nanocomposite were comparable to the other alloy reinforced with micro-composite.

Despite their enormous potential, aluminum-based nanocomposites are still not produced on a large industrial scale. Among possible production methods, liquid or semisolid based production routes are considered to possess higher industrial scalability, although obtaining a homogeneous particle distribution is still challenging [15].

2.2.1 Properties of the AMNCs

The AMNCs show enhanced mechanical properties at both room temperature and elevated temperatures. The hardness, YS, and UTS are improved with increasing the volume fraction of the reinforcement particles added at room temperature (Figure 2.2). Significant enhancements in Young's modulus have also been obtained [39-41]. These improvements in the mechanical properties may be attributed to the increase in the dislocation density (Orowan strengthening mechanism) in nanocomposites in comparison to the aluminum matrix micro composites or that without reinforcement. Increasing the particle content up to 4.5-5 vol.% enhances the hardness to reach its peak and then declines with higher content [42-45]. It is observed that there is a critical weight or volume fraction of the nanoparticles added, beyond which a further addition of nanoparticles leads to retardation of the mechanical properties [42-45]. Further increase in the nanoparticles causes an increase in the degree of microporosity due to the agglomeration occurred to them [44], which lowers the flow stress in the AMNC. Besides, the bond at the interface between the nanoparticle and matrix could be released because of excessive dislocation density and other defects around hard particles generated by the thermal expansion coefficient difference between the particles and the matrix [15].

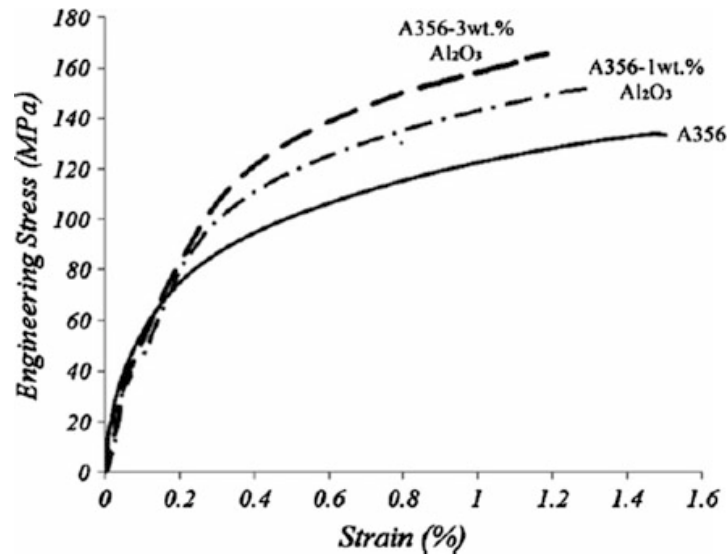


Figure 2-2: Representative tensile engineering stress-strain curves under tension for A356– Al₂O₃ [15]

The negative effect caused by porosity presence in the AMNC may be suppressed by subsequent mechanical deformation processes such as hot extrusion [44,46]. Ezatpour [44] observed that hardness and the tensile properties of an Al6061 alloy reinforced with Al₂O₃ nanoparticles in the as-cast state increased with increasing reinforcement weight fraction up to 1 % but then decreased, due to inhomogeneous distribution of nanoparticles and the presence of high porosity content. Mechanical deformation (e.g. hot extrusion) contributes in decreasing the amount of the porosity induced from the higher nanoparticles additions and uniform distributing of the nanoparticles among the matrix, which increase the mechanical properties of the fabricated AMNCs.

Grain refining is one of the important outcomes of the Nano-reinforcement processes, which influences the strengthening process directly or indirectly [39,47,48]. Wang [48] reported a remarkable decrease in the grain size of the ultrasonic processed Al–9 Mg when it was reinforced with TiC_{0.7}N_{0.3} nanoparticles (36, 42 and 73 μm for 1.5, 0.5 and 0.2 vol.% reinforced nanocomposites respectively) as compared to the unreinforced matrix (165 μm). Nanoparticles were reported not only to decrease the grain size (Hall-Petch strengthening mechanism) but also to have a direct effect on strengthening the composites. This effect was investigated when the same alloy refined through inoculation with Al–5Ti–1B, which resulted in similar grain sizes without a significant enhancement in tensile properties and ductility [15].

Heat treatments such as age hardening can add further improvements to AMNCs mechanical properties. However, the introduction of nanoparticles requires an optimized ageing conditions due to the change in aging kinetics accompanied with the nanoparticle's presence. The hardening treatment and the mechanical properties could be affected negatively by the formation of some segregations such as magnesium at the nano SiC_p/Al interfaces and at the grain boundaries. This effect was observed when an aluminum alloy Al7005 was prepared by powder metallurgy subjected to HIP and temper T6 treatment. Nanoparticles could also increase the effect of the equilibrium segregations, which are thermodynamically governed to minimize grain boundary

energy, free surface energy, or interface energy of the system [49-50]. El Mahallawi et al. [51] cleared that the hardness of the aged A356 unreinforced alloy remained higher than the aged A356 based nanocomposite when the alloy was fabricated by compocasting and reinforced by Al_2O_3 nanoparticles. Moreover, the addition of the nanoparticles with T6 heat treatment raised both tensile strength and elongation % of the nanocomposites compared to the matrix treated only with T6 [15,43,52-55].

Although the work carried out on the AMNCs to investigate their properties at elevated temperature in the literature is very limited, the AMNCs show enhanced stable properties even at high temperatures. The addition of 2 vol.% of MWCNT using compocasting method at the semisolid state with a solid fraction of 30 % resulted in nanocomposites able to retain 90 % of its yield strength at 300 °C compared to room temperature (142 and 158 MPa respectively). The unreinforced alloy prepared with the same route showed 79 MPa yield strength at 300 °C with 60% of that at the room temperature [15]. The reinforcement of the aluminum matrices with nanoparticles improves their creep performance by restricting the dislocation climb or gliding processes [56] and carrying a larger load than the matrix [57]. Furthermore, hot extruded Al- Al_2O_3 nanocomposite powder showed a threshold creep-stress having a magnitude, that decreases with increasing the testing temperature (from 8.3 MPa at 375°C to 2.7 MPa at 500°C) [58]. This effect was related to the disengagement of dislocations from the Al_2O_3 nanoparticles during the high-temperature extrusion. Since the dislocation's detachment-stress required for micrometric reinforcement particles is minuscule to be accounted in the estimation of the threshold stress, it can then be inferred that nanometric particles are more efficient in dislocation pinning than micrometric particles [15,59].

On the tribological properties, the Al-based metal matrix nanocomposites exhibit better tribological properties than that without reinforcement. Consequently, have been used for this purpose in the automotive industry [60-61]. Hosseini et al. [62] conducted experiments to evaluate the wear behavior of Al6061 alloy reinforced with 3vol.% Al_2O_3 sized 1 μm , 60 μm , and 30 nm. The wear test results indicated a lower wear rate by the nanocomposite than the micro-composites.

Hosseini et al. [63] also investigated the influence of reinforcement of Al6061 over a range of Al_2O_3 nanoparticles varied from 1 to 5 vol.% on the wear and friction characteristics by applying sliding carbon steel pin on a disk of the synthesized material. The results emphasized the relation between the wear resistance and the hardness, as both increased by increasing the Al_2O_3 volume percent up to 3% and then followed by dramatically decrease due to the agglomeration formed at high levels of Al_2O_3 . Akbari et al. [64] studied the wear performance of A356 alloy reinforced with Al_2O_3 nanoparticles with Al and Cu nano-powder additions produced by stir casting method and heat treated under temper T6. The better performance of these composites was attributed to the higher hardness and compressive strength with lower porosity [15].

Not only alumina nanoparticles enhance the tribological performance of the AMNCs, but also the addition of titanium carbide or silicon carbide could improve the tribological behavior due to their thermal stability and high strength resulted from heat treating of the AMNCs after fabrication. Nemati et al. [65] investigated the tribological performance of Al-Cu composites

with different reinforced by micro and Nano titanium carbide particles with different fractions (0–10 wt.%). The tested samples showed enhanced wear resistance for samples reinforced by nanoparticles than that with the microparticles having a critical weight fraction of TiC 5wt.%, which beyond it, a retardation of the wear performance due to agglomeration was reported. Sameezadeh et al. [66] examined AA 2024 Al-matrix reinforced with MoSi₂ nanoparticles prepared by mechanical alloying and undergone hot and cold pressing processes. Temper T6 was conducted to the prepared samples, and then the wear resistance was tested for the hot pressed and after T6 conditions. The results showed that temper T6 increased hardness and wear resistance of the samples compared to that after hot pressing with a critical volume fraction for agglomeration of 4% [15]. There are many factors influence the wear and friction properties of Al nanocomposites which could be summarized by the fabrication process and its parameters while adjusting the process and parameters leads to improved microstructural and mechanical properties. The selection of the reinforcement particles and its amount is also necessary by identifying the suitable nanoparticles which give the highest hardness and density without exceeding the critical volume fraction of it to prevent agglomeration and properties deceleration. Heat treatment also has a role in enhancing the tribological behavior of the aluminum nanocomposites by increasing the strength and hardness of the AMNCs, and thus raising their wear resistance [15].

The importance of the fatigue behavior of the AMNCs raises, especially when the cyclic loading is considered, which is dominant in aerospace and some automotive applications. However, the work carried out on the fatigue behavior of the AMNCs is very limited. Ghasemi Yazdabadi et al. [67] investigated the low and high cyclic fatigue behavior of a pure aluminum alloy reinforced by SiC. The fatigue life of the low and high cyclic fatigue regime was improved due to the locking effect of non-shearable particles on moving dislocations [15]. Srivatsan et al. [68] conducted high cyclic fatigue tests on a magnesium alloy similar to AZ91 with 3% higher aluminum content reinforced by Al₂O₃ nanoparticles. The results indicated a higher endurance limit for the unreinforced samples than that with nanoparticles due to the raised crack initiation and propagation caused by the nanoparticles. A similar work from the same authors but with replacing the Al₂O₃ nanoparticles by CNT using the same alloy [69] showed enhanced fatigue life of the reinforced alloy with a 40 % improvement 10⁶ cycles endurance limit. The CNT increases the resistance to crack initiation during cyclic stress-controlled fatigue and restricts its growth [69].

The corrosion resistance of the AMNCs based on the nature of their two-dissimilar materials form with different corrosion potential and properties. This combination could be affected by the chemical, physical, or galvanic interaction between them. The particle/matrix interface is the preferred site for corrosion to start with rapid penetration into the material could resulting in higher corrosion rate compared to the alloys without reinforcements [70,71,15].

Mahmoud et al. [72] studied the corrosion behavior of several aluminum alloys reinforced by SiC and Al₂O₃ nanoparticle produced by a powder metallurgy and tested in NaCl aqueous solution under different conditions. Both alloys with reinforcement exhibited better corrosion resistance than the unreinforced alloy with lower corrosion rate for that with the Al₂O₃

nanoparticle. Moreover, the corrosion rate of the AMNCs increases with the further addition of the reinforcing particles more than 3 vol.% because of agglomeration. El-Mahallawi et al. [73] also concluded an improvement in the corrosion resistance of an A356 matrix reinforced by sub-micron Al_2O_3 particles (nanoparticle size <500 nm) and produced by rheocasting. The reinforced alloy showed a higher corrosion resistance in 3.5% NaCl aqueous solution than the monolithic alloy. Nevertheless, further investigations on the corrosion resistance of AMNC should be carried out [15].

2.2.1.1 Enhancing the fatigue behaviour by mechanical surface treatments

Many factors affect the fatigue behavior such as the material strength, hardness, cyclic stress state, surface roughness, application temperature and environment, and the amount of the internal stresses stored in the material. The fatigue life can be improved by conducting some mechanical surface treatments such as peening processes and deep rolling. The role of the mechanical surface treatments is to apply a specific pressure on a certain area of the material, which exceeds its elastic limit induces plastic deformation and increases the dislocation density. The generated compressive residual stresses on the surface of the material not only retard the crack initiation process, but also restrict its propagation. There are many mechanical surface treatments e.g. conventional shot peening (SP), ultrasonic shot peening (USP), laser shock peening (LSP) and roller or ball burnishing [6]. Among the different mechanical surface treatments, the conventional shot peening (Figure 2.3) is considered as one of the most durable and low-cost techniques. The process involves bombarding the sample surface by hard relatively small shots with a certain pressure, distance, and peening angle, which attributes to increasing the dislocation density in a zone up to 0.4 mm under the surface. Just below the surface, the grains under compressive stresses try to restore its original shape resulting in high value of compressive residual stresses with a magnitude reaches at least the half of the material tensile strength. The process includes some surface changes such as inducing compressive residual stresses on the surface, microstructural alterations, increasing the surface roughness and hardness, formation of cracks, and crystallographic texture [6-7].

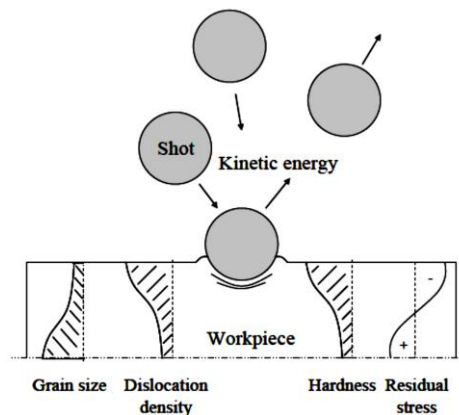


Figure 2-3: Conventional shot peening process [74]

The role of the compressive residual stresses is to squeeze the grain boundaries, and thus delay the fatigue crack initiation. Forasmuch, the crack initiation or propagation are difficult to occur in the layer of compressive stresses; the cracks initiate under the surface with a significant slow propagation rate leads to a prolonged fatigue life. These compressive stresses diminish the deleterious effect of tensile stresses (caused by externally load application or be residual stresses formed during the processing of the material such as welding, grinding or machining) on crack initiation or its propagation [6].

There are several parameters control the peening process such as the peening media, hardness and size of the shots, the impingement angel and distance, shots velocity, penning time and coverage. The process could be represented by the Almen intensity, which gives an indication of the kinetic energy transferred by the shots stream. The Almen intensity is measured by the Almen strip (with three classifications: 'N' (0.79 mm thick), 'A' (1.30 mm thick), and 'C' (2.38 mm thick)) and refers to the earliest point on the saturation curve, at which doubling the exposure time results in an increase in the arc height by 10% or less (Figure 2.4).

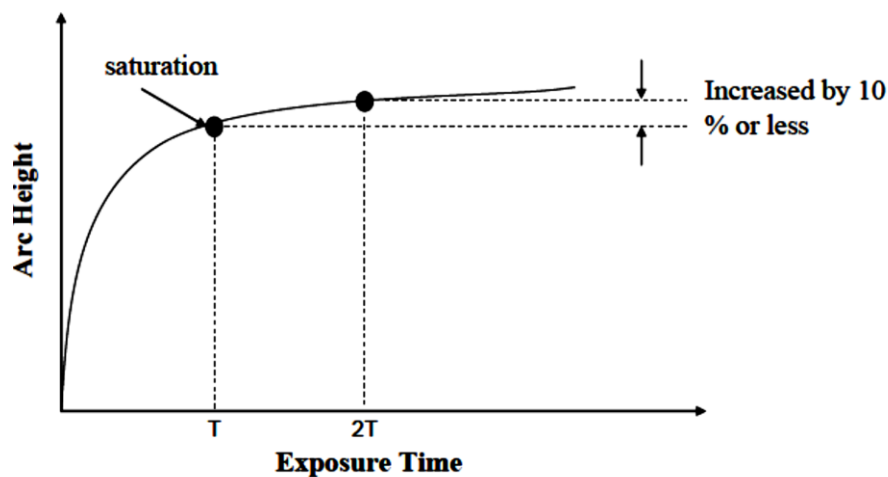


Figure 2-4: Arc height vs. exposure time scheme [74]

Another common mechanical surface treatment for improving the fatigue behavior is the burnishing process (Figure 2.5). The process concept is to induce plastic deformation through a rolling process using a roller or a ball with a predefined force perpendicular on the material surface and sufficient to deliver the material to its plastic zone. The process is commonly controlled by force used, the sample rotating speed, and the roller/ball feeding rate. The burnishing processes introduce some advantages which are not induced by shot peening such as the higher compressive residual stresses, deeper layer affected by the mechanical surface treatment, and smoother surfaces. However, the burnishing processes are restricted by the specimen geometry, unlike the shot peening which has the privilege of applying the mechanical surface treatments even on complex shapes [6-7].

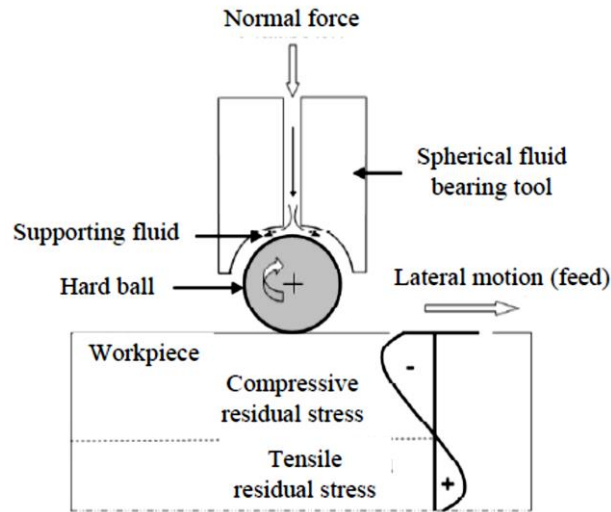


Figure 2-5: Ball-burnishing process [74]

2.2.1.2 Friction welding as an alternative for the MMNCs welding

Metal welding is the non-detachable joining of components through the application of heat or pressure. One of the welding techniques is the friction welding, in which the heat required for the welding process is obtained by the mechanical friction produced by the relative movement under a certain applied axial force between the two joining parts. The softening of the material occurs during the process is a significant advantage of the friction welding against the other melt welding techniques, due to the absence of a molten phase with a reduced new phases formation. Oxides and impurities on the joint surfaces are entrapped in the flash and pressed outwards. Furthermore, the friction welding can be performed without the use of additional materials or inert gas, which means high productivity with low cost, with the ability of welding both solid and hollow profiles. The usage of the friction welding has been recently spread to cover metals and thermoplastics in many applications either in aerospace or automotive industry [31-33,75].

The most common form of the friction welding is the rotary friction welding (RFW). During the rotary friction welding process, a part of the material is rotated, and the other is stationary leading to a material transfer from one surface to another. The increase in axial force leads to increase the specimen temperature due to friction heat, as well as the size of the individual adhesion junctions. After reaching the initial peak torque and the start of the shortening, the material temperature increases and tends to recovery with a rate higher than the work hardening rate. Then the material plastifies and behaves like a viscous fluid with constant axial shortening and torque. Finally, the rotational speed decreases, while the torque increases until reaching the peak value and drops to zero. The main process parameters are the friction pressure, the friction time, the forging pressure, forging time, and the rotational speed. In comparison to the other conventional fusion welding methods, RFW has a unique set of advantages such as the reduction of the solidification defects because of the absence of a molten pool, durability, and its compatibility of

welding dissimilar metals. Moreover, the process is performed without the need of shielding gas or fillers, self-clean capability due to wearing action of the relative movement of parts, the process cycle is very fast with high productivity rate, and high integrity characteristics with the bonding area may reach 100%. However, the process has some limitations, for example, it is restricted by the material geometry (suitable to join axisymmetric components, like tubes, shafts, and discs) and the difficulty of welding thin-wall structures like tubes and plates. Furthermore, the process is limited by flash forming where its removal could cause change the geometry of the design, and high capital cost of the welding equipment [31,33,75].

2.3 Synthesis of MMNCs

The production of the MMNCs could be divided mainly into two categories; in-situ and ex-situ routes. The in-situ routes involve the generation of the nanoreinforcement during the composite preparation by certain controlled reactions. When the process encountered the formation of the nanoparticles separately and added to the matrix, called this manufacturing route ex-situ. The ex-situ processing techniques are then classified into solid, semisolid and liquid states routes [15]. The solid-state processing includes powder metallurgy, immersion plating, chemical vapor deposition, diffusion bonding, physical vapor deposition. Of the ex-situ production routes, the liquid state method (such as squeeze casting, stir casting, compocasting, rheo-casting, and melt infiltration) is reported to be the most attractive owing to its simplicity and the ability to be applied on the industrial scale with near net shape parts [76-77]. Nevertheless, this technique faces some restrictions of the uniform dispersion of the nanoparticles in the matrix compared to this achieved by powder metallurgy. The high surface energy of the nanoparticles due to its tiny size increases the tendency to agglomeration, and low wettability within the molten matrix leads to the formation of clusters of nanoparticles. The clusters are not effective in hindering the movement of dislocations and can hardly generate a physical-chemical bond to the matrix with a detrimental effect on mechanical properties [78-79]. The poor wettability prompted the researchers to develop unconventional production methods to overcome this issue. The most studied methods could be classified into liquid, semisolid and solid processes [80].

2.3.1 Liquid Processes

The liquid state processing routes include stir casting, infiltration techniques, ultrasonically treated casting, and disintegrated melt deposition. They are the most attractive among the other manufacturing methods because of their relatively low cost, durability, and ability to produce large-scale parts with accurate near net dimensions. One of the disadvantages of this approach is the severe nanoparticles agglomeration, which occurs even with the application of the mechanical stirring before casting. The main reasons for agglomeration to occur are the poor wettability of the nanoparticles, which resulted from the high surface to volume ratio and high viscosity generated in the molten metal [80].

The ultrasonic assisted casting is one of the most efficient techniques used to eliminate the particles clusters formed due to agglomeration and low wettability of nanoparticles profiting the cavitation produced during the ultrasonic treatment [81-83]. During the process, the molten metal

is treated ultrasonically using waves in the frequency range 18–20 kHz during or after nanoparticles addition (Figure 2.6). The method could be used for synthesizing of both aluminum and magnesium-based alloys reinforced with SiC, B₄C, Al₂O₃, AlN, and CNTs [81,83-85]. The production of the Al/Al₂O₃ nanocomposite is performed under a non-contact ultrasonic treatment using an ultrasonic chamber [86].

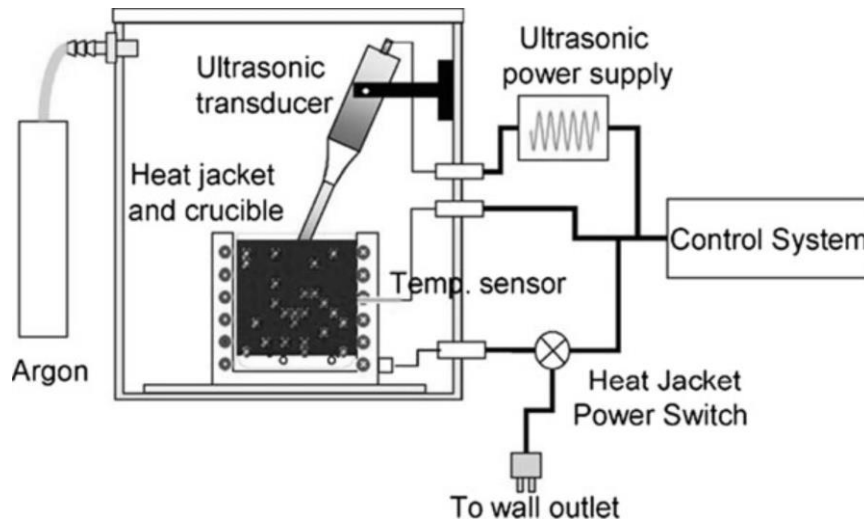


Figure 2-6: Ultrasonic assisted casting set-up [92]

Usually, the sonotrode is made of titanium alloy (Ti₆Al₄V), stainless steel or sometimes niobium-based alloy such as C-103 for the high-temperature applications providing the higher chemical inertness and minimum erosion caused by cavitation [85-86]. However, the usage of niobium based sonotrodes increases the process cost [85,89], thus the Ti-based sonotrodes are widely used owing to the relatively low cost compared to Nb sonotrodes. The cavitation produced during the ultrasonic application generates a localized pressure about 1000 atm and temperature could reach 5000°C with heating and cooling rates more than 1010K/s, which enhances the breaking of the nanoparticles clusters formed due to its agglomerations. The ultrasonic assisted casting process is restricted by the power of the ultrasonic source which limits the process to be applied on the industrial scale. However, some attempts were carried out to overcome this problem by treating the melt ultrasonically through its flow in a chamber which enables using a small sonotrode to deal with a large metal volume [90].

Disintegrated Melt Deposition (DMD) technique is a combination of casting and spray process, which was developed to produce near net shape parts, especially in magnesium based MMNCs [91]. The process involves merging the nanoparticles through stirring carried out by mechanical impeller during the melting process (Figure 2.7). Then the formed slurry is disintegrated at elevated temperature reaches 750°C using inert gas jets forcing it to be deposited on a metallic substrate. Finally, the ingot can be processed mechanically by extrusion to achieve the final shape.

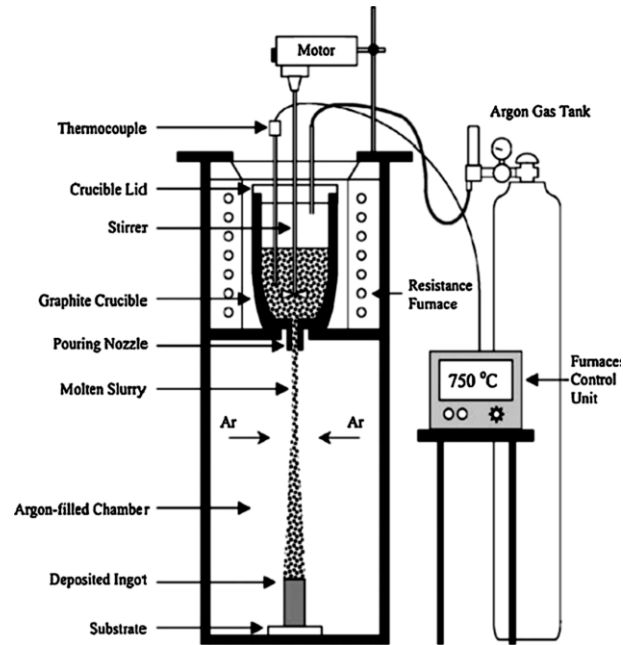


Figure 2-7: Schematic of the DMD process [93]

This synthesizing route is not only for magnesium based MMNCs, but also for the Aluminum based nanocomposites. But especially, it is often used for magnesium-based alloys to overcome the major obstacles occurred during the conventional manufacturing processes such as oxidation or nanoparticles retention in the crucible because of density differences. Furthermore, the microstructure of the extruded composites shows a uniform dispersion of the nanoparticles in the matrix and limited porosity, which resulted in significant improvement regarding both strength and ductility [94-95].

In the infiltration process, the molten metal is injected with the aid of an applied pressure into a porous preform placed between preheated punch and die. The preform is prepared by mixing the liquid carrier and the nanoparticle with a particular binder, and then the slurry is filtered followed by drying and heat treatment to ensure dimensions stability during the pressing process [96]. An infiltration technique was developed to decrease the process cost and the infiltration time based on the spontaneous infiltration of the ceramic preform neither with pressure application, nor vacuum [95,97].

Another technique for production of the MMNCs in the liquid state routes is the high pressure die casting (HPDC), which provides more detailed parts in comparison with the low pressure die casting and gravity casting. The process implies forcing the molten metal using an induced pressure to fill the die cavity with high filling speeds and solidification rates, which makes it a relatively fast cyclic route [15]. One of the technique's limitations is the gas entrapment caused by the turbulent flow of the melt which raises the porosity in the produced part and suppresses the mechanical properties [99-100].

2.3.2 Solid Processes

These production routes are based mainly on the powder metallurgy having the advantage of producing near net shapes and incorporating a higher volume fraction of reinforcement without

such issues of poor wettability occurred in other routes. The process drawbacks are mainly the relatively high cost and porosity compared to other routes. Through the powder metallurgy (PM) processes, a blend of the matrix alloy powder and reinforcing particles is prepared and compacted using cold pressing. Then the compacted structure is degassed to remove volatiles, gasses, and water vapor. Finally, the green compacts can be consolidated by different techniques such as hot isostatic pressing (HIP), direct sintering, or hot extrusion. To perform a high-energy mixing and eliminate the voids between the matrix and nanoparticles the mechanical alloying (MA) could be used, where the matrix and the nanoparticles are fused through cold welding together, fracturing, and rewelded again. When a solid-state reaction is accompanied by the mechanical alloying process (to produce a fine dispersion of oxides, nitrides, and carbides in the light alloy matrix) then the process is defined as reaction milling [15].

In microwave sintering, the heating process is generated by the conversion of electromagnetic energy into rapid, instantaneous, and highly efficient thermal energy, which is created within the material and spreads outwards by the microwaves [94]. The material absorbs the microwave energy undependable on the heat transfer from the outer surfaces, resulting in higher temperatures at the core with lower temperatures at the surface, which causes microstructure variation over the material thickness [92]. To overcome such issue, bi-directional hybrid microwave sintering was developed, in which the thermal gradient during sintering is reduced by using microwave susceptors such as SiC in the form of particles or rods [15]. The process uses two crucibles; one as an inner crucible and the other as an outer one. The compacted powders are placed in the inner crucible, and the SiC particles are placed between the two crucibles, which provide uniform heating through absorbing the microwaves and rapidly heat up the outer surface of the material. Bi-directional hybrid microwave sintering enables good nanoparticles bonding with eliminating the porosity. Moreover, it produces a dense material with fine microstructure with both time and energy saving [70].

2.3.3 Semi-solid-State Processes

Semi-solid casting processes are divided mainly into two groups, thixo-processes, and rheo-methods. They are characterized by forming a partially solid mixture (a slurry with a solid fraction from 20 to 60%) with relatively small near-globular grains, which produces low shrinkage and porosity composite with non-turbulent filling and lower processing temperature. The thixo-processes involve the reheating and partially melting of a proper solid feedstock (pre-casted billet with globular structure), and then injection of the slurry into dies made of hardened steel to obtain the final component. During the production of the feedstock, mechanical stirring, magneto-hydrodynamic stirring or ultrasonic treatment could be applied to obtain fine grain size [101-102]. Unlike the thixo-processes, the rheo-processes enable the formation of the semi-solid slurry from the liquid state utilizing cooling during the casting process instead of a pre-casted feedstock, which makes these processes easier to be performed in foundries with the standard equipment. After that, the slurry is transferred to the die casting machine hot sleeves following the same procedure to produce the final shape as in the thixo-casting. The slurry making process defines the rheo-processing approach. The new rheo-casting method is based on generating the

initial slurry by a cooling slope followed by pouring the melt at low superheat onto the holder to form minuscule crystals. To allow the crystals to grow and spheroidise under neither additional shearing nor stirring, the slurry is held for a preset time in the holder, and just before pouring, homogenization of the slurry temperature is performed [88]. In the Rheo-Die-Casting process (Twin Screw Rheo Molding), twin screws are used for mixing and supplying high shear to reduce the size of oxides enabling significant dispersion of them in the matrix. The slurry formation occurred by passing the melt through a cooled copper or iron block with the internal twisting channel. Another rheo-casting process is the semi-solid rheo-casting depends on the stirring and fragmentation to form the slurry. The presences of solid nuclei in the melt (cooled to near its liquidus) enhances its growth and rapidly spheroidizing with further cooling. The introduction of the nanoparticles in the matrix could be carried out using the compocasting technique which is similar in the concept to the stir casting but takes place in the semi-solid state of the material. The compocasting process ensures a uniform particle dispersion with enhanced particle wettability [103-104]. Moreover, this process is attributed to decrease the amount of porosity, which lowers the volume shrinkage in the MMNCs and reduce the nanoparticle tendency to agglomeration resulting in higher mechanical properties even than that obtained by stir casting. Notwithstanding, some agglomeration issues were reported because of the high surface-to-volume ratio and Van der Waals interactions [15].

2.4 Fabrication of the AMNCs by stir casting

Stir casting is probably the simplest and most economical technique used to produce MMNCs by a liquid state route. The process involves melting the matrix and addition of nanoparticles to the melt above its liquidus temperature with applying a proper mechanical stirring (Figure 2.8) to ensure a uniform particles dispersion in the matrix. Usually, the stirrer is dipped into the melt to create a vortex in it, which facilitates the dispersion of the nanoparticles through their addition in the vortex. Multiple stages stirrers could be used to produce a more uniform distribution during the nanoparticles addition, although the single stage stirrer is the most common one. Stir casting process shows many relevant advantages such as durability, low cost, and the ability to produce large quantities. However, the process is restricted by the high agglomeration rates resulted from the poor wettability of the nanoparticles and the air entrapment occurred during stirring with a tendency of the nanoparticles to sink or float due to the density difference between the matrix and particles. These obstacles make the nanoparticles dispersion difficult to be achieved and raise the challenges of developing new routes to enhance the particles wettability and facilitate their incorporation [15].

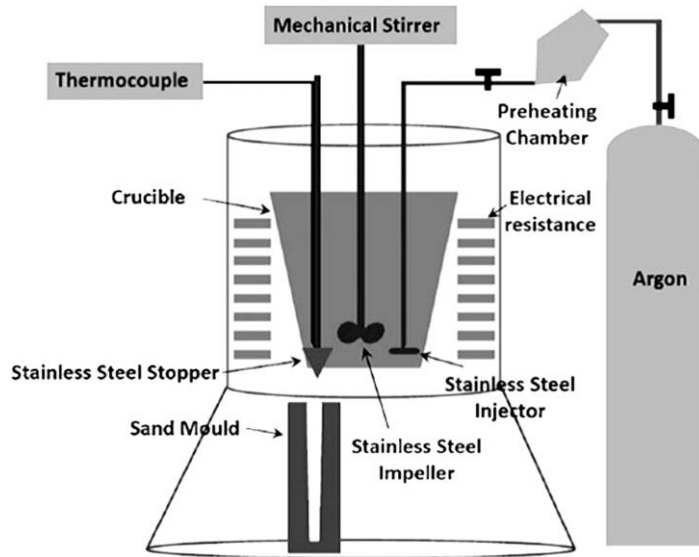


Figure 2-8: Typical stir casting experimental set-up [44,15]

The way, by which the nanoparticles are introduced into the melt, has a high impact on the reinforcement dispersion and it depends on the stirring temperature, speed, stirring time, and the stirrer position in the melt and its shape. The injected reinforcements could be carried by an inert gas from the bottom of the crucible, which makes the distribution occurs in the form of bubbles movement upwards through the melt. The wettability issue could be improved either by applying preheating to the nanoparticles or by alloying elements addition such as magnesium. Particles preheat eliminates the gasses content and impurities accompanied with the particles. Magnesium promotes the particles wetting through reducing the matrix surface tension and reacting with oxygen presents on the nanoparticles surface, as an oxygen scavenger, making thinner oxygen layer around the particle, and consequently improves wetting and reduces agglomeration tendency. Furthermore, the nanoparticles may undergo pre-milling with metallic powders to enhance their wettability, which involves repeated cold welding and fracture, and pressing of the nanoparticles into the soft metal powder during the ball milling process. Then the powders mixture (master powders) are introduced into the molten matrix attributed to a continuous discharge of nanoparticles within the matrix [15].

Stir casting was used to produce AMNCs reinforced by several types of nanoparticles like MgO, Al₂O₃, ZrO₂, and SiC. The early attempt of dispersion SiC in an aluminum matrix through the vortex method was carried out by Kawabe et al. [105]. Recently, Ansary Yar et al. [22] conducted from producing an A356-based composite reinforced with different ratios of MgO nanoparticles (50 nm) using stir casting at varies temperatures, that the agglomeration of MgO occurred at higher volume fraction with increasing the process temperature causing a decrease in the composite density. Abdizadeh et al. [46] compared the production of A356 reinforced with MgO nanocomposites by stir casting technique and powder metallurgy routes. Agglomeration was reported in cast samples with MgO addition higher than 5% caused mechanical properties retardation, while samples produced by powder metallurgy presented higher porosity accompanied with lower hardness and compressive strength, lower ability to crack imitation, and

better matrix continuity. Schultz et al. [107] studied the effect of magnesium addition to Al–Cu–Mg composites processed by gravity and squeeze casting and reinforced with varies volume fractions of preheated Al_2O_3 nanoparticles mixed with magnesium chips. Reactive wetting proved that it could induce an increase in the hardness of the samples fabricated by gravity casting, especially when it is combined with mechanical stirring. Besides, clustering was formed with increasing the nanoparticles volume fraction and the stirring time due to higher particle inconsistency. Sajjadi et al. [43] used stir casting to produce the A356 matrix reinforced with micro and Nano Al_2O_3 particles. The particles were pre-heated at 1100 °C for 20 min in an inert atmosphere and then introduced into the melt through argon gas. Mechanical stirring was carried out at different speeds before and after the particles addition to prevent particles settling. The best results were marked at 5 wt% of micro-sized and 3 wt% of nano sized alumina reinforcement with 300rpm stirring speed. The agglomeration tendency was higher in the nanoparticles compared to the micro reinforcement particles because of the higher surface energy and area. Mazahery et al. [95] compared the stir casting process to the compocasting in the manufacturing of A356 reinforced with SiC nanocomposites. The porosity increased with increasing the nanoparticles volume fraction, and the maximum hardness and strength were obtained at 3.5% SiC volume fraction. Samples, which were prepared by compocasting, had lower porosity with finer grains and enhanced mechanical properties than stir cast composites due to the particles movement restriction within the melt during solidification. Mazahery et al. [42,52] used the pre-milling technique and casting to produce an A356 alloy reinforced with Al_2O_3 nanocomposites and compared the results with pure Al_2O_3 . The powder mixture was prepared by milling the alumina nanoparticles with aluminum powders using balls of WC/C, cold pressed with 200 MPa, crushed and screened through 60mesh, and then added to the matrix after packing in aluminum foils. Mechanical stirring was conducted using a graphite stirrer at 600 rpm for 15 min, generating a vortex each 20 second. The results indicated an improvement in tensile properties and more uniform distribution of the nanoparticles in the sample produced by using the powder mixture than the pure alumina. Su et al. [106] used a wrought aluminum alloy AA2024 to fabricate an aluminum base composite reinforced by powder mixture (alumina nanoparticles and aluminum powders). The mixture was sintered at 400°C for 2.5 h and introduced into the melt under an argon atmosphere with the application of mechanical stirring for 10min. With 0.6 wt.% Al_2O_3 , the reinforced alloy with the powder mixture showed enhanced mechanical properties and hardness than the conventional produced by stir casting.

The stir casting parameters were discussed by several studies [52, 32]. It was found that the stirring speed and temperature have an essential role in controlling the process. The increase in the temperature at which stirring takes place, could increase the melt fluidity and induce a more turbulent flow which introduces more porosity in the melt, and thus retards the mechanical properties. Better nanoparticles dispersion could be achieved by increasing the stirring speed to a certain limit due to the high force applied to the melt and powders, although further increase beyond this limit may lead to turbulent flow and more gasses entrapment in the melt. Not only the stirring temperature and speed affect the stir casting process, but also the stirring time.

Increasing the stirring time assures more uniform particles distribution until a certain value, then rising the stirring time causes more porosity in the composite.

2.5 Strengthening mechanisms in the AMNCs

The nanoparticles reinforcement reveals significant improvements in the mechanical properties of the aluminum-based composites. However, the strengthening mechanism occurred during this reinforcement is not yet clear. The strengthening in the nanocomposites was discussed by several approaches and proposed to be attributed to Orowan strengthening, load transfer effect, Hall-Petch strengthening, the difference in the thermal expansion coefficient of thermal expansion, and/or mismatch of the elastic modulus [80].

The Orowan strengthening (also known as the Orowan mechanism) is based on the interaction between the closely spaced nanoparticles, as obstacles, with the dislocations. The non-shearable characteristic of the nanoparticles promotes the crossing dislocations to be pinned, and thus dislocations bow forming Orowan loops around the particles when an external load is applied. This mechanism is a dominant strengthening mechanism, especially when highly dispersed fine particles are present. The following expression can express the Orowan effect:

$$\Delta\sigma_{OR} = \frac{0.13bG}{d_p \left(\sqrt[3]{\frac{1}{2}v_p} - 1 \right)} \ln \left(\frac{d_p}{2b} \right) \quad [80]$$

where b is the Burger's vector, v_p is the volume fraction of the particles, d_p is the particle diameter, and G is the matrix shear modulus.

Load bearing (load transfer) effect involves the transfer of the shear load from the soft and compliant matrix to the nanoparticles under the application of an external load. This strengthening mechanism appears when a strong adherence between the particles and the matrix is achieved and its contribution in enhancement the MMNCs could be described through a modified shear lag model introduced by Nardone and Prewo [80]:

$$\Delta\sigma_{LT} = v_p \sigma_m \left[\frac{(l + t)A}{4l} \right] \quad [80]$$

Where σ_m is the yield strength of the unreinforced matrix, l is the size of particulate parallel to the loading direction, and t are the size of the particulate perpendicular to the loading direction. When equiaxed particles are presented this equation may be reduced to:

$$\Delta\sigma_{LT} = \frac{1}{2} v_p \sigma_m \quad [80]$$

Another strengthening mechanism is the Hall-Petch Strengthening, where the nanoparticles act as heterogeneous nucleation sites for the grains during the solidification process and enhance the formation of a large number of grains. The grain growth takes place at the same time forming fine equiaxed grains which can hinder the dislocation movement due to the large grain boundary area. Furthermore, the difference in the orientation and the high lattice disorder at the grain boundaries restricts the dislocations movement on a continuous slip plane. In wrought alloys, the nanoparticles restrict the grain growth during high-temperature plastic formation by hindering the thermally excited grain boundaries migration [1]. The Hall-Petch Strengthening is one of the dominant mechanisms in MMNCs strengthening and can be expressed by:

$$\Delta\sigma_{H-P} = \frac{k_y}{\sqrt{d}} \quad [80]$$

Where k_y is the strengthening coefficient (characteristic constant of each material).

Studies showed that MMNC's containing multiscale reinforcements and grain sizes provide the majority strengthening improvements by Hall-Petch mechanisms while the Orowan strengthening mechanism only provides a minor contribution with a large overlooking of the nanoparticles effect on the resultant grain size. During particle pushing, the nanoparticles with below a particular size are pushed ahead of the solidification front restricting the grain growth. The energy required for pushing varies from a point to another and could be less than the energy needed to branch a dendrite, which promotes the nucleation of new fine grains attributed to an increase in the mechanical properties. When nucleation occurs around nanoparticles, the grain size could be severely reduced, but the experimental results did not show that the nucleation occurs around the nanoparticles. The grain growth restriction caused by nanoparticles could be related to the lower thermal conductivity of the reinforcements which affects the temperature gradient at the solidification front preventing heat removal needed for further solidification. Moreover, the particles may hinder the solute diffusion at the dendrite tip causing concentration gradient change and limiting their growth [107].

Another concept relates the strengthening in the MMNCs to the difference in thermal expansion coefficient and elastic modulus between particles and matrix. During cooling from processing temperature and straining of the material, the thermal stresses arise around nanoparticles. The stress level is often sufficient to induce plastic deformation, which promotes the formation of geometrically necessary dislocations (GNDs) and increases the dislocation density in the matrix. The GND density due to CTE and EM mismatch can be expressed by:

$$\rho^{CTE} = \frac{A\Delta\alpha\Delta T v_p}{bd_p(1 - v_p)}$$

$$\rho^{EM} = \frac{6v_p}{\pi d_p^3} \varepsilon \quad [80]$$

Where A is a constant related to the material geometry, $\Delta\alpha$ is the difference in the thermal expansion coefficients, and ΔT represents the temperature difference between test and processing or heat treatment temperatures. The combined strengthening based on the CTE and EM mismatch can be calculated using the Taylor equation [78]:

$$\Delta\sigma_{CTE+EM} = \sqrt{3}\beta Gb \left(\sqrt{\rho^{CTE}} + \sqrt{\rho^{EM}} \right) \quad [80]$$

where β is a constant.

The final strength of the MMNCs could be a function in all the above contributions composite. The final composite strength was proposed by several methods considering the effects superposition. One of these methods introduces the final strength calculation as a function in all the single strengthening contributions.

$$\sigma_c = \sigma_m + \sqrt{\sum_i \Delta\sigma_i^2} \quad [80]$$

With considering Orowan strengthening mechanism, CTE mismatch effect, and load-bearing effect the final strength could be calculated according to:

$$\sigma_c = (1 + 0.5v_p) \left(\sigma_m + A + B + \frac{AB}{\sigma_m} \right) \quad [80]$$

where A refers to CTE mismatch and B is the coefficient related to Orowan effect.

$$A = 1.25G_m b \sqrt{\frac{12\Delta\alpha\Delta T v_p}{b d_p (1 - v_p)}}$$

$$B = \frac{0.13G_m b}{d_p \left[\left(\frac{1}{2v_p} \right)^{\frac{1}{3}} - 1 \right]} \ln \frac{d_p}{2b}$$

[80]

The final strength of the MMNCs was not covered by enough research, thus the approaches are reported without a deep discussion and a fair comparison between each method [1].

2.6 Recycling of the MMNCs

Recycling is one of the most important criteria which determines the economic future of a certain material. The importance of recycling raises due to the natural environment preservation, energy saving, and wastage reduction especially for the massive production amounts like automotive industry. The term recycling differs than reclamation which involves the separation of the nanoparticles and the matrix using de-wetting processes. The efficiency of the recycling process is determined by the ability of the MMNC to restore its properties and microstructure as that of the as-fabricated state. During multiple recycling, the extreme reactivity resulted from the high temperature and the contact between the matrix and nanoparticles could have a remarkable effect on the interfacial characteristics and the particles distribution. Furthermore, causing metallurgical changes which hinder the MMNC properties. A recent contribution of re-melting a magnesium AZ31 reinforced with Al_2O_3 nanoparticles by using disintegrated melt deposition method and then hot extruded, showed that the recycled nanocomposite did not show any significant change in microstructure and mechanical properties. The research in this concern is very limited and more studies should be issued to cover the recycling process parameters with a reliable determination of the cost and energy effectiveness [15].

3 Experimental Procedures

This chapter introduces the material processing and fabrication method, as well as the mechanical and functional tests carried out to identify the AMNCs characteristics. Firstly, the used materials, i.e. matrix and reinforcement particles are specified, and the purpose of their selection is given. Afterwards, the AMNCs production scheme is described. Furthermore, the methods used for evaluating microhardness, surface roughness, residual stress, wear and corrosion resistance, fatigue and creep behavior are described. Therefore, the output of this chapter is an extensive description of the Al6061/Al₂O₃ AMNCs and their mechanical / functional performance.

3.1 Materials

The metal material nanocomposites consist of at least two main elements, which are the matrix and the reinforcement. Other alloying elements may be added based on the composition and the intended application. In this work the matrix used was commercial Aluminum-Magnesium-Silicon-Copper (Al6061). The chemical compositions of this alloy (in wt. %) was determined using Spectrometer (Spectrolab; Spectro Analytical Instruments, GmbH) and it is illustrated by Table 3.1. The Aluminum matrix was used reinforced by Al₂O₃ nanoparticles provided by the company Alfa Aesar Germany having the properties indicated in Table 3.2.

Table 3-1: Chemical of Al6061 alloy (wt.%)

Element	Si	Fe	Cu	Mn	Mg	Zn	Cr	Pb	Ti	V	Zr	Al
Wt. %	0.7834	0.5229	0.3218	0.1387	0.932	0.0534	0.2804	0.005	0.0351	0.01	0.0125	96.9037

Table 3-2: Al₂O₃ nanoparticles properties

Material/ Purity	Al ₂ O ₃ nanoparticles/99.5%
Average particle size	40-50 nm
Melting point/ Boiling point	2045°C/2980°C
Molecular weight/ Specific density	101.96/3.89
Surface area	32-40m ² /g
Phase/ Morphology	γ/ Near-spherical
Refractive index	1.768
Solubility	Slightly soluble in strong acid and alkaline solution. Insoluble in water.

The aluminum 6061 alloy was chosen because of its attractive properties of relatively high strength to weight ratio, excellent joining characteristics, good workability, and high corrosion resistance. Furthermore, the alloy is widely used in many applications such as in aircraft fittings, electrical fitting and connectors, couplings, brake pistons, and other applications in the marine industry and structural parts. The solidus temperature of the Al6061 is 582 °C while its liquidus temperature is 652°C possessing a microstructure of α Aluminum and Mg_2Si precipitates at room temperature under temper condition [1]. The alumina nanoparticles were a good choice as reinforcement particles due to its common usage in the fabrication of AMNCs owing to the interesting combination of density, and effect on the enhancement of the AMNC after its addition, good dispersion in the matrix and its relatively low cost [3]. The Al6061 was received in the form of a plate with the dimensions 50×100×800 mm and was cut into small pieces weighing about 500gm by using an electrical metal cutting saw to give a more precise reading during weighing and speed up the melting process, as well as to fit into the crucible. The small aluminum blocks were washed and dried to remove any contaminations from chips, water, or greases after the cutting process. The quantity of the aluminum matrix and the nanoparticles were weight using a digital balance with an accuracy 0.001 gram.

3.2 Fabrication

An electrical resistance furnace was utilized for both melting the charge and holding the temperature during the stirring process. Each cast consisted of 1 kg of Al 6061 held in a graphite crucible. The Aluminum oxide nanoparticles were packed into aluminum foil packets with diameter 3 cm and length of 4cm; each pack was set to contain 5 grams of Al_2O_3 . The packets were preheated to 300°C for 30 minutes for drying and preventing any agglomeration due to humidity; then they were introduced into the molten metal at a rate of 5 g/min. The charge was heated to 750°C, and a thermocouple of type K was used to control the temperature during melting, before and after mechanical stirring and just before pouring. The mechanical stirrer (Figure 3.1) was dipped into the melt at 750°C with a speed of 450 rpm for 15 min. The nanoparticles were added during the stirring process and just after the vortex in the melt was created. After finishing the stirring process, the melt was poured at a temperature of 675°C into a cylindrical-shaped steel mold with a diameter 50 mm and 150 mm length. The pouring temperature was higher than the liquidus temperature of about 25°C to ensure proper pouring without an undesirable solidification caused by heat loss while transferring the molten metal from the melting furnace to the mold. The cast cylinders were then homogenized by soaking them in an electrical resistance furnace at a temperature of 427°C for two hours followed by furnace cooling with a cooling rate of 28°C per hour to 260°C and then air cooling to the room temperature. The homogenized cylinders were cut by an electrical saw and subjected to age-hardening temper T4 heat treatment after cooling down to the room temperature. The heat treatment was taken place in an electrical resistance air furnace by increasing the temperature of the fabricated cylinders to 530°C reaching the solution temperature of the Al6061, and the temperature was held for 90 minutes to complete the solution treatment through delivering the material to the single-phase zone. The samples were then quenched in water to the room

temperature to reach the supersaturated solid solution with a quenching delay time did not exceed 11 seconds. Finally, the samples were naturally aged at room temperature for four days to enable the formation of the final Mg_2Si precipitates which are attributed to increasing the hardness and tensile properties of the aluminum alloy. To accentuate the effect of different amounts of nanoparticles addition on the enrichment of the composite performance, several weight fractions of Al_2O_3 were used having the weight fractions of 1, 2, 3, and 5%.

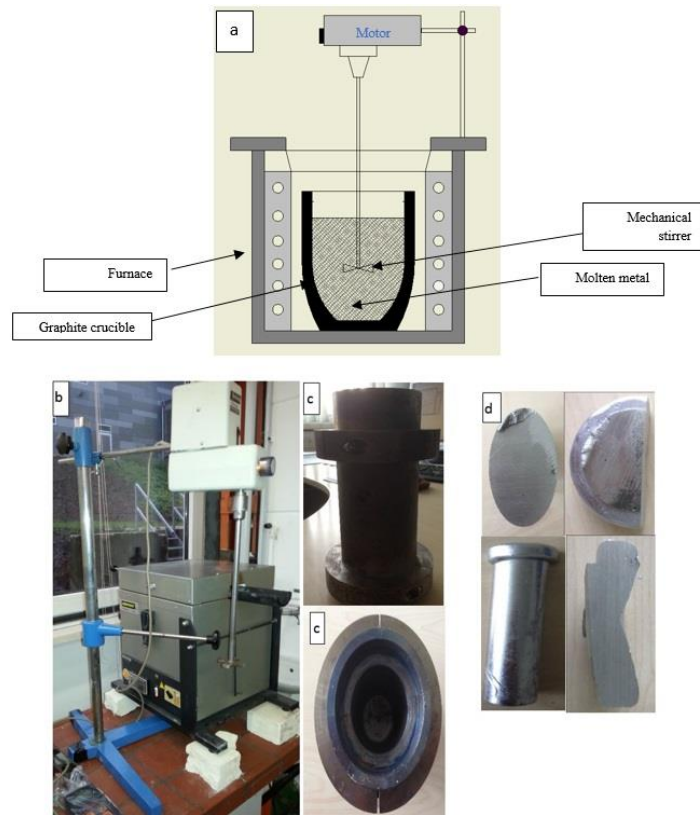


Figure 3-1: A Schematic drawing of the melting furnace and mechanical stirrer, b. Photograph of the furnace and the stirrer, c. The steel mold, and c. The casted sample

The casts were labeled according to the amount of the nanoparticles (weight fraction) added during reinforcement and indicated in Table 3.3.

Table 3-3: Samples designation

Sample name	As-Cast	1%	2%	3%	5%	Recy	1%SPD
Condition	Without Al_2O_3 addition	1 wt.% Al_2O_3	2 wt.% Al_2O_3	3 wt.% Al_2O_3	5 wt.% Al_2O_3	Recycled of the 1 wt.% Al_2O_3	1 wt.% Al_2O_3 and sever plastic deformation

Two other categories of samples were fabricated; the recycled samples to investigate the recyclability of AMNCs and the SPD (sever plastic deformed) samples to study the effect of sever plastic deformation on the performance of the MMNCs.

The recycled samples were manufactured by re-melting of the 1wt.% samples after finishing the conducted experiments on it and with the same manner of AMNCs fabrication. The samples were melted in the electrical resistance furnace and then its temperature was raised to 750°C with the application of the mechanical stirring for the same time of 15 minutes but without any further addition of Al₂O₃ nanoparticles.

The sever plastic deformation was conducted to the 1wt.% samples by rotary swaging (Figure 3.2). The process involves the closing and opening of the spindle dies several times during rotation cycle depending upon the number of rollers in the roller cage (B) and the number of dies used (D) with a closing time of 12 in one cycle. The spindle typically rotates at 300-500 rpm, with striking the rollers (B) by the hammer blocks during each cycle. The feeding occurs either automatically or manually with a little effort from the operator because of the frequent opening and closing process of the dies during swaging. The rotary swaging process was conducted after the manufacturing of the AMNCs and performing both homogenization and age-hardening heat treatments with a degree of deformation($\phi = \ln A_0/A_f$) 1.86 by reducing the diameter from 28mm to 11mm.

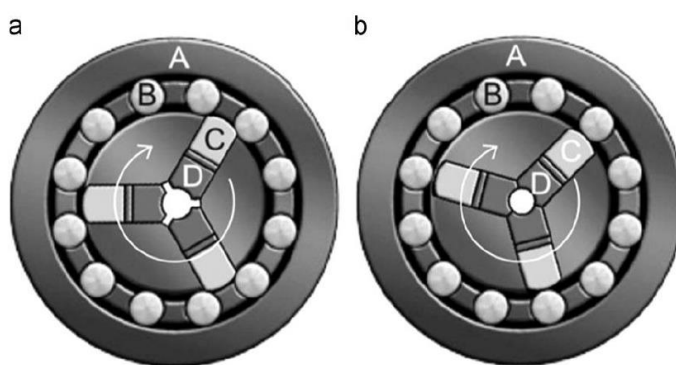


Figure 3-2: Schematic picture of a typical swaging unit [108]

3.3 Microstructure evaluation

Small samples were cut from the cast cylinder for the metallographical purpose. The microstructure samples were hot mounted using a Struers Labopress-1 hot mounting machine using Polyfast (bakelite and carbon filler), pressing force of 25 N and 10 minutes pressing time at temperature of 150°C. Small molds with a cylindrical shape having a diameter of 30 mm and length of 15 mm containing the samples were ground on four stages using emery papers of mesh number 320, 800, 1200, 2000 respectively the grinding direction 90° in each stage. Then the samples were polished on two steps by using an (Struers RotoPol-35) automatic polishing machine through using a soft polishing cloth impregnated with water and diamond suspension

(Dia-Duo 2) of 6, 3, and 1 μm respectively as a polishing media. The process parameters were 20 N pressing force, 250 rpm rotating speed in the opposite direction of the samples holding arm, and for 15 minutes for each stage. Etching of the samples was carried out with two different etchants. A general purpose reagent consisted of 0.5% HF with the balance distilled water was used for the grain size identification and microstructure examination by immersing the sample with a slight motion in the etchant for 20 seconds. Then washing it with water for three minutes followed by washing in an ultrasonic bath for another three minutes, and finally dried by hot air blowing. Weck's etchant with a composition of (100 mL water- 4 g KMnO_4 - 1 g NaOH) and 20 second immersion time was utilized for the polarized light examination. The Weck's etchant using polarized light was used to make the large-scale agglomerations better to be identified under the optical microscope. An (Zeiss Axioplan 2) optical microscope with an integrated camera connected to the computer was employed for the microstructure investigations of both etchants at different magnifications. The EDX measurements and the microstructure characteristics were examined by an energy dispersive X-ray spectroscopy (EDX) using Ultra Dry Compact (EDS) Detector from (Thermo-Scientific) and (Hitachi X650) scanning electron microscope with an accelerating voltage of 20 kV. Both ImageJ program and the Planimetric (Jeffries') procedure were employed to calculate the α -Aluminum grain size, the amount of porosity and agglomeration size. As a reference condition for fatigue test, electropolishing (EP) was implemented by using an electrolyte containing 60% Perchloric acid and water, a cell voltage of 24V, and temperature about -20°C for 30 minutes, to achieve a layer thickness removal from 50 to 100 μm .

3.4 Mechanical characterization:

3.4.1 Tensile test and Hardness measurements:

Tensile test samples were machined in accordance with DIN 50125 having the dimensions shown in Figure 3.3.

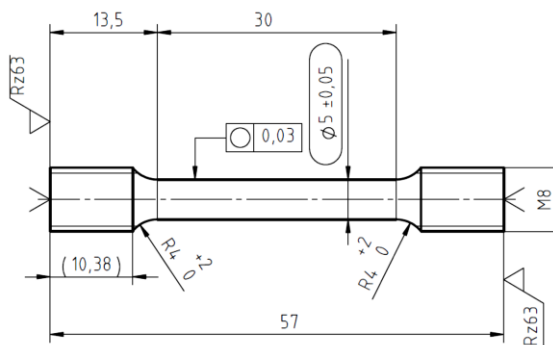


Figure 3-3: Tensile test sample dimensions

The tensile test was conducted at 50KN force Instron 5582 universal testing machine with 1mm/min strain rate at both room temperature and 300°C using. The tensile test at 300°C was conducted using a furnace supplied by ATS company (Applied Test Systems). The furnace was

utilized to heat the test sample before testing and to maintain its temperature during the test. For the tensile test at elevated temperature, the furnace was set to 300°C without installing the test sample to the tester grips. After reaching the test temperature, the sample was gripped, and the test started. The constant speed $v=1\text{mm/min}$ corresponds to an initial strain rates of $6.7 \times 10^{-4} \text{ s}^{-1}$. The tensile properties, yield strength, tensile strength, tensile ductility, uniform strain and tensile elongation were measured.

A (Wolpert Wilson) hardness tester, through implementing Vickers's indenter, was used with 5 Kg load for the hardness measurements. The indenter was a highly polished, pointed, square-based pyramidal diamond with face angles of $136^\circ \pm 30 \text{ min}$. The hardness measurements were conducted on the polished surface of the samples by taking the average of three points with enough spacing between each measurement, to prevent interaction between readings due to the plastic deformation caused by the indenter. The microhardness was performed by a Struers Duramin tester conforming DIN EN ISO 6507 and having a square base pyramid shaped indenter for testing (Vickers tester) using 50gF and a loading time of 15 s with taking the average of three measurements at each depth. The test was conducted to a 0.9 mm depth from the surface in a line with 0.05 mm spacing between each measuring point. The main objective of the microhardness measurements was identifying the effect of the shot peening and the roller burnishing as mechanical surface treatments on the surface hardness of the samples, as well as determining the hardness of some phases appeared in the microstructure. The microhardness measurements were taken place on a polished surface. The measurements followed the sequence of pressing the indenter on the mechanically polished surface sample by the loading force and maintained for a dwell time of 10 to 15 second. After the dwell time is completed, the indenter is removed leaving an indent in the sample that appears square shaped on the surface. The size of the indentation is determined optically by measuring the two diagonals of the square indentation. The hardness test was taken on transverse surface section of shot peened, roller burnished, and electropolished specimens.

3.4.2 Fatigue test

The fatigue tests were carried out by a (Sinco-Tech) rotating beam fatigue machine with a frequency of 50 hertz using cantilever rotating beam mechanism and loading ($R = -1$) both in air and 3.5 wt.% NaCl solution at room temperature. The fatigue strength was set at a fixed number of cycles for 10^7 cycles. The test was conducted on the electropolished reference samples as well as the mechanically surface treated samples. The fatigue samples were machined to an hour-glass shape conforming the ASTM-E466 with minimum gauge diameter of 6 mm as shown schematically in Fig. 3.4.

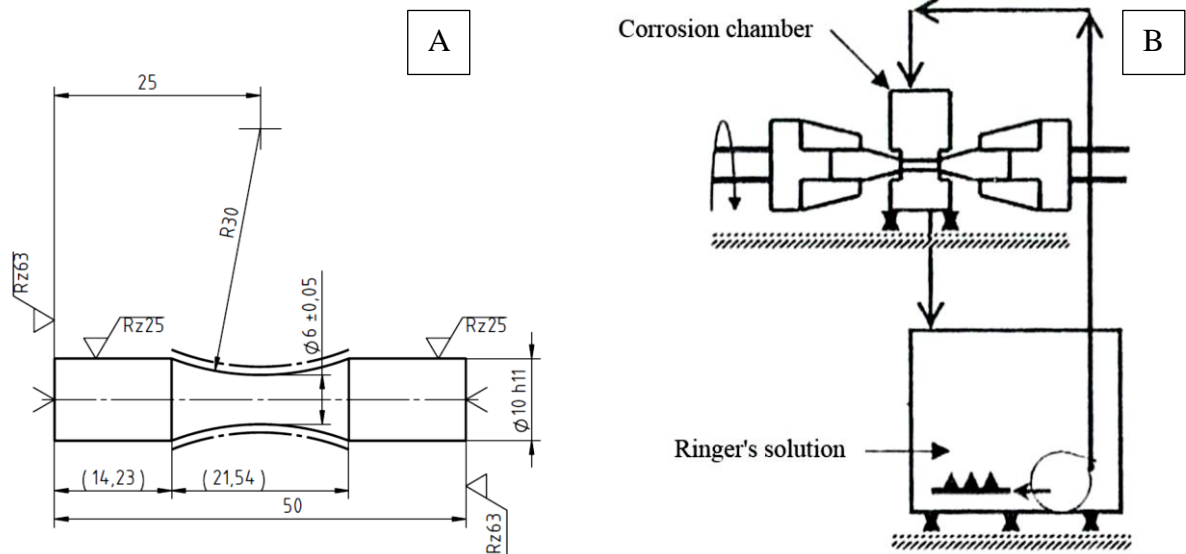


Figure 3-4: (A) The fatigue test specimen and (B) Corrosion fatigue cell

3.4.3 Creep-rupture test:

The test involved the measurements of the progressive specimen deformation and the time for rupture. The Creep (rupture test) was conducted by using an ATS series 2330 Stress Relaxation single-station direct load creep tester at constant stress amplitude of 40 MPa and 300°C conforming ASTM E139-00 designation (Figure 3.5). The creep tester had a capacity of 13.34 kN and 10:1 ratio using an ATS furnace series 3210 with 2640 Watts, 230 Volts, and maximum temperature of 1200 °C. The condition of 1wt.% Al₂O₃ was subjected to different creep-rupture tests at different stress amplitudes and constant temperature of 300°C to investigate the effect of the shot peening with different shots medium and Almen intensities on the creep behavior of the AMNC. Before the test start, the extensometers were calibrated and checked as well as the thermocouples. The test aperture used two extensometers for measuring the total plastic strain during the test and the temperature was controlled by using three thermocouples of type K during the soaking and test period. After the sample installation, the test machine furnace raised the sample temperature to the test temperature during a soaking time of two hours with a heating rate 555 °C/Hr. Just after the soaking process, the tester proceeded to the load application and the test continued until the specimen rupture.

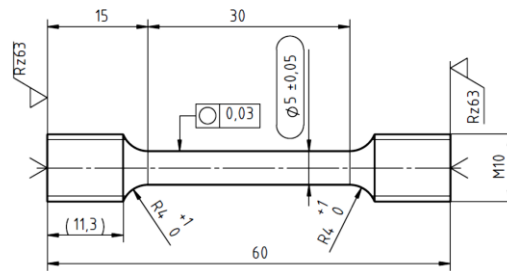


Figure 3-5: Creep-rupture test machine and specimen.

The creep data acquired from the test were the percentage of the total plastic deformation and the time to rupture under constant stress. These data were processed to identify the minimum creep rate by plotting the percentage of total plastic deformation divided by the run time in sec against the run time in sec. Another output of the creep test is the creep compliance “ C_{crp} ”, which is simply presented by the ratio of the strain to stress. The creep compliance roughly proportions inversely with the stiffness, which means a compliant material is a non-stiff material [35-36].

3.4.4 Wear resistance test:

Samples of each condition were taken and machined to have a rod profile with a diameter of 7.9 mm and length of 12 mm. The test machine uses a pin on disk testing mechanism with 265 rpm speed, 0.7 Bar load and 15 min test time. In this mechanism (Figure 3.6), a pin of the sample is loaded against a flat rotating steel disc. The machine is used to evaluate wear and friction properties of materials under pure sliding conditions. The wear rate was determined by weighing the sample before and after the test carefully with a precision balance, and the wear rate was

represented by the weight loss (the difference in the weight) of the sample and indicated by ($\mu\text{g/m}$)

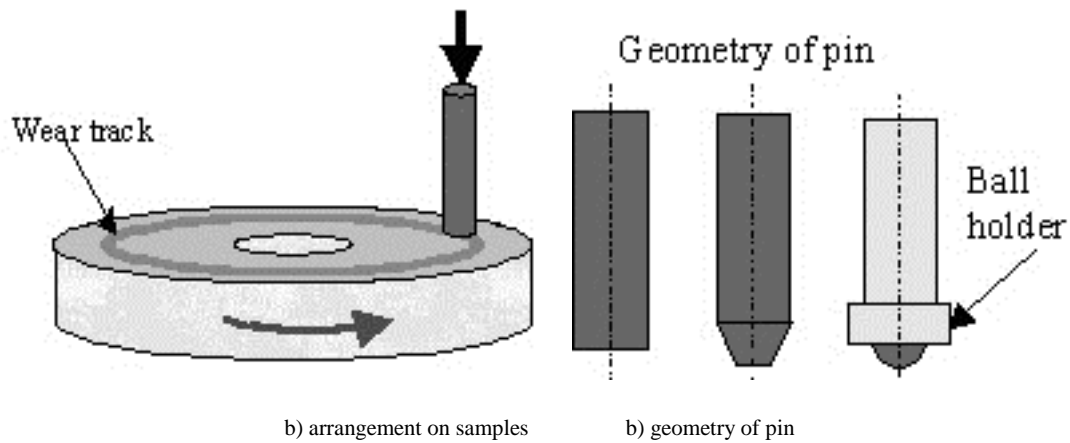


Figure 3-6: Schematic of a pin-on-disc wear test and the arrangement of samples [109]

3.5 Mechanical surface treatments

The mechanical surface treatments have a significant influence in enhancing the fatigue life of a certain material by inducing compressive residual stresses on the surface generated from the increased dislocation density after plastic deformation of a particular area. The samples were mechanically surface treated by shot peening and roller burnishing.

3.5.1 Shot peening

Shot peening was carried out using an automatic controlled shot peening machine manufactured by OSK-Kiefer GmbH (Figure 3.7). A pressure-suction system controlled the machine. The shot media was a spherically conditioned cut wire (SCCW 14), with an average diameter of 0.36mm and a hardness of 700 HV1. During the peening process, the rounded shots were accelerated by a stream of highly pressurized air and projected through a nozzle onto the specimen surface. The shots bombard the sample at a specific area with an adequate force acts as a peen hammer and ensures the creation of a small dimple, accompanies with a plastic deformation and high compressive residual stress on the surface. Shot peening is not only used for inducing compressive stresses, but also relieving tensile. The peening process is controlled by both the material strength and the shot peening parameters like peening media, peening intensity, peening angle, exposure time, and the degree of coverage. During shot peening, the distance between the nozzle and samples was kept at about 90 mm, and the samples were slowly rotated to obtain a roughly 100% coverage after 20 seconds. The Almen strip used to determine the Almen intensity was of type A having a thickness of 1.3 mm and made of SAE 1070 steel.

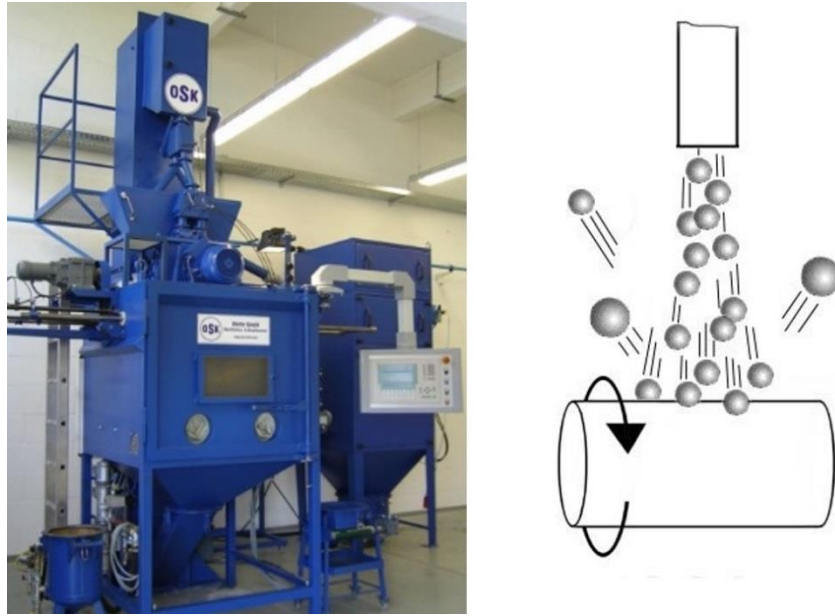


Figure 3-7: The shot peening machine and a schematic drawing of the bombarding of the shots with the sample.

3.5.2 Roller Burnishing:

The samples were roller-burnished (RB) using a conventional lathe (Weiller, Matador), equipped with a hydrostatically burnishing tool from ECOROLL Company (Figure 3.8).



Figure 3-8: Hydraulic roller-burnishing machine.

The cylindrical roller was made of steel EG45 ($\phi = 5$ mm) mounted in a holder, behind which a hydrostatic pressure was applied to generate a normal force on the surface. The sample was fixed in a holder and clamped to the conventional lathe. A hydraulic piston supported the holder to produce a constant regular rolling force at all contact points on the surface. The workpiece was spinning, and the roller was moved at a constant rate across the surface to deform the surface layer plastically with the introduction of a hydraulic fluid of water mixed with 3.5% oil as a

lubricant around the roller. The purpose of the hydraulic lubricant was to avoid the thermal friction and sticky contact with ensuring a free rotation of the roller in any direction.

3.5.3 Optimization of the shot peening and roller burnishing parameters:

The optimization of the shot peening and roller burnishing parameters were taken place on a wrought Al6061-T4. The shot peening optimization was carried out at a wide range of different pressures adjacent to variable Almen intensities (Table 3.4) and constant parameters of impingement angle of 90°, a separating distance between the workpiece and the nozzle of 90mm using shots of type SCCW 14 with average size 0.36 mm. The Almen intensities (Figure 3.9) were measured by identifying the arc height of the Almen strip type A after different peening time by using the Almen gauge. The SSCS program (Saturation Curve Solver by Shockform Aeronautique Inc.) was utilized to process the data of the arc height and the time to determine the Almen intensity values.

Table 3-4: The corresponding Almen intensity at different pressures

Peening pressure(bar)	Almen intensity(mmA)
1	0.1
2	0.14
3	0.16
3.5	0.17
4	0.2
5	0.22
6	0.23

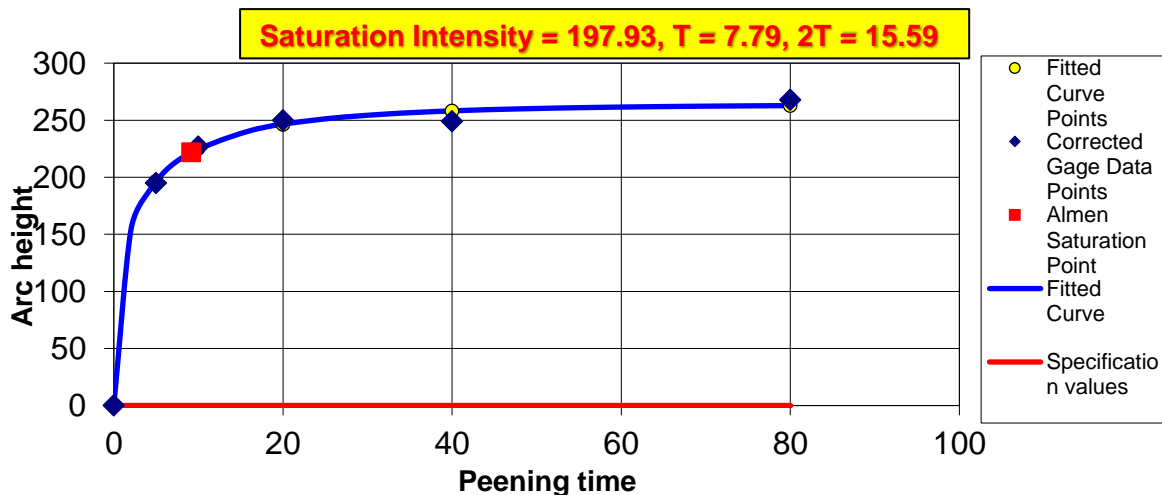


Figure 3-9: Example for calculation of the Almen intensity at 4 bars using SSCS program.

The roller burnishing optimization was undergone at constant feeding rate of 0.122 mm/rev, rotating speed 150 rpm and different pressures (0.3, 0.5, 0.7, 0.8, 1 and 1.2 bar). The optimization of the shot peening was conducted based on the fatigue performance, the microhardness of the

samples in the layer adjacent to the surface and the surface roughness of the samples after the mechanical surface treatments. Figure 3.10 a and b indicate the number of cycles to failure at constant stress amplitude of 225 MPa and at 250 MPa for shot peened roller burnished conditions respectively.

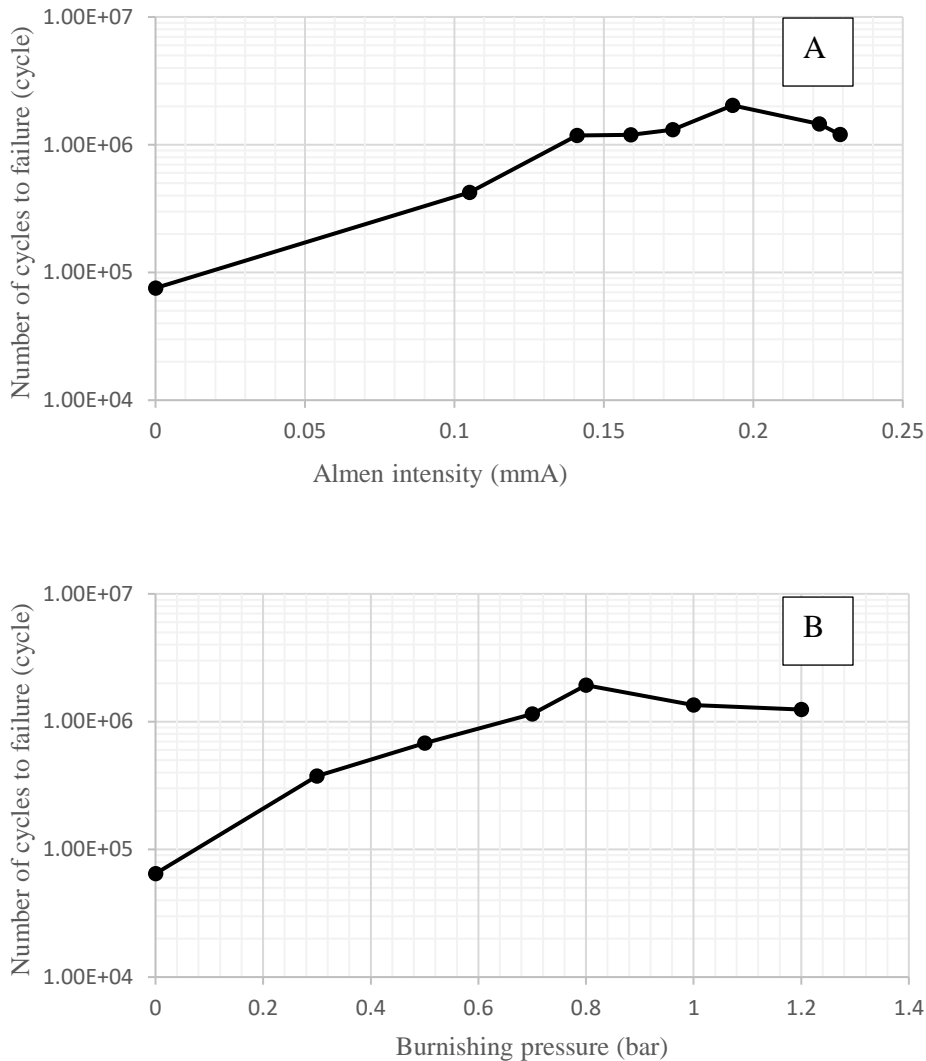


Figure 3-10: Number of cycles to failure of different Almen intensities and burnishing pressures conditions

The highest fatigue strength was obtained at 0.2 mmA Almen intensity and at burnishing pressure of 0.8 bar. The concept of mechanical surface treatment is to generate localized plastic deformation on the workpiece surface. High dislocation density identifies this layer with a thickness can reach to 0.2mm in shot peened and might be extended to 0.5mm in roller burnished. In this region, increasing the Almen intensity or burnishing pressure raising both the hardness and the amount of residual stresses stored in this area to a definite value. At a certain Almen intensity or burnishing pressure, further increase may lead to a saturation of the dislocation

density, and the hardness stops to have a constant value and reach the “over-peening” or “over-burnishing”. The term “over” describes the state of the material under heavy plastic deformation and thermodynamic instability, which may cause internal stress relief and decrease the amount of compressive residual stresses. When the process reaches this stage, localized high-stress concentrations or crack initiation sites are found in the material resulting in a reduction in the fatigue life [6-7,110-112].

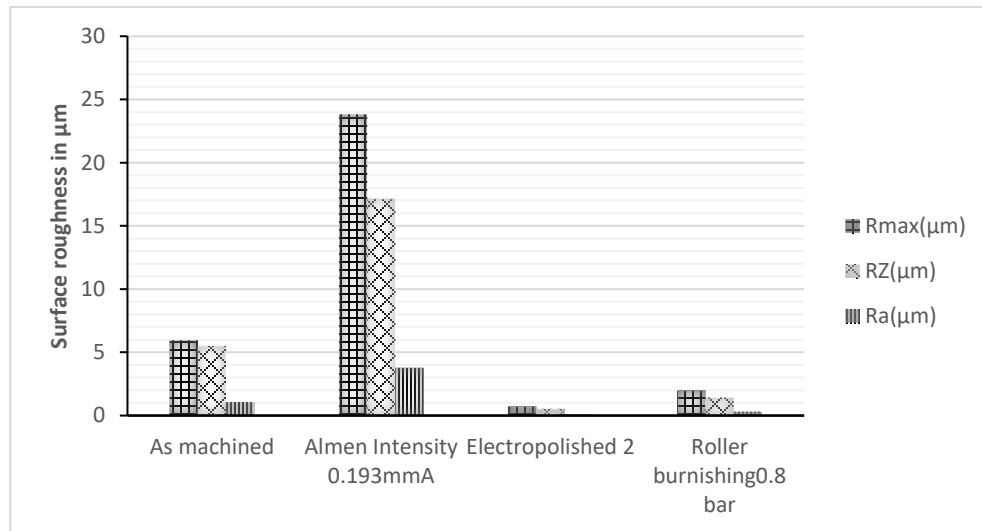


Figure 3-11: Surface roughness of selected samples under different surface treatments.

The fatigue behavior is affected by the crack initiation (which depends on the surface roughness) in the low cyclic fatigue. On the other side, the fatigue strength is more influenced by the crack propagation in the high cyclic fatigue, which is controlled by the amount of the induced compressive residual stresses. The surface roughness has a functional role in affecting the fatigue life by retarding or stimulating the crack initiation [6-7]. From Figure 3.11, it is evident that shot peening increases the surface roughness compared to roller burnishing and electropolishing. However, the final fatigue life is a function of the amount of compressive residual stresses (Figure 3.12), the surface layer hardness (Figure 3.13), and the surface roughness. The smoother surface, the lower probability of the crack initiation. However, the compressive residual stresses squeeze the grain boundaries and thus delay the fatigue crack initiation. Forasmuch, the crack initiation or propagation are difficult to occur in the layer of compressive stresses. Therefore, the cracks initiate under the surface with a significant slow propagation rate leading to a prolonged fatigue life [6-7,113-115].

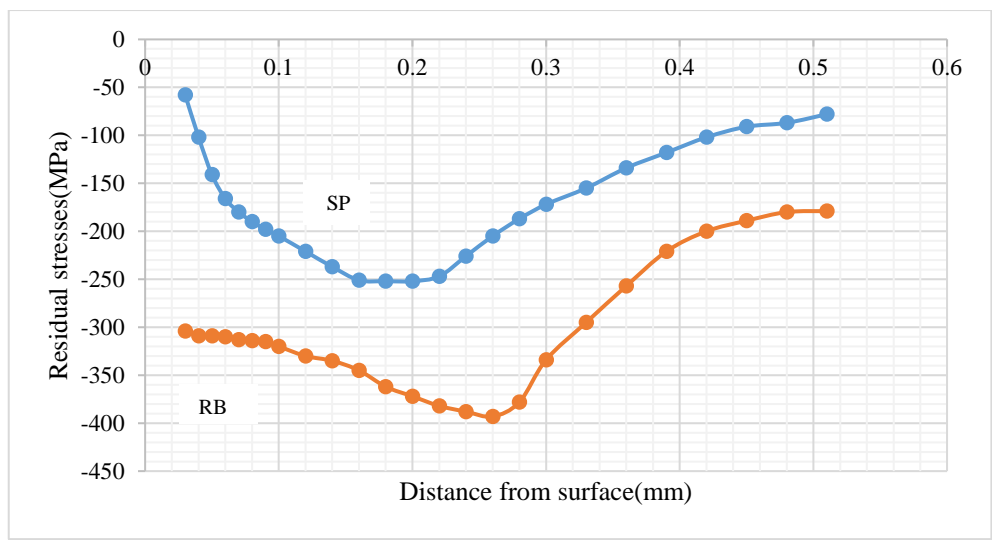


Figure 3-12: Residual stresses profile for shot peened and roller burnished conditions

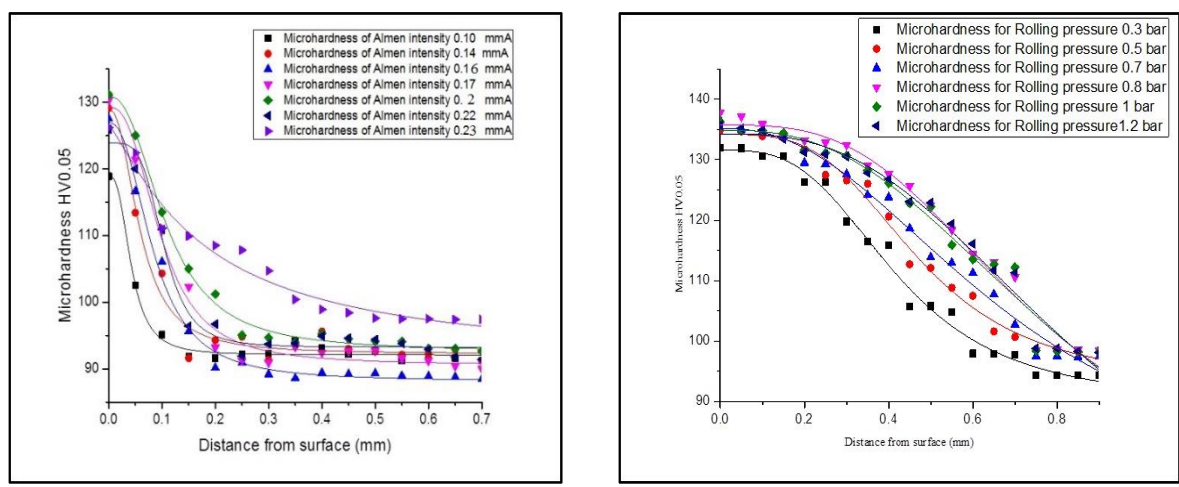


Figure 3-13: Microhardness of shot peened and roller burnished samples

3.6 Surface roughness

The surface roughness of the various surface treatments was measured using an electronic contact (stylus) profilometer instrument (Perpethometer). The Perthometer profilometer S8P supplied by the company Perthen Mathr using tester of RFHTB-250 of radius $5\mu\text{m}$, force 1.3mN , measurement angle 90° and $250\mu\text{m}$ measurement distance. The roughness parameter such as the arithmetic average roughness R_a , the maximum roughness height R_y and ten-spot average roughness R_z were determined and evaluated. R_a is the arithmetic mean of the absolute values of the roughness profile ordinates. The area within the roughness profile and its mean line, or the aggregate of the absolute height value of the roughness profile over the evaluation length refer to the average roughness. R_y or (R_{max}) – Maximum height of the roughness profile is the sum

of the highest profile peak height and the depth of the lowest profile valley within a sampling length. Rz is the parameter that averages the five highest peaks height plus the depth of the five deepest valleys over the evaluation length. The calculations were performed by taking the average of three values in accordance with (DIN 4768). The parameter (Rz) was used rather than the average roughness (Ra) comparing all the peaks and valleys to the mean line, since entirely different surfaces could have the same Ra and consequently perform differently [74].

The surface roughness is used to measure the surface texture and quantified by the vertical deviations of a real surface from its ideal form. Large deviations are indications for a rough surface with higher friction coefficients. Contrary, when these deviations are small refer to a smooth surface with lower friction coefficients. Roughness contributes significantly to determine how a real object will interact with its environment. The mechanical performance of an individual mechanical component could be predicted from the surface roughness value, where the irregularities in the surface may act as nucleation sites for cracks or corrosion causing a lower fatigue life and corrosion resistance [74].

3.7 Residual stresses measurements by Incremental Hole Drilling Method (IHD)

The incremental hole-drilling method (IHD) according to the ASTM E 837–01 was used to calculate the residual stresses from the values of the residual strain. The IHD method involves attaching strain gauge rosettes of 0.8 mm diameter (EA-06-03RE-120 supplied by VISHAY Company) to the sample surface and introducing a hole in the vicinity of the gauges by drilling. Then, measuring the relieved strain using an oscillating drill with 1.9 mm diameter driven by an air-turbine with a rotational speed of 200000 rpm. The induced strain in the surface layers were measured at each drilled depth of about 20 μm . The relieved principal stresses were calculated from the measured strains through a series of equations using the macroscopic Young's modulus and Poisson's ratio. A strain gauge rosette with three elements of the general type schematically illustrated in Fig.3.14 is placed on the area, to be measured. The numbering scheme for the strain gauges follows a clockwise convention. A hole is drilled at the geometric center of the strain gauge rosette to a depth of about 0.4 of the mean diameter of the strain gauge circle and then the residual stresses in the area surrounding the drilled hole relax. The entire measurement process is PC-controlled, which ensures a high degree of measurement reliability and good reproducibility [74].



Figure 3-14: Hole-drilling machine and rosette [74]

3.8 Corrosion resistance:

Corrosion rate was estimated by using a computer controlled VersaSTAT3 potentiostat from Princeton Applied Research company with round bottom cell. The composition of the electrolyte used was (in g/L) 35 NaCl dissolved in distilled water. The electrochemical test was used to directly amplify the impact of corrosion processes to accelerate the corrosion process. This was possible since electrochemical tests use a fundamental model of the electrode kinetics associated with corrosion processes to quantify corrosion rates. The experiments were performed according to ASTM G5-94 in a conventional three-electrode cell with a counter electrode of a platinum sheet including placing the Haber Luggin capillary close to the working electrode at room temperature. The potential values were reported relevant to saturated calomel electrode (SCE). The potentiodynamic polarization experiments were conducted after stabilization of the free corrosion potential among a scan rate of 1 mV/s. The samples were prepared by connecting a copper wire to one face of the specimen. The specimen with the attached wire were then cold mounted in resin and dried in air for 24 h at room temperature. The samples were consecutively wet ground with 800, 1200, 2000 and 4000 SiC paper and then polished sequentially using 1 and 0.3 μm alumina suspension. The samples were cleaned ultrasonically in an acetone bath and dried in a cold air stream before the electrochemical measurements. The Tafel extrapolation method was used to determine the corrosion rate [108]. The Corrosion rate (in mpy), which was extracted from the extrapolation of the Tafel lines of each polarization curve, is calculated by the following equation: $\text{C.R.} = (\text{I}_{\text{corr}} \times \text{K} \times \text{EW}) / (\rho \times \text{A})$

Where I_{corr} = corrosion current density in Ampere (A), K = constant that defines the units of corrosion rate (1.288×10^5 mils/A cm year), EW = equivalent weight in (g/equivalent), ρ = density and A = sample area in cm^2 . The equation indicates that corrosion rate is directly proportional to corrosion current density [108].

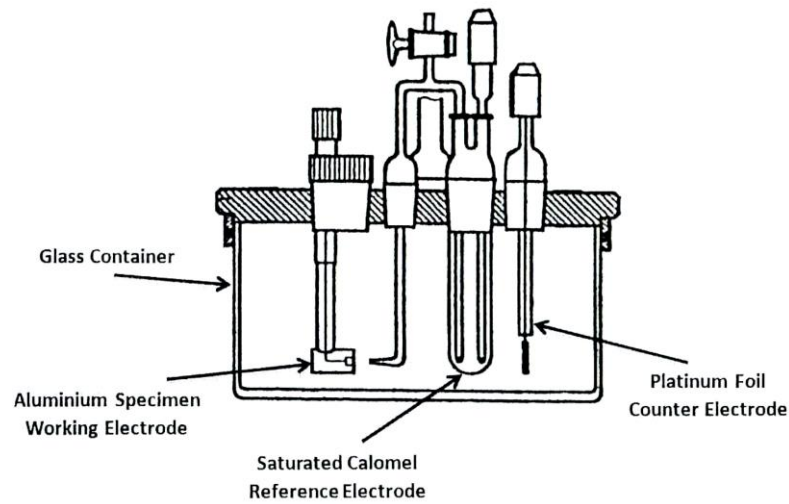


Figure 3-15: Schematic diagram of polarization of the three-electrode cell [108]

3.9 Weldability of the AMNCs

The weldability of the similar AMNCs was investigated by the rotary friction welding technique. Figure 3.16 illustrates the rotary friction welding machine used in the experiments supplied from IWS Service GmbH and of type RSM 200. The device is pneumatically driven having 1.85 kW power with an axial load capacity of 18 kN and can run at speed up to 23000 rpm. The friction welding process is controlled by the friction time or by the burn-off distance. Thus, the machine is a direct drive system. The welding samples were machined to have a diameter of 8 mm and 40 mm length with smooth oxide-free surfaces to ensure perpendicularity which is significant for achieving sound weld joints.

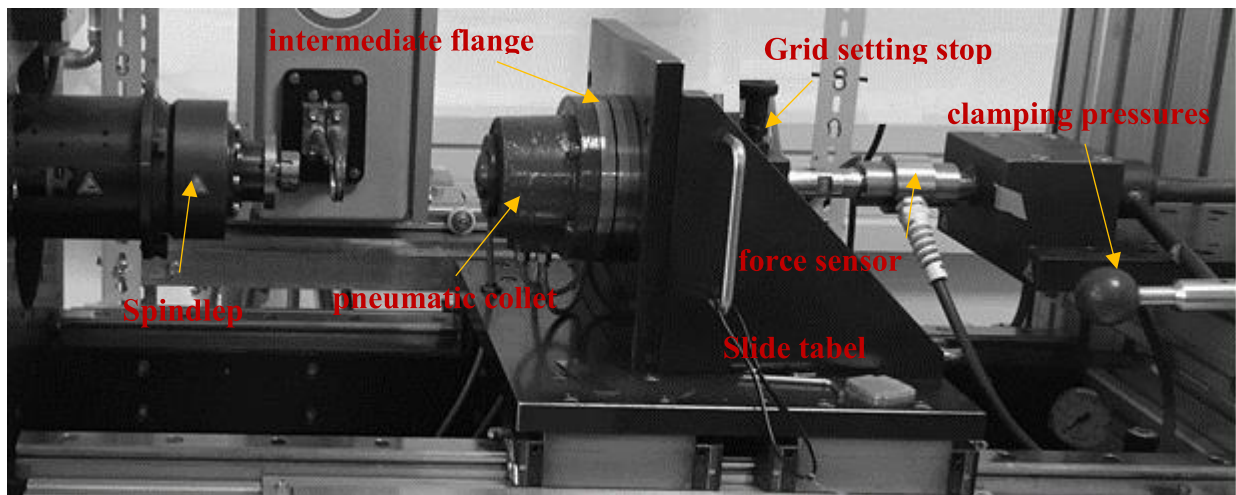


Figure 3-16: The used rotary friction welding machine RSM 200 [116]

The program Minitab 17.0 was used based on two different design of experiments (DoE) to identify the main friction welding parameters affecting the weld quality. Process variables were friction pressure, friction time, forging pressure, forging time and rotational speed. While the output variable (response) were the material loss and as-weld joint tensile strength. In this work, both Taguchi and factorial design approaches were used. Both approaches consist of a series of runs in which purposeful changes are made to the input variables and data were collected at each run. For the factorial design approach, two-level full factorial design matrix with three replicates has been used to create the design of the experiments. The Taguchi approach is based on executing one large comprehensive experiment and evaluating the data by analyzing the variance in terms of measured Taguchi function (known as a signal to noise ratio).

The welded joints quality depends on the amount of plastic deformation occurred after the welding process, the tensile strength of the welded joint and the fracture position (rejected when it is found on the weld line) [116]. A set of experiments has been conducted according to the data obtained by the two different approaches based on the input variables. The objective of the optimization was to obtain a maximum weld joint strength with a minimum final length reduction. The welded joints investigation based initially on visual examination and a macrostructural evaluation. Then, the welded samples were examined by metallographic means of microstructural evaluation to evaluate the metallurgical transformations, that took place within the joints. As a last characterization step, the mechanical properties of welded specimens were tested by the tensile test and microhardness measurements. The specimens were machined with flash removing to fit the test geometry. Tensile tests were carried out at room temperature (RT) under the (DIN 50125) standard with testing minimum three specimens at each attempt to obtain the mean value. Tests were carried out by an Instron 5582 universal testing machine using load of 50 kN, with straining rate of 1 mm/min. The microhardness was measured using a Struers Duramin tester of a square base pyramid shaped indenter for testing by a Vickers tester having a nominal force of 50 gf (HV0.05) and a loading time of 15 s in accordance with the DIN EN ISO 6507 standard. The average of three measurements was taken at each depth to construct the hardness-depth profiles.

4 Results and Discussion

Based on the systematic research methodology and the experimental procedures described earlier, the metallurgical, mechanical, and functional tests will be presented and discussed in detail in this chapter to accentuate the role of nanoparticles addition on the Al6061 performance.

4.1 Microstructure evaluation

Microstructural analyses of each condition were carried out using Optical Microscopy (OM) and Scanning Electron Microscopy (SEM) with Energy Dispersive X-ray spectroscopy (EDX) analysis. OM is used to characterize the casting structure and quantitatively assess the porosity and the grain size as well. While SEM and EDX were used to evaluate the agglomeration of the nanoparticles, elements distribution, and precipitations on grain boundaries. The objective of this section is to elucidate the dependence of the microstructure on the processing variables including mainly the Al_2O_3 weight fraction and the mechanical stirring regime.

4.1.1 Fundamental characterization of the Al6061 matrix

The microstructures of the as-cast Al 6061-T4 matrix are illustrated in Figures 4.1 A and B. The Figures indicate the microstructure obtained by general purpose reagent (0.5 % HF and the balance distilled water) using monochromatic light and Weck's tent etchant using polarized light at magnifications 200X and 500X.

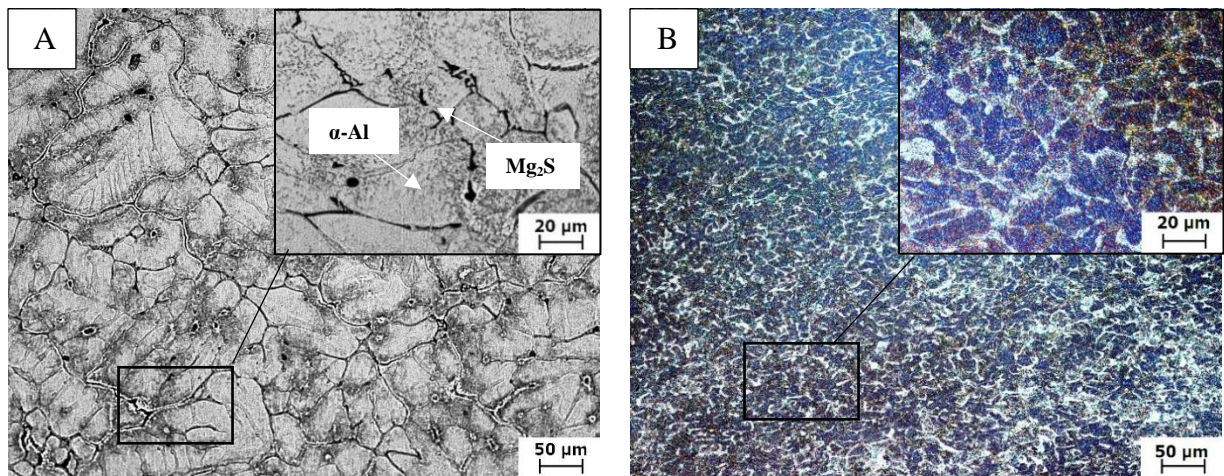


Figure 4-1: Microstructure of As-Cast Al6061; A. using general purpose etchant at magnification of 200 and 500X, B. using color etchant at magnification of 200 and 500X

The main constituents of the microstructure are α -Aluminum phase and Mg_2Si precipitates. The microstructure is characterized by coarse grain size (about $90\mu\text{m}$) caused by the relatively slow cooling rate (air cooling) during solidification after the casting process. The SEM micrographs are indicated by Figure 4.2 side by side with the EDX analysis of different regions in the matrix. Some intermetallic compounds were captured in the matrix and listed in Table 4.1. The SEM micrographs demonstrate the presences of typical porosity in the as-cast samples during casting and the existence of the Mg_2Si precipitates on two scales; large clustered precipitates (represented

by bright field on the micrograph (Figure 4.2 A)) and the other was fine precipitates appeared as a dark colored field on the SEM micrograph (Figure 4.2 B). The precipitates are distributed both along the grain boundaries and inside the grains. Figure 4.3 and Table 4.1 utilize the presence of some iron-rich phases (such as $\text{Fe}_3\text{SiAl}_{12}$, $\text{Fe}_2\text{Si}_2\text{Al}_9$, or a mixture of them depending on the distribution of magnesium, silicon, and iron among the matrix) on a small scale [1,9,14]. The small amounts of manganese and chromium (0.13 and 0.2 %) in the alloy could not fully overcome the negative effect of iron-rich intermetallic compound on the mechanical performance through the transformation of these Fe-rich intermetallic into less harmful morphologies. These thin plates or needle-like iron-rich phases are undesirable because they are difficult to be fragmented and/or spheroidized during the annealing process because of the thin, smooth planar nature of their surfaces [117-120]. Moreover, they are thermodynamically stable under this condition which makes the formation of consolidated particles in aluminum matrix more difficult. These restrictions on the modification by heat treatment make the chemical modification the most convenient modification method of such phase [1,9,14].

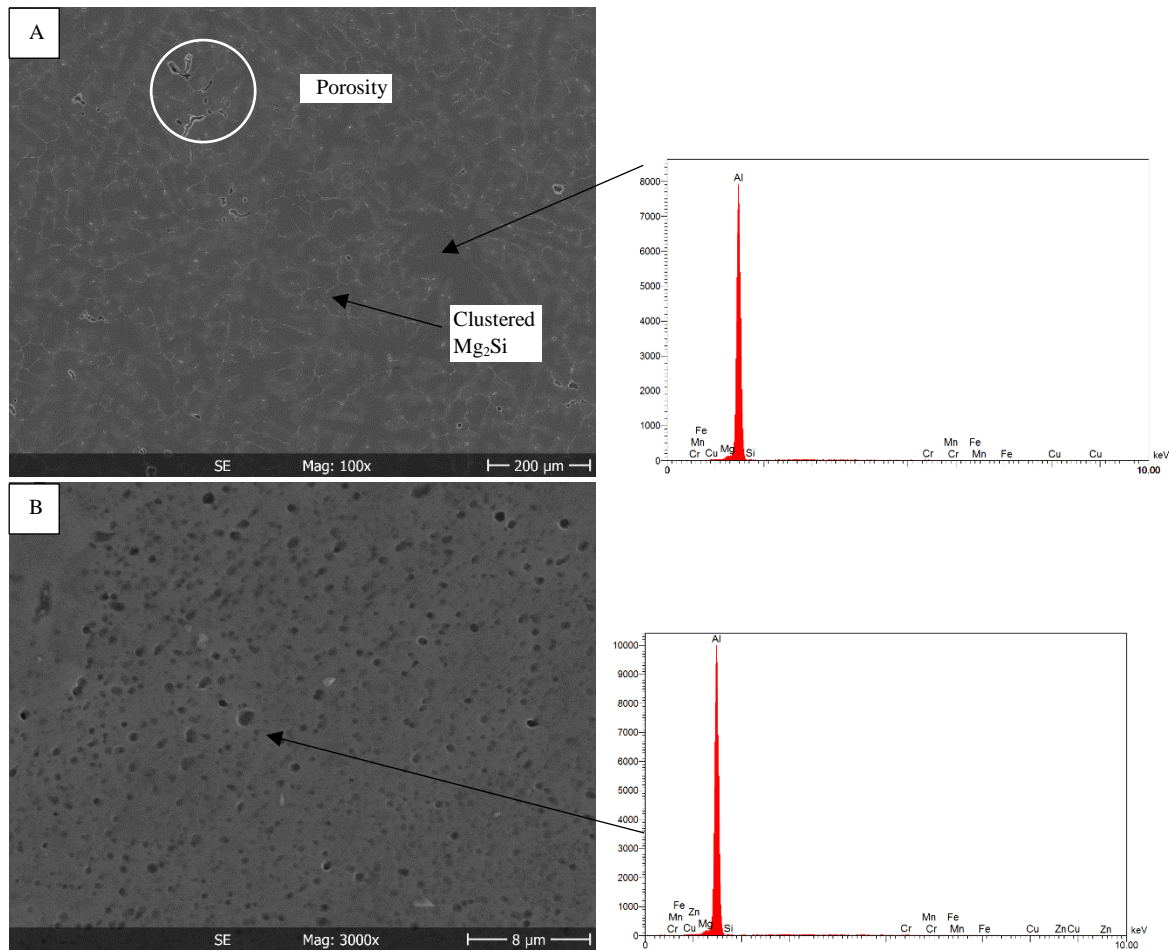


Figure 4-2: SEM and EDX spectrum of the as-cast samples; A. SEM micrograph of the matrix, B. SEM micrograph of the Mg_2Si precipitates in dark color, C. is the EDX of the as-cast matrix and D. is the EDX of the Mg_2Si precipitates

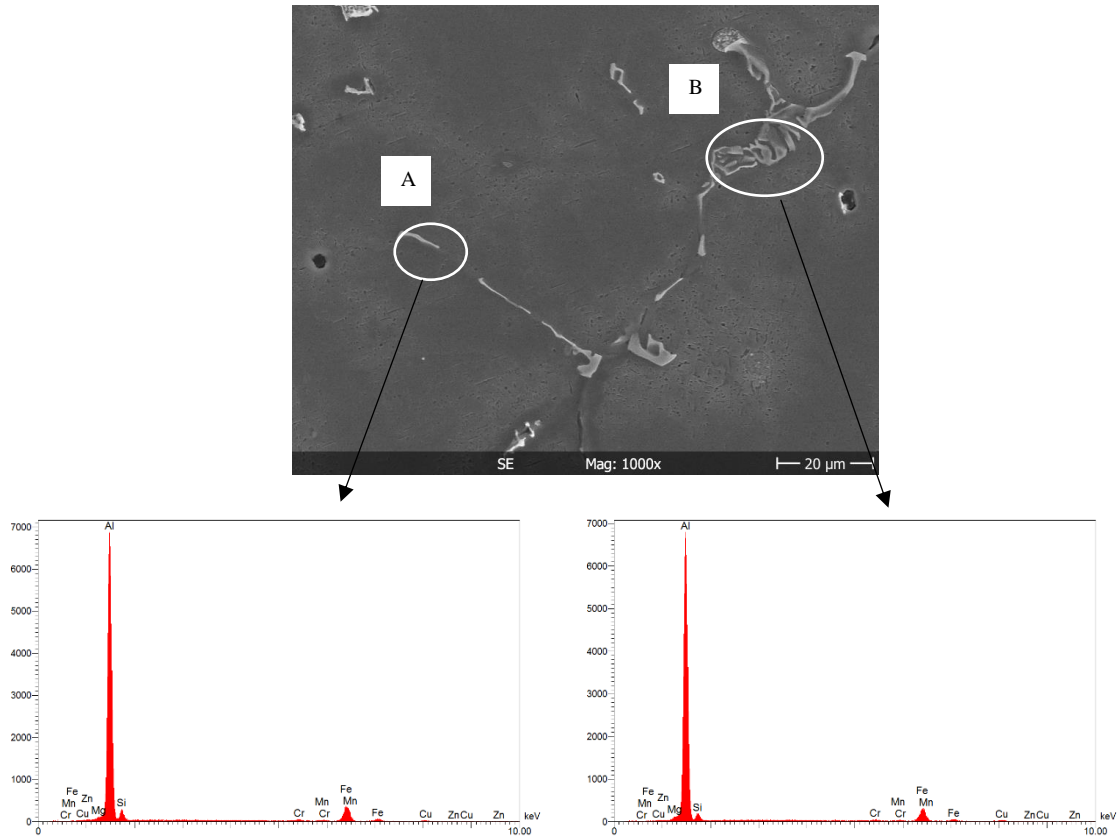


Figure 4-3: EDX of some $\text{Fe}_3\text{SiAl}_{12}$ and $\text{Fe}_2\text{Si}_2\text{Al}_9$ precipitates presented in as-cast micrographs

Table 4-1: Chemical composition of the matrix and the Mg_2Si precipitates for the as-cast condition

Element	Wt. % In the matrix	Wt. % In Mg_2Si	Wt. % A and B
Al	97.72	97.45	76.49-79.65
Mg	1.57	1.09	0.81-0.86
Si	0.05	0.65	3.37-4.87
Fe	0.11	0.21	13.87-15.68
Cu	0.24	0.33	0.99-1.32
Cr	0.20	0.18	0.63-0.72
Mn	0.10	0.09	0.34-0.39
Total	100.00	100.00	100.00

4.1.2 Characterization/Analysis of the Al6061/Al₂O₃ composites

The microstructure of the 1wt.% Al₂O₃ composites consists mainly of α -aluminum and Mg₂Si precipitates (Figure 4.4 A). Introducing the alumina nanoparticles to the Al6061 matrix with weight fraction of 1% leads to a decrease in the grain size of the α -aluminum. The grain refinement, occurred after nanoparticles addition, can be explained by increasing the nucleation sites during the solidification process or through pinning the grain boundaries causing a decrease in the dynamic recrystallization. [18-19].

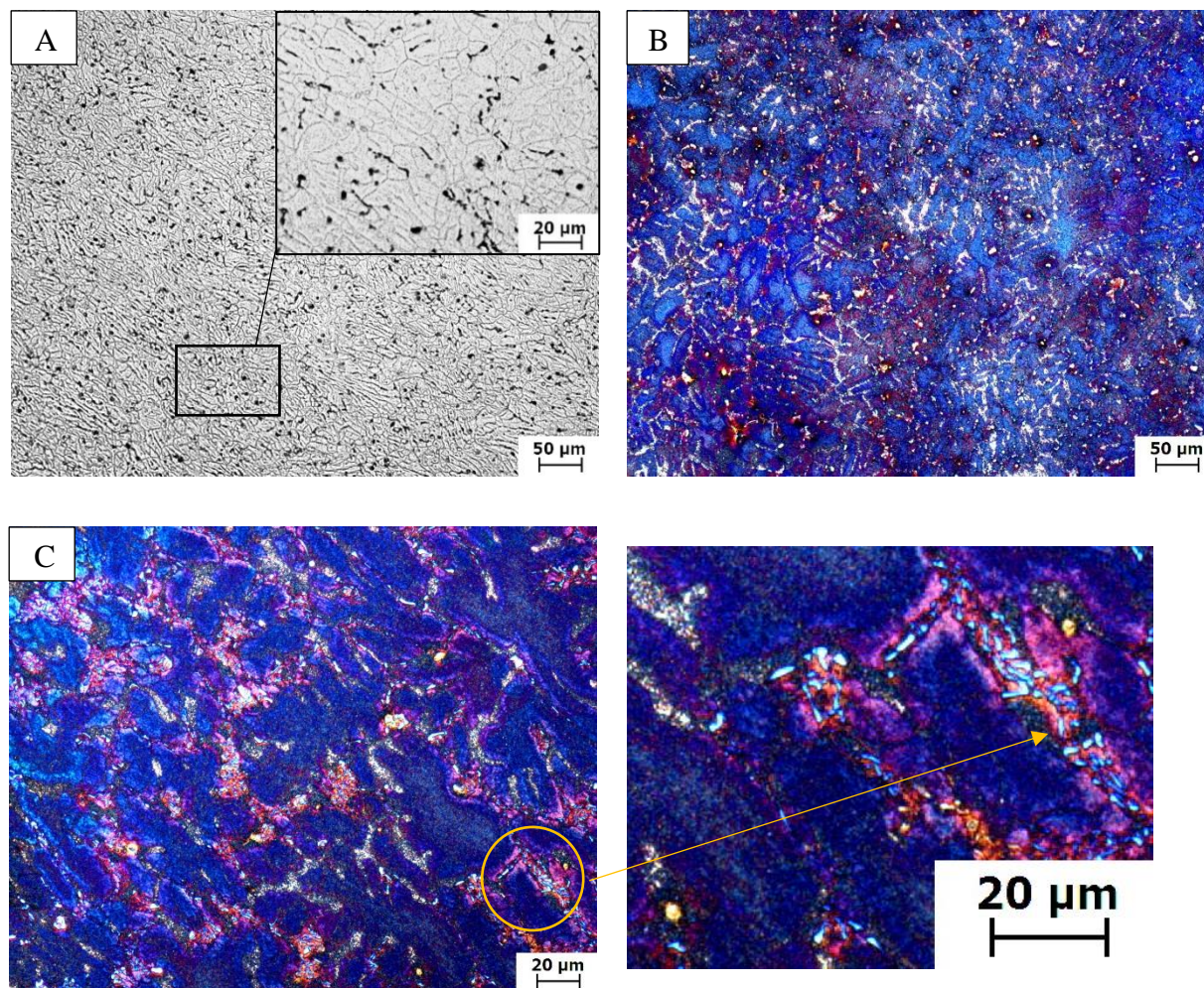


Figure 4-4: Microstructure of Al6061 reinforced by 1wt.% Al₂O₃: A. using general purpose etchant at 200 and 500X, B. using color etchant at 200 and 500X

The grain size of Al 6061 matrix and composites containing different weight percentages of Al₂O₃ nanoparticles was measured using the planimetric (Jeffries') procedure according to ASTM E112-96. The composites contain 1wt.% Al₂O₃ nanoparticles showed finer grain size with ASTM grain size number(G) of about 8.66 and average grain size of 17.88 μ m. Furthermore, the distribution and morphology of nanoparticles in the Al 6061 matrix were difficult to be identified by the OM using the monochromatic light and general-purpose etchant. Thus, the microstructure

was examined by Weck’s etchant using Polarized light and is indicated by Figures 4.4 B and 4.4 C. It is clear that, agglomeration of the nanoparticles was occurred, and the presence of porosity was observed. The agglomeration size of the nanoparticles and the amount of porosity were calculated based on the area fraction represented on the micrographs (Figure 4.5) and with the help of ImageJ program. The size of the agglomerated Al_2O_3 was about $2.15 \mu\text{m}$ and the micro-porosity percentage was approximately 0.7% with an average size of $46\mu\text{m}$.

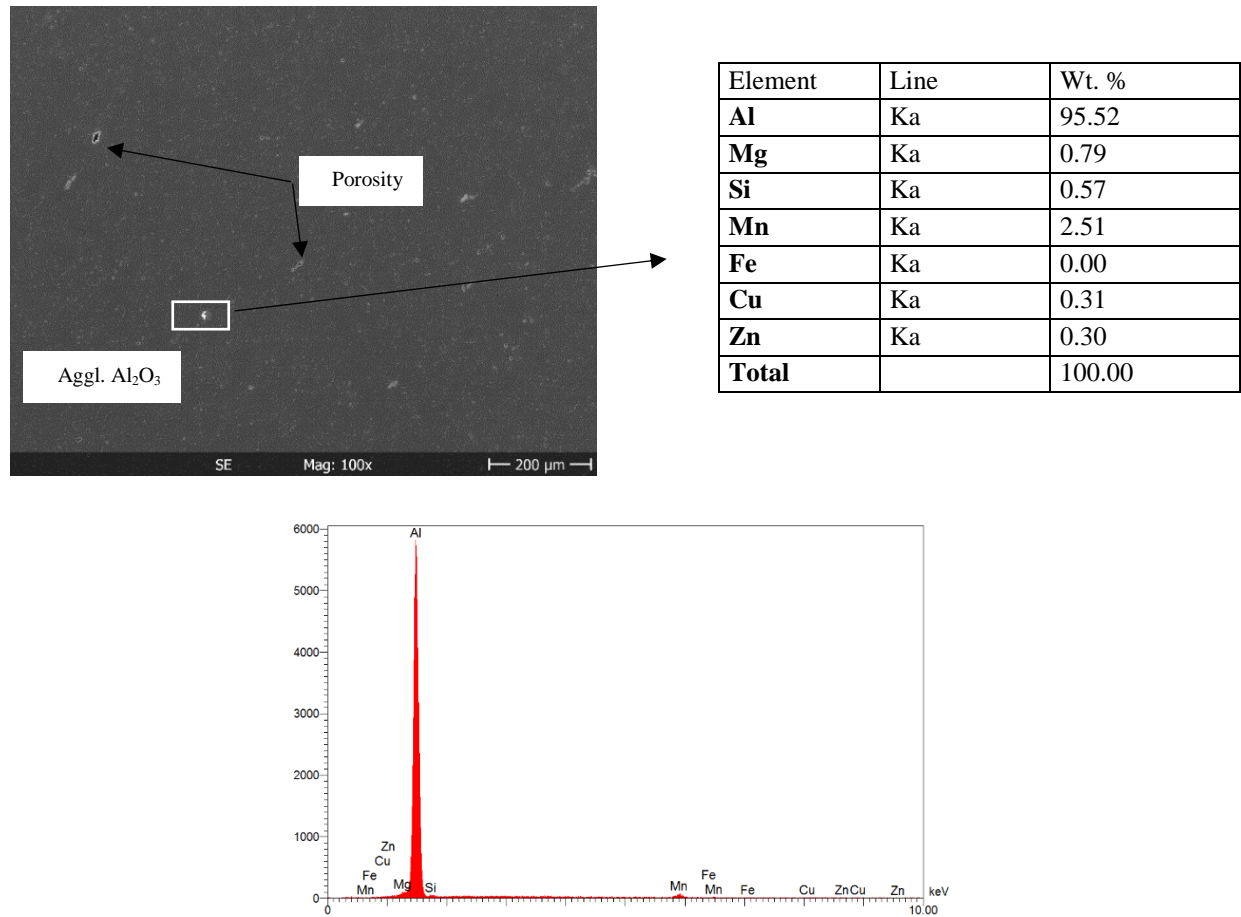


Figure 4-5: SEM and EDX of 1% condition showing some porosity and agglomeration of Al_2O_3 nanoparticles

Further addition of Al_2O_3 nanoparticles with different weight percentage leads to more agglomeration and porosity. Figure 4.6 indicates the optical micrographs of the nanoparticles additions with 2 and 3 wt.% to the Al6061 matrix. It is clear that the addition of alumina nanoparticles reduces the grain size of the α -aluminum but with a smaller impact compared to that resulted from the introduction of 1wt.% Al_2O_3 . The retardation in the grain refinement can be explained by the lag in influence caused by the nanoparticle on pinning the grain boundary and restricting the grain boundary growth [45-47]. This influence which resulted from the tendency of the alumina particles to agglomerate forming large clusters because of the low wettability and incorporation of particles within the melt. These clusters hinder the uniform dispersion of the particles in the matrix decreasing the ability of the nanoparticles to act as

nucleation sites of the newly formed grains and reduce the grain boundary pinning effect [46-48]. The grain sizes of 2 and 3 wt.% were 45.83 and 52.41 μm respectively.

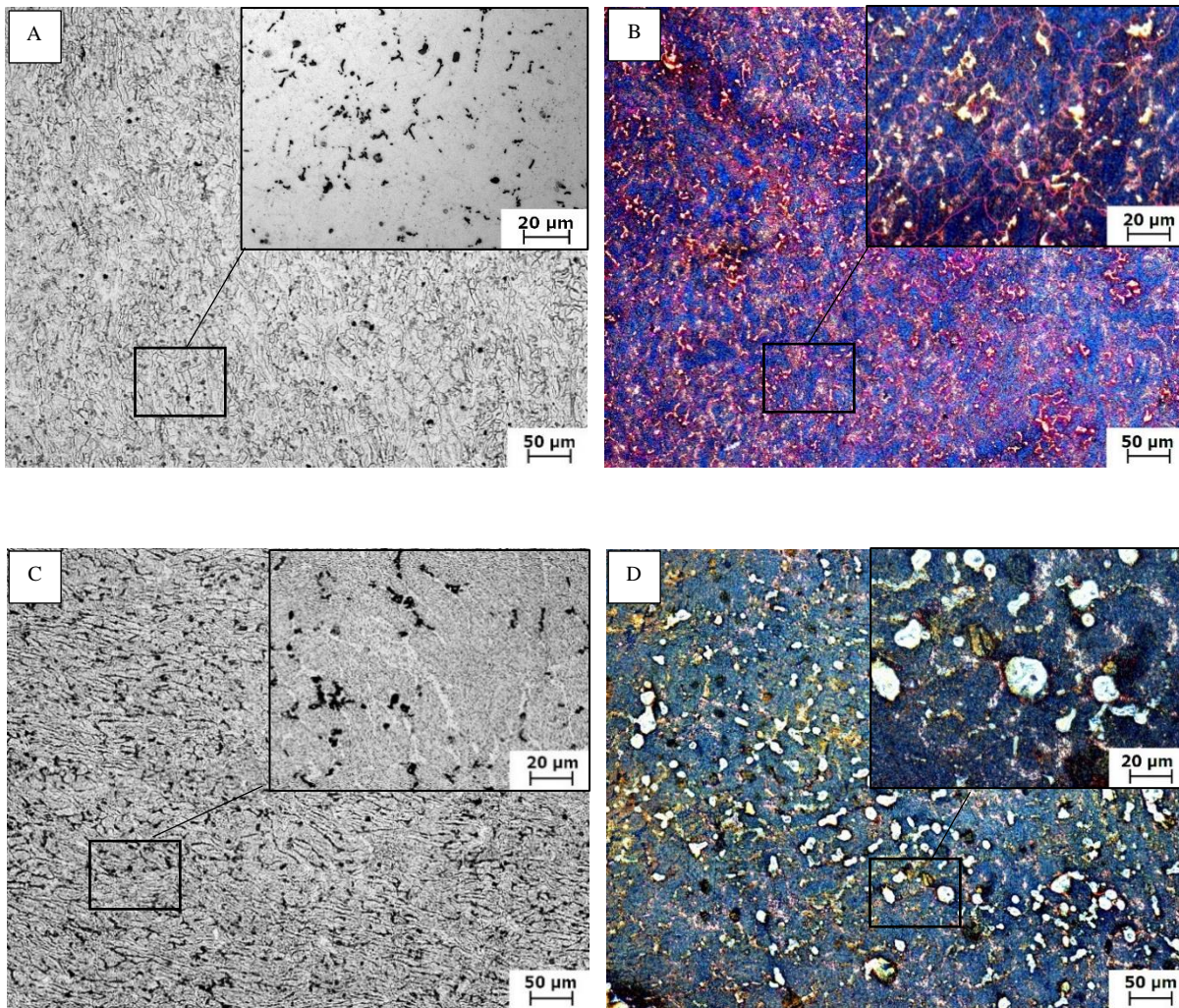


Figure 4-6: Microstructure of composites; A. 2wt.% using general purpose etchant at 200 and 500X, B. 2wt.% using color etchant at 200 and 500X, C. 3wt.% using general purpose etchant at 200 and 500X, D. 3wt.% using color etchant at 200 and 500X

The 5 wt.% Al_2O_3 composites differ in than the microstructure to the other addition of nanoparticles with the presence of $\beta\text{-Al}_5\text{FeSi}$ intermetallic phase (Figure 4.7). These intermetallic are responsible for the degradation in the mechanical properties of aluminum alloys such as tensile properties, fatigue strength, fracture toughness, and especially the ductility while it appears as a thin plate acting like needles in the microstructure [117-120]. The mechanism of $\beta\text{-Fe}$ intermetallic can be understood by the behavior of the liquid solubility of iron in aluminum alloys, which is 1.87 wt.% at 655 $^\circ\text{C}$ while its solid solubility at 570 $^\circ\text{C}$ is only 0.052 wt.% and it decreases to less than 0.01 wt.% at 427 $^\circ\text{C}$. Therefore, the solidification and cooling processes provide an adequate driving force for forming Fe-rich intermetallic compounds with Al and other

alloying elements. The formation of β - Al_5FeSi needles intermetallic compound can be taken place on the γ alumina at an angle of 70° to the tangent of intersection with alumina. Parent β -needles involve in branching of smaller ones spanning across the matrix. The morphology of this phase is characterized by needle like shape with a probable range of existence of 30-35% Fe and 6-12% Si and could be transformed into Chinese script in the presence of manganese forming α - $\text{Al}_{15}(\text{FeMn})_3\text{Si}$, which may reduce the harmful effect of that brittle hard phase in the soft matrix [117-120].

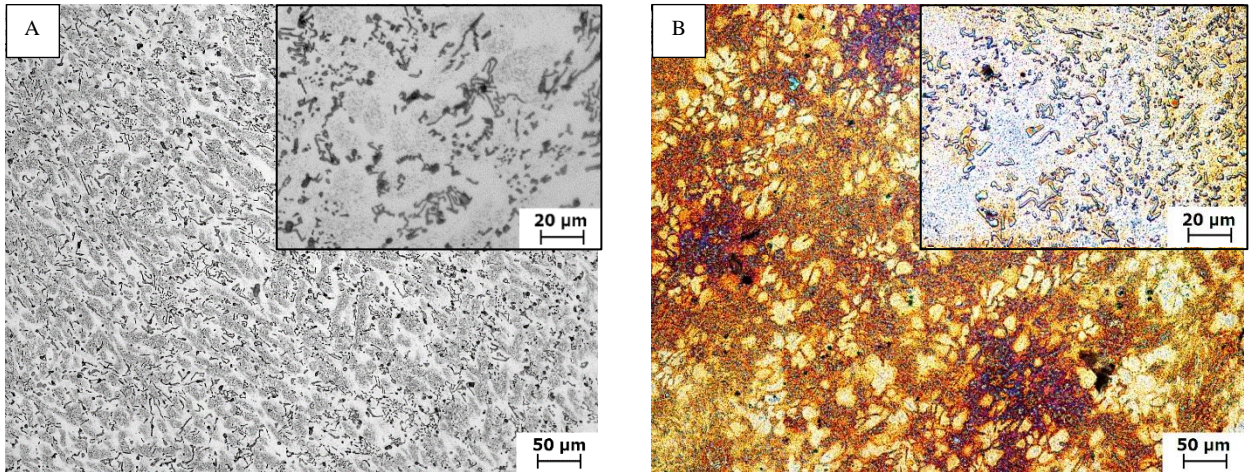
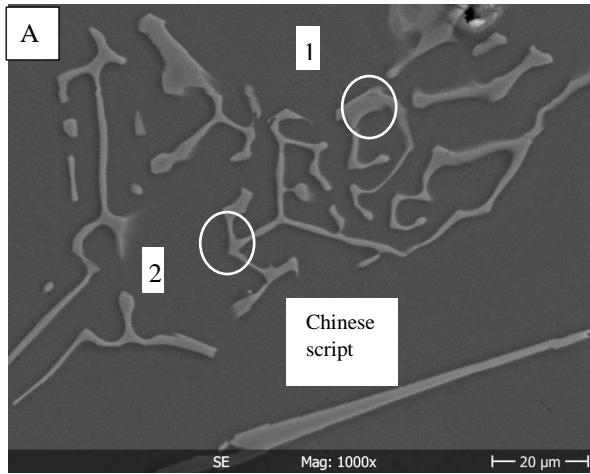
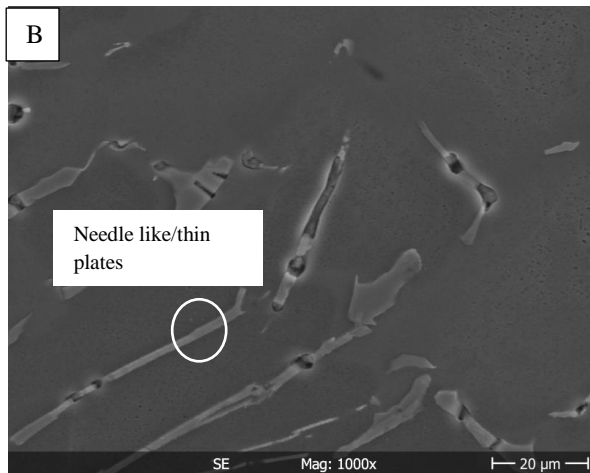


Figure 4-7: Microstructure of 5wt.% Al_2O_3 condition: A. using general purpose etchant at 200 and 500X, B. color etchant at 200 and 500X

The β -Fe intermetallic has a monoclinic crystal structure, or tetragonal for the Chinese script (Figure 4.8 a) which makes its growth is limited mainly to two dimensions with the formation of large plates (Figure 4.8 b). Contrary, the α -Fe has a body-centered cubic structure with more uniform surface energy allowing the formation of a variety of morphologies by growing in three dimensions. However, the change in crystallization from β to α -Fe is limited by the transformation of γ -alumina to α -alumina at high temperature, which favors the formation of α -Fe rather than β -Fe. The harmful effect of the presence of β - Al_5FeSi in the 5wt.% Al_2O_3 condition is attributed to its stress raising potential based on its plate-like morphology, and its apparently brittle nature with a hardness of 196.3 HV0.05 compared to 45.7 HV0.05 of the matrix (Figure 4.8 c). Furthermore, this brittle intermetallic compound increases shrinkage cavities and cracking during solidification by blocking the inter-dendritic channels resulting in hindering the melt flow to feed solidification shrinkage at the end of the solidification process [1,9-13,117].



Element	Wt.% point 1	Wt.% point 2
Al	71.09	56.16
Fe	21.41	34.17
Mg	0.28	0.00
Mn	1.59	2.35
Cu	0.80	0.99
Zn	0.16	0.12
Si	4.67	6.22
Total	100.00	100.00



Element	Wt.%
Al	56.15
Fe	34.11
Mg	0.05
Mn	1.53
Cu	2.04
Zn	0.09
Si	6.03
Total	100.00



Matrix hardness HV0.05	β -AlFeSi hardness HV0.05
45.7	196.3

Figure 4-8: A. Chinese script and B. thin plates of β -Fe intermetallic, C. microhardness of the β -Fe intermetallic and the matrix

The presence of the β -Fe is also associated with porosity formation, which can be explained by the formation of these intermetallic on one side of the oxide film giving a chance to the remaining part to be pulled away from its unbonded side and sucked into the dendrite mesh leaving either shrinkage or gas pore depending on the poor feeding or the gas content [117-119].

The modification of such intermetallic can be carried out chemically by the transformation of the β to α -Fe through adding some α -Fe stabilizers such as manganese, chromium, magnesium, strontium, lithium or beryllium which fix the oxide films in their convoluted state. Another approach to the removal of suspended oxide crack defects proposes using the precipitation and sedimentation of primary intermetallic compounds from the liquid metal. This method can be achieved by cooling the melt below the effective primary intermetallic precipitation liquidus and above the α -aluminum dendrites liquidus temperature which permits these primary intermetallic to precipitate on the oxide films and deposit in the bottom of the crucible because of its weight. [118-120]

The microstructure of the recycled 1wt.% composites fabricated by re-melting of the 1wt.% Al_2O_3 samples is shown in Figures 4.9 A and B.

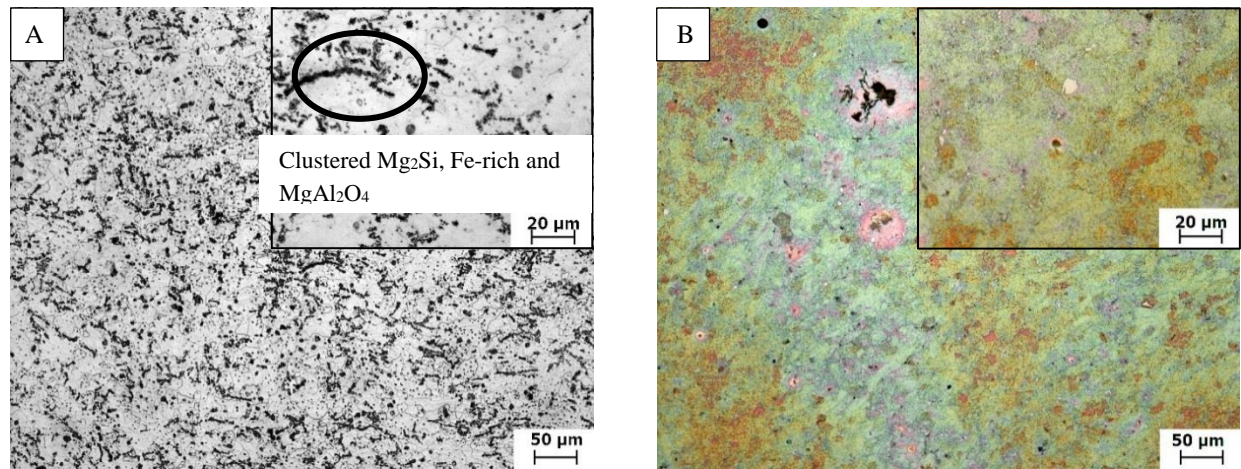


Figure 4-9: Microstructure of recycled 1wt.% Al_2O_3 : A. using general purpose etchant at 200 and 500X, B. using color etchant at 200 and 500X

The microstructure demonstrates the presence of both agglomeration and porosity in the recycled AMNCs. However, the grain refinement effect of the nanoparticles on the α -aluminum is still dominant. The grain size of the recycled condition is about 36.86 μm . Comparing the microstructure of the recycled condition with the 1wt.% condition, it may be noticed that both the grain size and the agglomeration were raised in the recycled condition. The improvement in the microstructure of the recycled AMNCs compared to the monolithic alloy can be attributed to the proper mechanical stirring during of the melt which provided a uniform distribution of the nanoparticles in the matrix and permitted it to act as grain growth restrictions by pinning the

grain boundaries during the recrystallization process. This refinement effect is lower than that achieved by the 1wt.% because of the agglomeration of the nanoparticles as the remelting process does not involve introducing freshly added particles to the melt. In this case, the agglomeration does not happen between the nanosized particles but between the already agglomerated particles from the fabricated AMNCs with a larger size (Figure 4.10).

The SEM micrograph (Figure 4.10) illustrates the presence of two constituents in this particles cluster of gray and white components. The microstructure shows also clustered particles (dark spots) which were found to disperse along the grain boundaries or the dendritic arm boundaries within the matrix. The chemical composition of the white and gray constituents was examined by the EDX and shown in the table in Figure 4.10. These clustered particles were found to be a cluster of Mg_2Si , iron-rich intermetallic and Al_2O_3 [117].

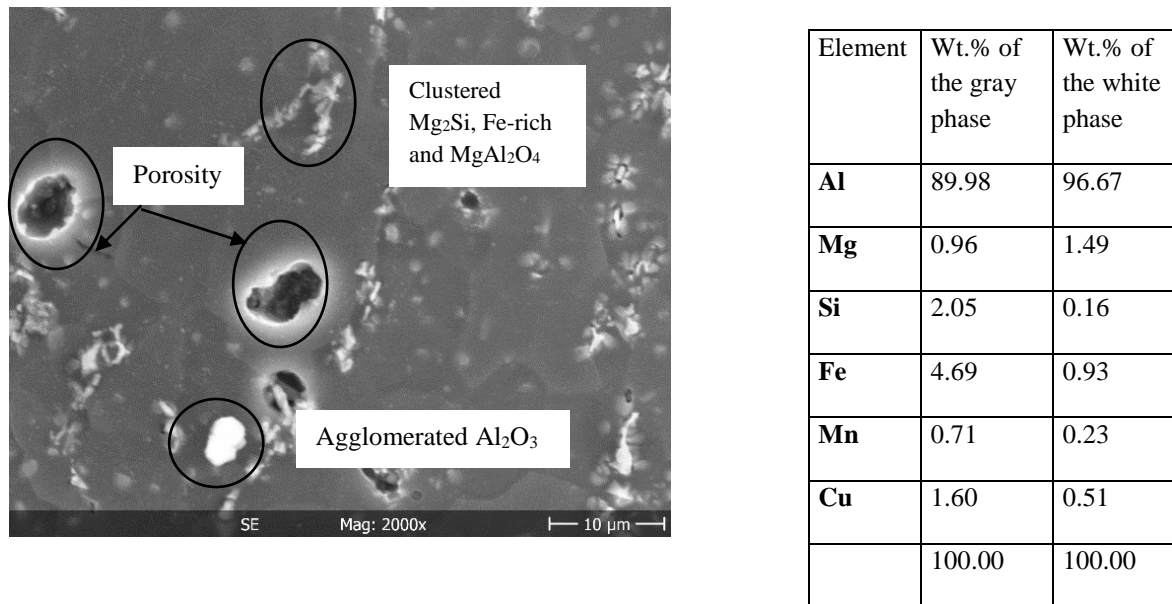


Figure 4-10: SEM and EDX of the recycled 1wt.% Al_2O_3

The gray constitute of the clustered particles could be (according to the chemical composition from EDX) $\alpha-Al_{15}(FeMn)_3Si$, where the white spots consisted of Al_2O_3 and Mg_2Si . The formation of these clusters might occur during the growth of crystals or the solidification process with a size of approximately $10\mu m$. The thermodynamic stability, temperature and time contribute to the consistency, growth, and clustering of these particles on the parent oxides which are Al_2O_3 in this case. Particles pushing, or entrapment occurs during the solidification based on their size or critical velocity of solidification front. Large particles (up to 100 microns) are entrapped within the grain boundaries causing blunting of the solidification front due to the thermal conductivity

means. The solidification front is likely to push or entrap smaller particles (up to few microns) between secondary dendrite arms, and it was possible that particles or their clusters were pushed by the growing dendrites at the beginning of solidification and entrapped within inter-dendritic regions during solidification. The pushed particle towards grain boundaries acts as barriers to grain growth resulting in grain refinement on the final microstructure. The grain refinement and change in the grain morphology propose that the clustered particles may also act as heterogeneous nuclei. Such clusters contribute to improvements in the stress and ductility of the recycled composites. These enhancements can be governed by different strengthening mechanisms such as load bearing, grain boundary, and coefficient of thermal expansion mismatch [121].

The microstructure of the sever plastically deformed (SPD) 1wt.% Al_2O_3 is shown in Figure 4.11. It is clear that the sever plastic deformation which carried out using rotary swaging leads to an additional grain refinement in the condition of 1wt.% Al_2O_3 .

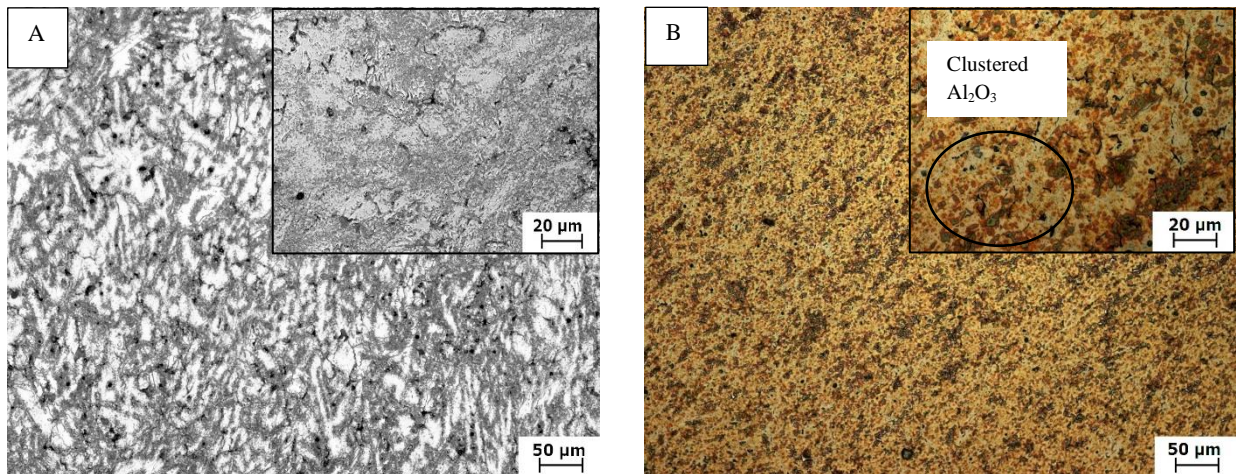


Figure 4-11: Microstructure of Al6061 reinforced 1wt.% Al_2O_3 under sever plastic deformation: A. using general purpose etchant at magnification of 200 and 500X, B. using color etchant at magnification of 200 and 500X

The grain size of the 1%SPD condition was found to be about $9.87\mu\text{m}$ having a grain size number (G) of 3.3. Moreover, the 1%SPD shows a reduction in the porosity volume fraction compared to the other conditions. Apparently, the mechanical deformation results in improving the microstructure densification, grain refining through the dynamic recrystallization by forming new grains and lowering the porosity. Furthermore, the particles are shown to be uniformly dispersed with low agglomeration because of the clustered particles breakup caused by the high strain rate effect. During mechanical deformation, the agglomerated particles act as harder zones than particles free zones which enhances the strain partitioning during flow. Therefore, the applied deformation is accommodated by the flow of the particles free zones at low strain rates. Deformation takes place in the particle agglomerated zones and results in shearing of the agglomerated particles when the strain rate sensitivity of the matrix exceeds that of the

agglomerated particles due to the high applied strain rate which raises the matrix flow stress [122].

4.1.3 Summary of the grain refinement, Porosity and agglomeration results

The grain size and the ASTM grain size number of different conditions of the As-Cast and reinforced Al6061 are shown in Figure 4.11.

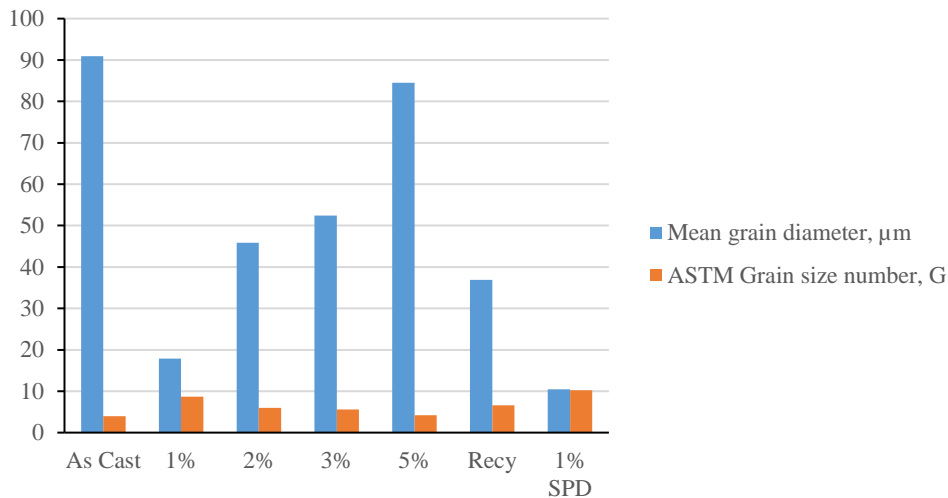


Figure 4-12: The mean grain diameter in μm and the grain size number of different conditions of Al_2O_3 addition

During particle pushing, nanoparticles below a certain size are pushed ahead of the solidification front acting as restrictions to the grain growth. Within some regions, the energy required to push the particles will be less than the energy needed for dendrite branching out from some gap in the surrounding particles resulting in new grains nucleation. The resultant grain morphology will be fine grain which impacts positively on the material strength [107].

The presence of the nanoparticles restricts the dendrite arm spacing as well as the dendrite tip radius. Theoretically, when nucleation occurs on the surface of the nanoparticles, a very small grain size could be acquired which is experimentally was not proved that individual grains are nucleating around nanoparticles [107]. The particle pushing process is characterized mainly by two restrictions. First, the effect of the lower thermal conductivity of the particle on the temperature gradient ahead of the solidification front, which acts as a barrier to the removal of the heat necessary for further solidification. The second factor can be the behavior of the solid particle in acting as a barrier preventing the solute diffusion away from the tip of the growing dendrite, thereby changing the concentration gradient and restricting growth. The critical velocity for the solidification front engulfed particle commensurate inversely with the particle size. Smaller particles have a greater tendency to be pushed rather than engulfed enabling restriction of the grain growth rather than larger particles resulting grain refinement in the final microstructure. The barrier effect of the nanoparticles impedes the solute diffusion during growth, and therefore the delayed growth from the melt allows additional time for the formation of nuclei, which can yield a refined structure [101-107].

One important factor which control the heterogeneous nucleation is the interfacial free energy at the nucleating interface. The classical nucleation theory has been cleared the importance of the low interfacial energy for a potent substrate. Nevertheless, the issues related to perfect wetting of exogenous inoculants with molten Aluminum often fail to decrease the interfacial energy to a lower value. Consequently, the mechanical stirring process was used during casting to break the dendritic structures with keeping the microstructure in the equiaxed form, enhance the wettability of the nanoparticles and ensure uniform dispersion of them over the matrix. Besides, the heat treatment process for the nanoparticles before dispersion into the melt was essential to remove the adsorbed gases and impurities from the particle surface and improves the wettability and distribution of Al_2O_3 particles in the Al6061 matrix alloy [103-105].

During solidification of Al6061/ Al_2O_3 composites, Al_2O_3 particles are cooled down more slowly than the melt. Thus, the temperature of the particles is somewhat higher than the liquid alloy because of lower heat diffusivity and thermal conductivity of Al_2O_3 particles in comparison with the metal matrix. This difference in the cooling rates may cause an additional heating source for the surrounding melt and delays its solidification making the nucleation of α -phase starts in the liquid lower temperature zones away from the nanoparticles [64-68,107].

The grain refinement occurred by the introduction of the alumina nanoparticles into the Al6061 matrix could be summarized by the action of the nanoparticles as heterogeneous nucleation sites during solidification, which contributes to more refined and possibly equiaxed microstructure, as shown in the microstructure of Al 6061 reinforced by 1wt.% Al_2O_3 . The role of nanoparticles could be extended to hinder the grain growth by restricting the migration of thermally excited grain boundaries during the recrystallization process which is known as the pinning effect. The influence of the nanoparticles addition on the grain refinement is also affected by the agglomeration of the particles. The more agglomeration size takes place in the matrix, the coarser grain size obtained. As a result, the reinforcing particles lose the privilege of grain boundary pinning and the ability to be dispersed widely and act as heterogeneous nucleation sites during solidification, which could explain the variation of the grain size over the different additions of the Al_2O_3 [107].

The presence of micro-porosities was apparent in the inter-grains region (Figure 4.13). Both the percent porosity and the average porosity size were calculated for each condition and illustrated by Figure 4.14.

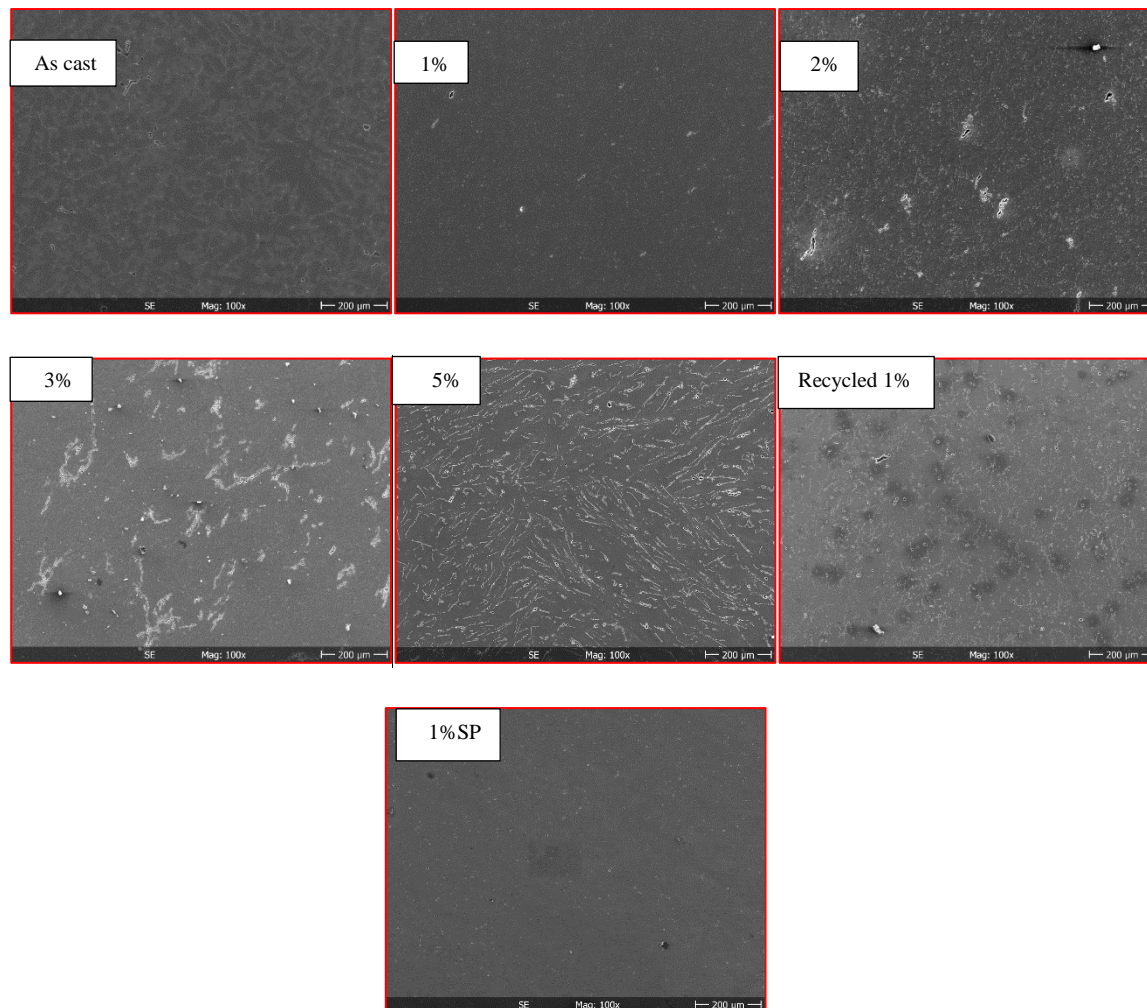


Figure 4-13: SEM micrographs show the porosity in the monolithic alloy and the reinforced AMNCs with different additions of nanoparticles

It is clear that the porosity percent of the composites is more than that of the non-reinforced alloy because of the low wettability and more agglomeration caused by nanoparticles clustering. The increase in the porosity content is attributed to various sources. It is mainly associated with the increase in contact surface area between two species resulted from introducing of the reinforcement powders in molten aluminum. The nanoparticles are attributed to increasing the percent porosity by pore nucleation at the Al_2O_3 particulate sites (porosity associated with individual particle) and hindering liquid metal flow due to agglomeration (porosity associated with the particle clusters) [32]. The micro porosities could also be attributed to gas entrapment during the mechanical stirring process. Increasing the stirring time results in more porosity, formation of oxide inclusions, reaction between reinforcement and metal favored by long contact times, particle migration and clustering during and after mixing. However, the mechanical stirring process is essential for ensuring homogeneous distribution of the powders in the matrix. It was also noted that the porosity volume percent increases with increasing the weight fraction of the alumina nanoparticles additions. It may be explained by decreasing the dynamic

recrystallization due to hindering the grain boundary migration effect by the nanoparticles and raising the viscosity associated with clustering of the nanoparticles [44]. Contrarily, the addition of 5wt.% Al_2O_3 shows lower percent porosity than that marked by 2 and 3% conditions. This decrease in the percent porosity can be understood by the tendency of the nanoparticles to act as nucleation sites for the formation of the β -Fe rich intermetallic rather than clustering in large agglomerates leaving porosity behind [117].

Porosity as a defect has a significant effect on retarding the mechanical properties of the composites due to the stress localization accompanied with the porosity presences. Secondary processes such as hot extrusion or swaging suppress or mitigate the negative effect of porosity, such as in the 1%SPD after application of rotary swaging. After application of second deformation process, the transport of matter via pressure-assisted diffusion becomes the dominant mechanism after eliminating interconnected porosity and only triple points and grain corners contain the remaining porosity. Moreover, the secondary processing of the discontinuously reinforced composites leads to break up of particle agglomerates and improved particle-to-particle bonding, all of which tend to improve the mechanical properties of these materials [121].

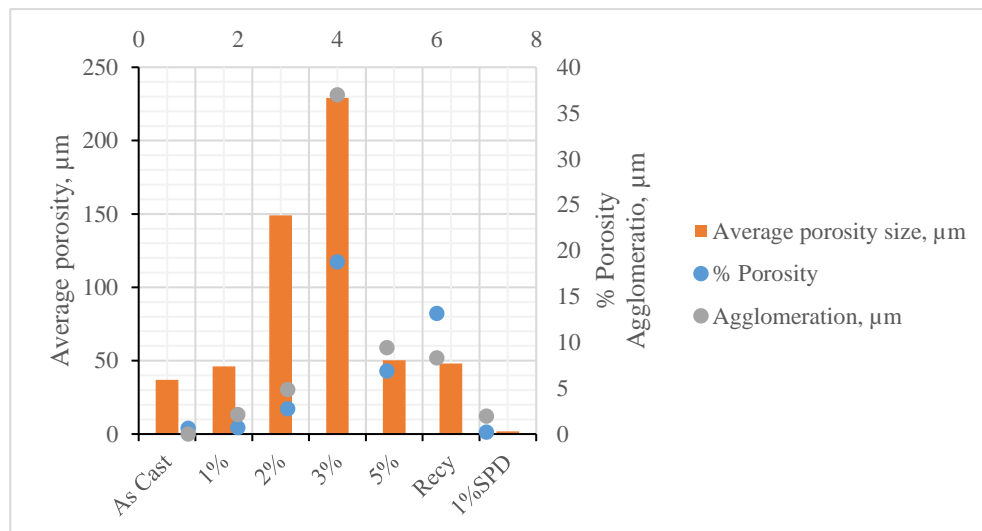


Figure 4-14: The percent porosity, average porosity and agglomeration size marked at the fabricated composites

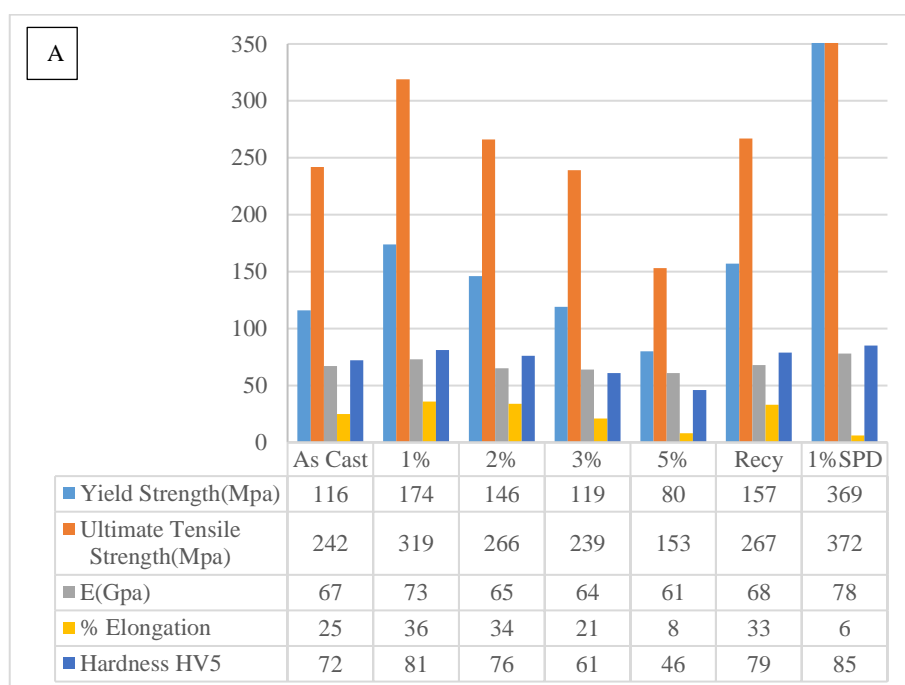
It was clear that further addition of more nanoparticles than 1% results in increasing the grain size than that obtained from the addition of 1wt.% Al_2O_3 . Increasing the weight fraction of alumina particles causes more agglomeration and clustering of the nanoparticles, which limits the grain refinement by restricting the new nuclei formation and retarding the grain growth restriction. The agglomeration was calculated and illustrated in Figure 4.14. Particles agglomeration occurs when a solid particle encounters a non-wetting medium such as alumina in this case because of increasing the surface area and surface energy. Even though the nanoparticles were added into the melt with pre-dispersion treatment, it is extremely difficult for mechanical

stirring to break the clustering in the melt. Consequently, it is complicated to eliminate agglomeration and clustering in the fabrication of nanocomposite by stir casting process [44-45]. The undesirable effect of agglomeration can result in a reduction of the failure strain of the composite, and its degradation is responsible for more crack nucleation in the clustered zones as well as the final fracture proposed by crack propagation through the matrix to other clusters. The combined effect of agglomeration, particles pushing and sedimentation attributes in clustering formation according to the Gibbs free energy of the system. The system always seeks to equilibrium through physical configurations to lower the Gibbs energy, which enhances agglomeration or stability configuration caused by several alumina particles to cluster and reduce its surface area [49,80,107].

4.2 Mechanical characterization

4.2.1 Tensile properties and hardness

Figures 4.15 A and B demonstrate the tensile properties (at room temperature and 300°C based on the alloy applications at high temperature) and the hardness (HV5) of the monolithic matrix and the composites with different weight fractions of Al_2O_3 .



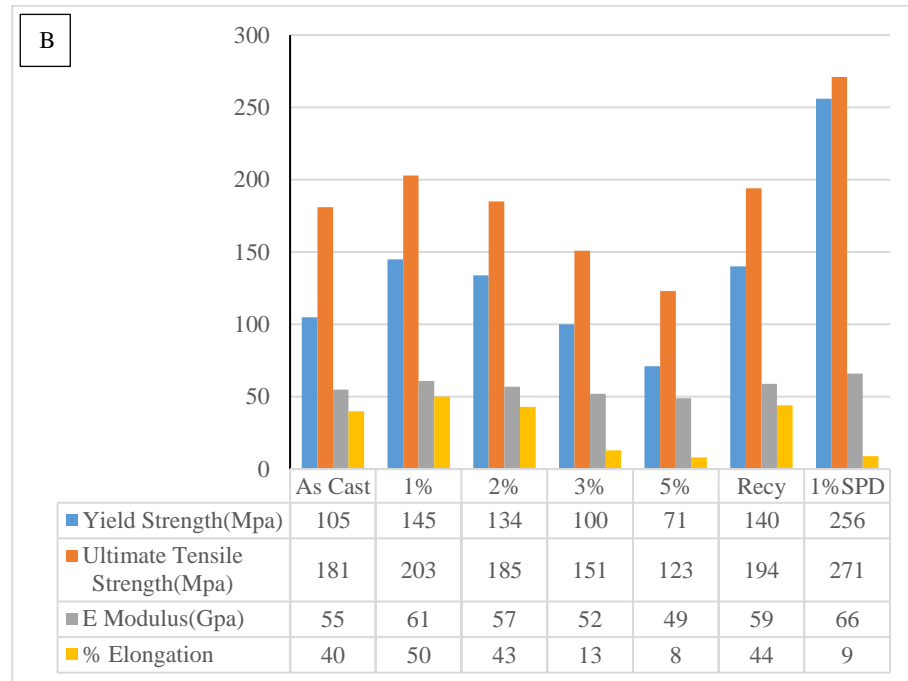


Figure 4-15: Tensile properties and hardness of the monolithic matrix and reinforced Al6061 with nanoparticles; A. at room temperature. B. at 300°C

It can be observed clearly that the addition of the nanoparticles results in improvement not only the tensile properties at room temperature and high temperature but also the hardness at the room temperature. However, there was no possibility to measure it at such elevated temperature but based on the behavior of the UTS at 300C, the hardness is expected to increase as well. The increase in the tensile properties and hardness is affected by the weight fraction of the alumina nanoparticles added to the matrix. Comparing the different Al₂O₃ additions to the monolithic alloy, the addition of 1wt.% alumina nanoparticles to the Al6061 resulted in a notable enhancement in the tensile properties and hardness. The yield strength increased by 50% from 116 MPa in the matrix to 174 MPa in the 1% composites at room temperature and by 38% at 300°C. Moreover, the ultimate tensile strength increased by about 32% from 242 MPa without reinforcement to 319 MPa in the 1% composites at room temperature and by 12% at 300°C. Furthermore, the % elongation was improved by 40% from 24.5 to 34.4 % at room temperature and 16% at 300°C while the hardness increased by about 14% from 71.6 to 81.4 HV5. However, the tensile properties and hardness of the 2, 3 and 5wt.% Al₂O₃ retarded compared to that obtained at 1wt.% Al₂O₃. It is likely attributed to the agglomeration of the nanoparticles, and the increase in the porosity occurred in these processing conditions. It could be expected that at customized and optimized casting process and parameters to restrain the particles clustering and hence reducing the percent porosity, the mechanical properties may further be enhanced [44-53].

The severe plastic deformation condition of the 1wt.% Al₂O₃ shows a significant increase in the tensile strength and hardness compared to that obtained by the normal 1wt.% Al₂O₃ composites

with a retardation in the ductility at both room temperature and 300°C. This improvement in the tensile strength could be resulted from the increase in the dislocation density in the alloy by inducing plastic deformation through rotary swaging, where the amount of dislocations produced is much higher than that recovered during the dynamic recovery. During work hardening, the dislocations are tangled, cells and sub-grain walls are formed causing a change in the grain shapes and the internal structure. Furthermore, this process leads to decrease the mean free slip distance, which proposed the alloy strength increase [121].

The recycled 1wt.% Al₂O₃ shows promising tensile properties compared to both the monolithic alloy and 1wt.% composites. The yield strength of the recycled condition increased by 35% compared to the monolithic alloy and retarded by 10% than the 1wt.% composites at room temperature and by 33% and 3% at 300°C respectively. This increase in the yield strength at both room and elevated temperatures was accompanied with an increase in the ultimate tensile strength, hardness and % elongation compared to the alloy without nanoparticles additions. The enhancement of the tensile properties and hardness of the recycled condition may be explained by the presence of the nanoparticles and their strengthening effect. On the other side, the retardation of the recycled condition tensile properties compared to the 1wt.% Al₂O₃ can be related to the agglomeration and porosity found in the composite with higher size and amount than that obtained by the 1% composite [44-51].

The improvement in the tensile properties of the composites could be accredited to the high stiffness induced by the nanoparticles. Their stiffness is much higher than that of the matrix which enhances microplasticity to take place in AMNCs at a low stress resulting in a slight deviation from linearity in the stress-strain curve (proportional limit stress). This microplasticity can negatively affect the properties by generating stress concentrations in the matrix at the poles and sharp edges of the reinforcement. Increasing the reinforcement weight fraction increases the existence of the stress concentration points which causes decreasing the micro-yielding stress. The introduction of the nanoparticles in the matrix contributes to decidedly rising the work hardening of the material due to the geometric constraints imposed by the presence of the reinforcement. Thus, the strain relaxation is very constrained to occur and causes commencement of void nucleation and propagation to exist in a lower far field applied strain than that observed in the unreinforced material. The higher weight fraction, the higher elastic modulus, and tensile strength are observed because of the more load transferred to the nanoparticles [123].

The strengthening in the AMNCs can be attributed to four mainly mechanisms; load bearing, grain refinement, Orowan's strengthening, and mismatch in the coefficient of thermal expansion and Young's modulus [51]. The load-bearing effect of the reinforcement in strengthening the matrix is characterized by the strong cohesion between the nanoparticles and the matrix due to the Nano-size of the reinforcement particles and the sound synthesizing methods. It also explains the direct strengthening contribution from the presence of reinforcement particles. The strengthening takes place because of the increase in the stress required to operate dislocation sources and to overcome the obstacles which restrict the dislocation movement in the matrix.

Generally, the contribution of the load bearing strengthening in the final strengthening of the AMNCs is small compared to the other mechanisms and could be ignored [51-80].

The grain refinement or Hall-Petch strengthening mechanism is also a vital strengthening mechanism in the AMNCs especially when the nanoparticles lead to a significant grain refinement in the matrix. Decreasing the grain size increases the grain boundaries and influences the matrix strength positively by hindering the dislocation movement. The dislocation movement restriction occurs at the grain boundaries is resulted from the different crystal orientation and the high lattice disorder, which makes the dislocation movement on a continuous slip plane very difficult. The grain boundaries retard the extensive plasticity beginning, and thus enhance the yield strength. Under an external shear stress, dislocations move until reaching the grain boundaries and then they pile up. Pile up is usually accompanied with generating extensive repulsive stress fields, that act as a driving force to reduce the energetic barrier for their diffusion through the boundary. The amount of the extensive pile-ups is directly proportional to the grain size. So that, the decrease in the grain size leads to a reduction in the amount of the pileups, and hence increases the strength required to enable the dislocation movement and improves the final yield of the composite. The refinement caused by the nanoparticles could be explained by the interaction of the nanoparticles with the grain boundaries and acting as pinning points to retard or stop the grain growth at higher temperature processes. Increasing the nanoparticles volume fraction should lead to a decrease in the grain size until a certain limit. When the grain size reaches the threshold value, at which the grain size approaches the dislocations size, dislocation could not pile up and exhibit instead grain boundary sliding or rotation. Therefore, the final yield strength of the composite decreases and the ductility raises causing softening of the material [51-80].

One of the important strengthening mechanisms in the AMNCs is the Orowan's strengthening mechanism (sometimes second-phase particle strengthening). This strengthening mechanism is caused by the dislocation movement restriction due to the closely spaced hard particles. The Orowan's strengthening is more significant when the reinforcement particles size is about a few nanometers (100 nm or less) to ensure a small interparticle spacing and hinder the dislocation movement. During the dislocation movement, the dislocations bypass the nanoparticles by bowing and then reconnecting resulting in formation of dislocation loop around the particles. These loops increase the work hardening in the matrix and thus lead to improve the strength. When the nanoparticles are spherical shaped the maximum tensile and shear stresses occur at the surface of the particles and they decrease with distance from the surface of particles [15].

Strengthening could also occur due to the mismatch in the coefficient of thermal expansion (CTE) and the elastic modulus (EM). The dislocation density in the composite increases because of the residual thermal stresses even after perfectly dispersion processes. This increase in the dislocation density results from the difference in the CTE between the matrix and the nanoparticles during the thermal processing such as cooling through the relaxation of the high-

stress field around the particles by generating more dislocations (geometrically necessary dislocations (GNDs)) at the matrix/ Al_2O_3 interface to reduce the stored energy. Moreover, the significant difference between the elastic modulus of the matrix and nanoparticles could also contribute to creating of additional GNDs during the elastic straining. The GNDs density is determined by the magnitude of the thermal and elastic strains within the composite, and the increase in the GNDs density leads to improve the final yield strength of the composite [124-125]. There are other several strengthening mechanisms which are superimposed and connected to each other and could affect the final strength of the composite such as work hardening due to plastic deformation and the increase in the dislocation density through multiplication or development of dislocation structures. Thus, the final strength of the composite is difficult to be predicted and to be attributed to a single individual contribution [15,80,124-125].

4.2.2 Fatigue behavior:

4.2.2.1 Electropolishing

Figures 4.16 A and B illustrate the fatigue behavior of the monolithic alloy in the different conditions of the nanoparticles concentrations in air and corrosive medium (3.5% NaCl solution) in the electropolished state. The tensile properties had a direct impact on the fatigue life of the different conditions, as proven in [6-7]. The enhancement in the tensile properties of the 1wt.% composites contributes in improving the fatigue behavior of this conditions. The fatigue strength of the 1wt.% composites increased by about 26% (from 135 MPa to 170 MPa) compared to the monolithic alloy in air and by about 64% (from 55 MPa to 90 MPa) in 3.5% NaCl solution. The high cyclic fatigue was dramatically affected by the corrosive environment (3.5% NaCl solution) due to the formation of pitting, which acts as crack nucleation sites and decreases the fatigue strength [111]. Furthermore, the agglomeration and porosity found with higher particle concentrations in the other conditions affected the fatigue life negatively compared to the 1wt.% Al_2O_3 . Nevertheless, the composite reinforced with 2wt.% Al_2O_3 showed a slight improvement in the fatigue strength compared to unreinforced with about 11% in air and 9% in the 3.5% NaCl solution. This enhancement in the fatigue life could be explained by the relatively lower agglomeration and porosity achieved by the 2wt.% Al_2O_3 composites compared to both 3 and 5wt.% Al_2O_3 composites.

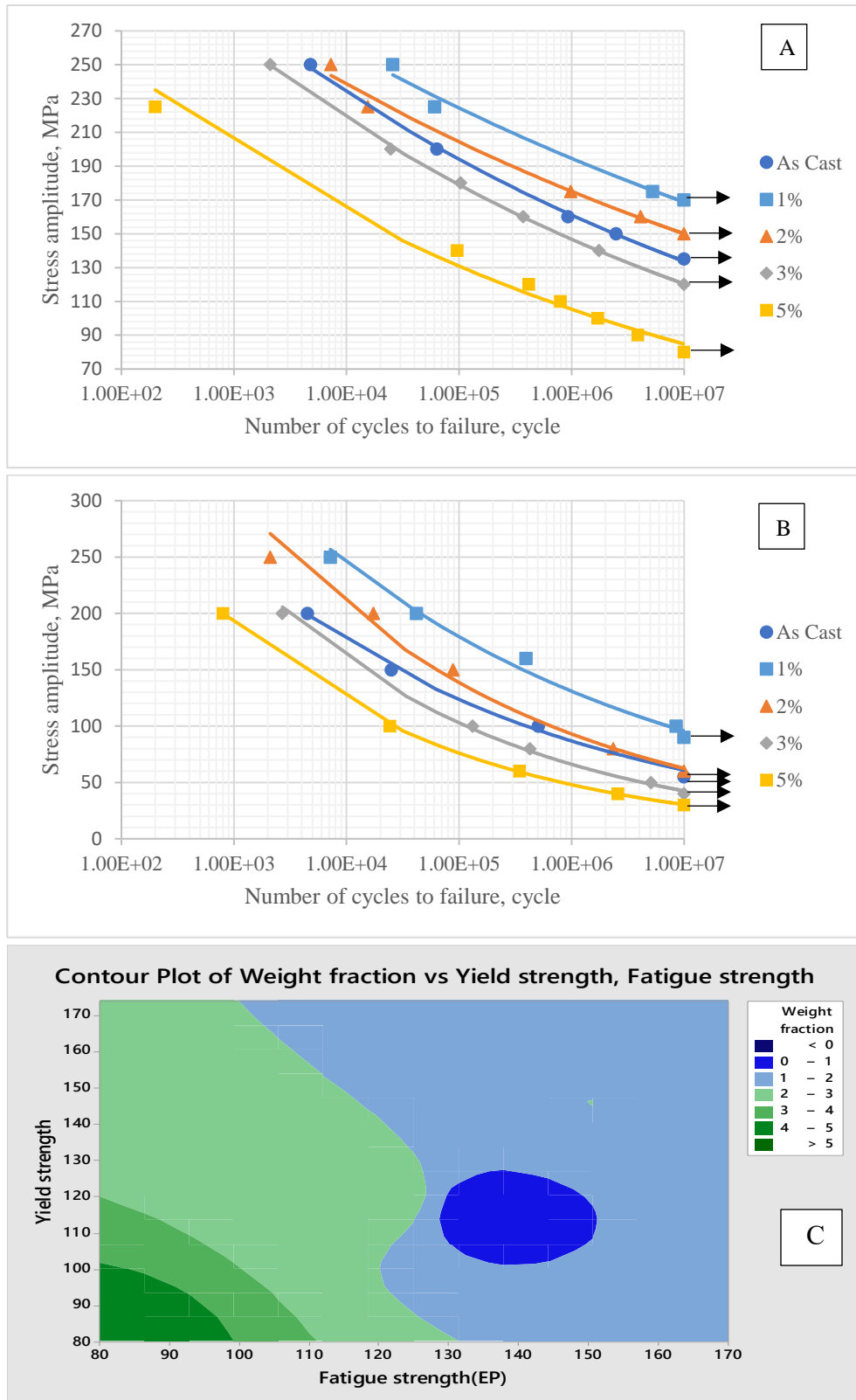


Figure 4-16: S-N curves of electropolished samples; A.in air and B. in 3.5% NaCl, and C. contour plot of the weight fraction vs yield strength and the fatigue strength in air of the electropolished samples

The higher fatigue life obtained by the composites reinforced with nanoparticles could be explained by considering the load carrying capabilities offered by the high strength and elastic modulus nanoparticles. Thus, the composites exhibit a lower average strain compared to the monolithic alloy with an extended fatigue life. Furthermore, the presences of the nanoparticles attributes to enhance the rate of cyclic hardening (number of cycles to reach the steady state strain amplitude) resulted from the locking effect of moving dislocations. The nanoparticles act as barriers for the reversible slip motion that takes place during fatigue due to the small interparticle spacing, which is comparable to the self-trapping distance of dislocations. Consequently, the reinforcement particles cause a decrease in strain localization by cyclic slip refinement and favors crack growth impedance either by crack deflection or crack trapping. The enhancement in the fatigue life in the AMNCs is remarkable at high cyclic fatigue (low-stress amplitude) than the low cyclic fatigue due to the ductility retardation in the high cyclic regime. Increasing the weight fraction of the reinforcement particles (such as 3 and 5 %) favors the formation of clusters with large size. Therefore, the fatigue life is retarded due to growing the particles cracking, and hence the reinforcement fracture predominates [67,123].

The previous fatigue results can be also clarified by the microstructure of the different reinforced conditions. The grain size of the matrix, the morphology of the phases, and the presence of some Fe-rich intermetallic are affecting the fatigue behavior of the composites. Decreasing the grain size of the matrix contributes to prolonging the fatigue life by restricting the dislocations movement and favoring pileup at precipitates and reinforcement particles enabling cracking along slip bands. Contrary, the extensive presence of Fe-rich intermetallic (in the case of 5wt.% Al_2O_3) causes the declination of the fatigue limit due to acting as nucleation sites for cracks. Throughout cyclic loading, cracks are initiated at some process-related defects such as particle clusters (the case in 2 and 3wt.% Al_2O_3) and intermetallic inclusions due to the high local stress intensity.

The crack initiation probability at the surface-inclusions are higher than within the matrix because of the higher stress concentrations at the surface. When nanoparticles surround the inclusions, the load is shared by these high stiffness particles and the inclusion is subjected to a lower stress than that could be found in the monolithic alloy. The formation of pores and its heterogeneous distribution among the matrix reduces also the fatigue life significantly because of the high-stress concentrations at the pores tip. Other factors such as nanoparticles coherency, distribution, and size control the fatigue life of a given composite by enhancing dislocations cutting or looping around particles/precipitates during cycling loading [67,123].

The surface roughness has an important effect on the crack initiation during the cyclic load application. The rougher surfaces, the more probability of initiating cracks during the fatigue loading. However, the surface roughness of the As Cast condition and the other composites with Al_2O_3 additions does not have a significant impact on the fatigue life due to the unnoteworthy variation between them [6-7,113,115]. Figure 4.17 indicates the surface roughness of the different conditions of nanoparticles addition compared to the unreinforced alloy in the electropolishing (EP) state.

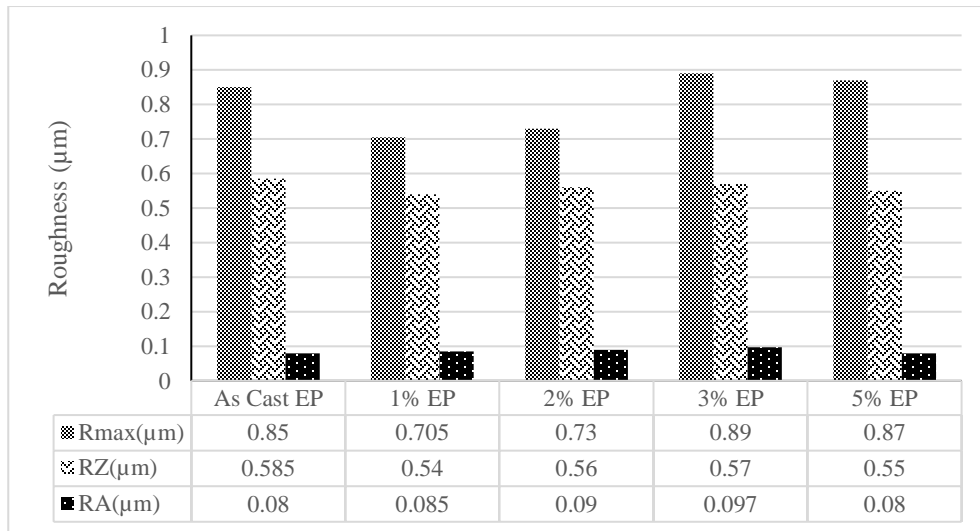


Figure 4-17: Surface roughness of the electropolished sample

The microhardness results are illustrated by Figure 4.18 and demonstrates the behavior of the composites reinforced with nanoparticles in respect to the unreinforced alloy. The 1 and 2 wt.% Al_2O_3 composites reveal a higher microhardness compared to the unreinforced alloy. On the other side, the 3 and 5wt.% Al_2O_3 show lower microhardness than the monolithic alloy. The decrease in the microhardness occurred at high levels of nanoparticles addition can be cleared by the higher agglomerations and porosity formed after the introduction of the nanoparticles.

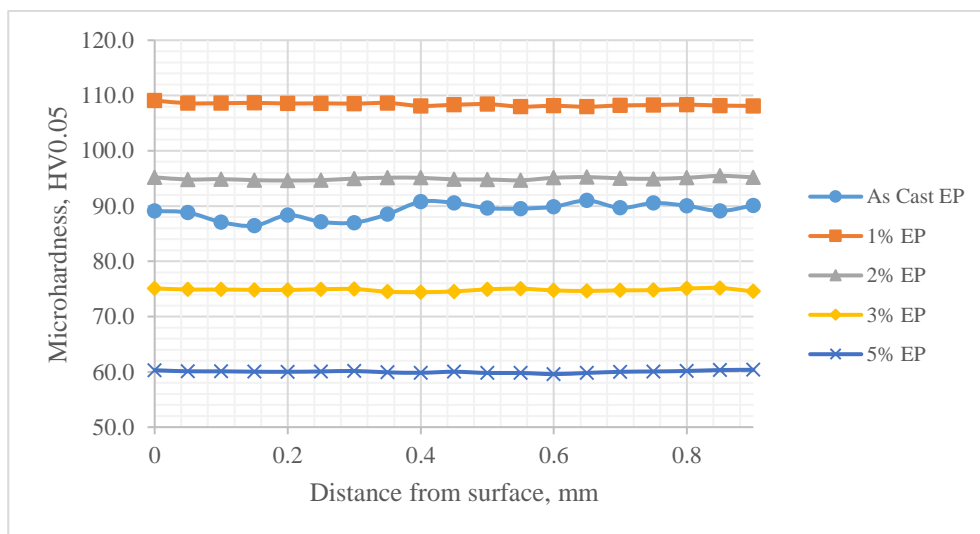


Figure 4-18: The microhardness of the electropolished samples

The observed 22% increase in the microhardness of the 1wt.% composites is attributed to the presence and the uniform distribution of the nanoparticles among the matrix, increase in the

resistance to localized matrix deformation and a visible indication of the grain refining obtained by the addition of the Al_2O_3 . This increase in the microhardness can be probably the responsible of the increase in the endurance limit, where the crack closure stress in the low stress ratio region is strongly affected by material hardness. The crack opening stress increases with increasing the hardness of the material [68].

The fatigue behavior in air and 3.5% NaCl of the 1wt.% Al_2O_3 , recycled as well as the sever plastically deformed (SPD) in respect to the unreinforced alloy is indicated by Figure 4.19. The composites contain 1wt.% alumina under sever plastic deformation show an increase in the fatigue strength, which was improved against the other composites including the different post-processing conditions in air as well as the corrosive medium. The SPD composites show an increase in the fatigue strength with about 18% than the composite reinforced with 1wt.% without SPD and with about 48% than the monolithic alloy in the air. Moreover, the fatigue life was also improved in the corrosive medium with about 33% and 118% than the composite reinforced with 1wt.% alumina without SPD and the monolithic alloy respectively. The relation between the fatigue strength and the tensile properties was firstly found by Wohler in 1860s as the first quantitative relation between fatigue strength and other mechanical properties. The increase in the HCF of the 1%SPD could be explained by the significant increase in the yield strength from 116 MPa in the As Cast and 174 MPa in the 1% to 369 MPa for the SPD. Furthermore, the fine grain size induced by the application of the rotary swaging and the presence of the nanoparticles limits the cyclic softening that could occur in the HCF through restricting the dislocations movement among the matrix. In addition, the induced mechanical deformation is associated with a decrease in the overall size of inclusions and consequently improves the fatigue life [123,127-128].

Figures 4.20 and 4.21 indicate the surface roughness and the microhardness profiles of the 1% SPD and recycled composites compared to the monolithic alloy and normal 1wt.% composites. On one hand, it can be clearly observed that the surface roughness was not remarkably affected by the different post-processing methods as they are mainly bulk-processing techniques. Therefore, the effect of the surface roughness on changing the fatigue limit can be ignored. On the other hand, the microhardness profile of the composites containing the same content of the Al_2O_3 was significantly changed after the post-processing methods. On that, the effect of the surface roughness has not a significant influence on the fatigue behavior. Mainly, the strengthening occurred through the mechanical deformation, which is evident in the microhardness profile (Figure 4.21), has the dominant effect on enriching the fatigue life of the 1% SPD. Since the cyclic response of the AMNCs is controlled by the matrix microstructure, the finer grain size induced by the mechanical deformation in the 1%SPD condition influenced by increasing the fatigue life compared to the other composites [67].

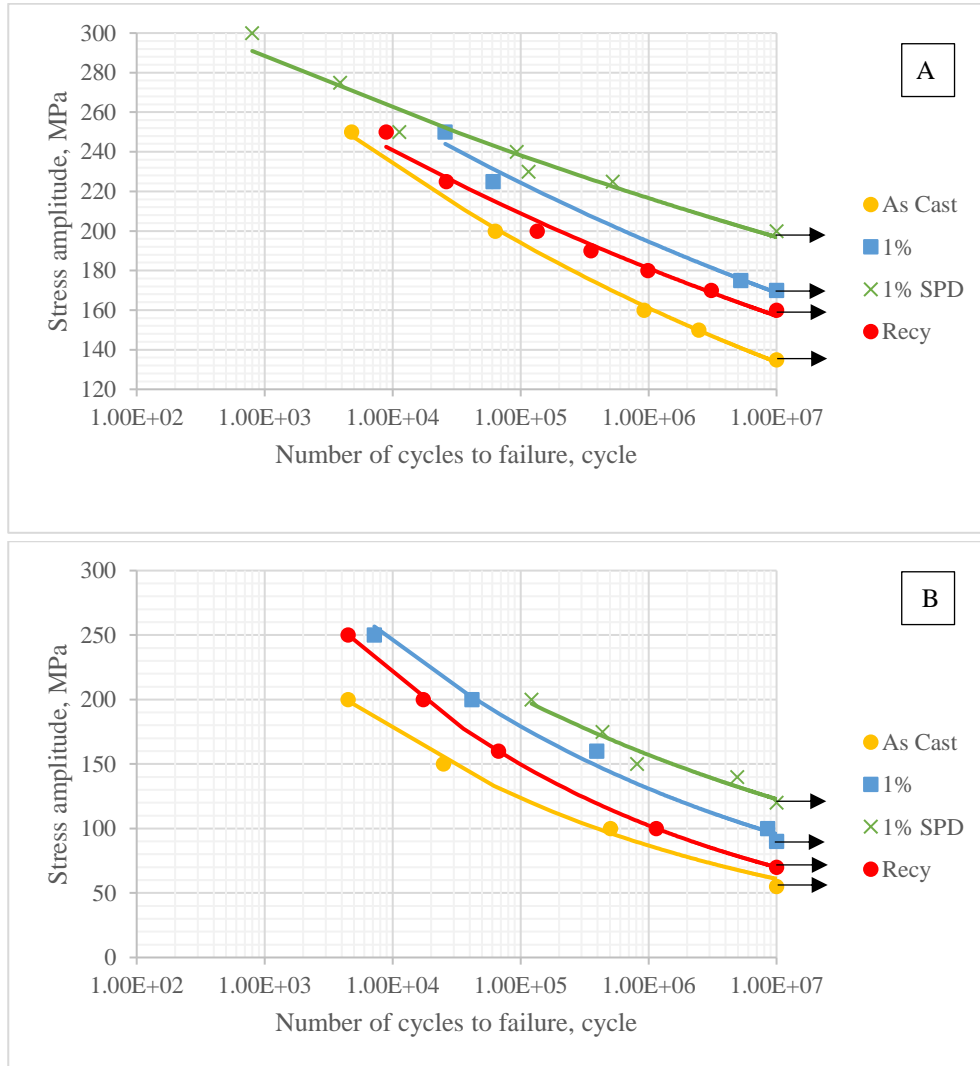


Figure 4-19: S-N curves of the electropolished monolithic alloy against 1wt.%, 1%SPD and Recycled composite; A. in air and B. in 3.5% NaCl

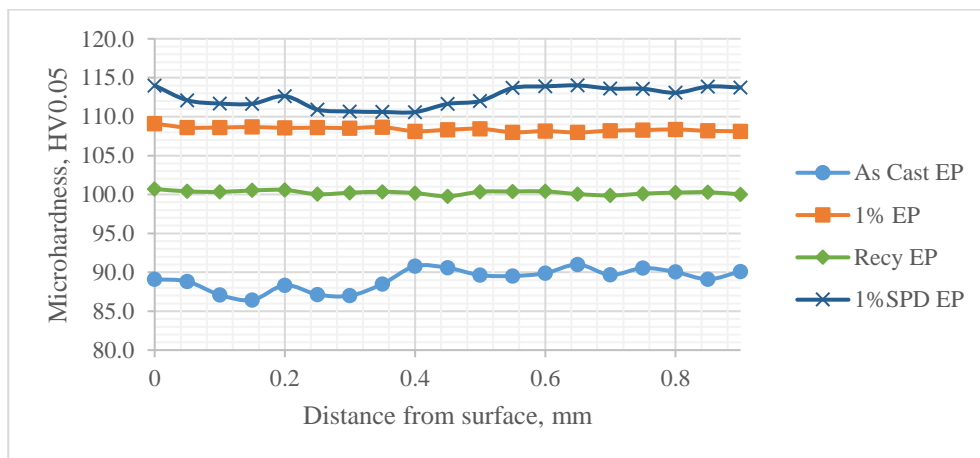


Figure 4-20: Microhardness of the electropolished monolithic alloy against 1wt.%, 1%SPD and Recycled composite

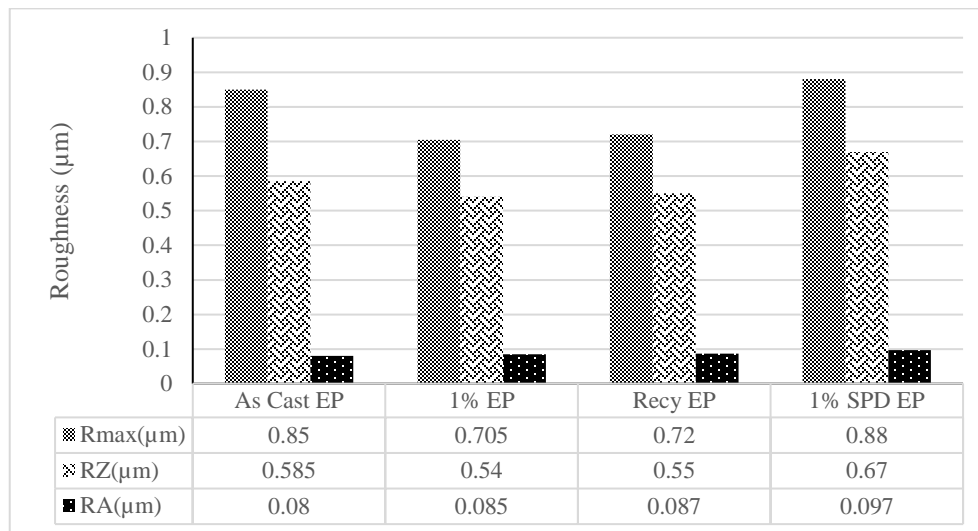


Figure 4-21: The surface roughness of the electropolished monolithic alloy against 1 wt.%, 1% SPD and Recycled composites

The decline in the fatigue life of the recycled 1% samples can be referred to the large size of particles clustering ($8.32 \mu\text{m}$) compared to that occurred in the 1% ($2.15 \mu\text{m}$) or 1% SPD ($1.98 \mu\text{m}$). Particles clustering accelerates the matrix cracks either by particle de-bonding or particle fracture in the electropolishing state. Both damage types are located in the clustering zones and initiated from sharp edges that could be produced by particles agglomeration. The crack propagates initially along a slip band in a free particle area until the crack front faces the clusters. Consequently, the crack changes its path causing the damage to be developed in the agglomerates assisted by particle de-bonding or particle fracture, which is a predominant phenomenon in the high cyclic fatigue regime. The fatigue failure is associated with rapid crack propagation at the clustering regions due to the high local stresses and the defects found in clusters such as contacted particles, larger particles, and fractured particles [44-45,123-126].

4.2.2.2 Shot peening

Figures 4.22 A and B show the S-N curves of composites containing different additions of alumina nanoparticles and the monolithic Al 6061 matrix after conducting shot peening as a mechanical surface treatment in the air and 3.5 wt.% NaCl solution.

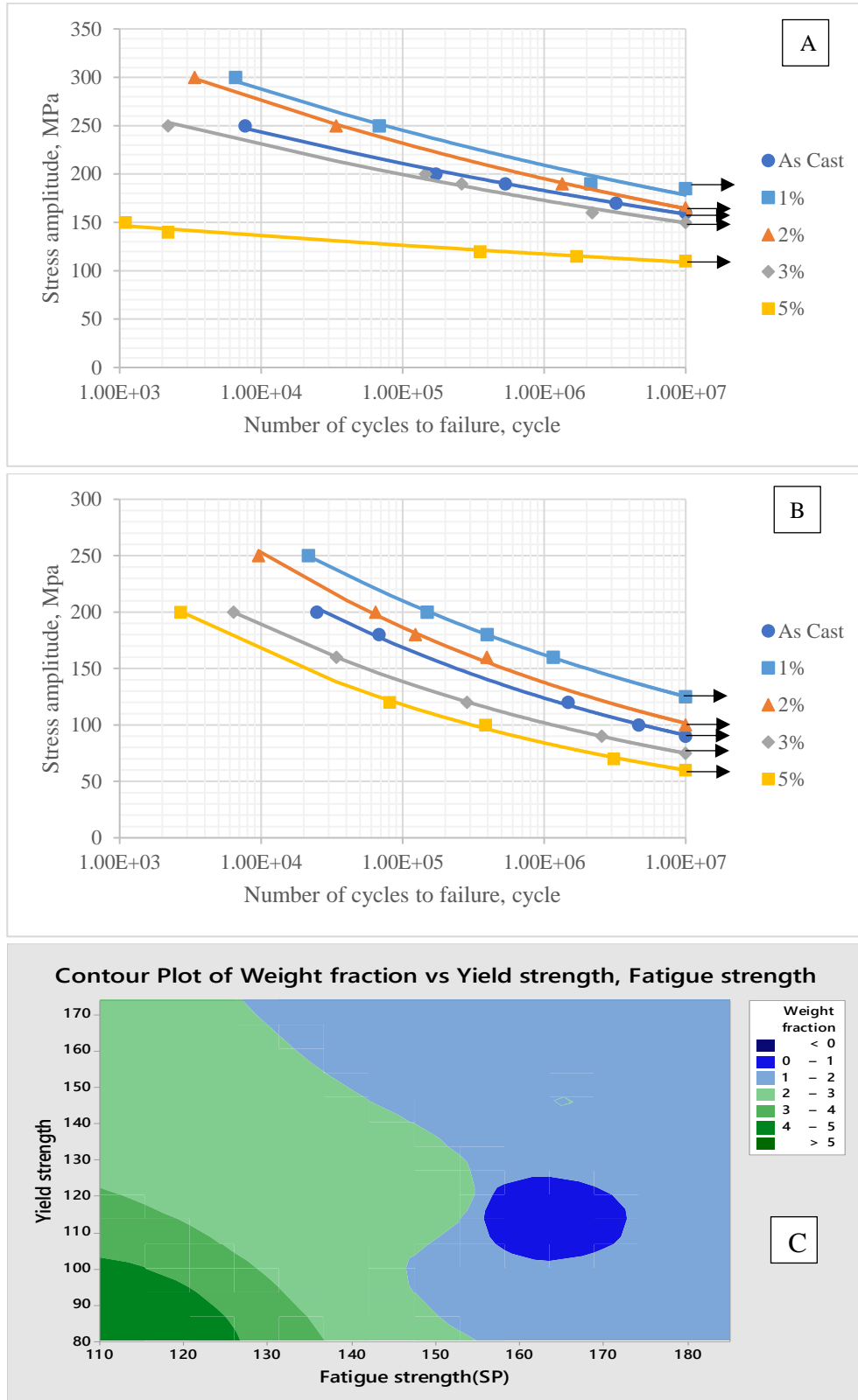


Figure 4-22: S-N curves of shot peened samples; A:in air, B: in 3.5% NaCl, and C. contour plot of the weight fraction vs yield strength and the fatigue strength in air of the shot peened samples

From Figure 4.22, it can be clearly observed that the fatigue life of the 1wt.% Al_2O_3 composites was enhanced compared to the Al6061 matrix with 16% and 39% in air and 3.5% NaCl solution respectively. The improvement in fatigue life of the nanocomposites is related to the enhancement of the mechanical properties occurred after the Al_2O_3 nanoparticles additions [67-68]. The further improvements in the fatigue life of the both materials, compared to the electropolished state, could be attributed to the increase in surface hardness and the amount of the compressive residual stresses remained in the material after shot peening (Figures 4.23 and 4.24).

The main aim of the mechanical surface treatments is to apply a localized pressure on a particular area of the working sample that should exceed its elastic limit. This pressure is assumed to deliver the material to its plastic zone, increase the dislocation density in the matrix, and generate internal stresses between the outer layer and the inner layer which did not reach the elastic limit and tended to restore its position. Thus, compressive residual stresses arise between the inner layers and the plastically deformed outer layer [6-7]. The resulted compressive residual stresses force the crack initiation to occur under the surface and thus prolong the material fatigue life. Therefore, the harder and the more compressive residual stresses under the surface, the higher fatigue life [128].

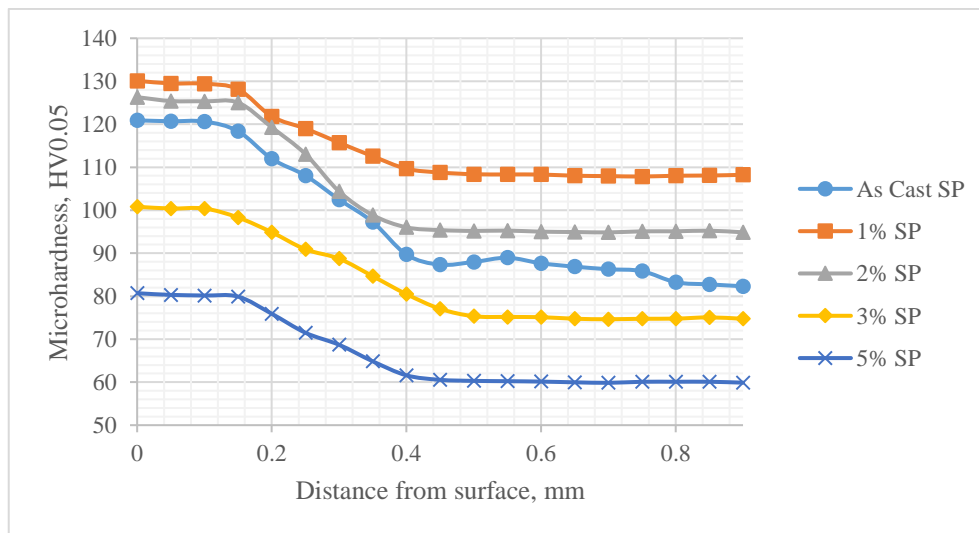


Figure 4-23: The microhardness of the shot peened samples

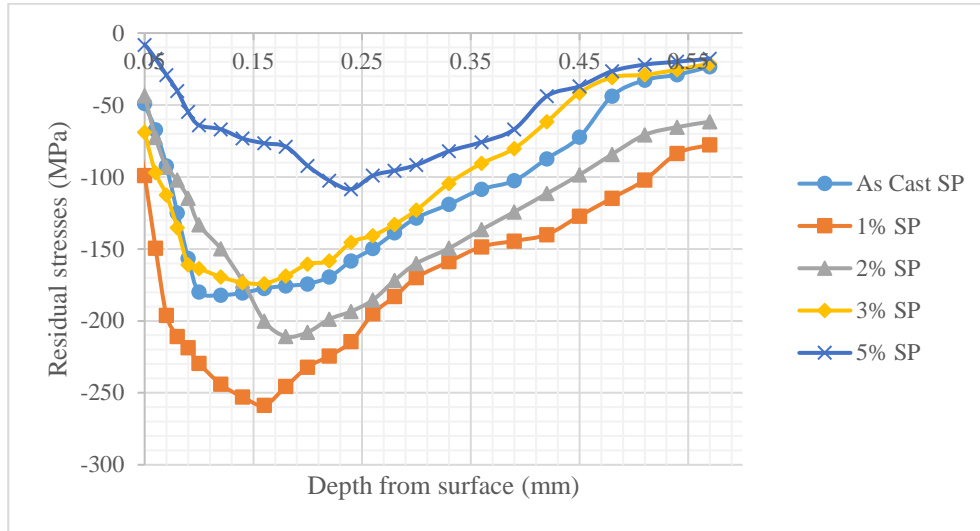


Figure 4-24: The residual stresses of the shot peened samples

From Figures 4.23 and 4.24, it appears that the highest microhardness and the value of the compressive residual stresses in the near-surface region was achieved at the 1wt.% composites. This increase in the near-surface properties could explain the remarkably improved fatigue life of the 1wt.% condition. The fatigue behavior is also affected by the crack initiation probability (which depends on the surface roughness) in the low cyclic fatigue, where it is more influenced by the crack propagation in the high cyclic fatigue controlled by the amount of the induced compressive residual stresses. The surface roughness has a functional role in affecting the fatigue life by retarding and stimulating or increasing the crack initiation [110-115].

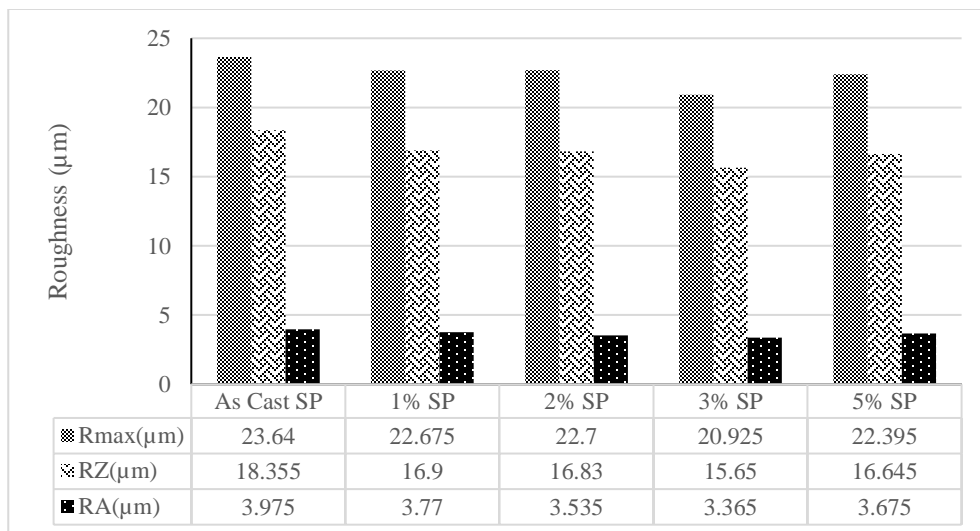


Figure 4-25: The surface roughness of the shot peened samples

It is evident from Figure 4.25 that shot peening leads to a marked increase in the surface roughness compared to the electropolished specimens. The fatigue performance of shot-peened

specimens is dependent on the combined effects of strain hardening, surface roughness, and residual compressive stresses produced by shot peening. Basically, the increase in the surface roughness leads to raising the probability of the crack nucleation and its early propagation. Unlike, the strain hardening retards the propagation of cracks by increasing the resistance to plastic deformation, as well as the compressive residual stresses provide a corresponding crack closure stress which contributes to hinder the crack propagation. The enhancement in the fatigue behavior of the shot peened samples is attributed to restricting the microcracks growth. This restriction is caused by the induced compressive residual stresses and compensating the decrease in the fatigue life resulted from crack initiation caused by higher surface roughness after shot peening [111-115].

The effect of the shot peening on the fatigue life in air and 3.5% NaCl solution of the recycled composites and 1% SPD compared to the monolithic and 1wt.% Al₂O₃ is indicated by Figures 4.26 A and B.

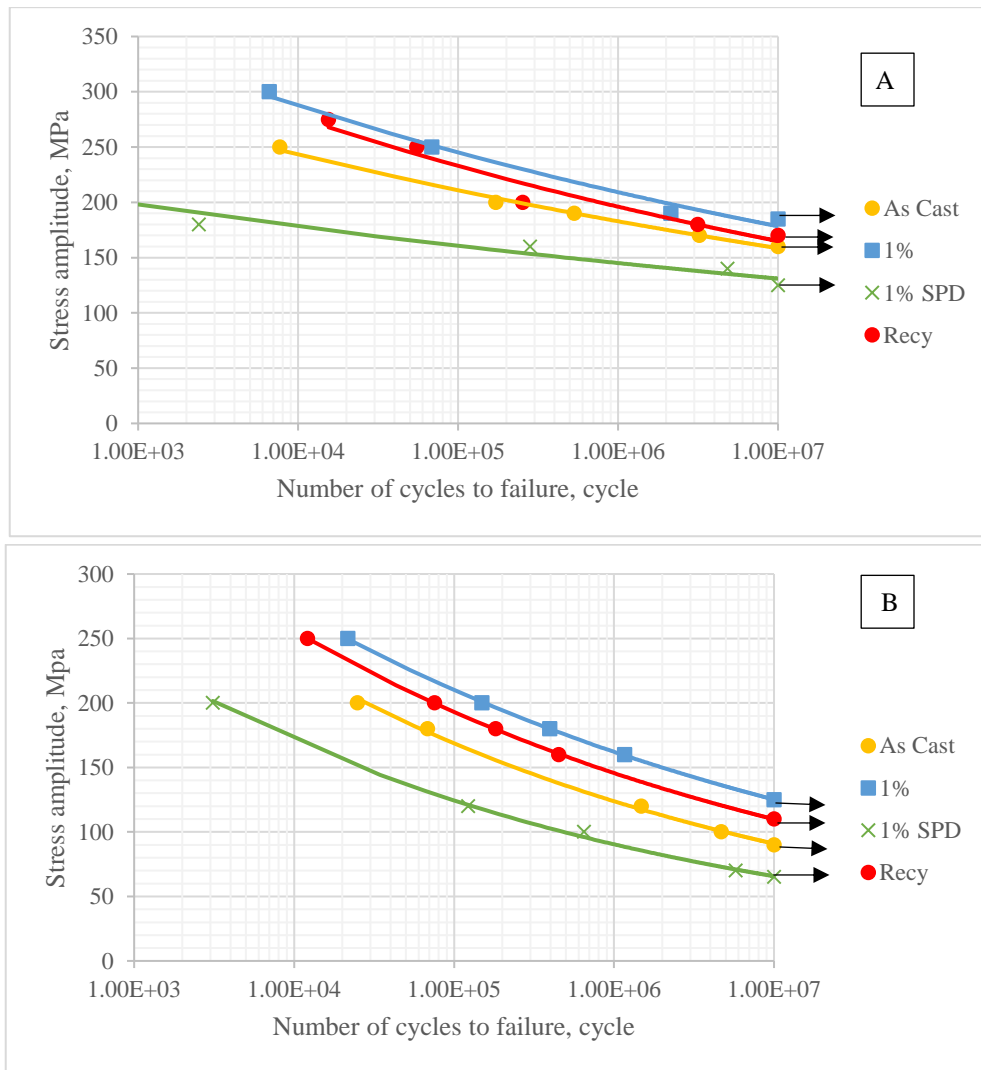


Figure 4-26: S-N curves of the shot peened monolithic alloy against 1wt.%, 1%SPD and Recycled composite; A. in air and B. in 3.5% NaCl

The recycled composites show a slight improvement in the fatigue behavior compared to the monolithic alloy with an increase of about 6% in air and 22% in 3.5% NaCl. Nevertheless, the fatigue life of the recycled composites was retarded compared to the 1wt.% Al_2O_3 with about 13% in both air and 3.5% NaCl solution. The enhancement in the endurance limit of the recycled composites could be accredited to lower surface roughness among the other conditions (Figure 4.27) and the amount of the compressive residual stresses induced by shot peening (Figure 4.28) with about 238 MPa behind the 1wt.% composites (259 MPa). The decrease in the surface roughness and the increase in the compressive residual stresses attribute to prolong the fatigue life by diminishing the crack nucleation and standing against plastic deformation enabling crack blunting and retarding the crack propagation.

Despite the enhancement in the fatigue behavior of the 1% SPD specimens at the electropolished state (Figure 4.19), the shot peened 1% SPD samples show a reduction in the endurance limit (Figure 4.26) with 32% and 22% than the 1wt.% Al_2O_3 and the monolithic alloy respectively in air and with 48% and 27% in 3.5% NaCl.

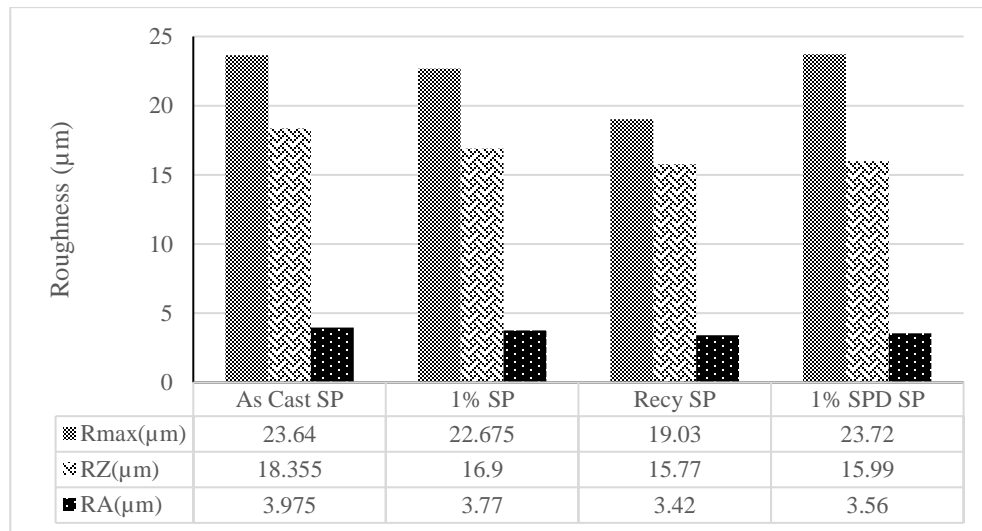


Figure 4-27: The surface roughness of the shot peened monolithic alloy against 1wt.%, 1%SPD and Recycled composite

This reduction in the fatigue life after SPD can be explained by the concept of the mechanical surface treatments. Accordingly, the role of any mechanical surface treatment is to induce plastic deformation to a given area of the sample with an effect reaches a fraction of millimeter under the surface depending on the severity and the art of the mechanical surface treatment. In this layer, the material is cold worked with an increase in the dislocation density, which by the role raises the compressive residual stresses in the effective region. These compressive stresses, as discussed earlier, aim to restrict the crack propagation or growth and extend the fatigue strength of the material [6-7,128].

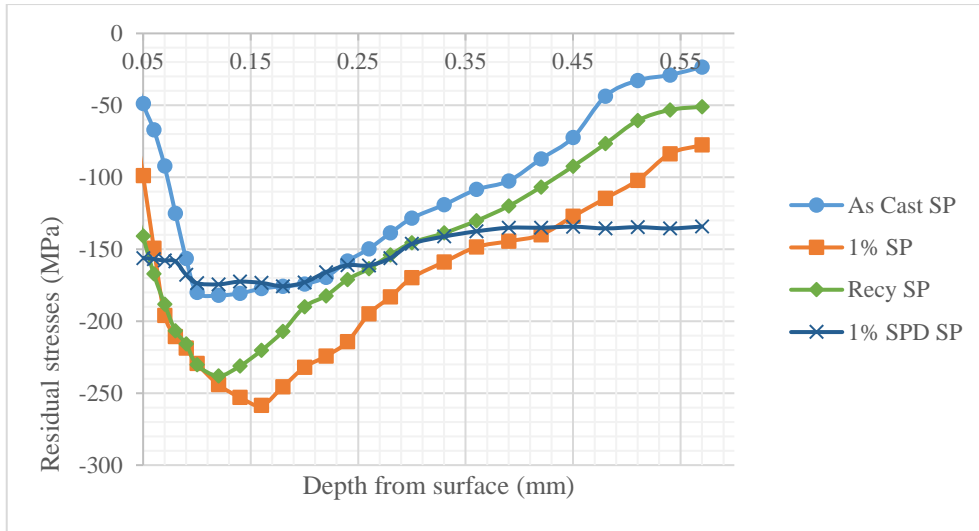


Figure 4-28: The residual stresses of the shot peened monolithic alloy against 1wt.%, 1%SPD and Recycled composite

In the case of the 1% SPD, the material is already plastically deformed by the rotary swaging process which also resulted in stored compressive residual stresses in the specimens and caused the increase of the fatigue life of the electropolished samples (Figure 4.19). Moreover, the introduction of such plastic deformation causes the diminution of the work hardening capability which decreases the ability of the material to store further deformation. Applying the mechanical treatments such as shot peening, in this case, attributes to increase the surface roughness of the specimens (Figure 4.27) without a significant increase in either the compressive residuals stresses (Figure 4.28) or the microhardness under the surface (Figure 4.29).

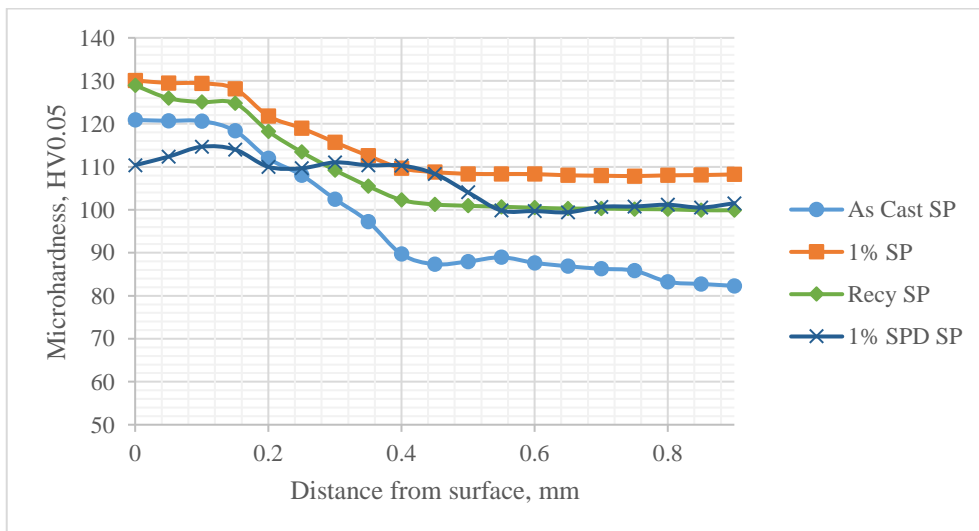


Figure 4-29: The microhardness the shot peened monolithic alloy against 1wt.%, 1%SPD and Rec composite

As mentioned before, the fatigue strength of a given material after performing mechanical surface treatments is a function in the surface roughness, compressive residual stresses and strain hardening. Therefore, the fatigue strength is affected by the surface roughness more than the two other influences resulting in increasing the crack initiation at the surface and decreasing the fatigue limit of the 1% SPD [128].

4.2.2.3 Roller burnishing

The S-N curves in air and in 3.5% NaCl of the as-cast alloy and the Al6061 composites with different additions of alumina nanoparticles are indicated in Figure 4.30. The composite contains 1% Al_2O_3 exhibits the most enhanced fatigue life among the other composites and the monolithic alloy in air and in corrosive medium. The fatigue strength increases with about 18% and 27% in air and corrosive environment respectively compared to the as-cast condition. The other composites with 3wt.% and 5wt.% Al_2O_3 show a lag in the fatigue performance behind the as-cast, 2wt.% and 1wt.% conditions due to the retardation in the tensile properties caused by the agglomeration and high porosity formed after casting. Besides, the work hardening capability of these conditions was low to permit more plastic deformations to be stored in the material, which are responsible for increasing the magnitude of the compressive residual stresses and prolong the fatigue life by restricting the crack propagation [6-7,111].

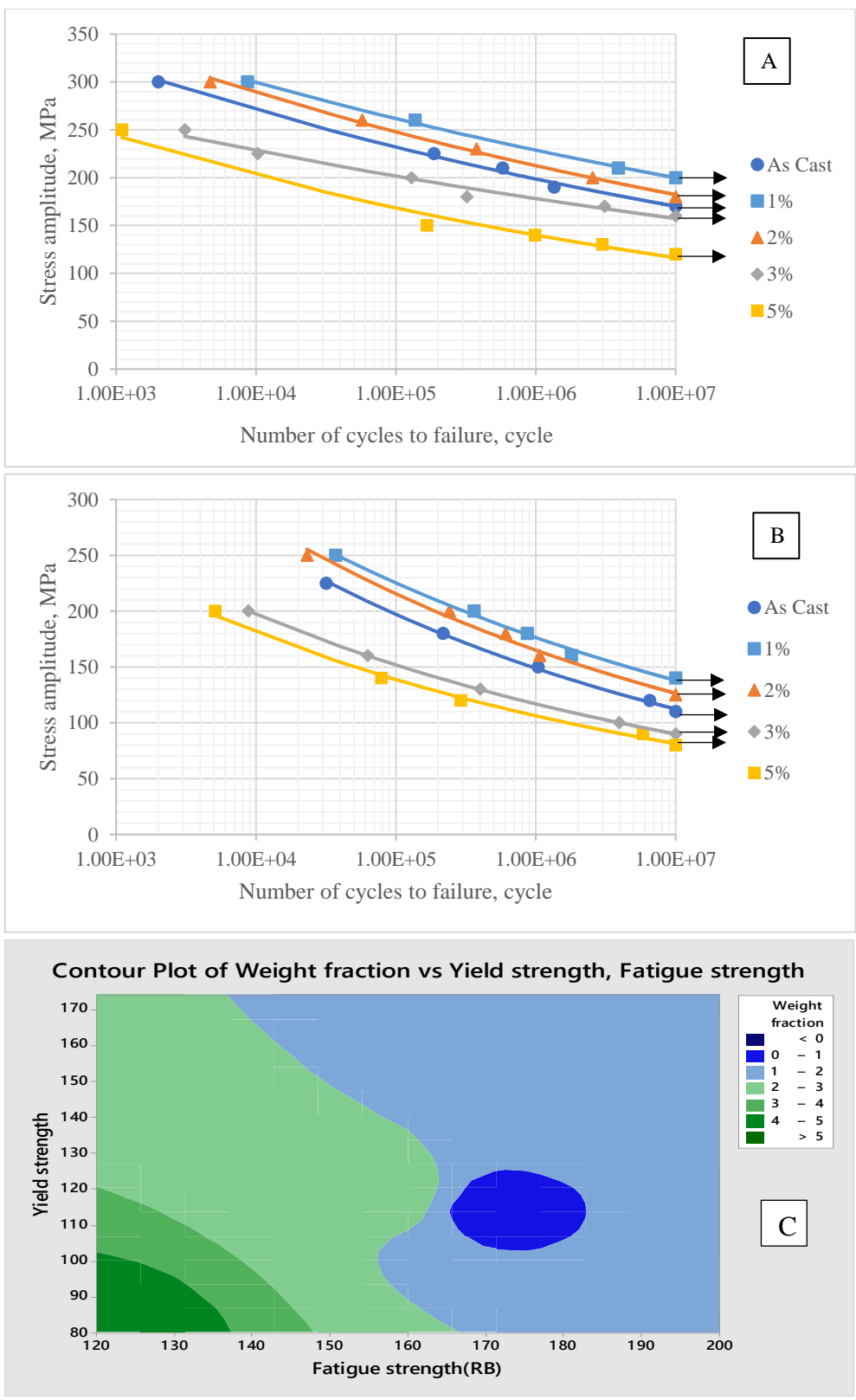


Figure 4-30: S-N curves of the roller burnished samples; A: in air and B: in 3.5% NaCl, and C. contour plot of the weight fraction vs yield strength and the fatigue strength in air of the roller burnished samples

Roller burnishing, as a mechanical surface treatment, improves the surface characteristics and the fatigue life. Based on the elastic/plastic cold-working in the near-surface region, the induced plastic deformation through the cold working of the surface layers provides higher resistance to crack invitation or propagation. The impact of the roller burnishing treatment on fatigue life depends on the fatigue failure nature (crack initiation for unnotched samples/propagation for notched samples), as well as the material yield strength. In the experiments' case, unnotched specimens, the fatigue life is dominated by the crack initiation where a large number of cycles are consumed in initiating cracks. The fatigue behavior after roller burnishing also depends on the ultimate tensile strength to yield strength ratio. The increase in this ratio attributes to improve the endurance limit due to the induced compressive residual stresses caused by roller burnishing, which prevents small cracks propagation. Contrarily, when the ratio reaches about one, the enhancement in the fatigue life is caused by the work hardening caused in the few fractions of millimeters adjacent to the surface without significant influence of the compressive residual stresses because of their partial relaxation [111-115].

Unlike the shot peening treatment, roller burnishing is considered as one of the surface finish processes, where the smoother surfaces after roller burnishing can markedly improve the resistance of fatigue crack initiation and hence enhance the fatigue life. The surface roughness of the specimens under roller burnishing (Figure 4.31) is much lower than that obtained after conducting shot peening due to the low burnishing speeds and high depths of penetration. Therefore, the roller burnishing treatment is much dependent on the work hardening, where the fatigue life is controlled by the crack initiation [6-7].

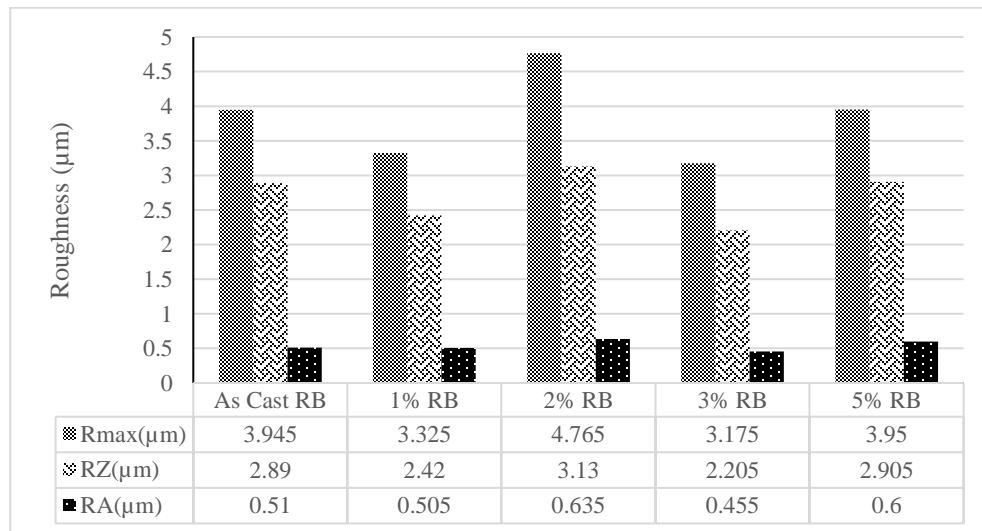


Figure 4-31: The surface roughness of the roller burnished samples

During the early stages of crack initiation, the work hardening induced by roller burnishing in the near-surface layer controls the cyclic deformation behavior. The high dislocation density in this region reduces the plastic strain amplitude and prolongs the endurance limit of the material. The further increase in the rolling pressure causes deeper layer with smaller plastic strain

amplitude and higher fatigue strength. Just after crack initiation stage, the crack propagation is controlled by the amount of the compressive residual stresses (Figure 4.32) stimulating the propagation deceleration or crack arrest. Moreover, the compressive residual stresses reduce the effective cyclic stress intensity factor against the crack length extension and force the crack movement below the surface through a maximum of compressive stresses. Because of their direct influence on performance in service, residual stresses are probably the most critical aspect in assessing the surface integrity of a burnished workpiece. The position of the maximum residual stress depends on the rolling force and the exact contact geometry of the involved specimen and roller. Increasing the burnishing pressure increases the amount of the compressive residual stresses until a saturated level is achieved (marked at 0.8 bar in experiments) [111-115].

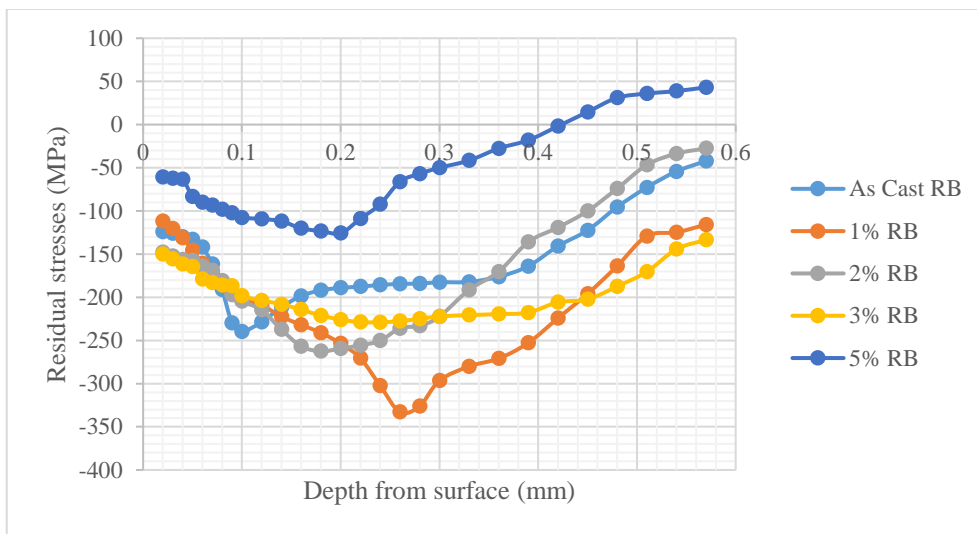


Figure 4-32: Residual stresses of the roller burnished samples

Further increase in the burnishing pressure leads to shift the area of compression into greater depth. Not only the compressive residual stresses are affected by roller burnishing, but also the near surface hardness is increased by work hardening effects (Figure 4.33). The thickness of the deformation layer can be estimated to be about 0.4-0.5 mm by the change in microhardness, which is much deeper than that in the shot-peened specimens. Finally, it can be summarized that the fatigue life increases after roller burnishing due to the reduction in the surface roughness caused by the burnishing action, the elimination of surface flaws by the burnishing effect. Furthermore, the burnishing process produces metal plastic flow and provides filling existing voids or defects and setting compressive residual stresses in the outer circumferential area of the workpiece [112-114].

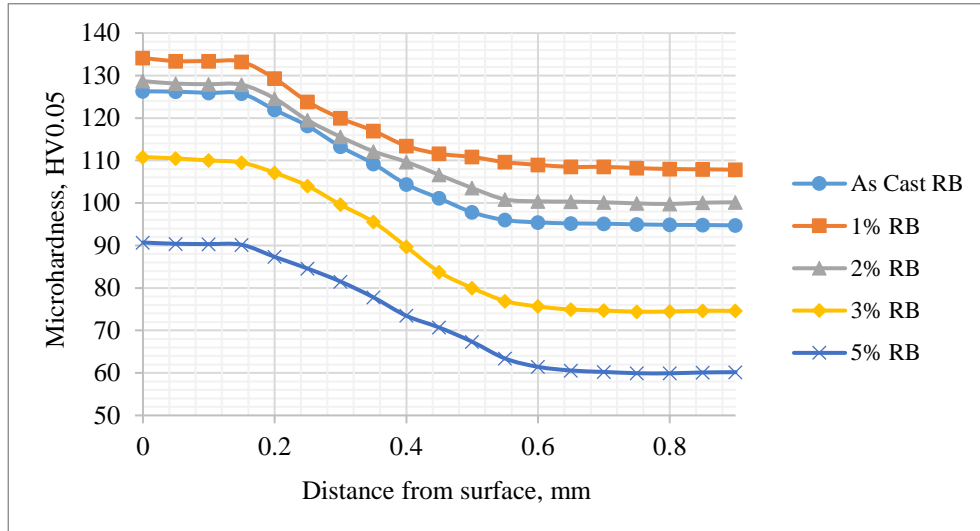


Figure 4-33: Microhardness of the roller burnished samples

Figures 4.34A and B illustrate the S-N curves of the recycled, 1wt.% and 1%SPD composites compared to the monolithic alloy in air and 3.5% NaCl solution. It can be observed that the fatigue life of the 1wt.% Al_2O_3 composite still leading over the other conditions under roller burnishing. However, the recycled composite shows an enhancement in the fatigue strength than the monolithic alloy with 9% and 18% in air and 3.5% NaCl respectively. Furthermore, the 1%SPD condition shows a reduction in the endurance limit under roller burnishing compared to the monolithic alloy with about 24% in both air and 3.5% NaCl solution. While the fatigue life of the 1%SPD after roller burnishing is slightly improved than that obtained after shot peening. This enhancement could be attributed to the decrease in the surface roughness after roller burnishing (Figure 4.35) in contrast with surface roughness after shot peening (Figure 4.27).

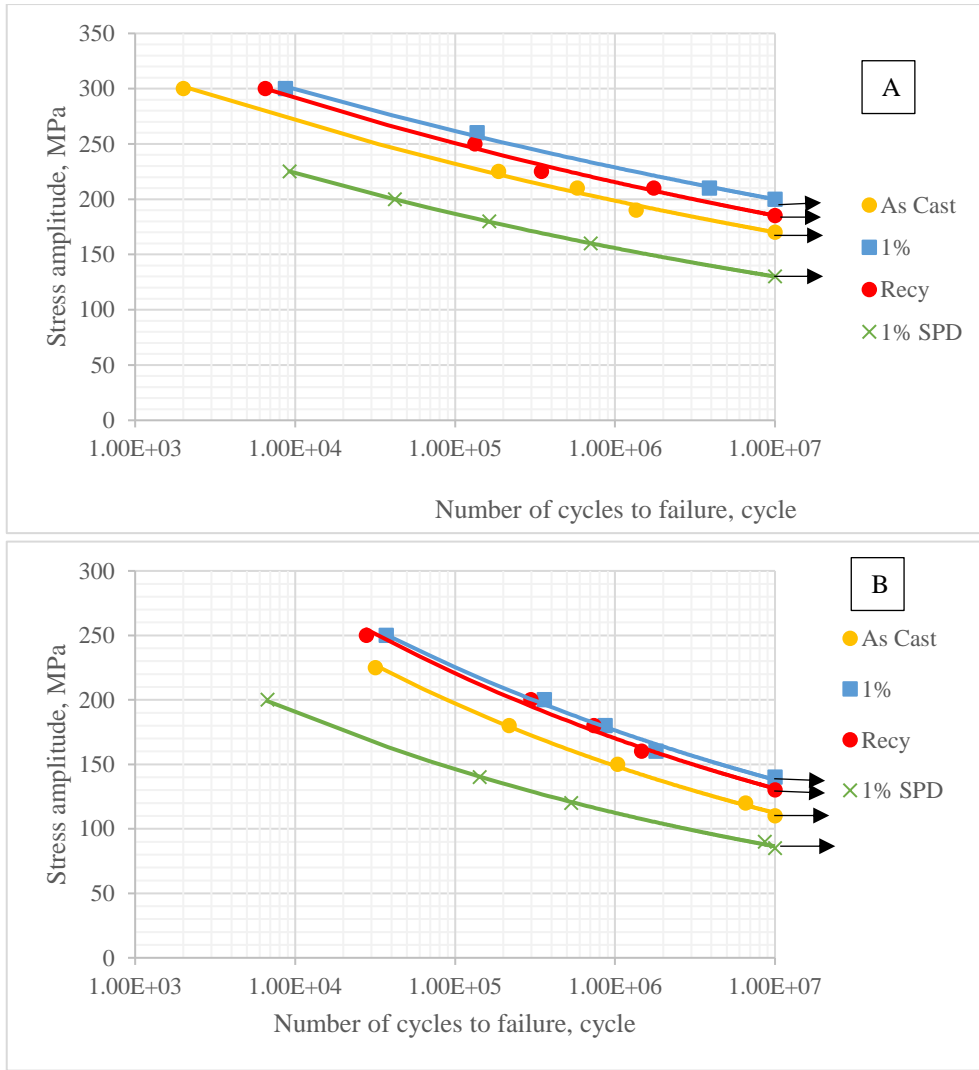


Figure 4-34: S-N curves of the roller burnished monolithic alloy against 1wt.%, 1%SPD and Recycled composite; A. in air and B. in 3.5% NaCl

Decreasing the surface roughness leads to retarding the crack initiation stage in the fatigue failure, and thus prolong the fatigue life of the material. However, the surface roughness is not only the factor which controls the fatigue behavior of the material, but also the amount of the compressive residual stresses induced after conducting a certain mechanical treatment. The retardation of the 1%SPD fatigue strength compared to the other conditions could be related to main two factors. Firstly, the higher surface roughness than the other conditions which is indicated in Figure 4.35. This increase in the surface roughness accelerates the crack initiation, and consequently lowers the endurance limit [6-7,128].

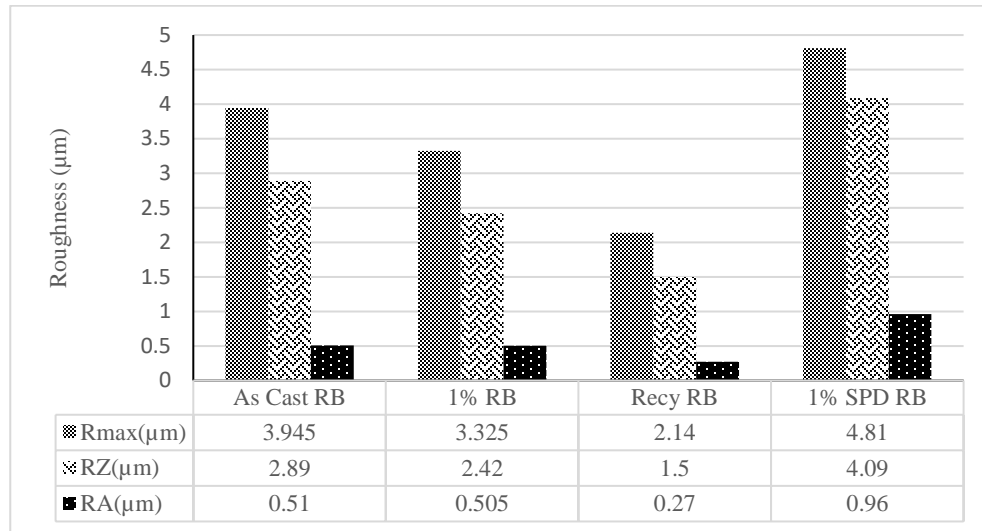


Figure 4-35: The surface roughness of the roller burnished monolithic alloy against 1wt.%, 1%SPD and Recycled composites

The other constituent is the compressive residual stresses magnitude in the 1%SPD samples after roller burnishing. From Figure 4.36, it could be clearly reported that roller burnishing has a slight impact on the residual stresses of the 1%SPD in contrast with the other conditions. This phenomenon may be explained by the lower work hardening capability due to severe plastic deformation, which is exhibited by the material before applying the mechanical surface treatment. Under these residual stresses, the material resistance to the crack propagation was low and not enough to ensure crack arrest, and therefore, the fatigue strength is reduced. The change in the residual stresses after roller burnishing compared to electropolished 1%SPD could also be predicted from the microhardness profile under the surface. Comparing the microhardness of electropolished (Figure 4.20) with roller burnished (Figure 4.37) condition, the microhardness profile varies around 110 ± 5 HV0.05 for the electropolished while it varies around 115 ± 5 HV0.05 for the roller burnished specimens. This small difference in the microhardness value under the surface emphasizes that the roller burnishing process had a slight impact on the subsurface characteristics, especially the residual compressive stresses [115-128].

For the recycled composites, the improved fatigue life could be a direct result of the increase in the compressive residual stresses (Figure 4.36) and the reduced surface roughness (Figure 4.35). The surface roughness has a functional role in affecting the fatigue life by retarding or stimulating the crack initiation, as the smoother surface means lower probability of the crack initiation. Besides, the compressive residual stresses squeeze the grain boundaries, and thus delay the fatigue crack initiation. Forasmuch the crack initiation or propagation are difficult to occur in the layer of compressive stresses, and hence the cracks initiate under the surface with a significant slow propagation rate leading to a prolonged fatigue life [6-7].

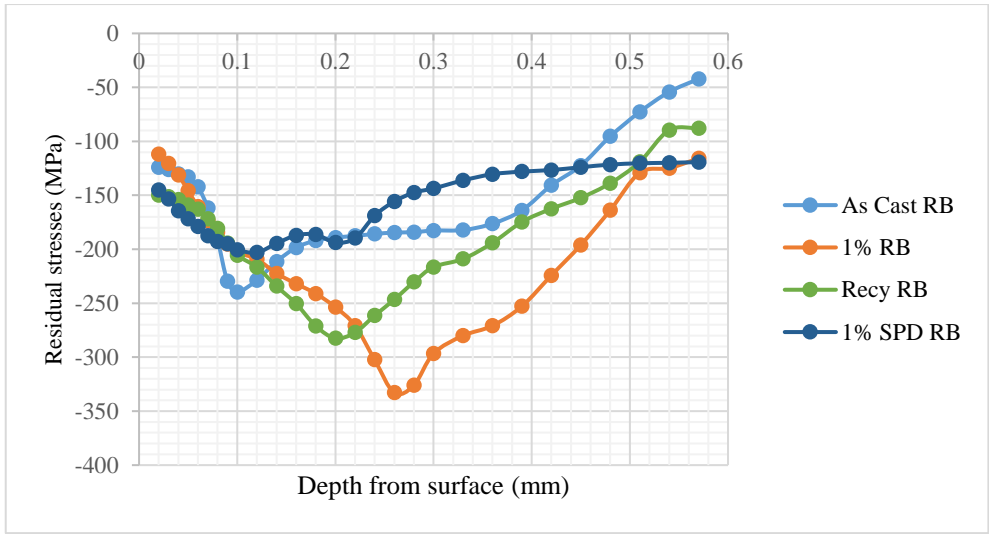


Figure 4-36: The residual stresses of the roller burnished monolithic alloy against 1wt.%, 1%SPD and Recycled composites

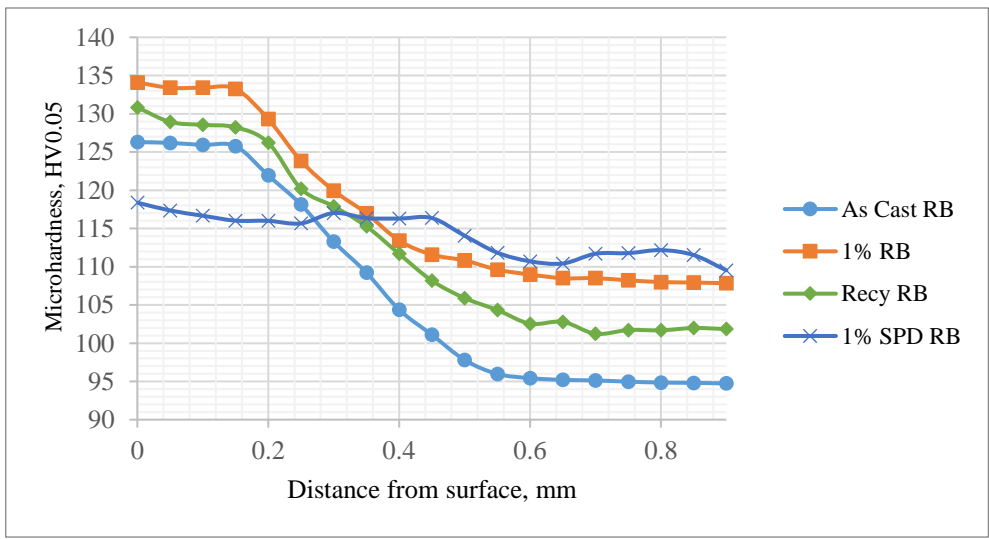


Figure 4-37: The microhardness of the roller burnished monolithic alloy against 1wt.%, 1%SPD and Recycled composites

4.2.3 Creep behavior

The creep rupture test was carried out for the monolithic alloy and composites with different fabrication conditions and additions of Al₂O₃ specimens at 300°C and constant stress of 40 MPa. The test was conducted on peened and un-peened samples. The percent of total plastic deformation against the run time are plotted and indicated by Figures 4.38 A and B for un-peened and peened specimens.

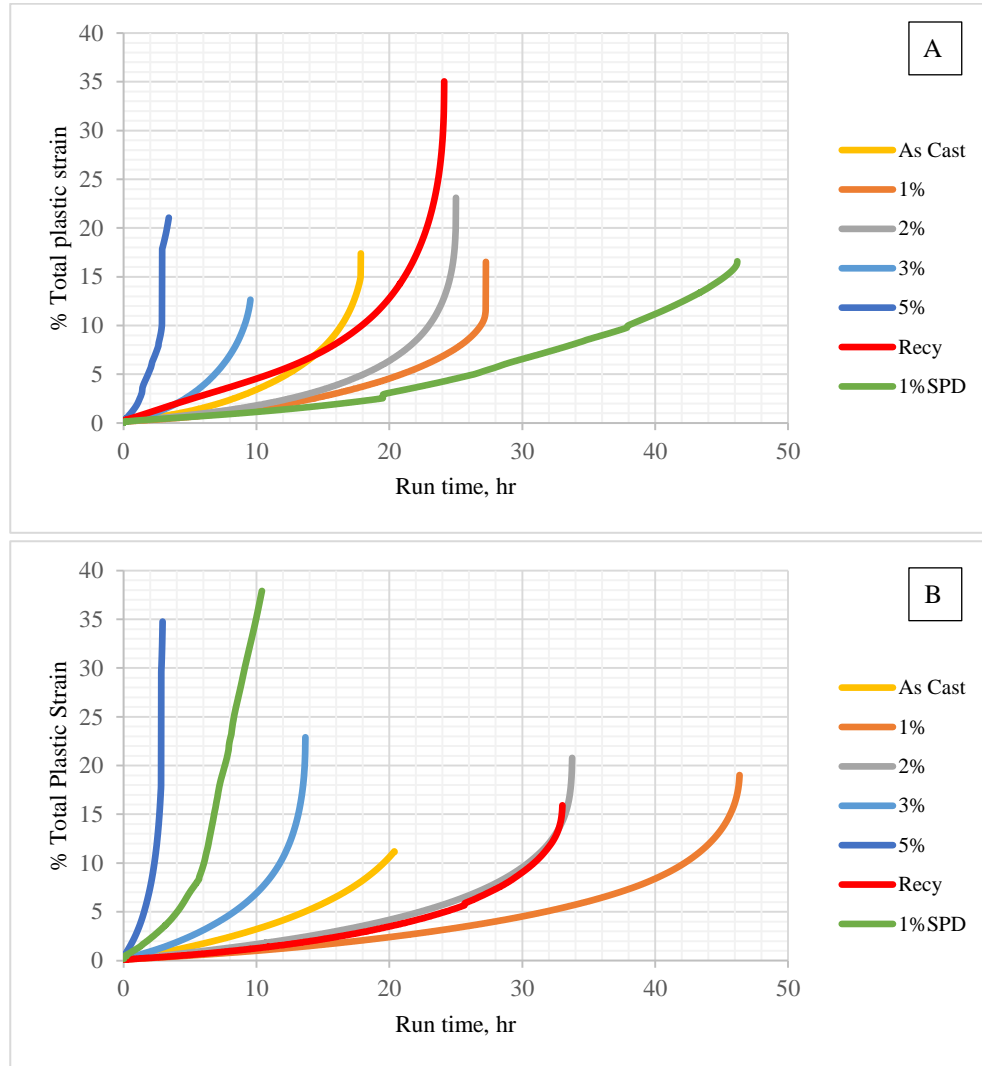


Figure 4-38: % Total plastic strain vs run time of monolithic alloy against composites; A. un-peened and B. peened samples

It could be observed that the monolithic alloy, 3%, 5% peened and un-peened samples and the peened 1%SPD conditions demonstrate short primary and steady-state regimes with a more extended tertiary regime. Furthermore, one or two stages of the curve may be absent because of the creep behavior is characterized by an extensive tertiary stage. Besides, the secondary creep is extremely short and very difficult to be identified. Therefore, the “minimum creep-rate” value is considered rather than a steady-state value [129]. Contrarily, the samples group (1%, 2%, Recy peened and un-peened and the un-peened 1%SPD) show an enhanced length of the primary regime as compared to the other conditions. The creep curves consist mainly of three regions: primary stage, which is distinguished by decreasing the strain rate with the run-time and the material experiences strain hardening due to the high deformation resistance with increasing the strain. The primary stage ends with the start of the secondary stage (or steady state), which is characterized by a constant strain rate, which could be explained by the balance occurred between recovery (due to the high temperature) and strain hardening. Finally, the strain rate increases with

time during the tertiary stage causing rupture of the component. In this stage, failure occurs due to the reduction in cross-sectional area under constant load with a continuous increase in applied stress [129]. The decrease in the cross-sectional area is resulted by different mechanisms such as cavities nucleation and growth, cracks formation, and extensive macroscopic necking. Generally, at higher temperatures and stresses, the primary creep made a transition into steady-state creep faster and had a higher steady-state creep rate than tests conducted at lower temperatures and stresses. Furthermore, the Figure gives a clear indication of the time to rupture for all conditions under shot peening and without shot peening. The time to rupture could be perhaps the most useful from an engineering point of view, as it is an indication of how much time could the sample withstand under given strength and temperature [56-57,129]. For the un-peened specimens, the 1% SPD composites show a superb time to rupture with about 46 hours compared to 27 hours and 17 hours obtained by the 1% composites and the monolithic alloy respectively. This improvement in the time to rupture in the 1% SPD condition could be related to the improvements in the tensile properties introduced after subjecting to severe plastic deformation. However, the 1% SPD under shot peening exhibits lower time to rupture with about 10 hours compared to 47 hours and 19 hours obtained by the 1% composites and the monolithic alloy. Basically, this decrease in the time to rupture could be caused by the increase in the surface roughness of the 1% SPD after shot peening without a significant increase in the compressive residual stresses, unlike the other conditions. Therefore, the crack formation and propagation capability raise for the 1% SPD with accelerating the failure and reasons the retardation of the time to rupture [111]. The steady-state or minimum creep rate is considered as the second important parameter, mainly when the creep behavior is tested under creep-rupture. When the operating stress is low, rupture may not occur during the life of the part. Thus, for design considerations, the magnitude of the secondary creep rate can be used to evaluate the steady accumulation of strain with time in service [129]. Furthermore, instead of using the slope of the linear steady-state regime, the minimum creep rate can be used, and the secondary creep regime is considered to cover the range of data where the creep rate falls within 10% of the minimum creep rate. The minimum creep rate magnitude is directly affected by the temperature and applied stress. Increasing both the applied stress and temperature will correspond to raise the steady-state creep rate [129]. The minimum creep rate of the up-peened and peened specimens from monolithic alloy and composites with different Al_2O_3 addition is illustrated in Figures 4.39 A, B, and C. The lowest minimum creep rate was obtained by the 1%SPD in the un-peened condition with about 0.0011 1/hr. for the shot peened samples, the minimum creep rate of the 1% condition was at lowest with about 0.0011 1/hr. The improvement in the minimum creep rate occurred by the 1%SPD condition could be attributed to the increase in the tensile properties introduced by the plastic deformation after cold working. This plastic deformation contributes to increasing the dislocation density, and therefore hinder the recovery and recrystallization processes resulting in a prolonged creep life [128].

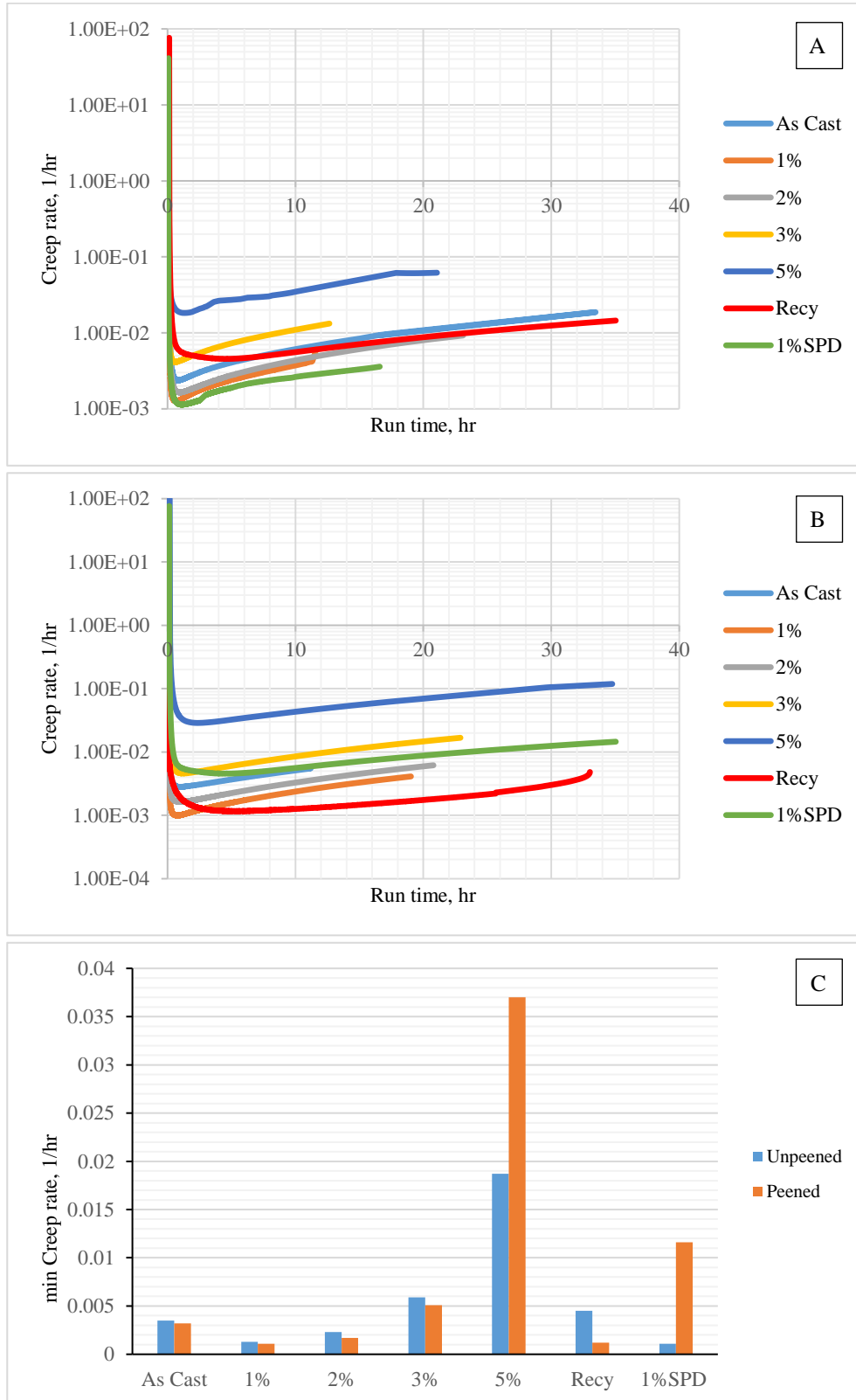


Figure 4-39: The minimum creep rate vs the run time; A. un-peened samples, B. shot peened samples and C. comparison of the minimum creep rate magnitude between peened and un-peened specimens

The enhancements in the creep behavior of the 1% Al₂O₃ composites could be cleared in accordance with the dislocation creep, through reducing the dislocation mobility after the addition of the nanoparticles to the Al6061 matrix. Moreover, the introduction of the nanoparticles might slightly increase the melting point of the produced composite and attribute to raise the material resistance to the creep deformation by hindering the diffusional flow. Even the Mg₂Si precipitates produced after conducting T4 heat treatment contribute as obstacles to the grain boundary sliding during the creep test. However, the precipitates chains could reduce the creep life as it may secure paths for the cracks [123,129-130]. Considering the creep curves, the creep curve for unreinforced 6061 is shifted towards significantly shorter times, and smaller strains as compared to the composites contain 1, 2% Al₂O₃ and the recycled 1%. The primary regime for the composites tends to last for significantly longer times and higher strains than that of the unreinforced alloy. This behavior can be explained by considering the introduction of high stiffness reinforcements (due to load transfer from matrix to the reinforcements), such as nano-alumina particles. These reinforcements attribute to increase the creep resistance compared to the monolithic alloy [123].

Further, both the activation energy (Q) and stress exponent (n) increase in the case of the AMNCs as the presence of the nanoparticles. According to the threshold stress theory of creep deformation, at high values of Q and n in the presence of the incoherent nanoparticles in the matrix, raise the threshold stress of creep and the creep stress exponent by acting as effective barriers for the dislocations movement. However, the influence of the nanoparticles was not remarkable in the 3% and 5% conditions due to either particles agglomeration in the 3% and 5% conditions or by acting as nucleation sites for brittle sharp-edged Fe-intermetallic in the 5% condition [55-59].

Further creep data which can be obtained from the creep curves are the relaxation modulus and the creep compliance. Figures 4.40 (A and B) and 4.41 (A and B) show the relaxation modulus (E) and the creep compliance of the monolithic alloy and the different nanoparticles reinforced composites. Creep compliance and relaxation are both manifestations of the same molecular mechanisms, and it could be expected that E_{rel} and C_{crp} are related. But the relaxation response moves toward its equilibrium value more quickly than does the creep compliance. The importance of the relaxation modulus and the compliance arises especially in design during a material selection for structural applications. In some biomedical applications, the higher compliance materials are desired to reduce the mechanical shocks transmission to the joints and bones [128].

From Figures, it could be reported that the creep compliance and the relaxation modulus depend on the material creep behavior, i.e. the total plastic deformation against the run time. For the unpeened samples, the 1%SPD composites possess the highest creep compliance and the most extended relaxation modulus adjacent to the higher strain obtained against the run time. Nevertheless, both compliance and relaxation modulus of the same condition were retarded after conducting shot peening.

This decrease in E_{rel} and C_{crp} occurred to 1%SPD composites after introducing shot peening may be resulted from the surface roughness increase without a significant improvement in the

compressive residual stresses und the surface. Therefore, the ability of crack formation raises without a sufficient opposite reaction (compressive residual stresses), which could resist the crack propagation and the creep failure by hindering the dislocation movement and prevent the dislocation relaxation [123,128].

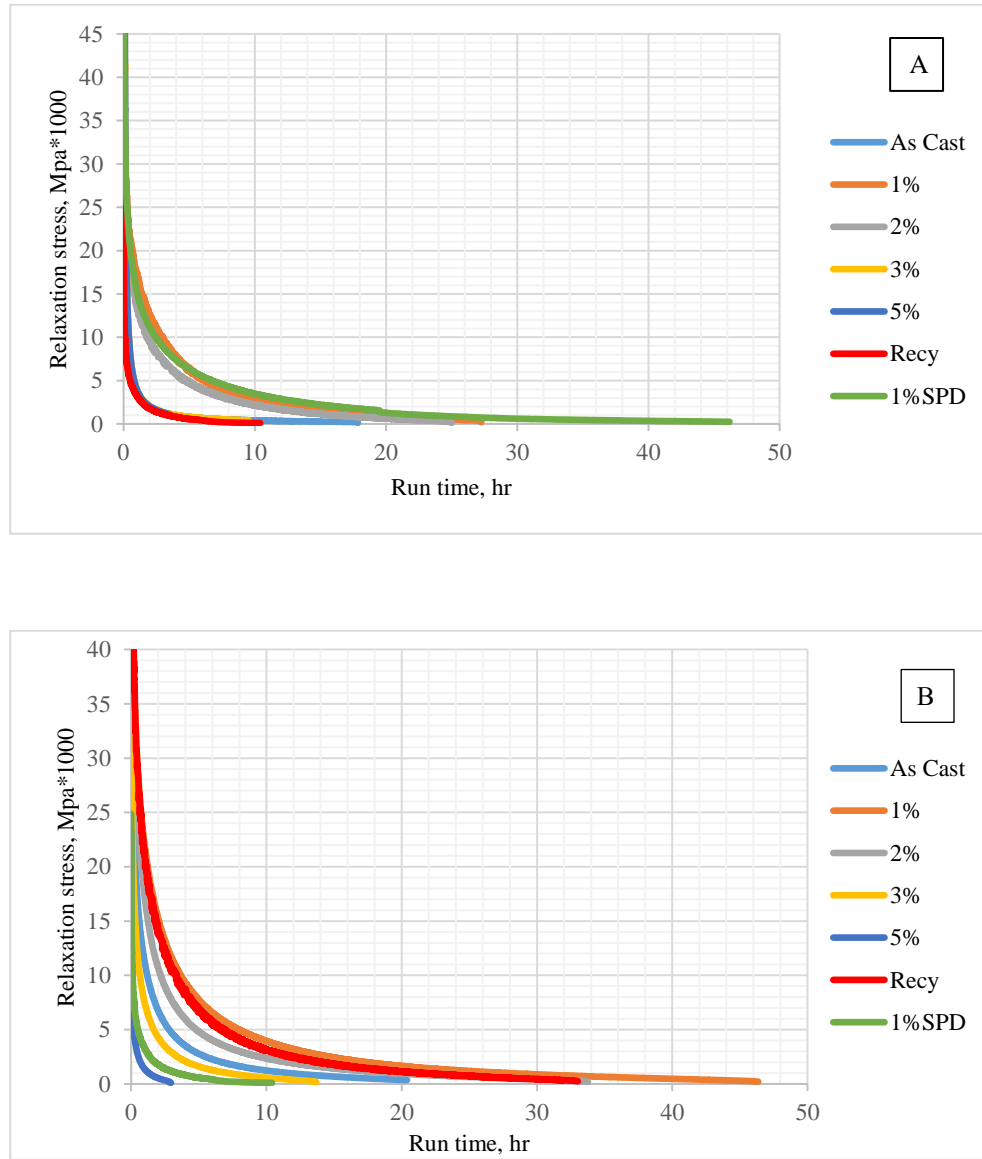


Figure 4-40: The relaxation modulus vs the run time; A. un-peened samples and B. peened samples

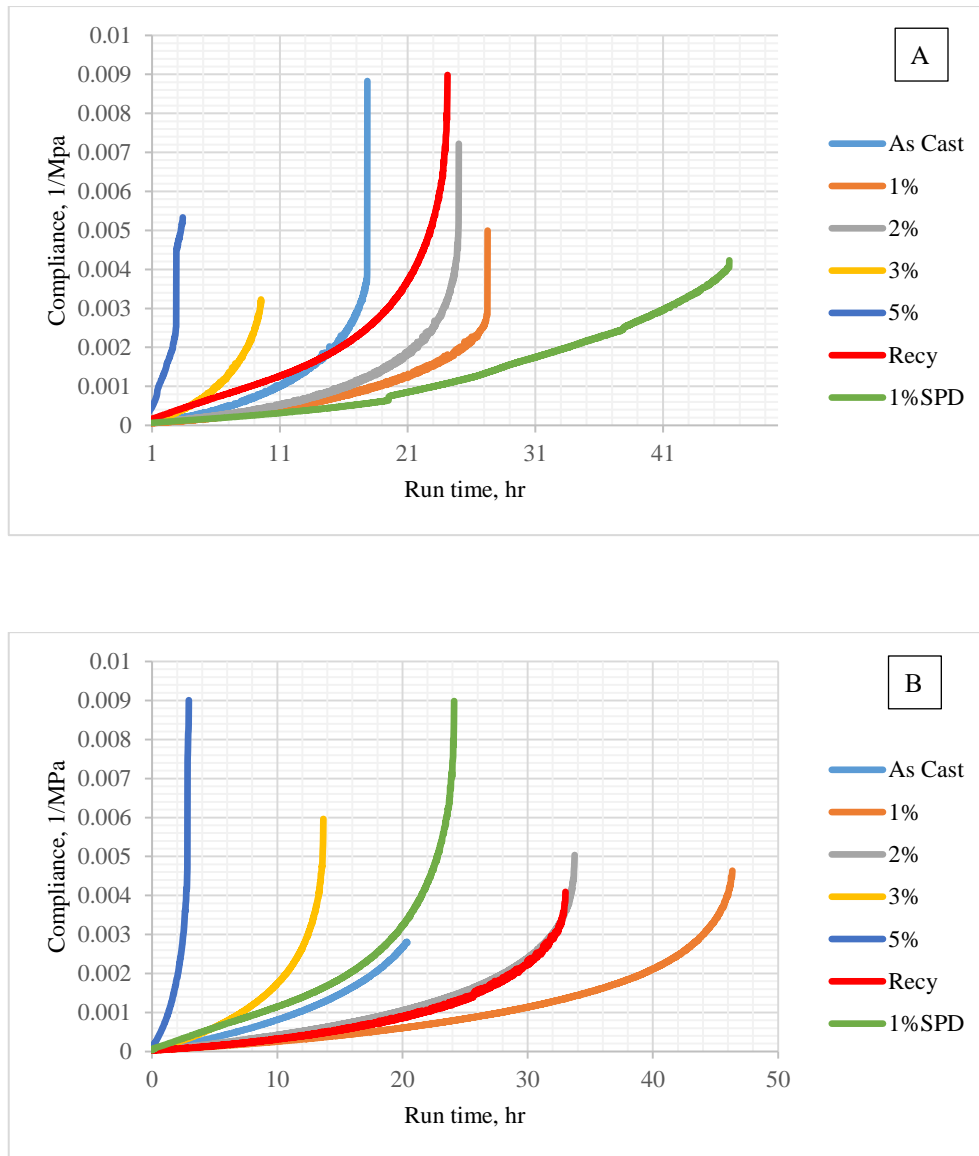


Figure 4-41: The creep compliance vs the run time; A. un-peened samples and B. peened samples

The Ashby-type deformation mechanism map (Figure 4.42) can be considered to understand the dominant creep mechanism, as a simple indication with considering the σ/G and the homologous temperature (T/T_m). For aluminum Al 6061, the shear modulus equals to 26 GPa, and the test stress was 40 MPa, where the test temperature was 300°C, and the melting point of Al6061 is 652°C. Validating these values on the map, it was found that the dominant creep mechanism in the conditions of the experiments was the dislocation creep. According to dislocation creep mechanism, creep occurs through dislocation movement among a specific slip plane by slipping (dislocation glide). The bonds between the atoms should be broken during the creep deformation to enable the dislocation motion. At low-stresses, the creep rate decreases, and the deformation is controlled by the dislocation climb rate over obstacles through vacancy diffusion. During the dislocation climb, dislocations may be pinned by various obstacles such as intermetallic

inclusions or oxide particles (nano-alumina particles) and the material consumes more time until rupture [131].

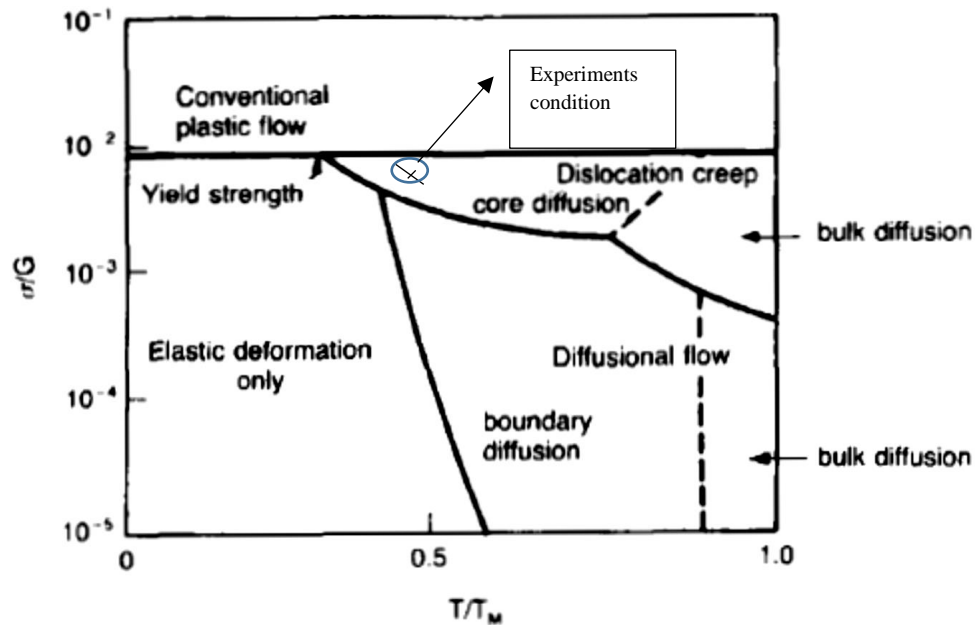


Figure 4-42: Deformation mechanisms at different stresses and temperatures [131]

Considering the dislocation creep mechanism, the creep life is controlled by either higher dislocation density produced by the excessive plastic deformation (which is the case in the unpeened 1%SPD) or by the presence of the nano-reinforcement (which resist the dislocation movement and retard the dislocation climb). The improvement in the creep behavior of the peened 1% could also be explained by the higher dislocation density formed under the surface after performing shot peening. Contrarily, the creep behavior was negatively affected by the higher surface roughness in the peened 1%SPD in the absence of a further increase in the dislocation density after shot peening. For the other composites, the agglomeration accompanied with the nanoparticles additions is attributed to the declination of the creep life due to the nonhomogeneous distribution of the particles, which act as barriers to the dislocation movement and favor the creep failure [123,130-131].

The significant effect of the shot peening on extending the creep life not only of the composites reinforced with alumina nanoparticles but also of the monolithic alloy was a suitable reason to study the creep behavior of the 1% composite after subjecting to different shot medium and Almen intensities. Figure 4.43 illustrates the % total plastic deformation of the 1% after conducting shot peening using two types of shots (SCCW and ASR) and two different Almen intensities of 0.2 and 0.23 mmA compared to the un-peened specimen. It is clear that shot peening has a remarkable effect on determining the creep life of the material, as using shot peening with inappropriate parameters leads to a dramatic decrease in the creep life. The highest creep life is obtained when the samples were peened by SCCW shot medium and with Almen Intensity of 0.2

mmA (the same Almen intensity which gives the higher fatigue life), where the other shot peening conditions cause creep life declination compared to the un-peened sample. The enhancement occurred after SCCW 0.2 mmA than that of the other peening media may refer to the amount of the compressive residual stresses formed under the surface and the surface roughness change after conducting shot peening [116].

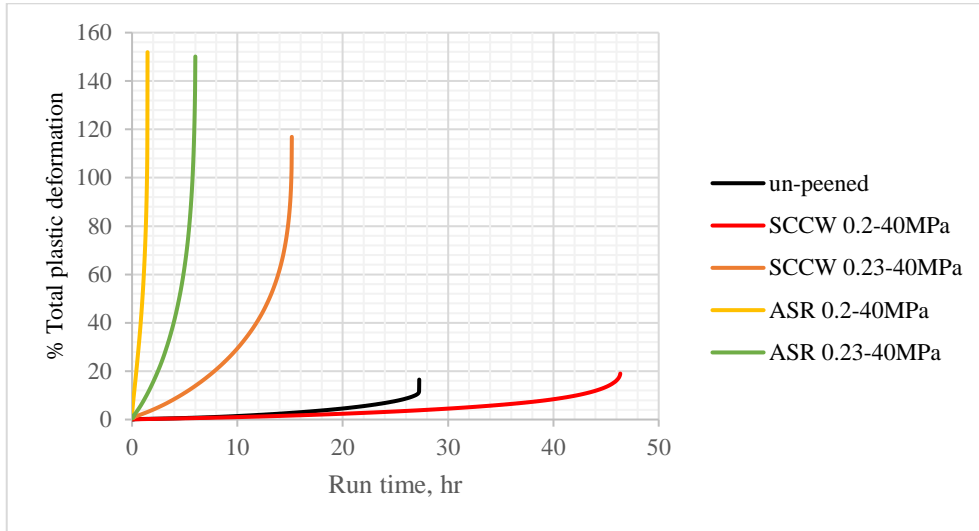


Figure 4-43: % Total plastic deformation of 1% Al₂O₃ subjected to different peening medium and Almen intensities vs the run time under constant stress of 40MPa

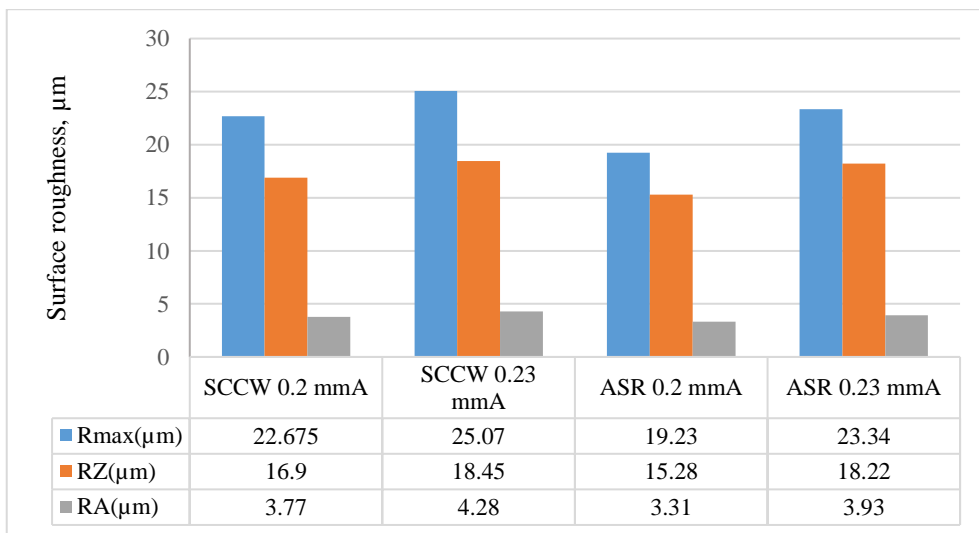


Figure 4-44: Surface roughness of 1% Al₂O₃ subjected to different peening medium and Almen intensities

The surface roughness of the different peening conditions is shown in Figure 4.44, and it is clear that the surface roughness does not severely change between each peening case. This result emphasizes that the creep life is mainly dependent on the amount of the residual stresses formed after shot peening. It was studied before that peening samples with SCCW shot medium gives

higher compressive residual stresses than that created by using the ASR shots, which explains the higher creep life obtained after peening using these shots than the ASR [116]. Comparing the SCCW 0.2 and 0.23 mmA, the Almen intensity of 0.23 mmA increases the surface roughness and does not add significant residual stresses compared to the 0.2 mmA. Therefore, the creep life under SCCW 0.23 mmA decreased compared to the 0.2 mmA and even the un-peened samples.

It is also of a great interest to determine the threshold stress of the composites reinforced by 1 wt.% Al₂O₃, which is defined as a stress level below which no creep occurs at a given temperature. To calculate the threshold stress the creep exponent (n) and creep activation energy should be calculated by considering the general equation relating steady-state creep to temperature and stress proposed by Dieter [132]:

$$\dot{\epsilon}_{ss} = \frac{16 \pi^3 c_j D_v G b}{k T} \left(\frac{\sigma}{G} \right)^n \quad \text{Equation 1}$$

[132]

where ϵ_{ss} is the steady-state creep rate, c_j is the concentration of dislocation jogs, D_v is the bulk or lattice self-diffusion coefficient, G is the shear modulus, b is the burgers vector of the dislocation, k is Boltzmann's constant, T is the absolute temperature, σ is the applied stress, and n is the creep stress exponent. This equation could be simplified to:

$$\dot{\epsilon}_{ss} = A_1 \sigma^n e^{-\left(\frac{Q_{app}}{RT}\right)} \quad \text{Equation 2}$$

[132]

where ϵ'_{ss} is the steady-state creep rate, A_1 is a constant for all stresses and temperatures, σ is the applied stress, n is the creep stress exponent, Q_{app} is the apparent activation energy for creep, R is the universal gas constant, and T is the absolute creep test temperature. The stress exponent can be calculated directly, although a graphical representation is easier to understand. By plotting the logarithm of the minimum creep strain rate on the ordinate, against the logarithm of the applied stress (Figure 4.45), where the slope of these lines is the creep exponent, n [132].

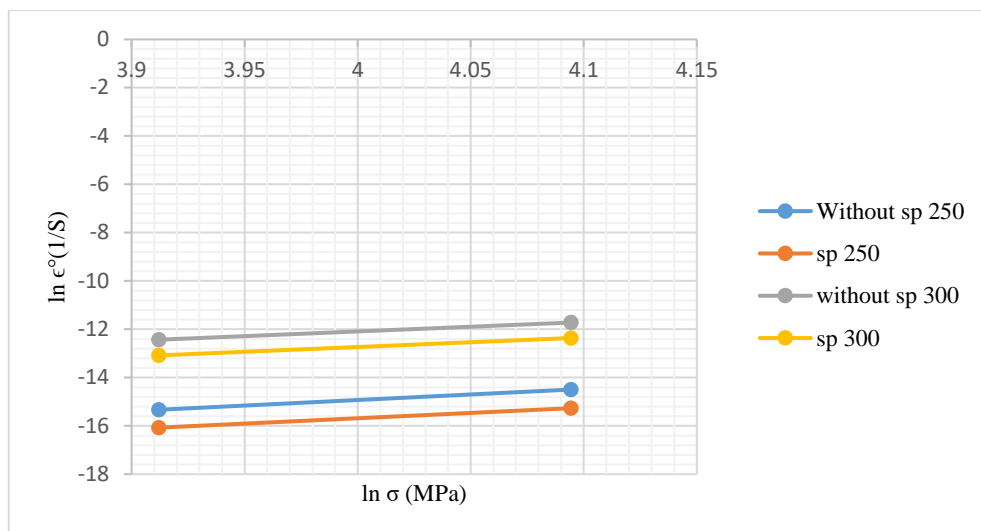


Figure 4-45: Minimum creep rate vs applied stress of un-peened and peened Al6061 reinforced with 1wt.% Al₂O₃

The values of n were calculated to be 4.25 for the un-peened samples and 4.2 for the peened specimens. Using equation 2 and the creep data from Figure 4.45, the Q_{app} could be estimated as 156 and 169 KJ/K.mol for the un-peened and peened 1% Al₂O₃ composites respectively. the values of n and Q (n is about 5 and Q varies from 156 and 169 KJ/K.mol based on the surface treatment) are higher than that reported for unreinforced materials. The Q value when $n=5$ is generally of the order of the value for lattice self-diffusion (which is 143.4 kJ/K.mol in pure Al). [13]. Therefore, it is appropriate to analyze the data by considering the threshold stress, where the creep equation could be modified to:

$$\dot{\epsilon}_{ss} = A (\sigma - \sigma_{th})^{n^{\circ}} e^{-\left(\frac{Q}{RT}\right)} \quad \text{Equation 3} \quad [132]$$

where n° is the true stress exponent and σ_{th} is the threshold stress. The values of σ_{th} could be estimated by plotting $\epsilon^{\circ 1/n}$ vs σ and extrapolating linearly to zero strain rate by considering specific values for n° of order 3, 5 and 8 based on the deformation mechanisms; such as viscous glide high temperature climb. As the apparent values of n are lower than 8, the creep data in this work could not be analyzed using $n^{\circ} = 8$. Thus, the data were plotted using values for n , of 3 and 5. the best analysis was achieved at $n^{\circ} = 3$, where the extrapolating at $n^{\circ} = 5$ gives negative values of σ_{th} . Figure 4.46 shows a plot of $\epsilon^{\circ 1/3}$ vs. σ for peened and un-peened samples of 1% Al₂O₃ at 250°C and 300°C. By extrapolating each line to $\epsilon^{\circ 1/3} = 0$, the values of σ_{th} where estimated to be: 5, 12.5, 18.5 and 26 for un-peened 1% at 300°C, peened 1% at 300°C, un-peened 1% at 250°C and peened 1% at 250°C. It could be reported from these values that shot peening could increase the threshold stress compared to the samples without shot peening. This enhancement in the threshold stress may be attributed to the compressive residual stresses induced by shot peening which could delay the creep deformation and prolong the creep life [6,67].

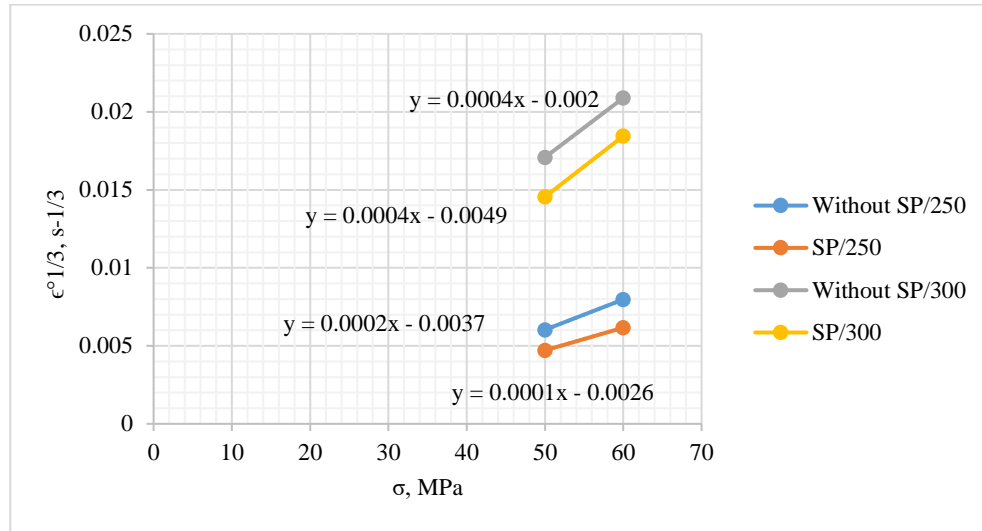


Figure 4-46: Variation of $\epsilon^{1/3}$ with σ on linear axes, showing evidence for the presence of a threshold stress, σ_{th} .

The true activation energy for creep can be then recalculated by using the value of true $n^{\circ}=3$ and $(\sigma-\sigma_{th})$. The true activation energy for creep was 149 and 161 KJ/K.mol for un-peened and peened 1% Al_2O_3 respectively. It is clear from the analyzed data that the creep of the 1% Al_2O_3 composites takes place under the presence of true stress component, threshold stress and true creep activation energy (149 and 161 KJ/K.mol for un-peened and peened), which may be originated from the addition of the nanoparticles because of the presence of fine incoherent arrays of nanoparticles. Based on these values, the creep mechanism in the 1% Al_2O_3 composites may be viscous glide in the matrix [129-132].

4.3 Wear resistance

Figure 4.47 illustrates the wear resistance based on the weight loss after conducting the pin to disk wear test for 15 minutes under 0.7 bar and a rotating speed of 265 rpm. It could be noticed that some AMNCs exhibit a lower weight loss compared to the unreinforced matrix. The highest wear resistance was obtained by the 1%SPD condition with about 45% improvement than that obtained by the matrix without nanoparticles addition. Furthermore, the 1% condition performs an enhancement about 32% compared to the monolithic alloy. Adversely, composites contain 3 and 5 wt.% Al_2O_3 possess the highest weight loss when compared to the other conditions.

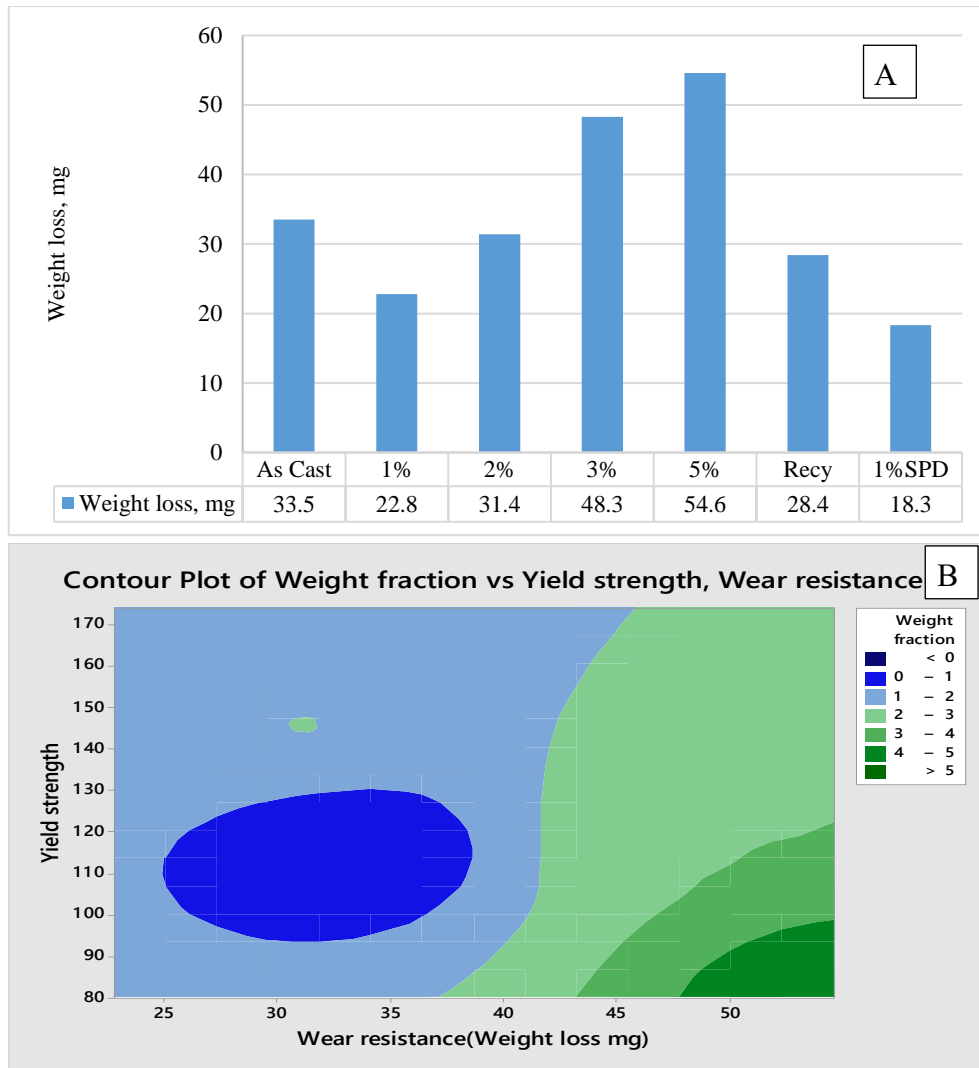


Figure 4-47: Wear rates of the monolithic and different composites based on the weight loss, and B. contour plot of the weight fraction vs yield strength and the wear resistance

It is well known that Al-based metal matrix composites are used as tribological parts in some vehicles because of the better mechanical and tribological properties than conventional aluminum alloys [61-62]. Since the AMNCs exhibit higher mechanical properties than the AMCs, the tribological properties of the AMNCs should be better than that of the AMCs. The wear performance of the AMNCs depends on many variables such as particles dispersion and distribution, the composite hardness and its relative density. Studies reported that lower volume fractions of nano-sized reinforcement are sufficient to achieve better mechanical properties when compared to higher volume fractions needed for micron-sized reinforcements [63-64]. Several investigations were carried out to evaluate the wear resistance of the AMNCs [63-66], and it was observed that hardness and strength of the composites mainly control the wear until a critical velocity and load, below which nanocomposites exhibit excellent wear resistance [15]. The higher hardness and strength the lower wear rate. Increasing the nanoparticles weight fraction also led to an increase in the hardness, and hence improves the wear resistance. However, at

higher weight fractions agglomeration of nanoparticles led to the lowering of relative density (increase in porosity) that reduced the hardness, and thereby increase the wear. These conclusions could explain the higher weight loss obtained by the 3 and 5% conditions and the improvement in the wear rate of the other specimens [15].

4.4 Corrosion behavior

The corrosion rate measured by the potential dynamic method are illustrated in Figure 4.48 and the corrosion rates are summarized in Table 4.2. The figure demonstrates the current density versus the potential of monolithic matrix and different nanocomposites conditions, which can be used to identify the corrosion current density (I_{corr}), corrosion potential (E_{corr}) and the corrosion rate (CR). The maximum CR of 0.44 mpy obtained at 5% samples while the minimum CR 0.2134 mpy is marked at 1%SPD with an improvement approximately 52%.

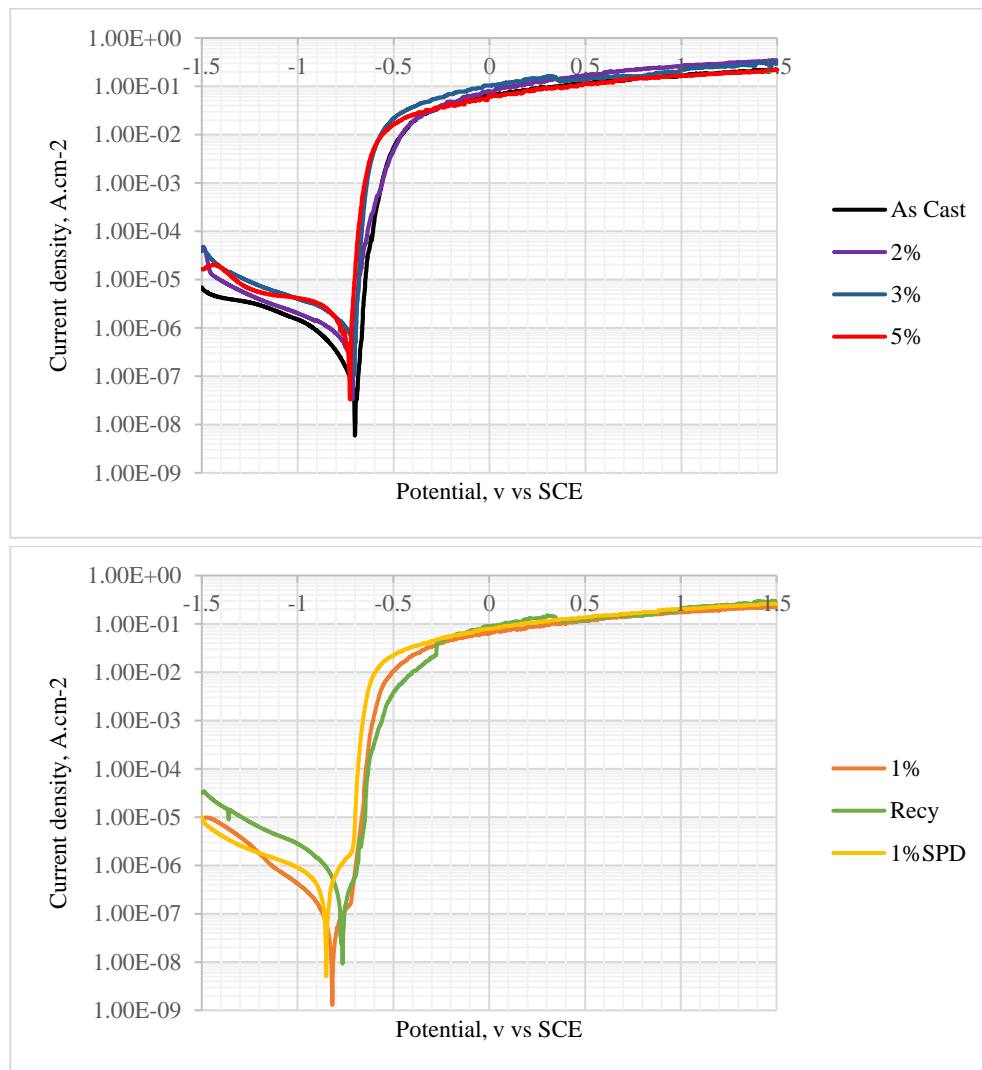


Figure 4-48: Potentiodynamic polarization curves of the as-cast Al6061 matrix and composites

Table 4-2: I_{corr} , E_{corr} and corrosion rate of the as-cast Al6061 matrix and composites

Sample	Current density, $I_{\text{corr}}(\mu\text{A}\cdot\text{cm}^{-2})$	Potential, $E_{\text{corr}}(\text{mV})$	Corrosion rate, mpy
As Cast	0.911	-684	0.394
1%	0.524	-832	0.223
2%	0.687	-778	0.3022
3%	0.947	-766	0.4167
5%	1	-752	0.44
1%SPD	0.485	-854	0.2134
Recy	0.657	-783	0.289

It could be recognized that all composites, other than the 3 and 5%, show an improved corrosion resistance compared to the monolithic alloy. Generally, the tendency of the composite to galvanic corrosion between alumina nanoparticles and aluminum matrix is very low, because of the high resistivity of the alumina particles. Thus, the AMNCs possess excellent corrosion resistance due to a lack of galvanic reaction with the alumina particles. The enhancement in the corrosion resistance can be credited to the grain refinement occurred after nanoparticle addition. The grain boundaries possess high reactivity due to the increased dislocation density found at the grain boundary. Therefore, it may be possible that near E_{corr} , fine grain material could rapidly form an oxide, which is characterized as protective, controlling the anodic reactions, and capable of decreasing I_{corr} [70-73]. Consequently, when the potential is raised, the oxide growth rate also increases forming higher passive current densities and lower corrosion rates. Grain size reduction could also affect the corrosion rate regarding the surface roughness. Decreasing the grain size attributes to lowering the surface roughness of the specimen under the same machining processes. The corrosion rate is dependent on the surface roughness, as corrosion resistance decreases when a rougher surface is considered because of increasing the actual surface area subjected to the reaction with the environment [108].

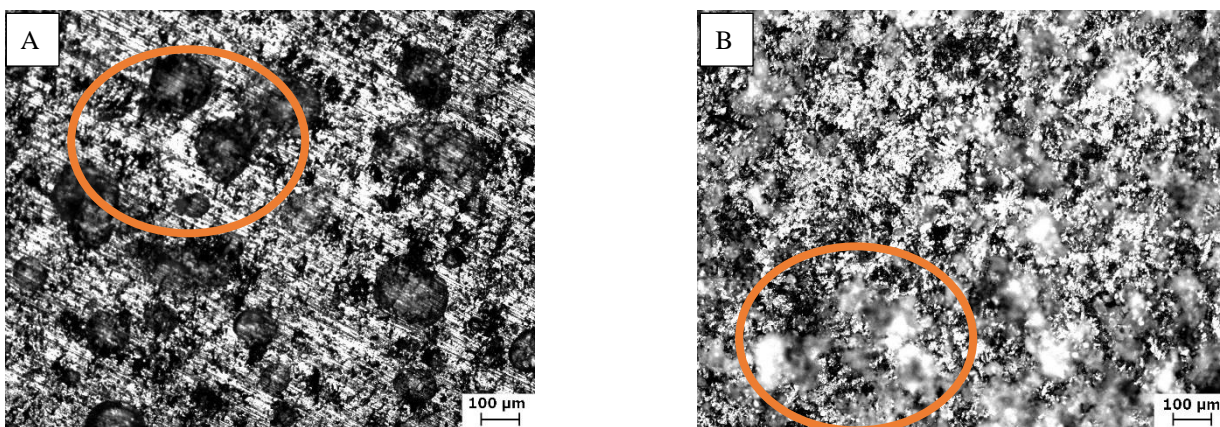


Figure 4-49: Optical micrographs of the surface topography after electrochemical corrosion in 3.5% NaCl solution; A. for the 1% condition and B. for the 5% condition

Increasing the reinforcement weight fraction leads to increase the cathodic areas to localized regions such as impurities, porosities and agglomeration as well, which reduces the corrosion resistance of the composite. Furthermore, the residual stresses in the matrix resulted from the difference in thermal and mechanical properties between the matrix and reinforcement are considered preferred sites for dissolution and pitting [70]. These pits act as initiation site for the galvanic corrosion on the interface between the hard-ceramic particles and soft matrix alloy [71]. Figure 4.49 illustrates the surface topography of the conditions 1% and 5%. It can be observed that the composite reinforced by 1wt.% Al_2O_3 has shallow pits and the pits density is lower and smaller pits than the 5% composites because of the lower CR and cathodic area which is attributed to decrease the pits size and its propagation [133].

4.5 Weldability of the 1wt.% Al_2O_3 Aluminum Matrix Nanocomposites

The optimization of the friction welding parameters of the similar Al 6061 reinforced with 1% Al_2O_3 nanoparticles was conducted with the aid of the design of experiment (DoE) method using Minitab 17. The initial welding parameters impact at the primary characterization are indicated by Table 4.3 based on the variation of: friction pressure (Pr, bar), forging pressure (Ps, bar), friction time (tr, sec), forging time (ts, sec) and rotational speed (rpm).

Table 4-3: Initial weld samples optimization based on the tensile properties

Sample	Pr	tr	Ps	ts	rpm	σ_y	σ_{uts}	elon%	L	L_f
1	1	1	0.5	0.5	10000	80	80	7.6	80	76.26
2	1	0.5	0.5	0.5	10000	100	100	2.8	80	77.86
3	1	0.5	0.5	0.5	14000	99	99	3	80	77.84
4	1	1	0.5	0.5	14000	104	108	2.5	80	77.42
5	0.5	1	2	4	10000	127	131	1.5	80	70.7
6	0.5	1	1	4	10000	139	211	4.6	80	76.97
7	1	1	1	4	10000	125	133	3.5	80	75.35
8	0.5	1	1	4	10000	134	153	4.2	80	76.85
9	1	1	1	4	10000	132	166	3.3	80	74.92
10	1	2	1	4	10000	119	119	1.6	80	73.52
11	1.5	1	1	4	10000	130	134	2.1	80	71.82
12	0.5	2	0.5	2	14000	69	69	1.1	80	78.2
13	1	2	0.5	2	14000	65	80	1	80	77.4
14 (broken during machining)	1.5	2	0.5	2	14000	0	0	0	80	71.65
15	0.5	0.5	0.5	4	14000	80	80	1.6	80	78.8
16	1	0.5	0.5	2	14000	71	72	1.3	80	78.53
17	1	1	0.5	2	14000	73	76	1	80	78.57
18	1	3	0.5	2	14000	65	74	1.1	80	77.36
19	0.5	1	0.5	4	10000	108	128	1	80	78.29
20	1	1	0.5	1	14000	60	60	1.7	80	78.55
21	1	1	0.5	2	14000	74	77	1.5	80	78.19
22	1	1	0.5	3	14000	58	68	1.1	80	78.38
23	1	1	0.5	4	14000	57	76	0.7	80	78.41

As previously described in the experimental section, two approaches were used by the Minitab 17 program; the factorial and Taguchi design. At the beginning of the experiments, trial runs were performed (samples of numbers 1 to 23 on the factorial design method) by changing one of the process variables and keeping the others constant. Therefore, all friction welding parameters have been varied to identify the effective variation range of the parameters on the material response.

The objective of the optimization is to achieve a maximum tensile strength through the statistical analysis by introducing an optimal combination of the processing parameters. The estimated effects, analysis of variance (ANOVA), normal probability plots, and main effects plots were used to analyze and interpret the results. Through these runs, the significant factors were determined with proposed values of the variables.

For the factorial design approach, factorial design five parameters variables (rotational speed, friction pressure, forging pressure, forging time and friction time) and the response was set to maximize the ultimate tensile strength. The initial data from the pre-optimization experiments were used to define the factorial design with considering the minimum and maximum values of the parameters to be automatically detected. Then, the model analyzed the significant effect of each parameter using a normal probability plot of standardized effect at 5% significance level for the ultimate tensile strength of the weld joints (UTS) with a random order to minimize the unexpected variability of the response. The program underwent several runs at which the response optimizer (which is introduced by the software through searching for a combination of parameters that simultaneously satisfy the ultimate goals and limits placed on the response and each of the parameters) parameters in each run. The variables given by the response optimizer were welded, and their tensile properties were identified. Furthermore, the new samples obtained from the response optimizer were re-entered in the design as a new sample, the analysis was repeated until a high ultimate tensile strength value was reached with a fracture found outside the welding line. The data obtained from the design analysis illustrates that the forging pressure (Ps) and the interaction between the (Pr and ts) were the most significant parameter which affect the ultimate tensile strength of the friction welded AMNCs containing 1% Al₂O₃ (Figure 4.50).

Table 4-4: The DoE matrix and corresponding results of the full factorial design

Sample	Ps	ts	Pr	tr	rpm	σ _{uts}	StdOrder	RunOrder	Blocks	CenterPt
1	0.5	0.5	1.0	1.0	10000	80	1	1	1	1
2	0.5	0.5	1.0	0.5	10000	100	2	2	1	1
3	0.5	0.5	1.0	0.5	14000	99	3	3	1	1
4	0.5	0.5	1.0	1.0	14000	108	4	4	1	1
5	2.0	4.0	0.5	1.0	10000	131	5	5	1	1
6	1.0	4.0	0.5	1.0	10000	211	6	6	1	1
7	1.0	4.0	1.0	1.0	10000	133	7	7	1	1

8	1.0	4.0	0.5	1.0	10000	153	8	8	1	1
9	1.0	4.0	1.0	1.0	10000	166	9	9	1	1
10	1.0	4.0	1.0	2.0	10000	119	10	10	1	1
11	1.0	4.0	1.5	1.0	10000	134	11	11	1	1
12	0.5	2.0	0.5	2.0	14000	69	12	12	1	1
13	0.5	2.0	1.0	2.0	14000	80	13	13	1	1
14	0.5	2.0	1.5	2.0	14000	0	14	14	1	1
15	0.5	4.0	0.5	0.5	14000	80	15	15	1	1
16	0.5	2.0	1.0	0.5	14000	72	16	16	1	1
17	0.5	2.0	1.0	1.0	14000	76	17	17	1	1
18	0.5	2.0	1.0	3.0	14000	74	18	18	1	1
19	0.5	4.0	0.5	1.0	10000	128	19	19	1	1
20	0.5	1.0	1.0	1.0	14000	60	20	20	1	1
21	0.5	2.0	1.0	1.0	14000	77	21	21	1	1
22	0.5	3.0	1.0	1.0	14000	68	22	22	1	1
23	0.5	4.0	1.0	1.0	14000	76	23	23	1	1
24	2.0	0.5	1.5	3.0	14000	168	24	24	1	1
25	1.0	2.0	1.0	1.0	14000	139	25	25	1	1
26	2.0	2.0	1.0	1.0	14000	195	26	26	1	1
27	1.0	2.0	1.0	1.0	12000	106	27	27	1	1
28	1.0	2.0	1.0	1.0	10000	149	28	28	1	1
29	1.0	2.0	1.0	1.0	8000	126	29	29	1	1
30	2.0	0.5	1.5	0.5	10000	179	30	30	1	1
31	2.0	2.0	1.0	1.0	12000	214	31	31	1	1
32	2.0	2.0	1.0	1.0	10000	225	32	32	1	1
33	2.0	2.0	1.0	1.0	8000	223	33	33	1	1
34	2.0	4.0	1.5	3.0	14000	186	34	34	1	1

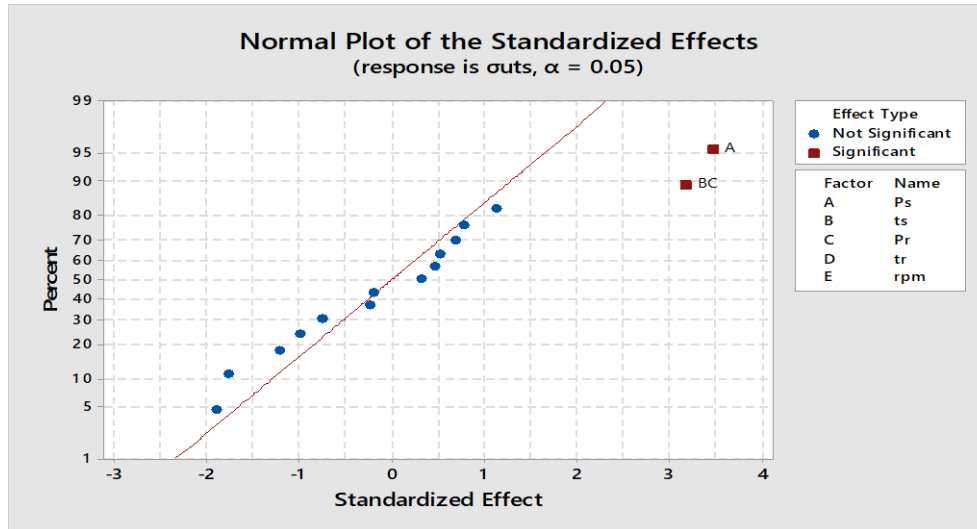


Figure 4-50: Normal probability plot of standardized effects for the ultimate tensile strength

Table 4.5 illustrates the analysis of variance (ANOVA) of the regression model for the ultimate tensile strength of the welded AMNCs.

Table 4-5: ANOVA of the regression model

Source	DF	Adj SS	Adj MS	F-Value	P-Value
Model	15	88130.3	5875.36	10.21	0.000
Linear	5	32964.4	6592.89	11.46	0.000
Ps	1	6916.8	6916.75	12.02	0.003
ts	1	33.6	33.58	0.06	0.812
Pr	1	859.9	859.92	1.49	0.237
tr	1	2054.1	2054.09	3.57	0.075
rpm	1	24.5	24.54	0.04	0.839
2-Way Interactions	10	12390.2	1239.02	2.15	0.075
Ps*ts	1	564.4	564.40	0.98	0.335
Ps*Pr	1	355.3	355.33	0.62	0.442
Ps*tr	1	320.1	320.11	0.56	0.465
Ps*rpm	1	57.4	57.41	0.10	0.756
ts*Pr	1	5816.3	5816.35	10.11	0.005
ts*tr	1	122.1	122.05	0.21	0.651
ts*rpm	1	1809.9	1809.90	3.15	0.093
Pr*tr	1	722.1	722.11	1.26	0.277
Pr*rpm	1	267.6	267.61	0.47	0.504
tr*rpm	1	149.5	149.50	0.26	0.616
Error	18	10355.4	575.30		
Lack-of-Fit	15	8128.4	541.89	0.73	0.710
Pure Error	3	2227.0	742.33		
Total	33	98485.8			

The linear variable term of the forging pressure and the interaction between the friction pressure and the forging time in the model show P values less than 0.05, thus are statistically significant. The high P value ($P > 0.05$) of lack-of-fit indicates that the model is adequate for predicting the ultimate tensile strength of the welded AMNCs. Figure 4.51 shows the adequacy of model indicated by the normal probability plot of standardized residuals for the tensile strength of the welded AMNCs.

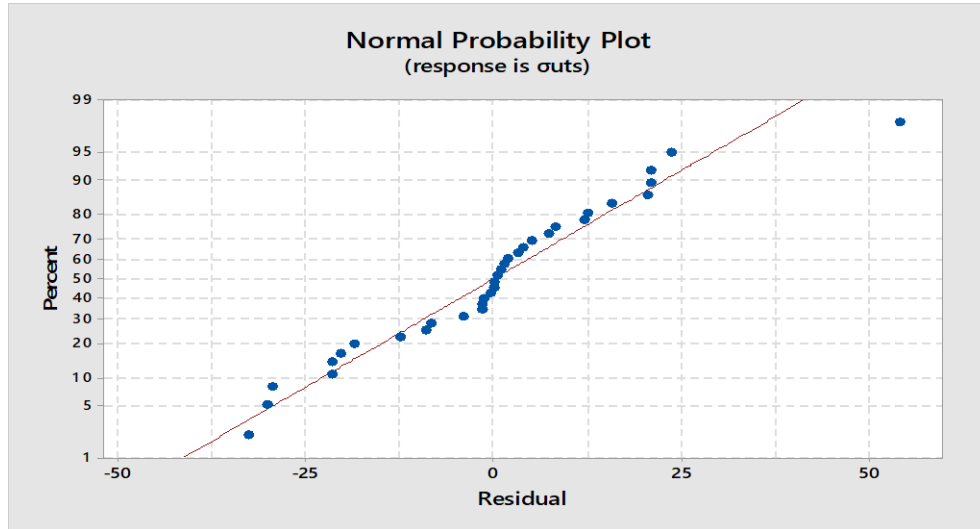


Figure 4-51: Normal probability plot of standardized residuals for weld strength

It could be observed that all points cluster along the straight line, which clarifies that the implied regression assumptions are satisfied [134-135]. The estimated coefficients (Coef) of each variable term in a regression model for the tensile strength of the welded AMNCs are indicated by Table 4.6. The values are estimated with the corresponding standard deviation (SEcoef), t-statistics (t-Stat) and probability (P) values determined at 5% significance level. Variable terms with $P < 0.05$ (Ps, tr, ts*rpm and Pr*ts) are considered statistically significant. The regression equation could be expressed as:

$\sigma_{uts} = 617 + 57 Ps + 10.9 ts - 574 Pr - 159 tr - 0.0150 rpm - 24.1 Ps*ts + 77.9 Ps*Pr - 20.5 Ps*tr + 0.00137 Ps*rpm + 65.6 ts*Pr + 7.6 ts*tr - 0.00557 ts*rpm + 65.6 Pr*tr + 0.0145 Pr*rpm + 0.0055 tr*rpm$, and it is given in the terms of the linear and interactions between the variables on the tensile of the welded AMNCs, where the positive coefficients of variable indicate their synergistic effect, whereas negative sign indicates antagonistic effect. The contour plots and the main effects of welding variables on the ultimate tensile strength of the AMNCs are indicated by Figure 4.52a and b.

Table 4-6: The estimated coefficients of the regression model

Term	Effect	Coef	SE Coef	T-Value	P-Value	VIF
Constant		119.7	17.8	6.71	0.000	
Ps	89.6	44.8	12.9	3.47	0.003	6.19
ts	-5.7	-2.9	11.8	-0.24	0.812	4.32
Pr	-54.6	-27.3	22.3	-1.22	0.237	9.53
tr	-103.2	-51.6	27.3	-1.89	0.075	12.93
rpm	-9.8	-4.9	23.6	-0.21	0.839	16.39
Ps*ts	-63.2	-31.6	31.9	-0.99	0.335	22.30
Ps*Pr	58.4	29.2	37.2	0.79	0.442	18.70
Ps*tr	-38.4	-19.2	25.7	-0.75	0.465	13.50
Ps*rpm	6.18	3.09	9.78	0.32	0.756	2.52
ts*Pr	114.9	57.4	18.1	3.18	0.005	4.71
ts*tr	33.1	16.5	35.9	0.46	0.651	22.43
ts*rpm	-58.5	-29.3	16.5	-1.77	0.093	3.73
Pr*tr	82.0	41.0	36.6	1.12	0.277	12.69
Pr*rpm	43.5	21.7	31.9	0.68	0.504	9.86
tr*rpm	41.4	20.7	40.6	0.51	0.616	29.79

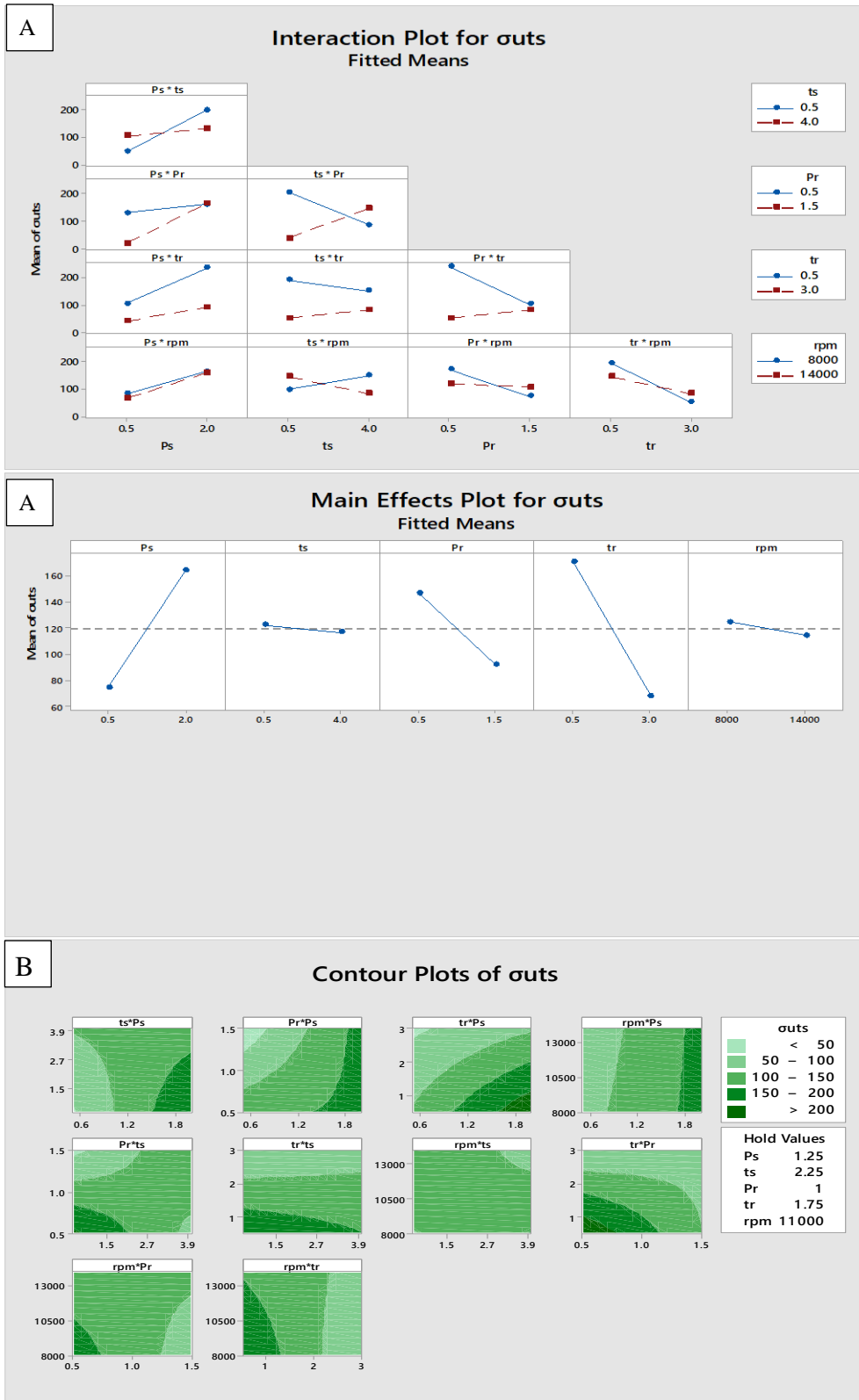


Figure 4-52: A. The main effect of the linear and interactions between the welding parameters on the ultimate tensile strength, B. Contour plots of the ultimate tensile strength

Following the Taguchi approach, the same variables were selected in the optimization using the friction pressure, friction time, forging pressure, forging time and the rotational corresponding a L8 Taguchi model design. The Taguchi method was conducted to the process variables with two levels of variation (Table 4.7). The signal to noise ratio (S/N) for each level of process parameters were identified based on the S/N analysis considering the higher S/N ration is corresponds to a better weld joint ultimate tensile strength. To assess the significance of the variables, a detailed ANOVA framework was also conducted.

Table 4-7:Taguchi parameters and design levels

Parameter	Unit	Symbol	Level 1	Level 2
Friction pressure	bar	Pr	1	2
Friction time	sec	tr	0.5	2
Forging pressure	bar	Ps	1	2
Forging time	sec	ts	0.5	2
Rotational speed	rpm	rpm	9000	11000

The first run of the Taguchi design analysis gives, based on the variables and their levels, eight samples. The suggested samples by the software were welded and the tensile data were entered. At each run, the software suggested a new set of parameters based on the S/N ratio (the higher is better). The sample with the given parameters was then welded, tested and data reentered to the software. This step was repeated until the fracture was moved away from the weld zone and the welded joint tensile strength reached a propriate value, which could be compared with the base material tensile strength [136-137]. The Taguchi experimental results are summarized in Table 4.8 and indicated by Figure 4.53.

Table 4-8:Taguchi experimental suggestions based on the process variables and levels

Pr	tr	Ps	ts	rpm	σ _{uts}
1	0.5	1	0.5	9000	113
1	0.5	1	2.0	11000	128
1	2.0	2	0.5	9000	230
1	2.0	2	2.0	11000	219
2	0.5	2	0.5	11000	217
2	0.5	2	2.0	9000	211
2	2.0	1	0.5	11000	132

2	2.0	1	2.0	9000	145
2	2.0	2	2.0	11000	155
2	2.0	2	2.0	9000	186
2	2.0	2	0.5	11000	207

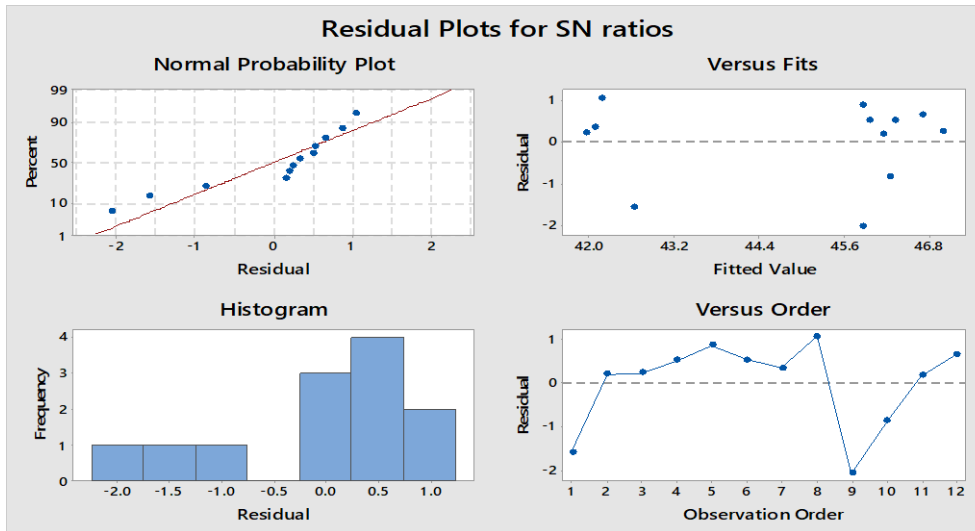
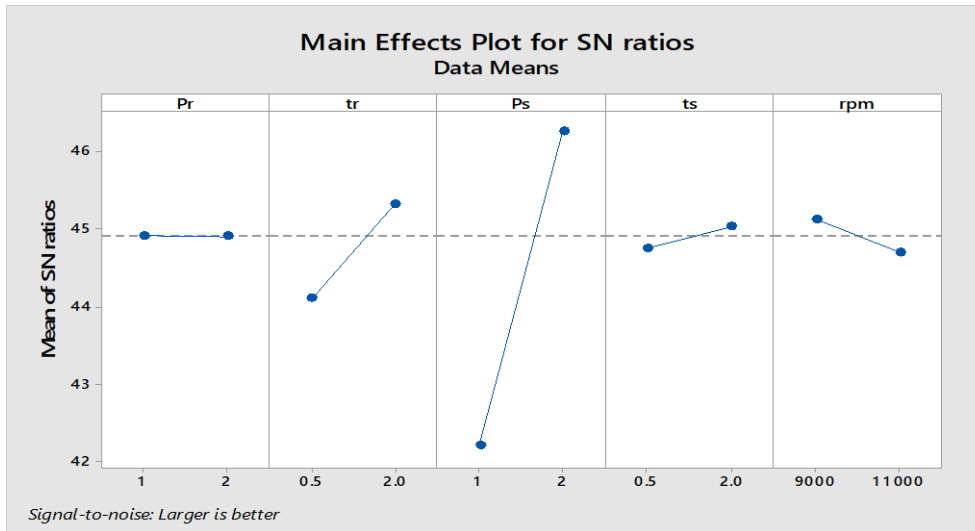


Figure 4-53: The effect of parameters Ps,ts, Pr, tr and rpm on the tensile strength of the welded joint and S/N ratio of the responses

From Figure 4.53 and based on the S/N ration the higher is better, the highest tensile strength was achieved when Pr, tr, Ps, ts and rpm were chosen according to level 1,2,2,2 and 1 respectively. i. e the values corresponding 1,2,2,2 and 9000. This sample was given the number 12. To identify the most effective process parameters which influence the tensile strength of the welded joint, the Analysis of variance (ANOVA) test was conducted (Table 4.9), where the

precision of a parameter estimation is based on the degree of freedom (DOF). The degree of freedom is the number of experiments minus the number of additional parameters estimated for that calculation [136-137].

The results of ANOVA illustrate that Ps, tr, rpm, ts and Pr are the process parameters order that have significant contribution on the tensile strength of the welded joint.

Table 4-9: Analysis of Variance for SN ratios and Response table for signal to noise ratios

Analysis of Variance for SN ratios

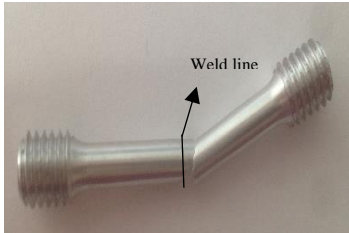
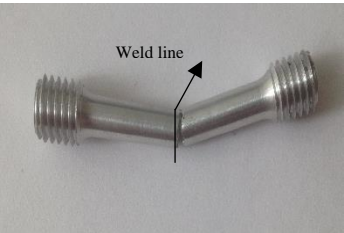
Source	DF	Seq SS	Adj SS	Adj MS	F	P
Pr	1	0.0003	0.5564	0.5564	0.32	0.592
tr	1	3.9885	0.2033	0.2033	0.12	0.744
Ps	1	40.6714	40.7748	40.7748	23.42	0.003
ts	1	0.1565	0.2500	0.2500	0.14	0.718
rpm	1	0.4454	0.4454	0.4454	0.26	0.631
Residual Error	6	10.4473	10.4473	1.7412		
Total	11	55.7093				

Response Table for Signal to Noise Ratios (Larger is better)

Level	Pr	tr	Ps	ts	rpm
1	44.92	44.11	42.21	44.75	45.12
2	44.91	45.32	46.27	45.03	44.70
Delta	0.01	1.21	4.05	0.28	0.42
Rank	5	2	1	4	3

Flowing the two design of experiment approaches, one sample from each approach was selected. The sample introduced by the factorial design had the number 34 and from Taguchi was numbered 12 with tensile properties indicated in Table 4.10.

Table 4-10: Tensile properties of the samples from factorial design and Taguchi

Sample	σ_{uts}	σ_y	ΔL	% elongation
12 	233	130	7.7	12.8
32 	225	185	6.1	2.1

To compare the weld zone proprieties of the different samples introduced by the two approaches, the microstructure was examined by optical and scanning electron microscope and the microhardness of each sample weld zone was measured. Furthermore, the elements along the weld zone were analyzed using the EDX to accentuate the role of the nanoparticles on the interface between the two welding parts.

The microstructure of the samples recommended by using Taguchi and factorial design approaches are indicated by Figure 4.54. The typical gradual microstructure change could be observed from the weld interface towards the parent materials. The weld zone is characterized by a fine grain induced by the dynamic recrystallisation because of the high temperature, rapid cooling and strain produced at the weld interface. The weld joint thickness varies from 0.34 mm to 0.77 mm for sample 12 and 32 respectively.

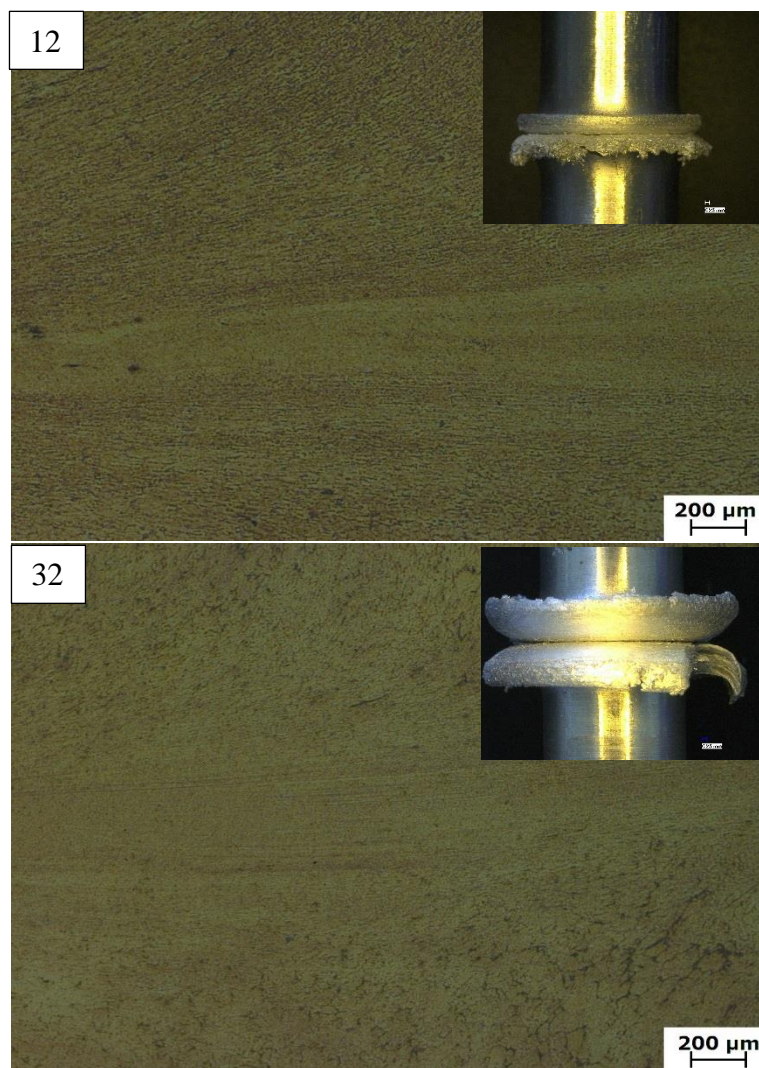


Figure 4-54: Optical micrographs of the weld zone at magnification 50X of samples 12 and 32 (sub-micrographs are the flash shape of each sample)

This weld interface contains a fine- recrystallized microstructure of highly deformed grains due to the high temperature induced during the welding process. Increasing the thickness of the weld interface favors the inhomogeneity between the welded parts with expanding the region of higher residual stresses and hardness. Consequently, the flash width and the material loss increase. It was also observed that samples show small unbonded regions (Figure 4.55) at the corners of the weld interface. These regions had a length of 0.24 and 1.27 mm for sample 12 and 32 respectively. The unbonded interface is attributed to poor mechanical properties and low burn-off length. Moreover, the conducted heat from the flash and interface to the corners is responsible for the softening and plastic deformation occurred at these zones by merging the corner material with the rest of the interface, forming a bond and retarding the weld joint mechanical properties [138].

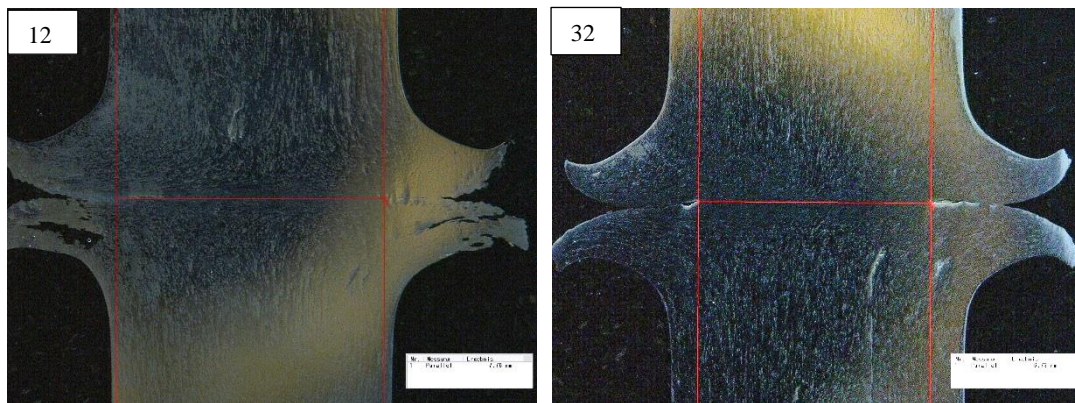


Figure 4-55: Unbonded regions at corner of the weld interface of samples 12 and 32

The variation of the elements along the weld joint interface over a length of 60 μ m was determined by using the EDX linear scanning function and illustrated in Figure 4.56. It could be detected that there is not a significant change in the concentration of the element over the weld interface between both samples. The microhardness measurement is also useful criteria to identify the strengthening and softening processes by the microstructure development in the weld zone. The microhardness profiles obtained from samples 12 and 32 are presented in Figure 4.57. The average of three measurements was taken at each point across the weld line. The average hardness of the base metal was about 85 HV0.05 for both samples and increase to reach 105 HV0.05 at the weld interface for sample 12 and 102 HV0.05 for sample 32. This increase in the weld joint interface hardness may be attributed to the grain refinement caused by dynamic recrystallization in the central weld zone. Generally, both samples microhardness profile behavior could be the same with a slight difference between each condition. Finally, the friction welding of the Al6061 composites contains 1 wt.% Al₂O₃ was relatively successful using the optimum variables given by the software according to factorial design and Taguchi approaches. However, the number of experiments to reach these optimum parameters was significantly reduced following the Taguchi method, which means more trials, costs, and efforts can be avoided by considering this method [29,134-138].

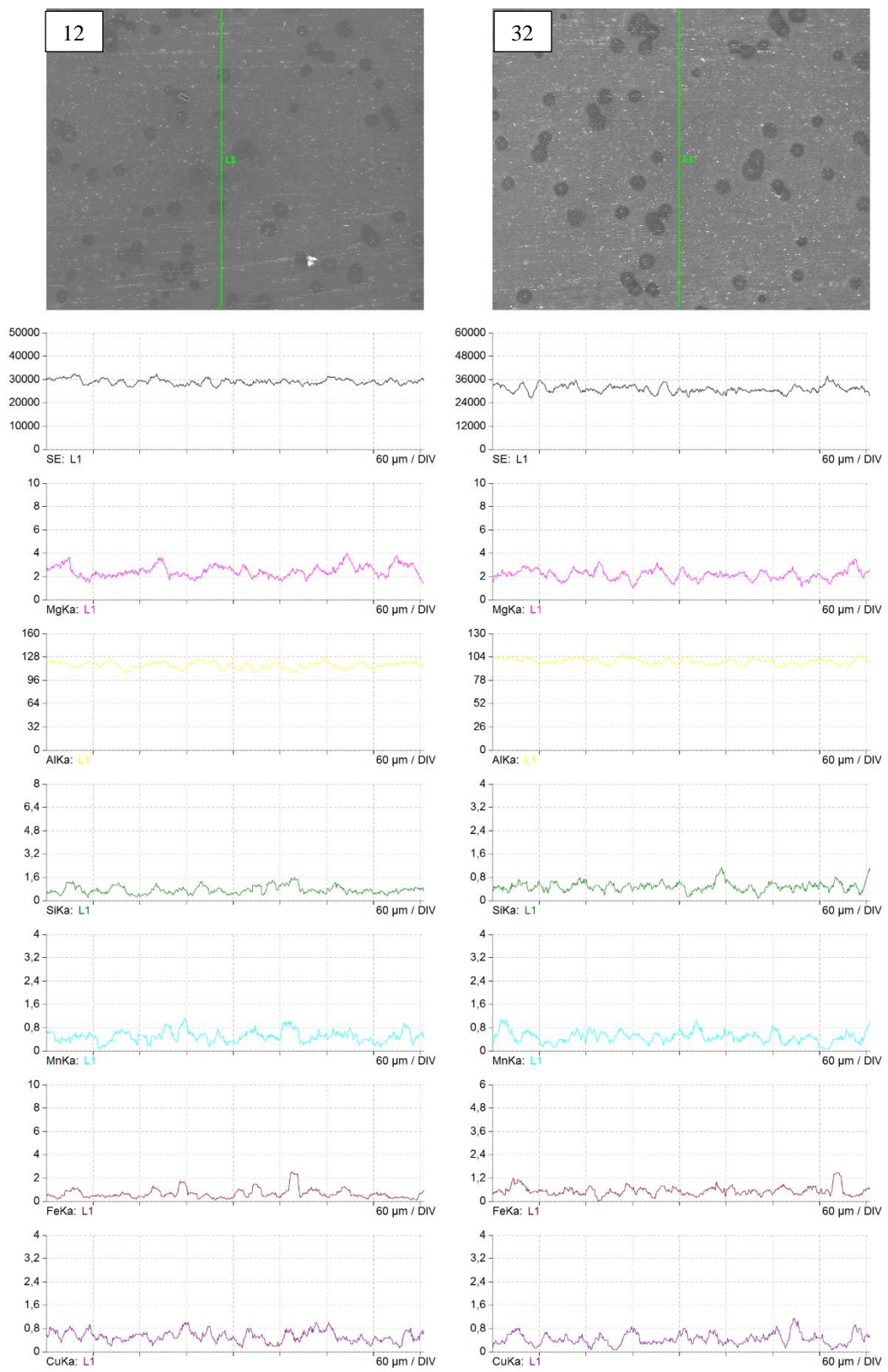


Figure 4-56: The EDX linear scanning of samples 12 and 32 over 60μm of the weld interface

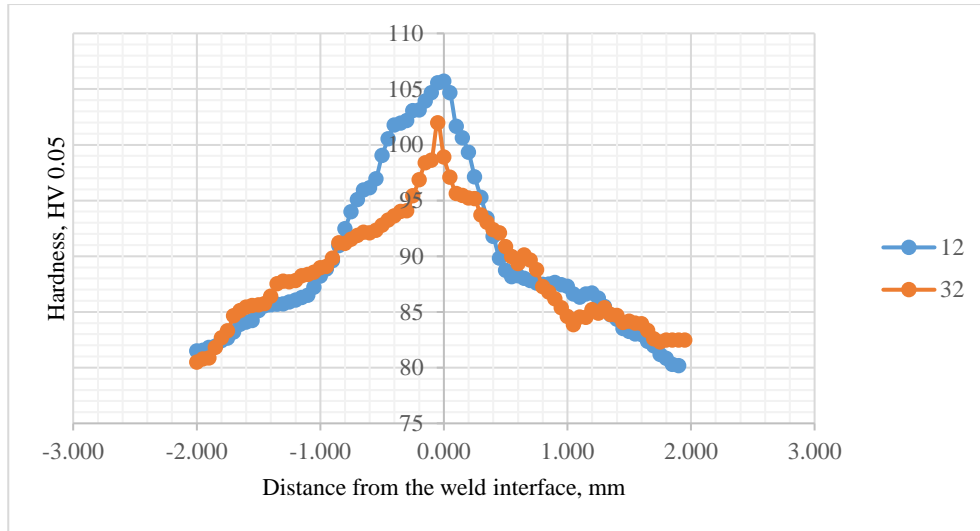


Figure 4-57: The microhardness distributions across the weld line of samples 12 and 32

4.6 Analytical model of the strength contributors in the AMNCs

The addition of nanoparticles during this work was also associated with the modification of the cast structures, which originated the question is the nanoparticles a reinforcement or a refining role? The nature of the AMNCs is fine structured composites, and thus, it is essential at this stage to understand the active strengthening mechanisms in these materials, as this will be the key to develop new structures.

The following discussion presents an approach for predicting the final yield strength of an aluminum alloy reinforced with alumina nanoparticles based on the strengthening contributions, particle size and volume fraction. The yield strength of a crystalline material based on dislocation mechanisms may be taken as the additive effects of five factors: 1) σ_o = inherent resistance of the lattice to dislocation motion, 2) σ_{ss} for solid solution, σ_{gs} for grain size, σ_{sh} for strain hardening (dislocations) and σ_p is for dispersed phases and/or particles. Thus,

$$\sigma_{ys} = \sigma_o + \Delta\sigma_{ss} + \Delta\sigma_{gs} + \Delta\sigma_{sh} + \Delta\sigma_p$$

Mainly four dominating strengthening mechanisms are known to apply [14]; Load transfer, Hall-Petch Strengthening, Orowan Strengthening and thermal mismatch. The developed formula is based on the following concepts and assumptions.

1. Load bearing strengthening = $\frac{1}{2}Vp\sigma m$; Where Vp is the volume fraction and σm is the matrix yield strength.
2. Hall-Petch (grain refining strengthening) = $ky/\sqrt{\left(\frac{4\alpha dp}{3vp}\right)}$;

Where ky is the strain hardening coefficient, α is a constant and dp is the particle diameter in nm. Assume an average $ky = 1.3$ value for aluminum alloys, $\alpha = 3$.

Then the equation can be simplified to = $500\sqrt{\left(\frac{vp}{dp}\right)}$

3. Orowan's strengthening = $\frac{0.13bG}{dp\left(\left(\sqrt[3]{\frac{1}{2vp}}\right)-1\right)} * \ln\left(\frac{dp}{2b}\right)$, where b is the Burger's vector and G

is the shear modulus in GPa. Assume average values of G = 26900 MPa and b = 0.286 nm. When the volume fraction value is between 0 and 0.01(10%), the term

$\left(\left(\sqrt[3]{\frac{1}{2vp}}\right) - 1\right)$ could have an average of 1.85. **Then the equation could be simplified to:**
 $\frac{500}{dp} * \ln(1.5dp)$

4. Coefficient of thermal expansion (CTE) and elastic modulus (EM) mismatch=

$\sqrt{3} * \beta Gb\left(\sqrt{\frac{12vp\Delta\alpha\Delta T}{(1-vp)bdp}}\right) + (\sqrt{3} * \alpha Gb * \sqrt{\frac{6vp\varepsilon}{bdp}})$, where β is the dislocation strengthening coefficient, $\Delta\alpha$ is the difference in CTE between matrix and particles, ΔT is the temperature change, α is the material specific coefficient and ε is the bulk strain of the composite. Assume **average $\alpha(\text{reinforcement})=10$** and for the aluminium matrix 21 with $\Delta\alpha = 11$, average $\varepsilon = 0.025$, $\beta = 25 * 10^{-5}$, $\alpha = 35 * 10^{-3}$. Then the equation can be simplified to:

$$= (70 * \sqrt{\frac{vp\Delta T}{(1-vp)dp}}) + (350 * \sqrt{\frac{vp}{dp}})$$

When the volume fraction value is between 0 and 0.01(10%), the term (1-vp) could be neglected and the equation (1) is reduced to $(70 * \sqrt{\frac{vp\Delta T}{dp}})$. The final yield strength of a certain composite based on an aluminium matrix and Al₂O₃ nanoparticles reinforcements is shown in equation (2).

$$\sigma f = \sigma m + \frac{1}{2}Vp\sigma m + 500\sqrt{\frac{vp}{dp}} + \left(\frac{500}{dp} * \ln(1.5dp)\right) + (70 * \left(\sqrt{\frac{vp\Delta T}{dp}}\right)) + (350 * \sqrt{\frac{vp}{dp}}) \quad (1)$$

$$\sigma f = (1 + \frac{1}{2}Vp)\sigma m + (850 + 70 * \sqrt{\Delta T})\sqrt{\frac{vp}{dp}} + \left(\frac{500}{dp} * \ln(1.5dp)\right) \quad (2)$$

The equation given above could be considered for nanocomposites produced by ECAP or powder metallurgy having a factor of 1 multiplied by the summation of the different strengthening contributors. Different nanoparticles introduction technique could affect the magnitude of the strengthening contribution. Such factor should be 1/3 for MMNCs produced by stir-casting and could reach 1/2 for those produced by compo or rheo- casting. The equation for stir-casting could be rewritten as:

$$\sigma f = (1 + \frac{1}{6}Vp)\sigma m + (280 + 20 * \sqrt{\Delta T})\sqrt{\frac{vp}{dp}} + \left(\frac{160}{dp} * \ln(1.5dp)\right) \quad (3)$$

, where for compo or rheo- casting could be:

$$\sigma f = (1 + \frac{1}{4}Vp)\sigma m + (425 + 35 * \sqrt{\Delta T})\sqrt{\frac{vp}{dp}} + \left(\frac{250}{dp} * \ln(1.5dp)\right) \quad (4)$$

Figures 4. (58: 60) (modified from [80,43]) present the five strengthening components and the final effect resulting from all five components, according to this work. The figures depict the effect of each strengthening contribution and the total strengthening increment calculated according to Equation (2) for a reinforced Al matrix reinforced by 0-10% nanoparticles. It is interesting to regard that the main strength contributors are the Orowan strengthening and CTE mismatch, mainly at small reinforcement particle diameter ($d_p < 50$ nm). Considering the MMNCs, introducing small fractions of reinforcement particles is used to enhance the matrix strength without diminishing toughness, and other properties (e.g., electrical and thermal conductivity), and thus the strengthening caused by load transfer is expected to be very small compared to the other contributors. The same graph shows that for the system Al/2wt.% Al₂O₃ the proposed model is consistent with experimental data, reported by [80].

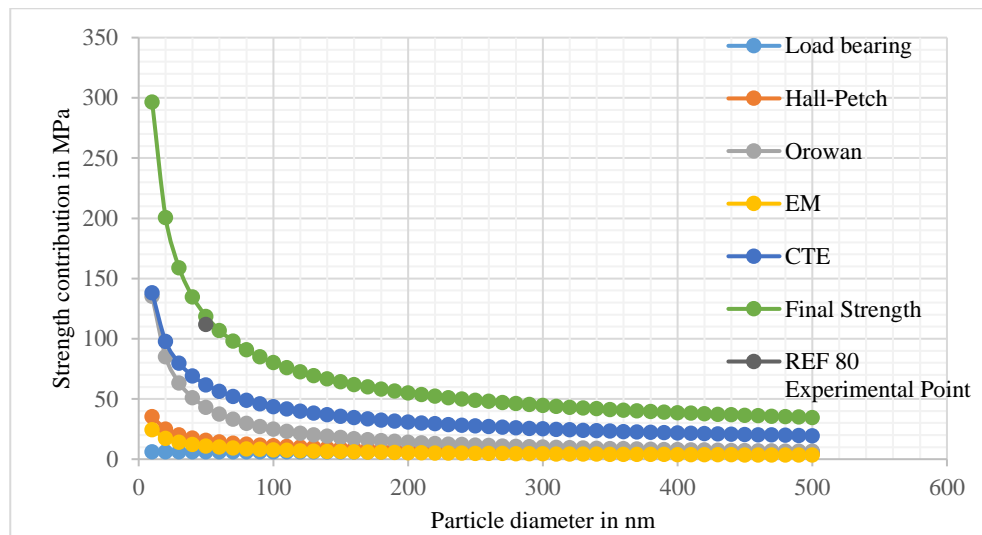


Figure 4-58: Validation of the proposed equation based on the work carried out in [80]

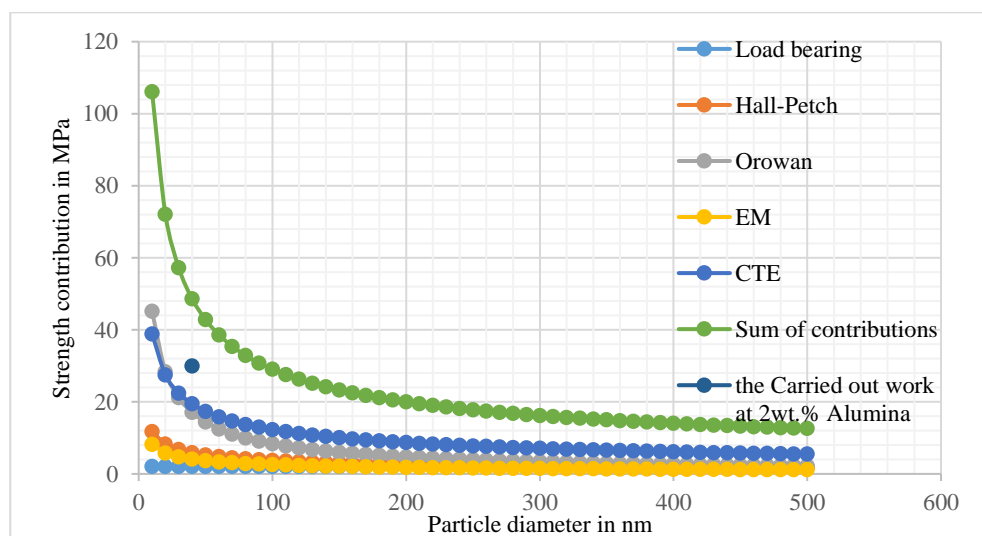


Figure 4-59: Validation of the proposed equation based on the experimental work carried out at 2wt.% Alumina

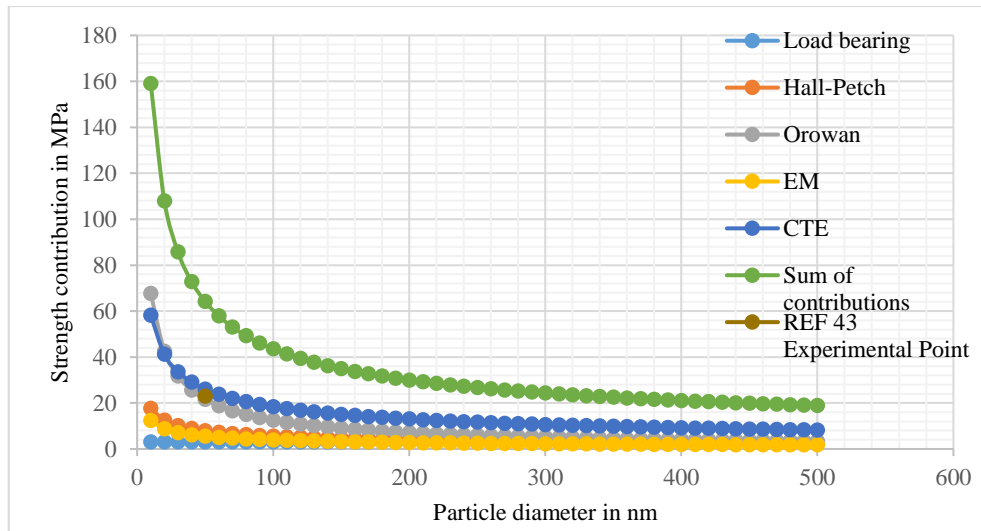


Figure 4-60: Validation of the proposed equation based on the work carried out in [43]

The second approach adopted in this work for predicting the final yield strength of an aluminum alloy reinforced with nanoparticles is presented based on statistical analysis of a series of data obtained from experimental work of presented in [27,73] and others [42-43]. A validation of the equation is made by data carried out at 2wt.% Alumina. The developed formula is based on the following concepts.

- V_f is the weight fraction and is given as 1, 2, 3....
- d_p is the particle diameter in nm.
- ΔT is the difference between the processing and the test temperature.
- σ_m and σ_f are the yield strength of the matrix and the final strength obtained after reinforcement respectively.
- These data are processed using the parameters boundary conditions listed in Table 4.11 and Figure 4.61 below:

Table 4-11: The boundary conditions used for the Minitab variables

vf	dp	ΔT	σ_m
0	40	100	75
10	1000	700	350

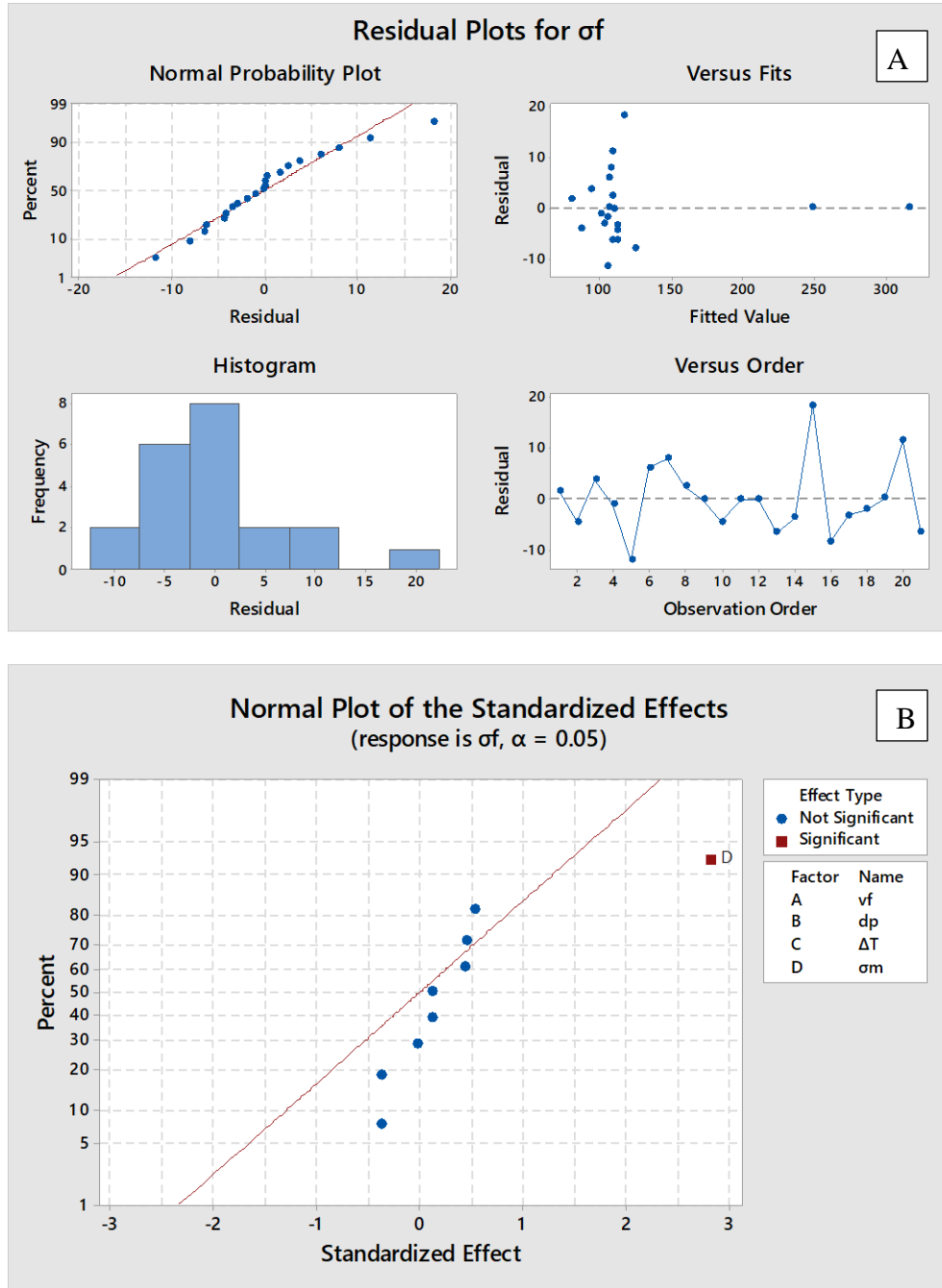


Figure 4-61: Minitab run outputs; a. residual plots for final strength, b. normal plot of the standardized effects at $\alpha=0.5$

The data analysis gives the equation below and indicates that the significant parameter in determining the final strength of an alloy reinforced with nanoparticles is the yield strength of the matrix:

$$\sigma_f = -1353 + 310 vf + 26.4 dp + 2.34 \Delta T + 1.042 \sigma m - 6.3 vf*dp - 0.56 vf*\Delta T + 0.065 vf*\sigma m - 0.0455 dp*\Delta T + 0.0113 vf*dp*\Delta T$$

Validation of the equation using $d_p=40\text{nm}$, $\Delta T=573$, and $V_f=2$, the resultant $\sigma_f = 135.6 \text{ MPa}$, and the experimental value was 146MPa .

From the two approaches it could be expected that the main strengthening mechanisms acting for MMNCs (contributing to the strengthening of the matrix) results from the contributions by Orowan strengthening and CTE and EM mismatch and depends basically on the matrix strength without any reinforcements.

5 Conclusions and prospective recommendations

Aluminum matrix/ Al_2O_3 nanoparticles composites were successfully fabricated by the stir casting process. Different weight fractions of the nanoparticles were introduced to the aluminum matrix and the manufactured composites were investigated to identify the optimum weight fraction at which the best performance is obtained. Considering the systematic methodology proposed for characterizing the Al matrix/ Al_2O_3 nanocomposites mechanical behaviour and functional performance, it could be possible to derive the following conclusions:

1. The distribution of the nanoparticles over the matrix was homogenous at low weight fractions (1wt.% Al_2O_3) with a good adhesion bond between the particles and the aluminum matrix due to good particles wetting by molten matrix and effective mechanical stirring, which attributed to break the agglomerated nanoparticles caused by attraction forces such as Van der Waal forces.
2. The introduction of the nanoparticles to the Al6061 matrix has a significant effect on reducing the α -aluminum grain size and reducing the dendrite arm spacing, as well as the dendrite tip radius by acting as grain growth restrictions during the particle pushing and impeding the solute diffusion during growth.
3. The finest grain size without additional treatment was achieved after the addition of 1wt.% Al_2O_3 (about $17\mu\text{m}$) with lowest % porosity and agglomeration size (0.7% and $2.15\mu\text{m}$ respectively), where the grain size was further refined with lower % porosity and agglomeration size after conducting sever plastic deformation on the 1wt.% Al_2O_3 ($10\mu\text{m}$, 0.23% and $1.9\mu\text{m}$ respectively).
4. Increasing the weight fraction of the nanoparticles more than 2 wt.% Al_2O_3 leads to higher agglomeration size because of increasing the surface area and surface energy of the non-wetting medium, such as alumina in this case, which makes it extremely difficult for mechanical stirring to break the clustering in the melt, and higher % porosity due to higher gas entrapment during mechanical stirring.
5. Higher weight fraction of the nanoparticles (5wt.% Al_2O_3) leads to formation of undesirable intermetallic phases such as β -Fe intermetallic, which hinders the mechanical properties of the AMNCs.
6. The tensile properties of the Al6061 matrix is enhanced after introducing the nanoparticles and reached a maximum at 1wt.% Al_2O_3 compared to the monolithic alloy at room temperature and 300°C with an increase of 50% and 38% in the yield strength. Moreover, the ultimate tensile strength increased by about 32% and 12%. Furthermore, the % elongation was improved by 40% and 16%, while the hardness increased by about 14% from 71.6 to 81.4 HV5 at room temperature.
7. The fatigue strength of the Al 6061 increase after 1wt.% Al_2O_3 addition in the electropolishing state by about 26% and 64% compared to the unreinforced alloy in air and in 3.5% NaCl solution, which could be attributed to the load carrying capabilities offered by the high strength and modulus nanoparticles.

8. Further improvement in the fatigue strength of the AMNCs could be achieved after conducting mechanical surface treatments, such as shot peening and roller burnishing, to reach 37% and 127% after conducting shot peening in air and 3.5% NaCl compared to the electropolished unreinforced alloy, while it reaches 48% and 154% after conducting roller burnishing.
9. The enhancement role of the mechanical surface treatments on the fatigue life is accredited to the induced compressive residual stresses, which restrict the crack propagation caused by the increase in the dislocation density added by the plastic deformation of a specific area. This role flourishes with applying roller burnishing than shot peening because of the lower surface roughness accompanied with roller burnishing compared to shot peening, which hinders the crack initiation stage.
10. The AMNCs (1wt.% Al_2O_3) exhibit higher creep life at 300°C and strength of 40 MPa than the unreinforced alloy. The increase is not only without further mechanical surface treatments, but also after conducting shot peening owing to reducing the dislocation mobility after the addition of the nanoparticles to the Al6061 matrix. Furthermore, the introduction of the nanoparticles might slightly increase the melting point of the produced composite and attribute to raise the material resistance to the creep deformation by hindering the diffusional flow.
11. The dominant creep mechanism in the 1wt.% Al_2O_3 composites is the dislocation creep with true activation energy of 149 and 161 KJ/K.mol for un-peened and peened samples and threshold stress (σ_{th}) of 5, 12.5, 18.5 and 26 for un-peened 1% at 300°C, peened 1% at 300°C, un-peened 1% at 250°C and peened 1% at 250°C.
12. Shot peening could increase the threshold stress compared to the samples without shot peening, owing to the compressive residual stresses induced by shot peening, which could delay the creep deformation and prolong the creep life.
13. AMNCs with low agglomeration and porosity exhibit lower wear rates (based on the weight loss) compared to the unreinforced matrix, where the 1wt.% Al_2O_3 performs an enhancement about 32% compared to the monolithic alloy. Adversely, composites contain 3 and 5 wt.% Al_2O_3 possess the highest weight loss when compared to the other conditions, which can be directly proportional to the tensile properties and hardness of the AMNCs.
14. All composites, except the 3 and 5%, show an improved corrosion resistance compared to the matrix due to the lower tendency of the galvanic corrosion between alumina nanoparticles (high resistivity particles) and aluminum matrix. Moreover, the grain refinement occurred after nanoparticle addition enhances the oxide formation, which is characterized as protective, controlling the anodic reactions, and capable of decreasing corrosion rate.
15. The 1wt.% Al_2O_3 composites were successfully welded by rotary friction welding with two different sets of parameters proposed by Minitab 17.0 using the DoE utilized through

factorial design (friction pressure: 1bar, friction time 1 second, forging pressure 2bar, forging time: 2seconds and rotating speed of 10000 rpm) and Taguchi (friction pressure: 1bar, friction time 2seconds, forging pressure 2 bar, forging time: 2seconds and rotating speed of 9000 rpm) methods.

16. First degree recycling of the AMNCs (using 1wt.% Al_2O_3 samples) gives promising properties could be compared to the fresh fabricated composites.
17. Conducting sever plastic deformation to the AMNCs improves some of their mechanical behavior (such as σ_y , σ_{uts} , and fatigue strength of the electropolished state), but deteriorates their ductility and fatigue strength after conducting mechanical surface treatments such as shot peening and roller burnishing. This effect could be explained by increasing the surface roughness without a signification increase in the compressive residual stresses, which catalyze the crack initiation.
18. The experimental results show good agreement with the proposed model for predicting the mechanical properties of the AMNCs. However, the model needs to be improved by considering the negative effect of porosity and agglomeration on the mechanical properties of the AMNCs.

5.1 Prospective recommendation

1. Studying the recyclability of AMNCs with higher weight fraction of Al_2O_3 nanoparticles than 1wt.% and the second-degree recycling of the AMNCs for the economic purpose.
2. Exploring the creep age-forming of the AMNCs for its importance in the aerospace applications.
3. Understanding the weldability of the AMNCs using another welding techniques, such as friction stir welding, to provide a welding data sheet suitable for any application and geometry.
4. Investigating the behavior of the AMNCs reinforced with different reinforcement according to the experimental procedure used in this work.

This page intentionally left blank

6 References

1. I. J. Polmear, "Light alloys: from traditional alloys to nanocrystals (fourth edition)," Oxford, Elsevier's Science and Technology, 2006, p. 15-21, 29-115.
2. E. Robert, Jr. Sanders, "Technology innovation in aluminum products," JOM, vol.53, no.2, pp. 21-25, 2001.
3. Y.T. Zhao, S.L. Zhang, G. Chen, X.N. Cheng, C.Q. Wang, "In situ (Al₂O₃+Al₃Zr) np/Al nanocomposites synthesized by magneto chemical melt reaction," Compos. Sci Technol, vol.68, pp.1463– 1470, 2008.
4. M. O. Shabani, A. Mazahery, "Application of finite element method for simulation of mechanical properties in a356 alloy," Int. J. Appl. Math, vol. 7, pp. 89, 2011.
5. M.O. Shabani, A. Mazahery, "Microstructural prediction of cast A356 alloy as a function of cooling rate," J. Mater. Sci, vol. 46, pp.6700-6708, 2011.
6. L. Wagner, T. Ludian, M. Wollmann, "Ball-burnishing and roller-burnishing to improve fatigue performance of structural alloys," Engineering against Fracture (S. Pantelakis and C. Rodopoulos, ed), Springer Netherlands, pp.1, 2009.
7. L. Wagner, "Mechanical surface treatments on titanium, aluminum and magnesium alloys," Mater. Sci. Eng. A, pp.263, 1999.
8. <https://paultan.org/2017/04/06/d5-audi-a8-to-use-multi-material-space-frame-chassis/the-new-audi-a8-6/>
9. L. F. Mondolfo, Aluminum Alloys: Structure and Properties. Butterworths, London, 1976.
10. J. Hirsch, B. Skrotzki, and G. Gottstein, Aluminum Alloys: Their Physical and Mechanical Properties. Weinheim, Germany, Wiley-VCH, 2008.
11. P.D. Stobart, Centenary of the Hall and Heroult Processes. International Primary Aluminum Institute, London, 1986.
12. Y. Murakami, "Aluminum-based alloys: a comprehensive treatment," Mat. Sci. and Tech, Vol. 8, pp.216, 1996.
13. E.G. West, "Aluminum – the first 100 years," Met and Mater, vol.20, pp.124, 1986.
14. M.F. Ashby, "On the engineering properties of materials," Acta Metall., vol.37, pp.1273, 1989.
15. L. Ceschini, A. Dahle, M. Gupta, A. Eric, W. Jarfors, S. Jayalakshmi, A. Morri, F. Rotundo, S. Toschi, R. Arvind Singh, Engineering materials: aluminum and magnesium metal matrix nanocomposite. Singapore, Springer, 2017.
16. V.K. Lindroos, M.J. Talvitie, "Recent advances in metal matrix composites," J. Mater. Process. Technol, vol.53, pp.273–284, 1995.
17. W.C. Harrigan, "Commercial processing of metal matrix composites," Mater. Sci. Eng. A, vol.244, pp.75–79, 1998.
18. J.W. Kaczmar, K. Pietrzak, W. Włosiński, "The production and application of metal matrix composite materials," J. Mater. Process. Technol, vol.106, pp.58–67, 2000.
19. D. Miracle, "Metal matrix composites-from science to technological significance," Compos. Sci. Technol, vol. 65, pp.2526–2540, 2005.
20. W.H. Hunt, D.B. Miracle, "Automotive Applications of Metal-matrix Composites," ASM Handbook, Material Park OH, ASM international, vol.21, 2001 pp. 1043– 1049.
21. R.L. Deuis, C. Subramanian, J.M.Y. Yellup, "Dry sliding wear of aluminium composites-a review," Compos. Sci. Technol, vol. 57, 1997.

22. M. Besterci, M. Slesar, G. Jangg, "Structure and properties of dispersion hardened Al-Al4c3 materials," *Powder Met. Int.*, vol. 24, 1992.
23. Y.C. Kang, S.L. Chan, "Tensile properties of nanometric Al₂O₃ particulate-reinforced aluminum matrix composites," *Mater. Chem. Phys.*, vol.85, pp.438–443, 2004.
24. L. Cronjäger, D. Meister, "Machining of fibre and particle-reinforced aluminium," *CIRP Ann. Manuf. Technol.*, vol.41, pp.63–66, 1992.
25. C.J.E. Andrewes, H. Feng, W.M. Lau, "Machining of an aluminum/SiC composite using diamond inserts," *J. Mater. Process. Technol.*, vol.102, pp. 25–29, 2000.
26. T. Ozben, E. Kilickap, O. Cakir, "Investigation of mechanical and machinability properties of SiC particle reinforced Al-MMC," *J. Mater. Process. Tech.*, vol.198, pp.220–225, 2008.
27. I. El-Mahallawi, H. Abdelkader, L. Yousef, "Influence of Al₂O₃ nano-dispersions on microstructure features and mechanical properties of cast and T6 heat-treated Al Si hypoeutectic alloys," *Mat. Sci. Eng. A*, vol.556, pp.76–87, 2012.
28. M.B.D. Ellis, "Joining of aluminium based metal matrix composites," *Int. Mater. Rev.*, vol.41, pp.41–58, 1996.
29. F. Rotundo, L. Ceschini, A. Morri, "Mechanical and microstructural characterization of 2124Al/25 vol.%SiCp joints obtained by linear friction welding (LFW)," *Compos. Part A*, vol.41, pp.1028–1037, 2010.
30. F. Rotundo, A. Marconi, A. Morri, L. Ceschini, "Dissimilar linear friction welding between a SiC particle reinforced aluminum composite and a monolithic aluminum alloy: microstructural, tensile and fatigue properties," *Mater. Sci. Eng. A*, vol.559, pp.852–860, 2013.
31. J.-Y. Lim, S.-I. Oh, Y.C. Kim, "Effects of CNF dispersion on mechanical properties of CNF reinforced A7xxx nanocomposites," *Mater. Sci. Eng. A*, vol.556, pp.337–342, 2012.
32. M. Karbalaei Akbari, O. Mirzaee, H.R. Baharvandi, "Fabrication and study on mechanical properties and fracture behavior of nanometric Al₂O₃ particle-reinforced A356 composites focusing on the parameters of vortex method," *Mater. Des.*, vol.46, pp.199–205, 2013.
33. S.C. Tjong, "Novel nanoparticle-reinforced metal matrix composites with enhanced mechanical properties," *Adv. Eng. Mater.*, vol.9, pp.639–652, 2007.
34. N. Nemati, R. Khosroshahi, M.Emamy, A. Zolriasatein, "Investigation of microstructure, hardness and wear properties of Al-4.5 wt% Cu-TiC nanocomposites produced by mechanical milling," *Mater. Des.*, vol.32, pp.3718–3729, 2001.
35. J. Cadek, K. Kucharova, V. Sustek, "A PM 2124Al-20SiC p composite: disappearance of true threshold creep behaviour at high testing temperatures," *Scr. Mater.*, vol.40, pp.1269–1275, 1999.
36. H.J. Choi, D.H. Bae, "Creep properties of aluminum-based composite containing multi-walled carbon nanotubes," *Scr. Mater.*, vol.65, pp.194–197, 2011.
37. S.A. Sajjadi, H.R. Ezatpour, H. Beygi, "Microstructure and mechanical properties of Al-Al₂O₃ micro and nano composites fabricated by stir casting," *Mater. Sci. Eng. A*, vol.528, pp.8765–8771, 2011.
38. Z.Y. Ma, Y.L. Li, Y. Liang, "Nanometric Si₃N₄ particulate-reinforced aluminum composite," *Mater. Sci. Eng. A*, vol.219, pp.229–231, 1996.
39. P. Luo, D.T. McDonald, W. Xu, S. Palanisamy, M.S. Dargusch, K. Xia, "A modified Hall-Petch relationship in ultrafine-grained titanium recycled from chips by equal channel angular pressing," *Scripta Mater.*, vol.66, pp.785–788, 2012.
40. K.P. So, J.C. Jeong, J.G. Park, "SiC formation on carbon nanotube surface for improving wettability with aluminum," *Compos Sci Technol.*, vol.74, pp.6–13, 2013.

41. M.K. Akbari, H.R. Baharvandi, O. Mirzaee, "Fabrication of nano-sized Al₂O₃ reinforced casting aluminum composite focusing on preparation process of reinforcement powders and evaluation of its properties," *Compos Part B Eng*, vol.55, pp.426–432, 2013.
42. A. Mazahery, H. Abdizadeh, H.R. Baharvandi, "Development of high-performance A356/nano-Al₂O₃ composites," *Mater Sci Eng A*, vol.518, pp.61–64, 2009.
43. S.A. Sajjadi, H.R. Ezatpour, M. Torabi Parizi, "Comparison of microstructure and mechanical properties of A356 aluminum alloy/Al₂O₃ composites fabricated by stir and compo-casting processes," *Mater Des*, vol.34, pp.106–111, 2012.
44. H.R. Ezatpour, S.A. Sajjadi, M.H. Sabzevar, Y. Huang, "Investigation of microstructure and mechanical properties of Al6061-nanocomposite fabricated by stir casting," *Mater Des*, vol.55, pp.921–928, 2014.
45. A. Mazahery, M. Ostadshabani, "Investigation on mechanical properties of nano-Al₂O₃ reinforced aluminum matrix composites," *J Compos Mater*, vol.45, pp.2579–2586, 2011.
46. A. Alizadeh, M. Hajizamani, "Hot extrusion process effect on mechanical behavior of stir cast al based composites reinforced with mechanically milled B 4 C nanoparticles," *J Mater Sci Technol*, vol.27, pp.1113–1119, 2011.
47. D.Wang, M.P. De Cicco, X. Li, "Using diluted master nanocomposites to achieve grain refinement and mechanical property enhancement in as-cast Al-9Mg," *Mater Sci Eng A*, vol.532, pp.396–400, 2012.
48. H. Su, W. Gao, Z. Feng, Z. Lu, "Processing, microstructure and tensile properties of nano-sized Al₂O₃ particle reinforced aluminum matrix composites," *Mater Des*, vol. 36, pp.590–596, 2012.
49. D. McLean, *Grain Boundaries in metals*. Oxford, Clarendon Press, 1957.
50. W.M. Zhong, G. L'Esperance, M. Suéry, "Interfacial Reactions in Al-Mg (5083)/SiCp composites during fabrication and remelting," *Metall Mater Trans A*, vol.26A, pp.2637–2649, 1995.
51. Z. Zhang, D.L. Chen, "Consideration of Orowan strengthening effect in particulate-reinforced metal matrix nanocomposites: A model for predicting their yield strength," *Scripta Mater*, vol.54, pp.1321–1326, 2006.
52. A. Mazahery, M. Shabani, "Mechanical properties of A356 matrix composites reinforced with nano SiC particles," *Strength Mater*, vol.44, pp.686–692, 2012.
53. H. Choi, M. Jones, H. Konishi, X. Li, "Effect of Combined Addition of Cu and Aluminum Oxide Nanoparticles on Mechanical Properties and Microstructure of Al-7Si-0.3 Mg Alloy," *Metall. Mater. Trans. A*, vol.43, pp.738–746, 2011.
54. S. Tahamtan, A. Halvae, M. Emamy, M.S. Zabihi, "Fabrication of Al/A206-Al₂O₃ nano/micro composite by combining ball milling and stir casting technology," *Mater Des*, vol.49, pp.347–359, 2013.
55. A. Dehghan Hamedan, M. Shahmiri, "Production of A356-1wt% SiC nanocomposite by the modified stir casting method," *Mater Sci Eng A*, vol.556, pp.921–926, 2012.
56. S. Purushothaman, J.K. Tien, "Role of back stress in the creep behavior of particle strengthened alloys," *Acta Metall*, vol.26, pp.519, 1978.
57. R.Fernández, G. González-Doncel, "Threshold stress and load partitioning during creep of metal matrix composites," *Acta Mater*, vol.56, pp.2549–2562, 2008.
58. A.H. Monazzah, A. Simchi, S.M.S. Reihani, "Creep behavior of hot extruded Al-Al₂O₃ nanocomposite powder," *Mater Sci Eng A*, vol.527, pp.2567–2571, 2010.
59. Z. Lin, Y. Li, F.A. Mohamed, "Creep and substructure in 5 vol.% SiC-2124 Al composite," *Mater Sci Eng A*, vol.332, pp.330–342, 2002.

60. D. Chellman, S. Langenbeck, "Aerospace applications of advanced aluminium alloys," *J Eng Mater*, vol.77, pp.49–60, 1993.
61. K. Shibata, H. Ushio, "Tribological application of MMCs for reducing engine weight," *J Tribol Int*, vol.27, pp.39–41, 1994.
62. N. Hosseini, F. Karimzadeh, M.H. Abbasi, M.H. Enayati, "Tribological properties of Al6061-Al₂O₃ nanocomposite prepared by milling and hot pressing," *Mater Des*, vol.31, pp.4777–4785, 2010.
63. N. Hosseini, F. Karimzadeh, M.H. Abbasi, M.H. Enayati, "A comparative study on the wear properties of coarse-grained Al6061 alloy and nanostructured Al6061-Al₂O₃ composites," *Tribol Int*, vol.54, pp.58–67, 2012.
64. M.K. Akbari, H.R. Baharvandi, O. Mirzaee, "Nano-sized aluminum oxide reinforced commercial casting A356 alloy matrix: Evaluation of hardness, wear resistance and compressive strength focusing on particle distribution in aluminum matrix," *Compos Part B*, vol.52, pp.262–268, 2013.
65. N. Nemati, R. Khosroshahi, M. Emamy, A. Zolriasatein, "Investigation of microstructure, hardness and wear properties of Al-4.5 wt.% C-TiC nanocomposites produced by mechanical milling," *Mater Des*, vol.32, pp.3718–3729, 2011.
66. M. Samezadeh, M. Emamy, H. Farhangi, "Effects of particulate reinforcement and heat treatment on the hardness and wear properties of AA 2024-MoSi₂ nanocomposites," *Mater Des*, vol.32, pp.2157–2164, 2011.
67. H. Ghasemi Yazdabadi, A. Ekrami, H.S. Kim, A. Simchi, "An investigation on the fatigue fracture of P/M Al-SiC nanocomposites," *Metall Mater Trans A*, vol.44, pp.2662–2671, 2013.
68. T.S. Srivatsan, C. Godbole, M. Paramsothy, M. Gupta, "The role of aluminum oxide particulate reinforcements on cyclic fatigue and final fracture behavior of a novel magnesium alloy," *Mater Sci Eng A*, vol.532, pp.196–211, 2012.
69. T.S. Srivatsan, C. Godbole, M. Paramsothy, M. Gupta, "Influence of nano-sized carbon nanotube reinforcements on tensile deformation, cyclic fatigue, and final fracture behavior of a magnesium alloy," *J Mater Sci*, vol.47, pp.3621–3638, 2011.
70. L.H. Hihara, R.M. Latanision, "Corrosion of metal matrix composites," *Int Mater Rev*, vol.39, pp.245–264, 1994.
71. A. Pardo, M.C. Merino, S. Merino, "Influence of reinforcement proportion and matrix composition on pitting corrosion behaviour of cast aluminium matrix composites (A3xx. x/SiCp)," *Corros Sci*, vol.47, pp.1750–1764, 2005.
72. T.S. Mahmoud, E.Y. El-Kady, A. Al-Shihri, "Mechanical and corrosion behaviours of Al/SiC and Al/Al₂O₃ metal matrix nanocomposites fabricated using powder metallurgy route," *Corros Eng Sci Technol*, vol.47, pp.45–53, 2012.
73. I. El-Mahallawi, K. Eigenfield, F. Kouta. F, "Synthesis and characterization of new cast A356/(Al₂O₃) P metal matrix nano-composites," In: *Proceedings 2nd International Conference Exhibition on Multifunctional nanocomposites Nanomater*, Sharm El Sheikh, Egypt, 2008.
74. E. K. S. Maawad, "Residual stress analysis and fatigue behavior of mechanically surface treated titanium alloys," Ph.D. dissertation. *Mater Sci and Eng Inst*, TU Clausthal, Clausthal-Zellerfeld, Germany, 2012.
75. W. Li, A. Vairis, M. Preuss, T. Ma, "Linear and rotary friction welding review," *Int. Mater. Rev*, vol.61, pp.71-100, 2016.
76. A.V. Muley, S. Aravindan, I.P. Singh, "Nano and hybrid aluminum-based metal matrix composites: an overview," *Manufacturing Rev*, vol.2, pp.15, 2015.

77. F.L. Matthews, R.D. Rawlings, *Composite materials: engineering and science*. New York, CRC Press, 1999.
78. S.R. Bakshi, D. Lahiri, A. Agarwal, "Carbon nanotube reinforced metal composites-a review," *Int. Mater. Rev*, vol.55, pp.42–64, 2010.
79. A. Sanaty-Zadeh, "Comparison between current models for the strength of particulate-reinforced metal matrix nanocomposites with emphasis on consideration of Hall-Petch effect," *Mat. Sci. Eng. A*, vol.531, pp.112–118, 2012.
80. R. Casati, M. Vedani, "Metal Matrix Composites Reinforced by Nano-Particles—A Review," *Metals*, vol.4, pp.65-83, 2014.
81. S. Donthamsetty, N.R. Damera, P.K. Jain, "Ultrasonic cavitation assisted fabrication and characterization of A356 metal matrix nanocomposite reinforced with Sic, B4C, CNTs," *Asian. Inter. J. Sci. Tech. in Pro.Manu. Eng*, vol.2, pp.27–34, 2009.
82. G. Cao, J. Kobliska, H. Konishi, X. Li, "Tensile properties and microstructure of SiC nanoparticle-reinforced Mg-4Zn alloy fabricated by ultrasonic cavitation-based solidification processing," *Metall Mater Trans A*, vol.39, pp.880–886, 2008.
83. G. Cao, H. Choi, J. Oportus, "Study on tensile properties and microstructure of cast AZ91D/AlN nanocomposites," *Mater Sci Eng A*, vol.494, pp.127–131, 2008.
84. J. Lan, Y. Yang, X. Li, "Microstructure and microhardness of SiC nanoparticles reinforced magnesium composites fabricated by ultrasonic method," *Mater Sci Eng A*, vol.386, pp.284–290, 2004.
85. G. Cao, H. Konishi, X. Li, "Mechanical properties and microstructure of SiC-reinforced Mg-(2,4) Al-1Si nanocomposites fabricated by ultrasonic cavitation based solidification processing," *Mater Sci Eng A*, vol.486, pp.357–362, 2008.
86. S. Mula, P. Padhi, S.C. Panigrahi, "On structure and mechanical properties of ultrasonically cast Al-2 % Al₂O₃ nanocomposite," *Mater Res Bull*, vol.44, pp.1154–1160, 2009.
87. M. Qian, A. Ramirez, "Ultrasonic grain refinement of magnesium and its alloys," *Alloy Des Process Prop*, pp. 163–186, 2011.
88. X. Li, Y. Yang, X. Cheng, "Ultrasonic-assisted fabrication of metal matrix nanocomposites," *J Mater Sci*, vol.39, pp.3211–3212, 2004.
89. Z. Zhang, D.L. Chen, "Contribution of Orowan strengthening effect in particulate-reinforced metal matrix nanocomposites," *Mat. Sci. Eng. A*, vol.483–484, pp.148–152, 2008.
90. H. Choi, W. Cho, X.C. Li, "Scale-up ultrasonic processing system for batch production of metallic nanocomposites," In: *AFS Proceedings*, Schaumburg, Germany, pp. 1–7, 2013.
91. L. Tham, M. Gupta, L. Cheng, "Influence of processing parameters on the near-net shape synthesis of aluminium-based metal matrix composites," *J Mater Process Technol*, vol.89–90, pp.128–134, 1999.
92. Y. Yang, J. Lan, X. Li, "Study on bulk aluminum matrix nano-composite fabricated by ultrasonic dispersion of nano-sized SiC particles in molten aluminum alloy," *Mater Sci Eng A*, vol.380, pp.378–383, 2004.
93. K. Ho, M. Gupta, T. Srivatsan, "The mechanical behavior of magnesium alloy AZ91 reinforced with fine copper particulates," *Mater Sci Eng A*, vol.369, pp.302–308, 2004.
94. M. Gupta, N.M.L. Sharon, "Magnesium, Magnesium Alloys, and Magnesium Composites. Weinheim, Germany, Wiley, 2011.
95. A. Mazahery, M.O. Shabani, "Characterization of cast A356 alloy reinforced with nano SiC composites," *Trans Nonferrous Met Soc China*, vol.22, pp.275–280, 2012.
96. S.W. Lai, D.D.L. Chung, "Fabrication of particulate aluminium-matrix composites by liquid metal infiltration," *J Mater Sci*, vol.29, pp.3128–3150, 1994.

97. S. Zhou, X. Zhang, Z. Ding, "Fabrication and tribological properties of carbon nanotubes reinforced Al composites prepared by pressureless infiltration technique," *Compos Part A Appl Sci Manuf*, vol.38, pp.301–306, 2007.
98. S. Jayalakshmi, "Processing and characterization of magnesium alloys (AM100 & ZC63) and their alumina short fiber reinforced composites using squeeze casting and squeeze infiltration techniques," PhD Thesis, Indian Institute of Science (IISc), Bangalore, 2002.
99. L. Wang, P. Turnley, G. Savage, "Gas content in high pressure die castings," *J Mater Process Technol*, vol.211, pp.1510–1515, 2011.
100. A. Long, D. Thornhill, C. Armstrong, D. Watson, "Predicting die life from die temperature for high pressure dies casting aluminium alloy," *Appl Therm Eng*, vol.44, pp.100–107, 2012.
101. Z. Fan, "Semisolid metal processing," *Int Mater Rev*, vol.47, pp.49–86, 2002.
102. M. Kenney, J. Courtois, R. Evans, "Semisolid metal casting and forging," *Met. Handb.* 9th ed. ASM International, Metals Park OH, USA, pp.327–338, 1998.
103. M.R. Kamali Ardakani, S. Khorsand, S. Amir Khanlou, M. Javad Nayyeri, "Application of compocasting and cross accumulative roll bonding processes for manufacturing high strength, highly uniform and ultra-fine structured Al/SiCp nanocomposite," *Mater Sci Eng A*, vol.592, pp.121–127, 2014.
104. B. Abbasipour, B. Niroumand, S.M. Monir Vaghefi, "Compocasting of A356-CNT composite," *Trans Nonferrous Met Soc China*, vol.20, pp.1561–1566, 2010.
105. A. Kawabe, A. Oshida, T. Toda, Hiroyuki, Kobayashi, "Fabrication process of metal matrix composite with nano-size SiC particle produced by vortex method," *J. Japan Inst. Light Met*, vol.49, pp.149–154, 1999.
106. H. Su, W. Gao, H. Zhang, "Study on preparation of large sized nanoparticle reinforced aluminium matrix composite by solid-liquid mixed casting process," *Mater. Sci. Technol*, vol.28, pp.178–183, 2012.
107. B.F. Schultz, J.B. Ferguson, P.K. Rohatgi, "Microstructure and hardness of Al₂O₃ nanoparticle reinforced Al–Mg composites fabricated by reactive wetting and stir mixing," *Mater. Sci. and Eng. A*, vol.530, pp.87–97, 2011.
108. A. Ahmed. "Coating and surface treatment for novel biomedical implants and their corrosion resistance," PhD thesis, Institute for materials engineering, Technical University Clausthal, Clausthal-Zellerfeld, Germany, 2017.
109. http://emrkt.unimiskolc.hu/projektek/adveng/home/kurzus/korsz_anyagtech/1_konzultacio_elemei/wear_testing_measurement.htm
110. M. Abdulstaar, M. Mhaede, M. Wollmann, L. Wagner, "Effects of shot peening and ball-burnishing on the fatigue performance of AA 6082 Shot Peening and Other Mechanical Surface Treatments," *Sci and Apps*, 2014.
111. M. Abdulstaar, M. Mhaede, M. Wollmann, L. Wagner, "Corrosion behaviour of Al 1050 severely deformed by rotary swaging," *Mater and Des*, vol.57, pp.325–329, 2014.
112. M. Abdulstaar, M. Mhaede, M. Wollmann, L. Wagner, "Fatigue behavior of commercially pure aluminum processed by rotary swaging," *Jour of Mater Sci*, vol.49, pp.1138–1143, 2014.
113. L. Wagner, M. Wollmann, "A unique forum of all aspects of mechanical surface treatments for improving fatigue behavior of metallic components," *MFN*, vol. 14, pp.10–11, 2013.
114. M. Abdulstaar, M. Mhaede, M. Wollmann, L. Wagner, "Pre-corrosion and surface treatments effects on the fatigue life of AA6082 T6," *Adv Eng Maters*, vol.15, pp.1002–1006, 2013.

115. A. Flejszar, T. Ludian, A. Mielczarek, W. Riehemann, L. Wagner, "Effects of shot peening on internal friction in CP aluminum and aluminum alloy 6008," *Inter Jour of Maters Res*, vol. 6, pp.892, 2009.
116. M. Basha, "Thermal and /or mechanical treatment effects on rotary and orbital friction welding," PhD thesis, Institute for materials engineering, Technical University Clausthal, Clausthal-Zellerfeld, Germany, 2018.
117. A. Griger, V. Stefaniay, "Equilibrium and non-equilibrium intermetallic phases in Al-Fe and Al-Fe-Si Alloys," *Jour of Maters Sci*, vol.31, pp.6645-6652, 1996.
118. Y. Liu, M. Liu, L. Luo, J. Wang, C. Liu, "The solidification behavior of aa2618 aluminum alloy and the influence of cooling rate," *Maters*, vol.7, pp.7875-7890, 2014.
119. V. D. Malakhova, D. Panahi, M. Gallerneault, "On the formation of intermetallics in rapidly solidifying al_fe_si alloys," *CALPHAD*, vol.34, pp.159-166, 2010.
120. M. Mahta, M. Emamy, X. Cao, J. Campbell, "Overview of β -Al₅FeSi phase in Al-Si alloys," *Maters Sci Res Tren*, vol.37, pp.251-271, 2008.
121. V. M. Sreekumar, N. H. Babu, D. G. Eskin, Z. Fan, "Structure–property analysis of in-situ Al–MgAl₂O₄ metal matrix composites synthesized using ultrasonic cavitation," *Mater Sci and Eng A*, vol.628, pp.30-40, 2015.
122. S. Suresh. *Fundamentals of Metal-Matrix Composites*. USA, Elsevier, 2013.
123. N. Chawla, Y. Shen, "Mechanical behavior of particle reinforced metal matrix composites," *Adv Eng Maters*, vol.3, pp. 357-370, 2001.
124. R.O. Scattergood, C.C. Koch, K.L. Murty, D. Brenner, "Strengthening mechanisms in nanocrystalline alloys," *Mater Sci and Eng A*, vol.493, pp. 3-11, 2008.
125. P. Ma, Y. Jia, P. Gokuldoss, Z. Yu, S. Yang, J. Zhao, C. Li, "Effect of Al₂O₃ Nanoparticles as Reinforcement on the Tensile Behavior of Al-12Si Composites," *Met*, vol.7, pp. 359-369, 2017.
126. Y. Kondo, C. Sakae, M. Kubota, T. Kudou, "The effect of material hardness and mean stress on the fatigue limit of steels containing small defects," *Fatig & Frac of Eng Maters & Strs*, vol. 26, pp. 675–682, 2003.
127. A. Vinogradov, S. Hasshimoto, "Fatigue of severely deformed metals," *Adv Eng Maters*, vol.5, pp. 351-358, 2003.
128. C. Teichmann, B. Eigenmann, M. Mhaede, L. Wagner, "Fatigue performance of shot peened cp-ti: effect of prior severe plastic deformation," *ICSP-12*, Goslar, Germany, 2014.
129. S.Spigarelli, "Creep of aluminium and aluminium alloys," *TALAT Lecture 1253*, European Aluminium Association, 1999.
130. Y. Ma, T. G. Langdon, "Creep behavior of an Al-6061 metal matrix composite produced by liquid metallurgy processing," *Maters Sci and Eng A*, vol. 230, pp. 183-187, 1997.
131. M. Ashby, D. Jones, "Engineering Materials 1: An introduction to their properties and applications," Oxford, Great Britain, Butterworth-Heinemann, 2002.
132. K. M. B. Taminger, "Analysis of creep behavior and parametric models for 2124 al and 2124 al + sicw composite," M.S. thesis, Virginia Polytechnic Institute and State University, Virginia, USA, 1999.
133. M. Abbass, K. Hassan, A. Alwan, "Study of corrosion resistance of aluminum alloy 6061/sic composites in 3.5% nacl solution," *Inter Jour of Maters, Mechs and Manu*, vol. 3, pp. 31-35, 2015.
134. N. Muhammad, Y. Manurung, "Design parameters selection and optimization of weld zone development in resistance spot welding," *Inter Jour of Mech, Aero, Indus, Mechat and Manu Eng*, vol.6, pp. 2464-2469, 2012.

135. S.T. Selvamani, K. Palanikumar, "Optimizing the friction welding parameters to attain maximum tensile strength in AISI 1035 grade carbon steel rods," *Measur*, vol.53, pp.10-21, 2014.
136. A. Pachal1, A. Bagesar, "Taguchi Optimization of Process Parameters in Friction Welding of 6061 Aluminum Alloy and 304 steel: A Review," *Explo Res and Inno*, vol.3, pp.2250-2259, 2013.
137. B. Jeslin, M. Kumar, P. G. Venkatakrishnan, "Parameter optimization on friction welding of aluminium alloy 6082t6 & copper," *IJIRT*, vol.1, pp.1547-1551, 2015.
138. R. McAndrew, P. Colegrove, B. Flipo, C. Bühr, "3D modelling of Ti-6Al-4V linear friction welds," *Sci & Tech of Weld & Joi*, vol. 22, pp.496-504, 2017.

List of Figures

Figure 1-1: Research flow chart [8]	4
Figure 1-2: Research methodology	5
Figure 2-1: Al-Mg-Si section from Al to Mg ₂ Si [12]	8
Figure 2-2: Representative tensile engineering stress-strain curves under tension for A356–Al ₂ O ₃ [15]	12
Figure 2-3: Conventional shot peening process [74]	15
Figure 2-4: Arc height vs. exposure time scheme [74]	16
Figure 2-5: Ball-burnishing process [74]	17
Figure 2-6: Ultrasonic assisted casting set-up [92]	19
Figure 2-7: Schematic of the DMD process [93]	20
Figure 2-8: Typical stir casting experimental set-up [44,15]	23
Figure 3-1: A Schematic drawing of the melting furnace and mechanical stirrer, b. Photograph of the furnace and the stirrer, c. The steel mold, and c. The casted sample	31
Figure 3-2: Schematic picture of a typical swaging unit [108]	32
Figure 3-3: Tensile test sample dimensions	33
Figure 3-4: (A) The fatigue test specimen and (B) Corrosion fatigue cell	35
Figure 3-5: Creep-rupture test machine and specimen.	36
Figure 3-6: Schematic of a pin-on-disc wear test and the arrangement of samples [109]	37
Figure 3-7: The shot peening machine and a schematic drawing of the bombarding of the shots with the sample.	38
Figure 3-8: Hydraulic roller-burnishing machine.	38
Figure 3-9: Example for calculation of the Almen intensity at 4 bars using SSCS program.	39
Figure 3-10: Number of cycles to failure of different Almen intensities and burnishing pressures conditions	40
Figure 3-11: Surface roughness of selected samples under different surface treatments.	41
Figure 3-12: Residual stresses profile for shot peened and roller burnished conditions	42
Figure 3-13: Microhardness of shot peened and roller burnished samples	42
Figure 3-14: Hole-drilling machine and rosette [74]	44
Figure 3-15: Schematic diagram of polarization of the three-electrode cell [108]	45
Figure 3-16: The used rotary friction welding machine RSM 200 [116]	45
Figure 4-1: Microstructure of As-Cast Al6061; A. using general purpose etchant at magnification of 200 and 500X, B. using color etchant at magnification of 200 and 500X	47
Figure 4-2: SEM and EDX spectrum of the as-cast samples; A. SEM micrograph of the matrix, B. SEM micrograph of the Mg ₂ Si precipitates in dark color, C. is the EDX of the as-cast matrix and D. is the EDX of the Mg ₂ Si precipitates	48
Figure 4-3: EDX of some Fe ₃ SiAl ₁₂ and Fe ₂ Si ₂ Al ₉ precipitates presented in as-cast micrographs	49
Figure 4-4: Microstructure of Al6061 reinforced by 1wt.% Al ₂ O ₃ : A. using general purpose etchant at 200 and 500X, B. using color etchant at 200 and 500X	50
Figure 4-5: SEM and EDX of 1% condition showing some porosity and agglomeration of Al ₂ O ₃ nanoparticles	51
Figure 4-6: Microstructure of composites; A. 2wt.% using general purpose etchant at 200 and 500X, B. 2wt.% using color etchant at 200 and 500X, C. 3wt.% using general purpose etchant at 200 and 500X, D. 3wt.% using color etchant at 200 and 500X	52
Figure 4-7: Microstructure of 5wt.% Al ₂ O ₃ condition: A. using general purpose etchant at 200 and 500X, B. color etchant at 200 and 500X	53
Figure 4-8: A. Chinese script and B. thin plates of β-Fe intermetallic, C. microhardness of the β-Fe intermetallic and the matrix	54
Figure 4-9: Microstructure of recycled 1wt.% Al ₂ O ₃ : A. using general purpose etchant at 200 and 500X, B. using color etchant at 200 and 500X	55
Figure 4-10: SEM and EDX of the recycled 1wt.% Al ₂ O ₃	56

Figure 4-11: Microstructure of Al6061 reinforced 1wt.% Al ₂ O ₃ under sever plastic deformation: A. using general purpose etchant at magnification of 200 and 500X, B. using color etchant at magnification of 200 and 500X	57
Figure 4-12: The mean grain diameter in μm and the grain size number of different conditions of Al ₂ O ₃ addition	58
Figure 4-13: SEM micrographs show the porosity in the monolithic alloy and the reinforced AMNCs with different additions of nanoparticles	60
Figure 4-14: The percent porosity, average porosity and agglomeration size marked at the fabricated composites	61
Figure 4-15: Tensile properties and hardness of the monolithic matrix and reinforced Al6061 with nanoparticles; A. at room temperature. B. at 300°C	63
Figure 4-16: S-N curves of electropolished samples; A.in air and B. in 3.5% NaCl, and C. contour plot of the weight fraction vs yield strength and the fatigue strength in air of the electropolished samples	67
Figure 4-17: Surface roughness of the electropolished sample	69
Figure 4-18: The microhardness of the electropolished samples	69
Figure 4-19: S-N curves of the electropolished monolithic alloy against 1wt.%, 1%SPD and Recycled composite; A. in air and B. in 3.5% NaCl	71
Figure 4-20: Microhardness of the electropolished monolithic alloy against 1wt.%, 1%SPD and Recycled composite	71
Figure 4-21: The surface roughness of the electropolished monolithic alloy against 1wt.%, 1%SPD and Recycled composites	72
Figure 4-22: S-N curves of shot peened samples; A:in air, B: in 3.5% NaCl, and C. contour plot of the weight fraction vs yield strength and the fatigue strength in air of the shot peened samples	73
Figure 4-23: The microhardness of the shot peened samples	74
Figure 4-24: The residual stresses of the shot peened samples	75
Figure 4-25: The surface roughness of the shot peened samples	75
Figure 4-26: S-N curves of the shot peened monolithic alloy against 1wt.%, 1%SPD and Recycled composite; A. in air and B. in 3.5% NaCl	76
Figure 4-27: The surface roughness of the shot peened monolithic alloy against 1wt.%, 1%SPD and Recycled composite	77
Figure 4-28: The residual stresses of the shot peened monolithic alloy against 1wt.%, 1%SPD and Recycled composite	78
Figure 4-29: The microhardness the shot peened monolithic alloy against 1wt.%, 1%SPD and Rec composite	78
Figure 4-30: S-N curves of the roller burnished samples; A: in air and B: in 3.5% NaCl, and C. contour plot of the weight fraction vs yield strength and the fatigue strength in air of the roller burnished samples	80
Figure 4-31: The surface roughness of the roller burnished samples	81
Figure 4-32: Residual stresses of the roller burnished samples	82
Figure 4-33: Microhardness of the roller burnished samples	83
Figure 4-34: S-N curves of the roller burnished monolithic alloy against 1wt.%, 1%SPD and Recycled composite; A. in air and B. in 3.5% NaCl	84
Figure 4-35: The surface roughness of the roller burnished monolithic alloy against 1wt.%, 1%SPD and Recycled composites	85
Figure 4-36: The residual stresses of the roller burnished monolithic alloy against 1wt.%, 1%SPD and Recycled composites	86
Figure 4-37: The microhardness of the roller burnished monolithic alloy against 1wt.%, 1%SPD and Recycled composites	86
Figure 4-38: %Total plastic strain vs run time of monolithic alloy against composites; A. un-peened and B. peened samples	87
Figure 4-39: The minimum creep rate vs the run time; A. un-peened samples, B. shot peened samples and C. comparison of the minimum creep rate magnitude between peened and un-peened specimens	89

Figure 4-40: The relaxation modulus vs the run time; A. un-peened samples and B. peened samples	91
Figure 4-41: The creep compliance vs the run time; A. un-peened samples and B. peened samples	92
Figure 4-42: Deformation mechanisms at different stresses and temperatures [131]	93
Figure 4-43: % Total plastic deformation of 1% Al ₂ O ₃ subjected to different peening medium and Almen intensities vs the run time under constant stress of 40MPa	94
Figure 4-44: Surface roughness of 1% Al ₂ O ₃ subjected to different peening medium and Almen intensities	94
Figure 4-45: Minimum creep rate vs applied stress of un-peened and peened Al6061 reinforced with 1wt.% Al ₂ O ₃	96
Figure 4-46: Variation of $\epsilon^{ol/3}$ with σ on linear axes. showing evidence for the presence of a threshold stress, σ_{th} .	97
Figure 4-47: Wear rates of the monolithic and different composites based on the weight loss, and B. contour plot of the weight fraction vs yield strength and the wear resistance	98
Figure 4-48: Potentiodynamic polarization curves of the as-cast Al6061 matrix and composites	99
Figure 4-49: Optical micrographs of the surface topography after electrochemical corrosion in 3.5% NaCl solution; A. for the 1% condition and B. for the 5% condition	100
Figure 4-50: Normal probability plot of standardized effects for the ultimate tensile strength	104
Figure 4-51: Normal probability plot of standardized residuals for weld strength	105
Figure 4-52: A. The main effect of the linear and interactions between the welding parameters on the ultimate tensile strength, B. Contour plots of the ultimate tensile strength	106
Figure 4-53: The effect of parameters Ps,ts, Pr, tr and rpm on the tensile strength of the welded joint and S/N ratio of the responses	108
Figure 4-54: Optical micrographs of the weld zone at magnification 50X of samples 12 and 32 (sub-micrographs are the flash shape of each sample)	110
Figure 4-55: Unbonded regions at corner of the weld interface of samples 12 and 32	111
Figure 4-56: The EDX linear scanning of samples 12 and 32 over 60 μ m of the weld interface	112
Figure 4-57: The microhardness distributions across the weld line of samples 12 and 32	113
Figure 4-58: Validation of the proposed equation based on the work carried out in [80]	115
Figure 4-59: Validation of the proposed equation based on the experimental work carried out at 2wt.% Alumina	115
Figure 4-60: Validation of the proposed equation based on the work carried out in [43]	116
Figure 4-61: Minitab run outputs; a. residual plots for final strength, b. normal plot of the standardized effects at $\alpha=0.5$	117
Table 2-1: Al6061 Chemical composition [9]	9
Table 2-2: Mechanical properties of Al6061 at O, T4, and T6 temper conditions [14]	9
Table 3-1: Chemical of Al6061 alloy (wt.%)	29
Table 3-2: Al ₂ O ₃ nanoparticles properties	29
Table 3-3: Samples designation	31
Table 3-4: The corresponding Almen intensity at different pressures	39
Table 4-1: Chemical composition of the matrix and the Mg ₂ Si precipitates for the as-cast condition	49
Table 4-2: I_{corr} , E_{corr} and corrosion rate of the as-cast Al6061 matrix and composites	100
Table 4-3: Initial weld samples optimization based on the tensile properties	101
Table 4-4: The DoE matrix and corresponding results of the full factorial design	102
Table 4-5: ANOVA of the regression model	104
Table 4-6: The estimated coefficients of the regression model	105
Table 4-7: Taguchi parameters and design levels	107
Table 4-8: Taguchi experimental suggestions based on the process variables and levels	107

<i>Table 4-9: Analysis of Variance for SN ratios and Response table for signal to noise ratios</i>	<u>109</u>
<i>Table 4-10: Tensile properties of the samples from factorial design and Taguchi</i>	<u>109</u>
<i>Table 4-11: The boundary conditions used for the Minitab variables</i>	<u>116</u>

Curriculum vitae

Name: Othman Mohamed

Date of birth: 26.11.1986

Place of birth: Egypt

Education

04/2014 - present: Clausthal University of Technology (TU Clausthal), Institute of Materials Science and Engineering (IWW)

Target degree: Doctor of Engineering (Dr.-Ing.)

10/2009 - 11/2012: Cairo University, Faculty of Engineering, Egypt

Degree: Master's degree (M.Sc.) in metallurgical engineering

09/2003 - 07/2008: Cairo University, Faculty of Engineering, Egypt

Degree: Bachelor's degree (M.Sc.) in metallurgical engineering

Professional Experience

Since 04.2015: Doctoral candidate and research assistant, IWW, TU Clausthal

Since 02.2009: Teaching and research assistant, Cairo University, Faculty of Engineering, Egypt

08.2009 – 06.2014 Production Engineer (Copper production), EMW, Egypt

Scholarships/Awards

German-Egyptian long-term research fellowship "GERLS" -DAAD, for PhD in Germany (2014)

- Cairo University Award for Excellence (2008)
- Cairo University Award for Outstanding Study Achievements (2005)
- IAESTE scholarship for summer training at TU Freiberg (2007)
- Science and Technology Development Fund (STDF) Fourth Year Endorsement Fund, Egypt. Project: Development and production of molds. Participation: As coordinator with Prof. Dr. med. Iman El Mahallawi and Dr. Waleed Khalifa. Funds: 100,000 LE
- Innovation in Teaching and Learning Awards (INTLA), Egypt • Project: Development and Production of Molds. Participation: As coordinator with Prof. Dr. med. Iman El Mahallawi and Dr. Waleed Khalifa • Rank: First in the Engineering category; Third, in all categories

Further Qualifications

Languages: Arabic (native language), German and English

Computer skills: MS office, Autodesk INVENTOR, AutoCAD – Minitab 18